LI@C$_{60}$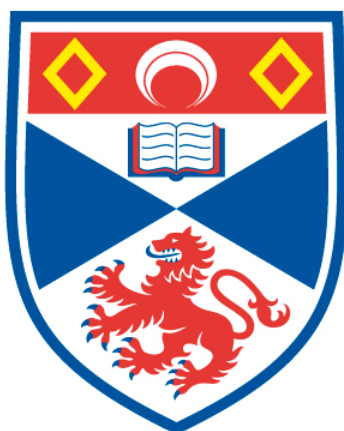, THE MOLECULAR MARACA : EXPLORING THE PROPERTIES OF LITHIUM ENDOHEDRAL FULLERENES ON TRANSITION METAL SURFACES FOR POTENTIAL USE IN MOLECULAR ELECTRONICSTITLE

Henry James Chandler

A Thesis Submitted for the Degree of PhD
at the
University of St Andrews

2020

Full metadata for this thesis is available in
St Andrews Research Repository
at:
http://research-repository.st-andrews.ac.uk/

Identifiers to use to cite or link to this thesis:

DOI: https://doi.org/10.17630/10023-20917
http://hdl.handle.net/10023/20917

Li@C$_{60}$, The Molecular Maraca:

Exploring the Properties of Lithium Endohedral

Fullerenes on Transition Metal Surfaces for Potential

Use in Molecular Electronics

Henry James Chandler
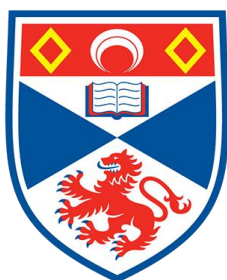
University of
St Andrews

This thesis is submitted in partial fulfilment for the degree of

Doctor of Philosophy (PhD)

at the University of St Andrews

July 2020

Declarations

Candidate's declaration

I, Henry James Chandler, do hereby certify that this thesis, submitted for the degree of PhD, which is approximately 62,000 words in length, has been written by me, and that it is the record of work carried out by me, or principally by myself in collaboration with others as acknowledged, and that it has not been submitted in any previous application for any degree.

I was admitted as a research student at the University of St Andrews in January 2016.

I received funding from an organisation or institution and have acknowledged the funder(s) in the full text of my thesis.

Date   27/07/20   Signature of candidate

Supervisor's declaration

I hereby certify that the candidate has fulfilled the conditions of the Resolution and Regulations appropriate for the degree of PhD in the University of St Andrews and that the candidate is qualified to submit this thesis in application for that degree.

Date   27/07/20   Signature of supervisor

Permission for publication

In submitting this thesis to the University of St Andrews we understand that we are giving permission for it to be made available for use in accordance with the regulations of the University Library for the time being in force, subject to any copyright vested in the work not being affected thereby. We also understand, unless exempt by an award of an embargo as requested below, that the title and the abstract will be published, and that a copy of the work may be made and supplied to any bona fide library or research worker, that this thesis will be electronically accessible for personal or research use and that the library has the right to migrate this thesis into new electronic forms as required to ensure continued access to the thesis.

I, Henry James Chandler, confirm that my thesis does not contain any third-party material that requires copyright clearance.

Henry Chandler   July 2020

The following is an agreed request by candidate and supervisor regarding the publication of this thesis:

Printed copy

Embargo on all of print copy for a period of 2 years on the following ground(s):

- Publication would preclude future publication

Supporting statement for printed embargo request

We are currently in discussion over further publication of work contained herein.

Electronic copy

Embargo on all of electronic copy for a period of 2 years on the following ground(s):

- Publication would preclude future publication

Supporting statement for electronic embargo request

We are currently in discussion regarding further publication of work contained herein.

Title and Abstract

- I agree to the title and abstract being published.

Date   27/07/20   Signature of candidate

Date   27/07/20   Signature of supervisor

<u>Underpinning Research Data or Digital Outputs</u>

Candidate's declaration

I, Henry James Chandler, understand that by declaring that I have original research data or digital outputs, I should make every effort in meeting the University's and research funders' requirements on the deposit and sharing of research data or research digital outputs.

Date   27/07/20   Signature of candidate

Permission for publication of underpinning research data or digital outputs

We understand that for any original research data or digital outputs which are deposited, we are giving permission for them to be made available for use in accordance with the requirements of the University and research funders, for the time being in force.

We also understand that the title and the description will be published, and that the underpinning research data or digital outputs will be electronically accessible for use in accordance with the license specified at the point of deposit, unless exempt by award of an embargo as requested below.

The following is an agreed request by candidate and supervisor regarding the publication of underpinning research data or digital outputs:

Embargo on all of electronic files for a period of 2 years on the following ground(s):

- Publication would preclude future publication

Supporting statement for embargo request

We are currently in discussion regarding further publication of data contained herein.

Date   27/07/20   Signature of candidate

Date   27/07/20   Signature of supervisor

<u>Acknowledgements</u>

A huge number of people have helped me through the 4 years that I've been working on this PhD. What follows is a special mention to those who went above and beyond.

Firstly, my thanks go to Dr Renald Schaub who has been a better mentor than I could hope for. His endless enthusiasm for this project is second only to his honest encouragement. He genuinely cares to see hard work rewarded for all who cross his path. We in his research group consider ourselves very lucky to have him as a supervisor. On that note, I'd like to thank all the members, past and present, of the Schaub group. With a special mention to Michael-John who diligently passed on his vast experience with the microscope.

Thank you to the technical staff in the Chemistry and Physics departments, but especially the Cryo-Gents. Without them my experiments would have warmed up numerous times.

For their contributions to various scientific discussions, I'd like to thank Professor Eleanor Campbell, Minas Stefanou and my colleagues within the surface science department.

My undying gratitude goes to Ben King who printed 3D models of Li@C_{60} for myself and Renald, and as a result directly facilitated a number of eureka moments. Similarly, thanks to Dr Rodrigo Ortiz de la Morena whose animated Li@C_{60} has been invaluable during presentations. Discussing 3D molecules is much easier with a visual aid.

10 years is a long time to be a member of the St Andrews community. I have met some truly wonderful people who are responsible for some of my fondest memories. A special mention goes to my various flatmates for dealing with the tempestuous mood swings, and to those who taught me that icosahedrons could also be a source of fun: Team tiny, VVV and Critical Role.

Lastly, my parents, my sister and my girlfriend are the foundation upon which this thesis was written. Renald made this PhD possible, but without these 4 I would have stopped long ago. They encouraged me when I struggled and celebrated each little achievement like it was a Nobel Prize. I dedicate this thesis to you: Philip, Martine, Natalie and Chloe.

<u>Funding</u>

Abbreviations

Li@C_{60}	Lithium endohedral fullerene
C_{60}	Buckminsterfullerene
UHV LT-STM	Ultra-high vacuum low temperature scanning tunnelling microscope
STM	Scanning tunnelling microscope (microscopy)
c.c. STM	Constant current scanning tunnelling microscopy
c.h. STM	Constant height scanning tunnelling microscopy
STS	Scanning tunnelling spectroscopy
c.h. *dI/dV* STS	Constant height scanning tunnelling spectroscopy
c.c. *dI/dV* STS	Constant current scanning tunnelling spectroscopy
SAMO	Super-atom molecular orbital
PES	Photoelectron spectroscopy
DFT	Density functional theory
TDDFT	Time dependent density functional theory
LDOS	Local density of states
C5-faces	Pentagonal faces on C_{60}
C6-faces	Hexagonal faces on C_{60}
fcc	Face-centred cubic
hcp	Hexagonal close-packed
HOMO	Highest occupied molecular orbital
LUMO	Lowest unoccupied molecular orbital
NFE	Nearly free electron
C6-fullerene	Fullerene adsorbed to a substrate by a C6-face
6:6-fullerene	Fullerene adsorbed to a substrate by a 6:6-bond
5:6-fullerene	Fullerene adsorbed to a substrate by a 5:6-bond
C-fullerene	Fullerene adsorbed to a substrate by a single C-atom
M-	Majority adsorption orientation
m-	Minority adsorption orientation

Abstract

The following thesis describes the exploration of lithium endohedral fullerenes (Li@C_{60}) on Au(111) and Cu(110)-(2×1)O utilising an ultra-high vacuum low temperature scanning tunnelling microscope (UHV LT-STM). In collaboration with researchers from the University of Edinburgh and the University of Liège, the effect of Li-encapsulation on the electronic structure of C_{60} has been experimentally identified on single molecules for the first time, with particular attention to the superatom molecular orbitals (SAMOs). It was hypothesised these would stabilise due to the hybridisation of orbitals from the carbon cage and lithium. However, since the Li is known to stabilise in an off-centre position within the C_{60}, this asymmetry induces a non-degenerate stabilisation of the SAMOs. This stabilisation is analysed with scanning tunnelling spectroscopy (STS), and our conclusions are confirmed by photoelectron spectroscopy (PES) and time dependent density functional theory (TDDFT) data provided by our collaborators.

Once the electronic structure is understood, the experiments detailed herein turn towards studying the Li@C_{60} for potential as a multi-state single molecular switch. Upon identifying a set of parameters which allow the repeated, and reversible, manipulation of Li@C_{60}, the process is studied methodically and reveals that Li@C_{60} can be switched between 14 distinct states. This is the highest number of discrete, accessible states to be observed on a single molecule switch to date. A mixture of scanning tunnelling microscopy (STM) and spectroscopy (STS) is required to identify these states, and high manipulation biases and tunnelling currents are needed to activate the switch. Since these parameters are orders of magnitude higher than those typically used, a new mechanism is required to describe the process. The suggestion made here is that resonant tunnelling electrons couple with the $p_{x,y}$-SAMOs to bypass the carbon cage thus activating the encapsulated Li and avoiding vibrational excitation of the C_{60}. Upon exciting the Li, it rattles around the interior of the fullerene before randomly stabilising in one of the identified 14 states.

List of Publications

(1) Stefanou, M.; Chandler, H. J.; Mignolet, B.; Williams, E.; Nanoh, S. A.; Thompson, J. O. F.; Remacle, F.; Schaub, R.; Campbell, E. E. B. Angle-Resolved Photoelectron Spectroscopy and Scanning Tunnelling Spectroscopy Studies of the Endohedral Fullerene Li@C_{60}. *Nanoscale* **2019**, *11*, 2668. https://doi.org/10.1039/c8nr07088a.

(2) Chandler, H. J.; Stefanou, M.; Campbell, E. E. B.; Schaub, R. Li@C60 as a Multi-State Molecular Switch. *Nature Communications* **2019**, *10*, 2283. https://doi.org/10.1038/s41467-019-10300-2.

(3) Campbell, E. E. B.; Chandler, H. J.; Schaub, R. Sublimation of Li@C_{60}. *The European Physical Journal D* **2020**, *74*, 122. https://doi.org/10.1140/epjd/e2020-10146-0.

Research Data/Digital Outputs Access Statement

Research data underpinning this thesis are available at https://doi.org/10.17630/9c7a8aa4-c8b7-465a-837d-9665119e64cd.

Table of Contents

1 - Introduction

1.1 - Molecular Electronics

Modern technology is predominantly built around the concept of solid state electronics. The use of materials like metals and semiconductors has allowed vast leaps in the functionality of computers such that we now have devices in our pockets that are more advanced than ones which filled a room 60 years ago. This miniaturisation of computing power was first predicted by Gordon Moore in 1965 whose initial prediction was that the density of transistors on an integrated circuit would double every year from 1965 to 1975[1]. After the extraordinary accuracy of his first statement, Moore re-addressed his prediction in 1975 and altered the timeline to doubling every 2 years from that point[2]. As if it were a challenge, research groups in both academia and industry maintained this level of progression remarkably consistently for almost the next 40 years. However, as the components shrank the physical limit of the materials was approached, heat generation due to current leakage increased, and continued progression became more expensive[3]. In 1974 Aviram and Ratner proposed one method to continue the miniaturisation of electronic technology: employing single molecules as replacements for solid state components within the electronic circuits[4]. Their calculations identified that a molecule composed of an electron accepting functional group and an electron donating functional group separated by a methylene bridge would act as a molecular rectifier[4]. Thus, the concept of molecular electronics was born.
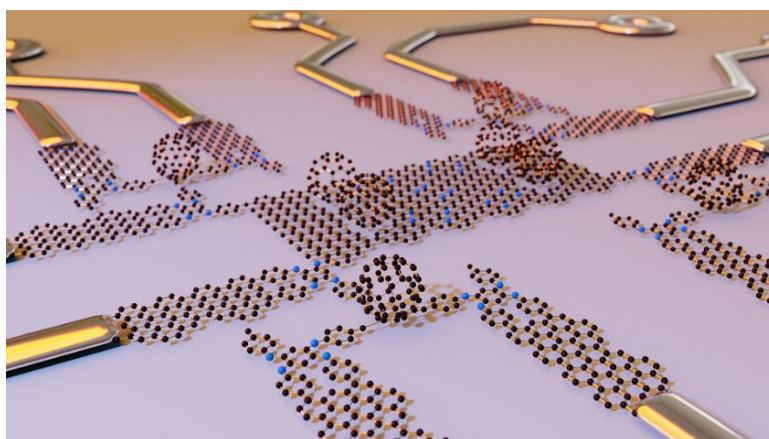
Figure 1.1: *Artistic rendition of how molecular electronic circuitry may appear. Schaub group image courtesy of Dr R.O. de la Morena (St Andrews, 2019).*

Molecular electronics is a thriving research area[5–15] with the end goal of replacing silicon-based technologies with molecular arrays which are capable of completing similar functions at a fraction of the size. One immediate example considers data storage density. Current technologies employ around 1 million atoms to encode a single bit (0 or 1)[16], however with correct application of a single molecule fewer than 100 atoms could store data encoded in two states or more[16–19]. Many researchers are exploring molecular equivalents for key components in electronic circuitry, for example transistors[20–27], wires[28–32], sensors[33], and switches[34–57] (see **Fig. 1.1** for an artistic rendition). But there are some who feel that simply mimicking the functionalities of silicon-based devices is limiting the potential of the field. Employing molecular arrays as components in circuitry could allow exploitation of numerous behaviours which are exhibited by molecules, such as self-assembly and finely tuneable properties by selective functionality. For example, the versatility of chemical design could produce microscopic components that are flexible, transparent, biocompatible and more energy efficient than solid state devices, provided appropriate molecular structures are identified. One group of molecular devices to explore this variation in functionality is the molecular switch.

1.2 - <u>Molecular Switches</u>

A molecular switch is defined as a molecule which, upon manipulation by some external stimulus, can be reversibly altered between two or more stable states. An ideal solid state switch is limited to two states which are discriminated by either measuring a conductance ("on") or not ("off"). Various stimuli can be utilised to change the properties of single molecules including: light[37,38,40,47,48], electric field[34,41–43,46,52,53], tunnelling current[36,39,45,54], mechanical interaction[50,55,57], and magnetic field[44,49]. However, some of these have been shown to simultaneously modify a vast number of different molecules. One requirement for many molecular devices is that only specifically selected molecules are controllably manipulated at any one time. The invention of the scanning tunnelling microscope (STM) in 1982[58], therefore, was a monumental boon to the research community. The resolution and fine control afforded by the STM allowed certain manipulation methods to be explored with single molecular selectivity.

The STM utilises an applied bias between an atomically sharp probe (tip) and a conductive surface, which are in very close proximity to each other, to promote directional quantum

tunnelling. The details of this process are discussed in greater depth in **Chapter 2**, but essentially, monitoring the current which results from quantum tunnelling during a raster scan of a surface can produce images of the electron density with atomic resolution. Alternatively, by recording the tunnelling current over a single point a signal which is proportional to the LDOS can be obtained. The three linked parameters within an STM are: the width of the tunnel junction (z) (i.e. the distance between the probe and the substrate), the bias applied across the tunnel junction (V) and the magnitude of the tunnelling current (I). By carefully regulating these parameters some of the above specified stimuli can be achieved with the STM and used as single molecule manipulation techniques.

By reducing the tunnel junction width (z), for example, the STM tip can be employed to mechanically alter a surface, as was first illustrated by Eigler and Schweizer in 1990 when they produced the famous image of "IBM" written in Xe atoms[59]. At low bias, the tip can be forced into close proximity such that it mechanically interacts with the molecule due to the resulting van der Waals forces.

Modulation of the tunnelling bias (V) varies the electric field which only molecules within the junction are exposed to. This affords the manipulation of molecules with a permanent dipole as was illustrated by Yasutake *et al*. and their work on $Tb@C_{82}$[53]. In their case, the direction of the applied electric field altered the orientation of the polar molecule by interacting with its dipole moment.

The final parameter, tunnelling current (I), can also be utilised to trigger molecular alterations. One example of this can be illustrated by the work of Simpson *et al*. and their use of inelastic electron excitations to actuate hydrogen tautomerisation[54]. They observed that exposing two different quinone derivatives to electrons of sufficient energy could excite the molecules and trigger a migration of two hydrogen atoms between two energetically equivalent positions. Thereby switching the molecule between two stable structural isomers.

Many of the molecular switches which have already been identified, including those examples above, employ reversible switching between two different states, i.e. isomerism[50,54], polarity[41,43,53], spin state[47,48] etc.. The versatility of molecular structures, however, can allow stability of more than just states which equate to "on" and "off".

1.2.1 - Multi-state Molecular Switches

Computer processing power has drastically increased with the shrinking of transistors such that current supercomputers are capable of completing more than 10^{13} commands per second[60]. However, the systems are based around binary logic gates (0/1) completing each command in a sequence. This somewhat limits their capacity. Despite neurons only triggering ~10^3 times per second, the human brain is more efficient at processing instructions than a supercomputer[60]. This is because neurons form an extensive network in which each neuron is connected to ~10^4 neighbours and are capable of processing information in parallel. This type of network requires each component to be able to adopt multiple discrete and stable states. This is not achievable with silicon-based solid state electronics but is within the remit of molecular electronics.

Increasing processing speeds is one option for employing a network of multi-state molecular switches, but another powerful use for such molecules is to increase the density of data storage. The same binary logic gates mentioned above are currently employed in storing data by forming strings of 1s and 0s. Though this behaviour can be imitated by molecular species[61], thus continuing the miniaturisation of technology by shrinking the components involved, employing molecules with multiple stable switch states has the potential to far exceed the storage capacity possible from binary systems. A simple example of this can be seen in **Fig. 1.2**. The top row shows 2 bits (capable of adopting states which correspond to 0 and 1) and the bottom row shows 2 multi-state components (let's call these quadrits since these are capable of adopting 4 states which correspond to 0, 1, 2 and 3). By considering the counting capacity of each pair of components (top and bottom rows), the quadrits are observed to be capable of storing much more data in the same number of units.

This simple illustration (bits counting from 0-3 and quadrits counting from 0-15) highlights the drastic increase in potential data storage when utilising multi-state components compared with those with only two states. By employing specially selected molecules and appropriate manipulation techniques, various research groups have managed to achieve this[17–19]. As **Fig. 1.2** shows, for 2 data storage units with n stable states the number of possible solutions can be described as n^2. So, for a bit ($n = 2$) there are 4 solutions. For a quadrit ($n = 4$) there are 16 solutions. The work in this thesis will illustrate a single molecule with 14 stable states resulting in a possible 196 solutions ($n^2 = 14^2 = 196$).
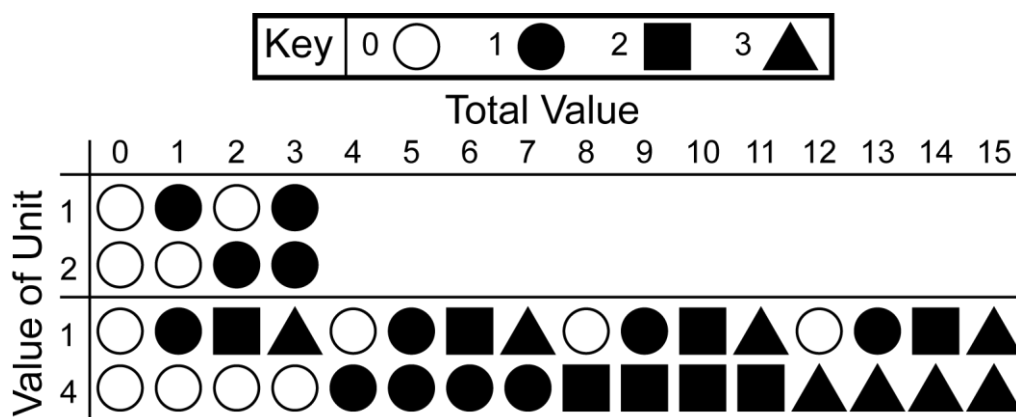
Figure 1.2: *Illustration of two data storage techniques; one composed of bits (a unit capable of adopting 2 different states [top row]), and one composed of "quadrits" (a unit capable of adopting 4 different states [bottom row]).*

The current maximum number of accessible and controllable discrete states on a single molecule is 6. This was achieved by Huang *et al.* using a low temperature STM (LT-STM) to actuate switching within an endohedral fullerene ($Sc_3N@C_{80}$) adsorbed on Cu(110)-(2×1)O[18]. Vibrational excitation of the Sc–N bonds by inelastic electron bombardment resulted in the rotation of the Sc_3N encapsulated within the C_{80} carbon cage which in turn altered the conductivity of the fullerene. One intriguing characteristic that Huang *et al.* identified is that the switching mechanism for this molecule is hierarchical. This means that the activation barriers between the various azimuthal states are non-uniform affording a degree of control over which states are available depending on the starting configuration and the energy of the incidental electrons.

One particular benefit of the $Sc_3N@C_{80}$, as highlighted by Huang *et al.*, is that the general shape of the fullerene is unaffected by the internal motion of the Sc_3N[18]. This is a very desirable feature for multi-state molecular switches because upon integration into a circuit the switch molecule could maintain permanent electrical contact regardless of the switch state. As a result of this consistent shape, endohedral fullerenes are of particular interest when considering potential structures for molecular electronics.

1.3 - Endohedral Fullerenes

Endohedral fullerenes are molecules composed of a closed carbon cage (e.g. C_{60}, C_{70}) containing another species (e.g. atom, ion or molecule)[62–65]. Depending on the size of the internal species there are a number of different methods of achieving encapsulation including molecular surgery for large molecules[66,67] and ion implantation[68,69]. Due to the ease of functionalisation and altering properties by changing the encapsulated species, endohedral fullerenes are being explored for a variety of applications to further the field of nanotechnology. For example, gadofullerene derivatives (i.e. $Gd@C_{60}(OH)_x$) are being studied for use as MRI contrast agents[70], and $Ce_2@I_h\text{-}C_{80}$ has exhibited unprecedented photo-induced charge transfer capabilities which could lead to efficient solar energy conversion[71]. From a molecular electronics perspective, Harneit proposed that pairs of group-V endohedral metallofullerenes (EMF) could be utilised as qubits[72]. The electron spins of the encapsulated atoms are protected by the fullerene cage and could therefore be encoded and used in the development of quantum computing. This concept of endohedral fullerenes acting as qubits is reminiscent of the idea of using these molecules as switches in molecular electronics. $Li@C_{60}$ is one of the simplest endohedral fullerenes and is the focus of the current work. In order to explore the properties of $Li@C_{60}$, however, it is useful to first consider those of the empty fullerene.

1.3.1 - C_{60}

C_{60}, also known as the buckminsterfullerene, was first identified in 1985 by Kroto *et al.*[73]. Due to its shape, the molecule was named after Richard Buckminster Fuller, an inventor and architect known for designing geodesic structures. In the years closely following the discovery of C_{60}, and especially after macroscale production of it was first realised[74], the examination of the fullerene was extensive[75–79]. Intriguing behaviour like the ability to contain other species[80] and form the basis of a high temperature superconductor[81,82] led to huge initial excitement as to the possible applications of the molecule. However, since C_{60} exhibits such low solubility[83] commercial-scale production proved evasive and interest waned. Over the last decade or so interest in the fullerene has experienced a resurgence, coinciding with both the discovery of C_{60} in the interstellar medium of space[84,85] and the further expansion of the available derivatives[86].

Modification of the C_{60} can allow easier handling of the molecule since properties like solubility can be altered by functionalisation[79,86]. Despite this facilitation in the production of fullerenes, the general properties of these derivatives remain consistent with the unaltered species[79]. There are numerous reviews which delve deeply into specific properties of C_{60}[75–79,86], but since a lot of these properties are irrelevant for the current discussion the following section will only provide a brief description of those most pertinent to this thesis.

1.3.1.1 - Structure and Properties of C_{60}

C_{60} is a truncated icosahedral molecule composed of 12 pentagonal faces (C5-faces) and 20 hexagonal faces (C6-faces) with a diameter of ~7 Å[73] (~10 Å including the π-electron cloud[76]) (see **Fig. 1.3**). The bonds between C5- and C6-faces (5:6 bonds) approximately resemble single bonds (~1.45 Å), and those between adjacent C6-faces (6:6 bonds) resemble double bonds (~1.39 Å)[87,88]. Each of the 60 carbon atoms, therefore, has 2 single bonds and 1 double bond so the truncated icosahedron forms a conjugated system. The spheroidal curve, however, prevents the preferred planar orientation of the sp^2-hybridised carbon atoms typical of a conjugated system. This out-of-plane shape induces strain across the surface of the carbon cage which is responsible for the high reactivity of the external C_{60} surface[89]. Despite this reactivity, C_{60} is the smallest stable cage system; i.e. reactions will not necessarily rupture the spheroid shape unlike fullerenes with fewer carbon atoms. This is because it abides by the isolated pentagon rule (see **Fig. 1.3**). Adjacent C5-faces, as is required on smaller fullerenes, demand greater curvature of the bonding plane thus increasing the strain and destabilising the molecule.
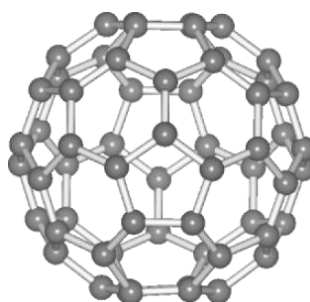
Figure 1.3: *Ball and stick model of C_{60}.*

When studied in the solid phase at room temperature, C_{60} adopts a face-centred cubic (fcc) crystal structure in which the nearest fullerenes are 10.01 Å apart[90]. There is no long range order in the alignment of the fullerenes since the activation barrier to rotation is easily overcome by the thermal energy of the system. As this solid is cooled past 249 K the crystal structure adopts a simple cubic structure and the free rotation is hindered[91,92]. The hindered rotations result in the fullerenes preferably adopting lower energy orientations such that the electron rich regions over the double bonds align with the electron poor C5-faces of the neighbouring fullerenes. Since electrons act as the charge carriers within the carbon cage, this interaction between neighbouring fullerenes results in the *n*-type semiconductor behaviour that is observed for C_{60} and can be utilised in the production of *n*-channel field effect transistors (OFETs)[25–27].

Though semiconducting behaviour is already useful for molecular electronics, further exploration of the electronic properties of C_{60} revealed greater versatility. For example, exploration of intercalation within the fcc crystal structure (but external of the C_{60} core) identified that Cs_3C_{60} exhibits superconductivity at high temperature (>35 K)[93]. This behaviour is known to relate to the electron affinity of C_{60} (2.65 eV[94]) which makes it an electron acceptor when interacting with alkali metals and noble metal surfaces. In the case of the alkali metal doped species (A_3C_{60} where A = any combination of alkali metal atoms), each metal donates a single electron to the fullerene[81,82,93,95]. According to the molecular model of C_{60}, the HOMO is completely filled by the 60 π-electrons[76]. As a result, the electrons donated by the dopant alkali metals half-fill the LUMO of the cage and are therefore responsible for the increased conductivity of doped C_{60}[76].

The movement of electrons through and around the C_{60} is of particular interest to the study of the use of fullerenes within molecular electronics. Identification of this behaviour, however, only becomes pertinent once the C_{60} is adsorbed to a surface and these effects can be observed within a junction. A myriad of surface science techniques have been employed in the characterisation of C_{60} on a plethora of substrates[78,96–124]. Since the vast majority of the analysis contained in this thesis focusses on the Au(111) substrate examined with scanning tunnelling microscopy, the next section will discuss STM studies on the C_{60}/Au(111) system.

1.3.1.2 - C$_{60}$ on Au(111)

Au(111) is a common surface to explore because it is largely inert allowing the adsorbates to be minimally affected by the process of adsorption, for example C$_{60}$ bonding to Au(111) is much weaker than Cu(111) and even slightly weaker than Au(110)[107]. It is also the only (111) surface of an fcc metal to undergo extensive reconstruction in order to maximise its stability[125]. Due to the zig-zag pattern first observed with an STM[126], the reconstruction is referred to as the herringbone reconstruction (see **Fig. 1.4** for an example). The reconstruction is the result of a long-range uniaxial compression along the {110} surface direction causing ripples in the top layer of Au atoms as 23 surface atoms are accommodated by 22 atoms on the second layer, essentially forming a 23×$\sqrt{3}$ overlayer.
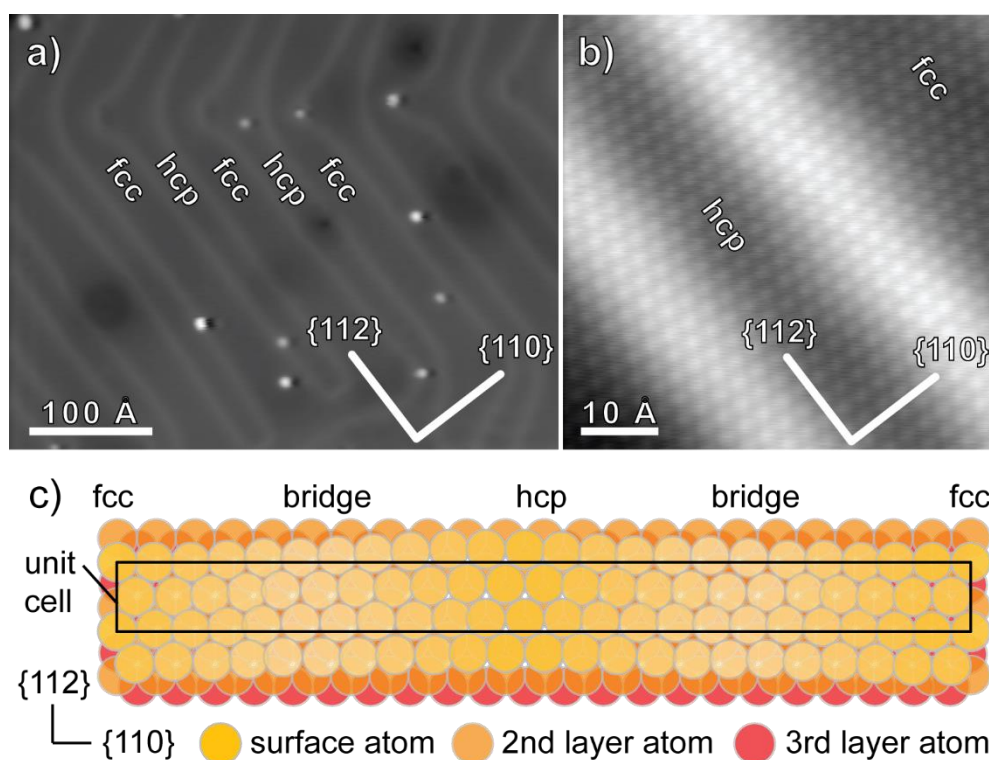
Figure 1.4: *STM images of the 23× $\sqrt{3}$ surface reconstruction of Au(111). The fcc and hcp regions of the herringbone reconstruction are labelled. **a)** (+0.23 V, 0.34 nA), **b)** (+0.02 V, 2.3 nA). **c)** Illustration of the atomic placement within the unit cell of the herringbone reconstruction. All images courtesy of the Schaub group.*

Barth *et al.* first reported on the herringbone reconstruction and identified a topographical displacement of 0.20±0.05 Å across the bright region of the surface[126]. Though the apparent height of other features in the STM images were bias dependent, i.e. adsorbed impurities, this "ripple" was not. It was therefore determined to be the region in which the top layer Au atoms are in transition from fcc-packing (wide regions of the herringbone reconstruction seen in **Figs. 1.4 (a)** and **(b)**) to hcp-packing (narrow regions in the figure). This changing atomic arrangement across the surface results in variations in the local reactivity of the surface sites[126]. When depositing small quantities of molecules, such as C_{60}[122], these changes in local reactivity cause preferential adsorption sites to be observed. Upon deposition of larger quantities of C_{60} on Au(111) the behaviour of the system becomes more complex.

Three ordered domains of C_{60} overlayers have so far been observed with STM when depositing ≤1 monolayer (ML): 38×38 (aka "in phase")[110], $(\sqrt{589}\times\sqrt{589})R14.5°$[127] and $(2\sqrt{3}\times2\sqrt{3})R30°$[119]. The prevalence of each 2D domain is closely related to the preparation conditions of the surface[119,122,128,129]. Similarly, under appropriate conditions, and despite the known weakness of its interaction with Au(111), the chemisorbed C_{60} is capable of lifting the herringbone reconstruction such that no ripples are observed across the 2D arrays of C_{60}[129].

The exact structure of the Au surface beneath these C_{60} arrays is difficult to determine. Techniques like STM cannot observe it since it is buried, and those which are capable of penetrating the overlayer, like surface x-ray diffraction (SXRD)[96], do not have the spatial resolution to identify specific molecules and the corresponding adsorption sites. The general description of this surface, however, states that the lifting of the herringbone reconstruction results in a decompression of the Au surface such that it instead resembles bulk Au(111) with a surface lattice constant of 2.88 Å. This is why the $(2\sqrt{3}\times2\sqrt{3})R30°$ packing structure of C_{60} (illustrated in **Fig. 1.5**) is the most thermodynamically stable of the three known domains[119]. The lattice constant of a $(2\sqrt{3}\times2\sqrt{3})R30°$ overlayer on the relaxed Au(111) is 9.98 Å which bears a remarkable similarity with the distance between nearest neighbours in the bulk phase of C_{60} (10.01 Å). Such close agreement results in a very high commensurability between the $(2\sqrt{3}\times2\sqrt{3})R30°$ C_{60} domain and the relaxed Au(111) substrate, hence the thermodynamic stability.
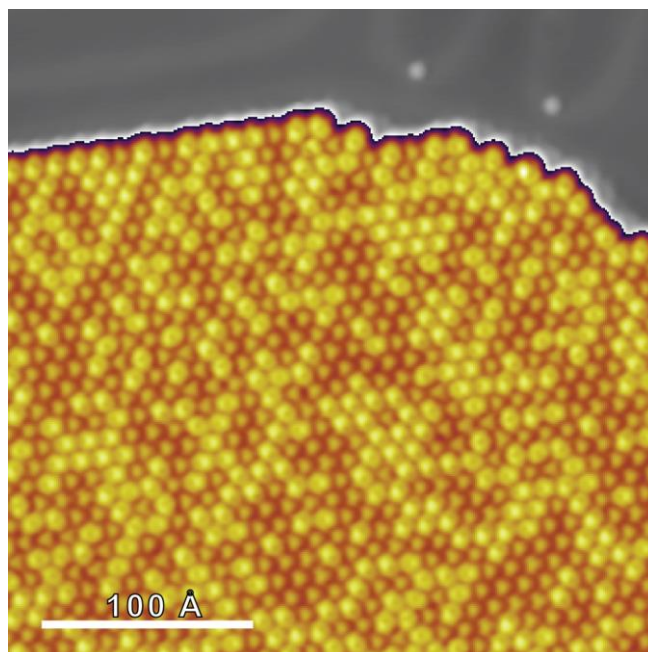
Figure 1.5: *Typical STM image (+1.0 V, 0.1 nA) of a portion of a large 2D array of fullerenes adopting the (2√3×2√3)R30° domain on Au(111). Image courtesy of the Schaub group.*

The STM image (+1.0 V, 0.1 nA) in **Fig. 1.5** depicts a portion of a large 2D array of fullerenes which has adopted the (2√3×2√3)R30° packing structure on the Au(111) substrate. Each shape within the array represents a fullerene. The variation in the appearance of the fullerenes is observed regardless of the packing domain that the molecules adopt. Similar to the prevalence of each domain, the distribution of these molecular appearances is closely linked to the preparation conditions[104,106,110,117,127,129].

The molecular appearances are bias dependent in STM images and are often described as shapes with segments of varying number, position and brightness. It is widely known that these segments relate to the intramolecular structure of the C_{60}[109,130]; the 6:6 bonds are electron rich resulting in the HOMO forming on the C6-faces, whereas the 5:6 bonds are electron poor and form the LUMOs on the C5-faces. Understanding this allows the adsorption orientation of each C_{60} to be identified by the molecular appearance at positive and negative bias. This is illustrated by the ball and stick models (top row) and the corresponding simulated STM images (bottom row, courtesy of Wang *et al*.[131]) in **Fig. 1.6**. The adsorption orientations are named for the uppermost feature of the carbon cage (coloured red to facilitate identification in **Fig. 1.6 (a)**).
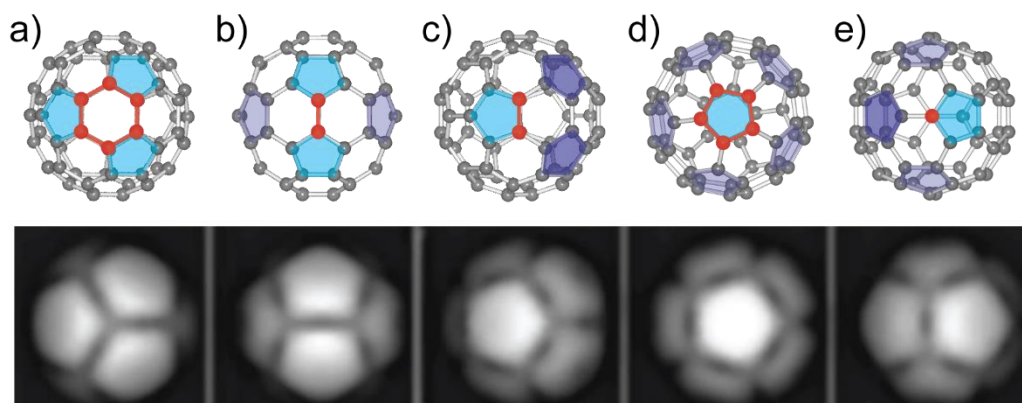
Figure 1.6: *Ball and stick models (top row) and simulated STM images of the unoccupied states of C_{60} (bottom row, reprinted figure with permission from [Wang et al., Physical Review B, 63, 085417 (2001).] Copyright 2019 by the American Physical Society[131]). These pairs illustrate the following adsorption orientations of C_{60}: a) $C6$-C_{60}, b) $6{:}6$-C_{60}, c) $5{:}6$-C_{60}, d) $C5$-C_{60}, and e) C-C_{60}.*

To simplify comparison between the simulated STM images and the ball and stick models in **Fig. 1.6,** the uppermost C5-faces are coloured with respect to their proximity to the STM tip. Blue C5-faces are uppermost on the C_{60} (closest to the tip) and purple C5-faces are further from the top. The position and relative height of the C5-faces is what determines their contribution to the contrast in the simulated STM images of the fullerenes. The further a C5-face is from the STM tip the dimmer the corresponding segment, hence the fading purple within the ball models.

Fig. 1.6 (a) depicts a C6-C_{60}, so called because of the C6-face at its apex. The adjacent C5-faces impart a three-fold rotational symmetry to the molecule. **Fig. 1.6 (b)** illustrates a fullerene with a double bond between two C6-faces uppermost on the cage and as such is referred to as a 6:6-C_{60} fullerene. This adsorption orientation has two C5-faces equally close to the STM tip so the corresponding segments are identical and therefore the molecule has a two-fold rotational symmetry. **Fig. 1.6 (c)** represents a fullerene with a single bond between a C5-face and C6-face uppermost on the cage and as such is referred to as a 5:6-C_{60} fullerene. The three C5-faces presented in this model result in a molecular appearance with three segments and one-fold rotational symmetry because one of them (blue) is closer to the apex of the cage than the other two (purple). **Fig. 1.6 (d)** depicts the C5-C_{60} orientation of a C_{60} molecule named after the C5-face at its apex which is

surrounded by C6-faces resulting in a fullerene appearance with five-fold rotational symmetry. Finally, **Fig. 1.6 (e)** illustrates a C_{60} that is adsorbed such that a single carbon atom is at the fullerene's apex and is henceforth referred to as a C-C_{60} fullerene. This adsorption orientation has two dominant C5-faces (blue and deep purple) which are asymmetrically displaced from the STM tip and this results in a molecule with two segments of inequivalent brightness and one-fold rotational symmetry. When imaging with mediocre STM resolution, C-C_{60} fullerenes are occasionally mistaken for 5:6-C_{60} due to both molecular appearances having asymmetrical segment structures and one-fold rotational symmetry in the STM images.

Observing the uppermost feature of a fullerene also allows identification of the feature of the C_{60} cage that is closest to the substrate due to the symmetry of the molecule. C_{60} is a truncated icosahedron, a shape with a point of inversion symmetry at its centre. This causes the uppermost cage feature, which can be observed by STM, to be equivalent to a 180° rotation of that which is adsorbed to the substrate, as is illustrated by the C6-C_{60} in **Fig. 1.7**. This is useful for identifying the C_{60} on the Au(111) surface but it becomes integral when considering the specific interactions within the molecular system.

As mentioned above, the $(2\sqrt{3}\times2\sqrt{3})R30°$ packing order is the most thermodynamically stable overlayer for C_{60} on Au(111)[119]. The high commensurability results in each C_{60} in the overlayer adopting the same adsorption site. Theoretical attempts to properly determine the most thermodynamically favourable adsorption configuration for C_{60} on Au(111) are numerous, but are yet to reach a unanimous description[96,104,106,117,132–136]. The adsorption configuration contains information on the C_{60} adsorption orientation (as illustrated in **Fig. 1.6**), the azimuthal orientation of the fullerene and the specific adsorption site on a Au(111) substrate (i.e. hcp, fcc, top or bridge site).

The interaction between C_{60} and the Au(111) has been identified as covalent-like since there is only minimal charge transfer between the molecule and the surface (~0.2 electrons)[133,134]. The covalent-like nature of this interaction leads to the suggestion that the 6:6 bonds (which form the HOMO) are dominant in the interaction since these are electron rich and can partially donate the electrons therein. Therefore, the greater number of 6:6 bonds in proximity to the surface, the stronger the interaction between
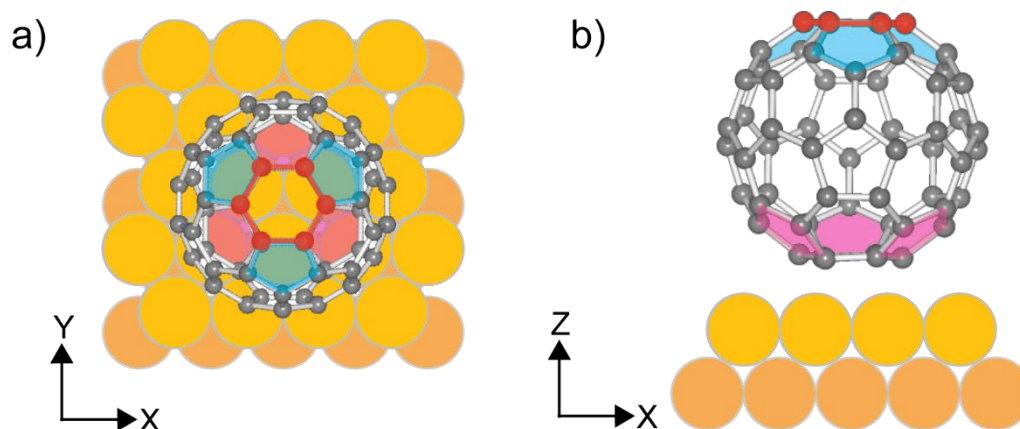
Figure 1.7: *Diagrams illustrating views of a C6-C$_{60}$ both **a)** orthogonal and **b)** parallel to the Au(111) substrate to facilitate differentiation between the C5-faces which are adjacent to the uppermost and lowermost C6-faces. These are indicated by the blue and pink pentagons, respectively.*

the two. This interaction explains why C6-C$_{60}$ is widely known to be the preferred adsorption orientation (as seen in **Fig. 1.7**). However, determination of the most favourable surface site configuration remains open for discussion.

Wang *et al.*[133,134] identified the adsorption configuration seen in **Fig. 1.7** to be preferable, considering both the azimuthal orientation of C$_{60}$ and the surface site. Their calculations revealed that the hcp surface site of a relaxed Au(111) substrate is preferable over fcc, top or bridge sites. They also observed minor activation barriers to rotation of the C$_{60}$, thus identifying this azimuthal orientation (**Fig. 1.7**) to be preferred over the others which were examined. Considering the position of the 6:6 bonds on the lowermost C6-face (see **Fig. 1.7 (a)**), this orientation matches what is expected from the covalent-like nature of the molecule-surface interaction. The 6:6 bonds are aligned with the 3 Au atoms which form the hcp surface site, thus resulting in greater overlap between the HOMO and the surface states, causing a stronger interaction. With a stronger interaction comes more charge transfer which will affect the molecular appearance of the fullerenes in STM images. The adsorption orientation is known to be at least partially responsible for the variation in brightness of the molecular appearances[109,130] (as illustrated by the simulated STM images in **Fig. 1.6**) but the charge transfer resulting from each orientation is expected
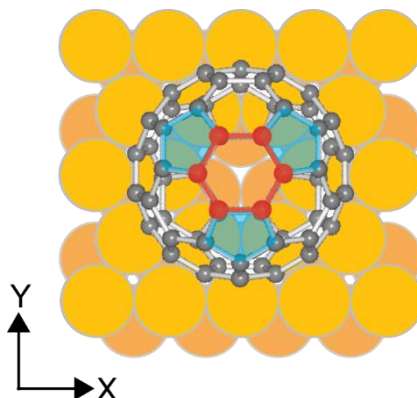
Figure 1.8: *Ball and stick model of C6-C$_{60}$ adsorbed to a nanopit (single atom vacancy).*

to exacerbate this. Stronger bonding with the substrate leads to greater charge transfer and thus provides one suggestion as to why the C6-C$_{60}$ are dimmer than the other adsorption orientations in the STM image in **Fig. 1.5**.

Other theories suggest that this enhanced charge transfer is insufficient to properly describe the "dimming" that is observed for the C6-C$_{60}$ in the above STM image (**Fig. 1.5**). Instead a topographic effect caused by a single atom vacancy, or "nanopit", was proposed by Gardener *et al*.[129]. Subsequent calculations identified that this would allow the adsorption configuration seen in **Fig. 1.8**, which is shown to be even more thermodynamically favourable than that depicted in **Fig. 1.7**[96,104,117,129]. The surface reconstruction resulting in these nanopits is thought to be sufficient to explain the "dimming" observed in the STM image for two reasons. Firstly, since each C-atom on the lowermost C6-face aligns with a surface Au-atom (see **Fig. 1.8**) this further increases the charge transfer from the substrate[104]. Secondly, the commensurability of the overlayer results in the non-C6-C$_{60}$ adsorbing to the top-sites. Without the reported strength of interaction exhibited by the C6-C$_{60}$ these other adsorption orientations do not cause the formation of a nanopit. This, in turn, causes a greater geometric height difference between the C6-C$_{60}$ and non-C6-C$_{60}$ exacerbating the difference in apparent height as seen in the STM image.

Theoretical and experimental data illustrating nanopits are reported, and widely accepted, on Cu(111)[137], Ag(111)[138], and Au(110)[139,140]. The identification of these reconstructions is often used as justification for suggesting nanopits on Au(111) too. However, these surfaces interact with C$_{60}$ more strongly than Au(111)[107]. In a recent

paper[132], Villagómez *et al.* identify that the theoretically calculated adsorption energy of a C6-C_{60} adsorbed to a nanopit (3.36 eV) is much greater than the experimentally observed value achieved by the monolayer thermal desorption experiments completed by Tzeng *et al.* (1.90 eV)[107]. This suggests that, though the C6-C_{60}/Au(111)-nanopit configuration may be the most thermodynamically favourable adsorption configuration[96,104], such large-scale reconstruction of the relaxed Au(111) substrate (resulting in ~4% surface vacancies[104]) is not achieved naturally during sample preparation. However, thermal desorption, much like LEED[104] and XRD[96], is an averaging technique, so these results must also be taken with some scepticism.

As the discussion above illustrates, the $(2\sqrt{3}\times2\sqrt{3})$R30° overlayer of C_{60} on Au(111) is a complex system and the configuration of it remains a topic of discussion. As such, this will be discussed in greater depth in **section 4.1.2.3** with reference to a Au(111) sample prepared during this work.

The main reason that the specific adsorption configuration for C_{60} on Au(111) is sought after is linked to the charge transfer since this is known to be affected by the adsorption orientation[101]. The variations in the charge transfer become particularly important when considering the molecule's uses within molecular electronics[20,141]. Both the charge transfer and shielding effect are thought to be closely linked to the molecular orbitals and how these interact, not only with the substrate but with neighbouring C_{60}.

1.3.1.3 - Super-atom Molecular Orbitals (SAMOs)

The molecular orbitals lying close to the Fermi level (HOMO, LUMO, LUMO+1 etc.) are centred on the atoms on the carbon cage, as was illustrated above when identifying the orientation of adsorbed species. However, upon imaging higher energy unfilled states of 1D and 2D arrays of C_{60}, Feng *et al.*[97] observed a delocalised band which resembled a nearly-free electron (NFE) band more closely than a combination of individual molecular orbitals. Studying the isolated species with STM and DFT, Feng *et al.* identified that the higher energy molecular orbitals adopt wavefunctions with unusual properties. These molecular orbitals are: more diffuse (extending far beyond the surface of the carbon cage), centred on the core of the C_{60} (rather than the carbon atoms), and symmetrically

Figure 1.9: *Calculated workfunctions of the three lowest-lying C$_{60}$ SAMOs for an isolated fullerene in the gas phase. Adapted with permission from Zhao et al., ACS Nano **3**, 853-864 (2009)[142]. Copyright 2020 American Chemical Society.*

similar to hydrogenic atomic orbitals (see **Fig. 1.9**, adapted from Zhao *et al.*[142]). As a result of this symmetry Feng *et al.* referred to these as super-atom molecular orbitals (SAMOs) and labelled each based on the atomic orbitals with which these shared a likeness: *s*-SAMO, *p*-SAMO, *d*-SAMO etc.[97,142,143].

The *s*-SAMO for C$_{60}$ (as seen in **Fig. 1.9**) is the lowest energy SAMO but is still observed several eV higher than the LUMO[57]. For the example above (isolated and in the gas phase) the *p*- and *d*-SAMOs are higher in energy still. This is due to the SAMOs being the result of the combination of the 3*s* (and higher) atomic orbitals from the carbon atoms on the C$_{60}$[65]. The hybridisation of these diffuse atomic orbitals results in the wavefunctions of the SAMOs also being very diffuse and extending far beyond the surface of the carbon cage, both inside and outside the fullerene. It is this diffusivity which lends itself to the formation of NFE bands when SAMOs hybridise in 1D and 2D assemblies of C$_{60}$. Further studies have found that SAMOs are not only limited to C$_{60}$ but that many systems share similar symmetries for higher energy molecular orbitals[144–150]. It is thought that these systems may also exhibit NFE band behaviours which could be exploited in the development of molecular electronics.

Since the SAMOs extend beyond the confines of the molecules, perturbations induced externally or internally can be employed to tune the properties of the SAMOs[142,147–151]. One simple method of applying an external perturbation to the SAMOs is adsorption to a substrate. Reecht *et al.*[115] acquired constant current differential conductance (*dI/dV*) STM images of an isolated fullerene in the C$_{60}$/Cu(111) system. Their images (see **Fig. 1.10**,
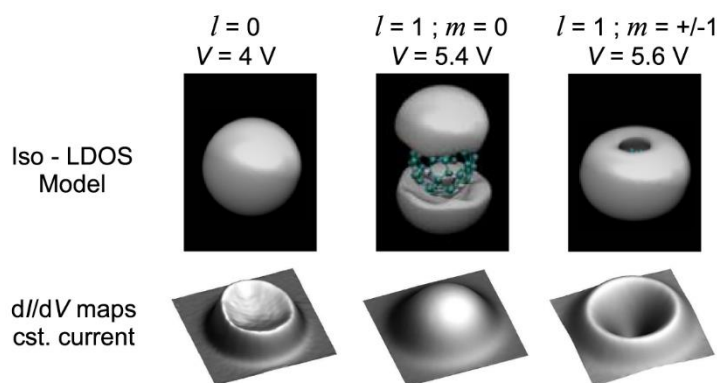
Figure 1.10: *Calculated wavefunctions (top row) and experimental constant current dI/dV images (bottom row) of an isolated C_{60} on the Cu(111) surface as studied by Reecht et al.[115]. The SAMOs are referred to by their quantum numbers rather than atomic orbital symmetries. From left to right these equate to the s-, p_z- and $p_{x,y}$-SAMOs. Figure adapted from Reecht et al., New Journal of Physics **19**, 113033 (2017)[115] courtesy of the CC-BY 3.0 license.*

adapted from Reecht *et al.*[115]) highlight the loss of degeneracy when a species is adsorbed to a surface; the p_x- and p_y-SAMOs remain degenerate (hence the ring shaped $p_{x,y}$-SAMO instead of lobes as suggested by **Fig. 1.9**) but the p_z-SAMO is stabilised due to greater interaction with the surface states.

Sufficient stabilisation of the SAMOs by adsorption to a substrate could provide a facile route for conduction. One application for such behaviour has been identified by Guo *et al.*[151] in their work towards molecular methods of solar energy conversion. In their molecular dynamics calculations, they observed that the interfacial charge transfer from the *s*-SAMO of the fullerene to the substrate in the C_{60}/MoS$_2$ system is 100 times faster than electron-phonon interactions which would lead to excitation of the molecule. This is the result of strong hybridisation between the substrate and the SAMO. This hybridisation is one method of manipulating the energy of the SAMOs by external perturbations, another method unique to fullerenes is encapsulation.

The SAMOs of fullerenes are centred on the core of the molecule. By encapsulating another species within that hollow the energies and symmetries of the SAMOs can be drastically altered by hybridising with the valence states of the dopant species[97,142].
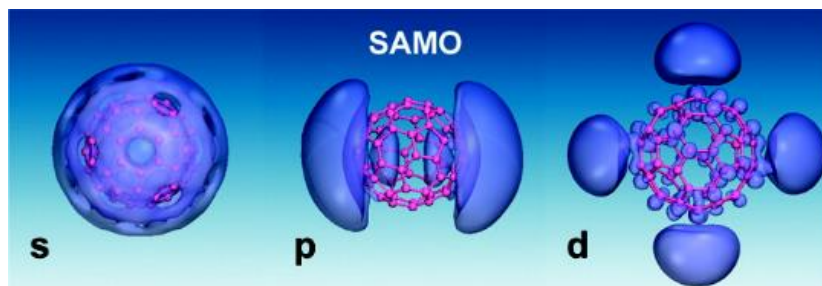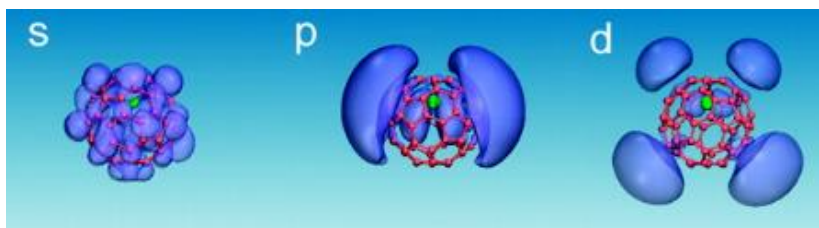
Figure 1.11: *Calculated workfunctions of the three lowest-lying Li@C$_{60}$ SAMOs for an isolated fullerene in the gas phase. Adapted with permission from Zhao et al., ACS Nano **3**, 853-864 (2009)*[142]*. Copyright 2020 American Chemical Society.*

Cu@C$_{60}$, for example, is suggested to exhibit metallic-like conduction because calculations indicate that the encapsulation of Cu lowers the *s*-SAMO of the endohedral fullerene below the Fermi level of the system[142]. Li@C$_{60}$ is another example of an endohedral metallofullerene (EMF) which calculations suggest exhibit SAMOs which are stabilised by the encapsulation of Li[97,142].

One important distinction between Cu@C$_{60}$ and Li@C$_{60}$ is the position of the dopant. Cu, with its high ionisation potential, remains central to the carbon cage resulting in stabilisation of the SAMOs but minimal alterations to the symmetries of them. Li, however, has a low ionisation potential. Combined with the high electron affinity of C$_{60}$[94], the Li partially donates its valence electron to the carbon cage and the consequent Coulomb interaction causes the Li to stabilise off-centre[152]. Not only does this affect the energies of the SAMOs but calculations indicate that it alters the symmetry too (see **Fig. 1.11**, adapted from Zhao *et al*.[142]). The off-centre position of the Li within the Li@C$_{60}$, and its subsequent effect on the SAMOs, is the particular appeal for this fullerene from a molecular electronics perspective. As such, the next section focusses specifically on the current status of research into the properties and hypothesised potential applications of Li@C$_{60}$.

1.3.2 - Li@C$_{60}$

The inclusion of a single atom within a fullerene was observed shortly after the first identification of C$_{60}$[80]. Encapsulating a Li atom within C$_{60}$, therefore, was an early consideration but due to its poor solubility the majority of preliminary works on Li@C$_{60}$
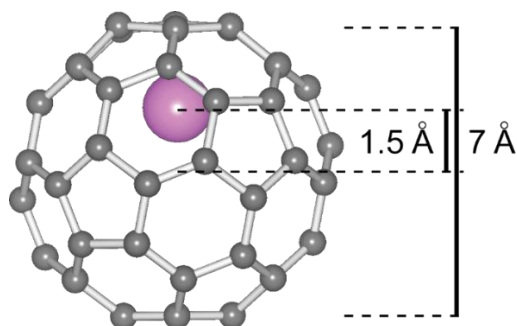
Figure 1.12: *Ball and stick model of Li@C$_{60}$*

were theoretical[153–157]. The concept of Li ion bombardment circumvented the solubility issues[158] but it wasn't until Tellgmann *et al.*[159] improved the method that experimental exploration of the Li$^+$@C$_{60}$ became more widespread. Okada *et al.*[69] further enhanced the production scale by employing Li$^+$ plasma instead of a beam, and this led to the reduction method which Ueno *et al.*[160,161] developed to produce the neutral molecule Li@C$_{60}$. With these methods allowing production of both Li@C$_{60}$ and Li$^+$@C$_{60}$ in workable amounts studies of the properties of both are numerous.

1.3.2.1 - <u>Structure and Properties of Li@C$_{60}$</u>

The first point to raise is the charge transfer within the molecules. As mentioned above, the low ionisation potential of the Li and the high electron affinity of the C$_{60}$ result in a charge transfer to the latter. This is calculated to be equal to ~0.65 e[152,162,163]. The Coulomb interaction resulting from these partial charges is the reason for the characteristic off-centre position of the Li within the carbon cage (see **Fig. 1.12**). Since the C$_{60}$ is known to act as an electron buffer for this molecule[164], the partially charged state of the encapsulated Li is consistent for both Li@C$_{60}$ and Li$^+$@C$_{60}$. This means that any difference between the properties of the two molecules can be largely associated with the oxidation state of the C$_{60}$ i.e. Li@C$_{60}$ is often referred to as Li$^+$@C$_{60}^-$. However, any differences that have been observed are merely quantitative, therefore, the endohedral fullerene shall simply be referred to as Li@C$_{60}$ for the remainder of this thesis. Another reason for this grouping is that adsorption to a metal substrate, as in the current work, neutralises any charge which has been induced on the carbon cage due to the electron source/sink nature of the metal. It is this surface interaction which could be the origin of the enhanced adsorption energy for Li@C$_{60}$ (2.91 eV) compared to that of C$_{60}$ (2.24 eV) observed by Yamada *et al.*[165], but this requires further exploration before it can be confirmed.

The ball and stick model above demonstrates the Li position to be displaced from the centre of the C_{60} along one of the 3-fold rotationally symmetric axes which passes through a C6-face and the centre of the carbon cage. Numerous calculations and experimental measurements have been conducted to determine the off-centre displacement of the encapsulated Li. These are seen to vary depending on the theoretical technique employed[153,157,162,163,165–171] and experimental environment in which the Li@C_{60} is observed[172,173], but the displacement is generally considered to be ~1.5 Å. Though the partial charge transfer from the Li to the C_{60} is sufficient to cause this displacement, it is a localised perturbation and thus is anticipated to have only a minor effect on the energies of the LUMOs when compared to those of an empty C_{60}[142]. However, the SAMOs are centred on the core of the carbon cage and theory suggests these will hybridise with the valence orbitals of any species which is encapsulated[97]. The asymmetry induced by the ~1.5 Å displacement, therefore, is expected to alter both the symmetries (as shown in **Fig. 1.11**) and energies of the SAMOs considerably[142,148]. However, this is yet to be experimentally observed.

Though the effect on the SAMOs is uncertain some other properties resulting from the encapsulation have been recorded. For example, the increased conductivity of the thin films when compared with those of C_{60}[174,175]. One suggestion for the origin of this property is the partial charge induced on the carbon cage by the donation from the Li. This lowers the LUMO sufficiently that it can be more easily accessed for conductance. Besides the enhanced conductivity of the molecule, which has obvious connections to molecular electronics, the manipulation of the Li within the carbon cage is also of interest as a potential single molecule switch.

1.3.2.2 - Migration of Li within Li@C_{60}

Migration of the Li around the internal surface of the C_{60} has been studied fairly consistently over the past 30 years[154,156,157,162,166,169,170,173,174,176–179]. After the off-centre position of the Li was identified it was a natural progression to consider harnessing this and employing the deliberate manipulation of the Li as a molecular switch. Early theoretical studies of Li@C_{60} identified that the energy barriers to migration are easily overcome at room temperature[156,170]. These were confirmed shortly after by Raman and infrared spectroscopic measurements completed by Gromov *et al.*[174,179]. Further studies,

both theoretical[166] and experimental[173,176–178], then identified that the Li retains its preference for the C6-faces of the C_{60} cage. This means that at temperatures greater than 100 K there are 20 distinct positions which can be adopted by the Li[177]. However, these experiments employed temperature[173,177] and terahertz radiation[176,178] to trigger the migration of Li within the solid phase $(Li^+@C_{60})[PF_6]^-$ salt. Different manipulation techniques are required to achieve the single molecular selectivity desired for the utilisation of Li@C_{60} as a molecular switch.

The STM has been shown as an effective tool for exploring single molecule manipulation, as is discussed above. With a mind to STM, Delaney *et al*. explored the potential for utilising an electric field for activating the Li-migration within a single Li@C_{60}[180]. However, their calculations identified a "Faraday cage-like" shielding effect of the C_{60} cage. This shielding is linked to the polarizability of the carbon cage which acts to protect the core of many fullerenes[66,181,182]. In the case of Li@C_{60}, the electric field which penetrated the carbon cage was reduced to only ~25% of the magnitude of that which was externally applied[180]. From their calculations Delaney *et al*. concluded that the magnitude of the electric field required to trigger a manipulation of the Li would preferentially cause desorption of the molecule instead.

Another technique which is afforded by the use of an STM tip is excitation by current injection. This is the direction Jorn *et al*. took with their calculations[162]. Similar to the experimental work of Park *et al*. in their studies of C_{60} as a single molecule transistor[20], Jorn *et al*. contained Li@C_{60} between two metallic electrodes and observed the nanomechanical oscillations under the applied current. These oscillations were as a result of both the C_{60} "rattling" against the adsorbed electrode and the Li "shuttling" between two fixed positions within the carbon cage. Jorn *et al*. identified that an inelastic, resonant tunnelling event was required to couple the injected current with the internal dynamics. Despite the promising results of these calculations, single molecule Li-manipulation has not been achieved experimentally until now.

1.4 - Justification of this Work

Bearing in mind the current status of research regarding Li@C_{60} as described in this introduction, the initial goal of our work was to experimentally determine, for the first time, the downshift of the SAMOs due to the encapsulation of Li. This work was achieved

in collaboration with Eleanor Campbell's research group at the University of Edinburgh who provided the DFT and gas phase photoelectron spectroscopy data which aided in this identification. Their gas phase techniques would allow this downshift to be observed with relative ease, however, due to the preparation methods required for the Li@C_{60} the results would be combined with those of C_{60}. By adsorption to a surface and observation with LT-STM techniques, we were able to achieve identification of single molecules and therefore, isolate the behaviour of Li@C_{60} from C_{60}. After introducing the experimental techniques utilised in this investigation (see **Chapter 2**) and the experimental set-up with which the data was acquired (see **Chapter 3**), the analysis of the surface-bound molecular system will be discussed (see **Chapter 4**).

At the time of starting the project there was no STM analysis of Li@C_{60}, since Yamada *et al.*[165] were completing their studies simultaneously. The first step, therefore, was to identify the Li@C_{60} on the chosen substrates: primarily Au(111) for its inertness but also Cu(110)-(2×1)O. Since Yamada *et al*. completed their research on Cu(111)[165] we remain the first to publish STM analysis of the molecule on these substrates[183]. The initial observations were towards determining the adsorption configuration of the Li@C_{60} under different preparation conditions and compare these with those known for C_{60}. Once the adsorption configuration was understood, the electronic structure was also explored such that the effect of the Li-encapsulation could be appropriately identified for the first time. Introducing a frame of reference, whilst also conducting the experiments at ~5 K, was expected to allow spatial distribution of the SAMOs to be determined too, similar to the work Reecht *et al*. reported for C_{60}[115]. This would provide further evidence to compare with the angularly resolved gas phase spectroscopy completed by our collaborators since their data, necessarily, is averaged over all possible orientations. Efforts towards both the identification of the surface-bound molecular system and observation of these SAMOs will be discussed in **Chapter 4**.

The final goal for this experimental investigation was to explore the potential for achieving single molecule manipulation of Li@C_{60} such that internal Li-migration could be actuated within selected stationary fullerenes. Not only in an attempt to localise the Li-migration which has been observed across samples of Li@C_{60}, but to determine the number of distinct final states which can be adopted with a mind towards its use as a multi-state molecular switch. The conclusive proof of these manipulations will be discussed in

Chapter 5, along with a proposed mechanism for the manipulation. This mechanism suggests the SAMOs allow the carbon cage to be circumvented, thus avoiding excessive molecular excitation.

After a conclusive identification of the molecular manipulation, **Chapter 6** will summarise the observations made throughout this project and propose further paths for exploration of surface-bound Li@C_{60}. Specifically focussing on experimental proof of the proposed manipulation mechanism.

1.5 - <u>References</u>

(1)   Moore, G. E. Cramming More Components onto Integrated Circuit. *Electronics* **1965**, *38* (8), 114–117. https://doi.org/10.1109/N-SSC.2006.4785860.

(2)   Moore, G. E. Progress In Digital Integrated Electronics. *Int. Electron Devices Meet. IEEE* **1975**, 11–13. https://doi.org/10.1109/N-SSC.2006.4804410.

(3)   Loeffler, J. No More Transistors: The End of Moore's Law https://interestingengineering.com/no-more-transistors-the-end-of-moores-law (accessed Dec 14, 2019).

(4)   Aviram, A.; Ratner, M. A. Molecular Rectifiers. *Chem. Phys. Lett.* **1974**, *29* (2), 277–283. https://doi.org/10.1016/0009-2614(74)85031-1.

(5)   Feringa, B. L. The Art of Building Small: From Molecular Switches to Motors (Nobel Lecture). *Angew. Chemie - Int. Ed.* **2017**, *56* (37), 11060–11078. https://doi.org/10.1002/anie.201702979.

(6)   Harris, J. D.; Moran, M. J.; Aprahamian, I. New Molecular Switch Architectures. *Proc. Natl. Acad. Sci. U. S. A.* **2018**, *115* (38), 9414–9422. https://doi.org/10.1073/pnas.1714499115.

(7)   Mathew, P. T.; Fang, F. Advances in Molecular Electronics: A Brief Review. *Engineering* **2018**, *4* (6), 760–771. https://doi.org/10.1016/j.eng.2018.11.001.

(8)   Ratner, M. A Brief History of Molecular Electronics. *Nat. Nanotechnol.* **2013**, *8* (6), 378–381. https://doi.org/10.1038/nnano.2013.110.

(9)   Seideman, T. Current-Driven Dynamics in Molecular-Scale Devices. *J. Phys. Condens. Matter* **2003**, *15* (14), R521–R549. https://doi.org/10.1088/0953-8984/15/14/201.

(10)   Xiang, D.; Wang, X.; Jia, C.; Lee, T.; Guo, X. Molecular-Scale Electronics: From Concept to Function. *Chemical Reviews*. 2016, pp 4318–4440. https://doi.org/10.1021/acs.chemrev.5b00680.

(11)   Zhang, J. L.; Zhong, J. Q.; Lin, J. D.; Hu, W. P.; Wu, K.; Xu, G. Q.; Wee, A. T. S.; Chen, W. Towards Single Molecule Switches. *Chem. Soc. Rev.* **2015**, *44* (10), 2998–3022. https://doi.org/10.1039/C4CS00377B.

(12)   Tao, N. J. Electron Transport in Molecular Junctions. *Nat. Nanotechnol.* **2006**, *1* (3), 173–181. https://doi.org/10.1038/nnano.2006.130.

(13)   Joachim, C.; Gimzewski, J. K.; Aviram, a. Electronics Using Hybrid-Molecular and Mono-Molecular Devices. *Nature* **2000**, *408* (6812), 541–548.

https://doi.org/10.1038/35046000.

(14)   Jan Van Der Molen, S.; Liljeroth, P. Charge Transport through Molecular Switches. *J. Phys. Condens. Matter* **2010**, *22* (13), 133001. https://doi.org/10.1088/0953-8984/22/13/133001.

(15)   Morgenstern, K. Switching Individual Molecules by Light and Electrons: From Isomerisation to Chirality Flip. *Prog. Surf. Sci.* **2011**, *86* (5–8), 115–161. https://doi.org/10.1016/j.progsurf.2011.05.002.

(16)   IBM. A Boy and His Atom: The World's Smallest Movie http://www.research.ibm.com/articles/madewithatoms.shtml?mhsrc=ibmsearch_a&mhq=atomic scale memory (accessed Dec 13, 2019).

(17)   Auwärter, W.; Seufert, K.; Bischoff, F.; Ecija, D.; Vijayaraghavan, S.; Joshi, S.; Klappenberger, F.; Samudrala, N.; Barth, J. V. A Surface-Anchored Molecular Four-Level Conductance Switch Based on Single Proton Transfer. *Nat. Nanotechnol.* **2012**, *7* (1), 41–46. https://doi.org/10.1038/nnano.2011.211.

(18)   Huang, T.; Zhao, J.; Feng, M.; Popov, A. A.; Yang, S.; Dunsch, L.; Petek, H. A Molecular Switch Based on Current-Driven Rotation of an Encapsulated Cluster within a Fullerene Cage. *Nano Lett.* **2011**, *11* (12), 5327–5332. https://doi.org/10.1021/nl2028409.

(19)   Iancu, V.; Hla, S.-W. Realization of a Four-Step Molecular Switch in Scanning Tunneling Microscope Manipulation of Single Chlorophyll-a Molecules. *Proc. Natl. Acad. Sci. U. S. A.* **2006**, *103* (37), 13718–13721. https://doi.org/10.1073/pnas.0603643103.

(20)   Park, H.; Park, J.; Lim, A. K. L.; Anderson, E. H.; Alivisatos, A. P.; McEuen, P. L. Nanomechanical Oscillations in a Single-C60 Transistor. *Nature* **2000**, *407* (6800), 57–60. https://doi.org/10.1038/35024031.

(21)   Bouvron, S.; Maurand, R.; Graf, A.; Erler, P.; Gragnaniello, L.; Skripnik, M.; Wiedmann, D.; Engesser, C.; Nef, C.; Fu, W.; Schönenberger, C.; Pauly, F.; Fonin, M. Charge Transport in a Single Molecule Transistor Probed by Scanning Tunneling Microscopy. *Nanoscale* **2018**, *10* (3), 1487–1493. https://doi.org/10.1039/c7nr06860c.

(22)   Heersche, H. B.; de Groot, Z.; Folk, J. A.; van der Zant, H. S. J.; Romeike, C.; Wegewijs, M. R.; Zobbi, L.; Barreca, D.; Tondello, E.; Cornia, A. Electron Transport through Single Mn12 Molecular Magnets. *Phys. Rev. Lett.* **2006**, *96* (20), 206801. https://doi.org/10.1103/PhysRevLett.96.206801.

(23)   Kobayashi, S.; Mori, S.; Iida, S.; Ando, H.; Takenobu, T.; Taguchi, Y.; Fujiwara, A.; Taninaka, A.; Shinohara, H.; Iwasa, Y. Conductivity and Field Effect Transistor of La2@C80 Metallofullerene. *J. Am. Chem. Soc.* **2003**, *125* (27), 8116–8117. https://doi.org/10.1021/ja034944a.

(24)   Okamura, N.; Yoshida, K.; Sakata, S.; Hirakawa, K. Electron Transport in Endohedral Metallofullerene Ce@C82 Single-Molecule Transistors. *Appl. Phys. Lett.* **2015**, *106* (4), 043108. https://doi.org/10.1063/1.4907009.

(25)   Haddon, R. C.; Perel, A. S.; Morris, R. C.; Palstra, T. T. M.; Hebard, A. F.; Fleming, R. M. C60 Thin Film Transistors. *Appl. Phys. Lett.* **1995**, *67*, 121.

(26)   Anthopoulos, T. D.; Singh, B.; Marjanovic, N.; Sariciftci, N. S.; Montaigne Ramil, A.; Sitter, H.; Cölle, M.; De Leeuw, D. M. High Performance n -Channel Organic Field-Effect Transistors and Ring Oscillators Based on C60 Fullerene Films. *Appl. Phys. Lett.* **2006**, *89* (21), 213504. https://doi.org/10.1063/1.2387892.

(27)   Zhang, X. H.; Domercq, B.; Kippelen, B. High-Performance and Electrically Stable C60

Organic Field-Effect Transistors. *Appl. Phys. Lett.* **2007**, *91* (9), 092114. https://doi.org/10.1063/1.2778472.

(28)   Nitzan, A.; Ratner, M. A. Electron Transport in Molecular Wire Junctions. *Science (80-.).* **2003**, *300* (5624), 1384–1389. https://doi.org/10.1126/science.1081572.

(29)   Ratner, M. A.; Davis, B.; Kemp, M.; Mujica, V.; Roitberg, A.; Yaliraki, S. Molecular Wires: Charge Transport, Mechanisms, and Control. *Mol. Electron. Sci. Technol.* **1998**, *852*, 22–37.

(30)   Robertson, N.; McGowan, C. A. A Comparison of Potential Molecular Wires as Components for Molecular Electronics. *Chem. Soc. Rev.* **2003**, *32* (2), 96–103. https://doi.org/10.1039/b206919a.

(31)   McCreery, R. L. Molecular Electronic Junctions. *Chem. Mater.* **2004**, *16* (23), 4477–4496. https://doi.org/10.1021/cm049517q.

(32)   Wang, C.; Batsanov, A. S.; Bryce, M. R.; Martín, S.; Nichols, R. J.; Higgins, S. J.; García-Suárez, V. M.; Lambert, C. J. Oligoyne Single Molecule Wires. *J. Am. Chem. Soc.* **2009**, *131* (43), 15647–15654. https://doi.org/10.1021/ja9061129.

(33)   Kumar, J. S.; Murmu, N. C.; Kuila, T. Recent Trends in the Graphene-Based Sensors for the Detection of Hydrogen Peroxide. *AIMS Mater. Sci.* **2018**, *5* (3), 422–466. https://doi.org/10.3934/matersci.2018.3.422.

(34)   Alemani, M.; Peters, M. V.; Hecht, S.; Rieder, K. H.; Moresco, F.; Grill, L. Electric Field-Induced Isomerization of Azobenzene by STM. *J. Am. Chem. Soc.* **2006**, *128* (45), 14446–14447. https://doi.org/10.1021/ja065449s.

(35)   Bissell, R. A.; Córdova, E.; Kaifer, A. E.; Stoddart, J. F. A Chemically and Electrochemically Switchable Molecular Shuttle. *Nature* **1994**, *369* (6476), 133–137. https://doi.org/10.1038/369133a0.

(36)   Choi, B. Y.; Kahng, S. J.; Kim, S.; Kim, H.; Kim, H. W.; Song, Y. J.; Ihm, J.; Kuk, Y. Conformational Molecular Switch of the Azobenzene Molecule: A Scanning Tunneling Microscopy Study. *Phys. Rev. Lett.* **2006**, *96* (15), 156106. https://doi.org/10.1103/PhysRevLett.96.156106.

(37)   Nickel, F.; Bernien, M.; Herder, M.; Wrzalek, S.; Chittas, P.; Kraffert, K.; Arruda, L. M.; Kipgen, L.; Krüger, D.; Hecht, S.; Kuch, W. Light-Induced Photoisomerization of a Diarylethene Molecular Switch on Solid Surfaces. *J. Phys. Condens. Matter* **2017**, *29* (37), 374001. https://doi.org/10.1088/1361-648X/aa7c57.

(38)   Matsuo, Y.; Ichiki, T.; Nakamura, E. Molecular Photoelectric Switch Using a Mixed SAM of Organic [60]Fullerene and [70]Fullerene Doped with a Single Iron Atom. *J. Am. Chem. Soc.* **2011**, *133* (25), 9932–9937. https://doi.org/10.1021/ja203224d.

(39)   Scheil, K.; Gopakumar, T. G.; Bahrenburg, J.; Temps, F.; Maurer, R. J.; Reuter, K.; Berndt, R. Switching of an Azobenzene-Tripod Molecule on Ag(111). *J. Phys. Chem. Lett.* **2016**, *7* (11), 2080–2084. https://doi.org/10.1021/acs.jpclett.6b01011.

(40)   Comstock, M. J.; Levy, N.; Kirakosian, A.; Cho, J.; Lauterwasser, F.; Harvey, J. H.; Strubbe, D. A.; Fréchet, J. M. J.; Trauner, D.; Louie, S. G.; Crommie, M. F. Reversible Photomechanical Switching of Individual Engineered Molecules at a Metallic Surface. *Phys. Rev. Lett.* **2007**, *99* (3), 038301. https://doi.org/10.1103/PhysRevLett.99.038301.

(41)   Raggi, G.; Stace, A. J.; Bichoutskaia, E. Polarisation Charge Switching through the Motion of Metal Atoms Trapped in Fullerene Cages. *Phys. Chem. Chem. Phys.* **2014**, *16* (43), 23869–23873. https://doi.org/10.1039/c4cp02672a.

(42)   Leoni, T.; Guillermet, O.; Walch, H.; Langlais, V.; Scheuermann, A.; Bonvoisin, J.; Gauthier, S. Controlling the Charge State of a Single Redox Molecular Switch. *Phys. Rev. Lett.* **2011**, *106* (21), 216103. https://doi.org/10.1103/PhysRevLett.106.216103.

(43)   Foroutan-Nejad, C.; Andrushchenko, V.; Straka, M. Dipolar Molecules inside C70: An Electric Field-Driven Room-Temperature Single-Molecule Switch. *Phys. Chem. Chem. Phys.* **2016**, *18* (48), 32673–32677. https://doi.org/10.1039/C6CP06986J.

(44)   Wu, B.; Wang, T.; Feng, Y.; Zhang, Z.; Jiang, L.; Wang, C. Molecular Magnetic Switch for a Metallofullerene. *Nat. Commun.* **2015**, *6*, 1–6. https://doi.org/10.1038/ncomms7468.

(45)   Pavliček, N.; Fleury, B.; Neu, M.; Niedenführ, J.; Herranz-Lancho, C.; Ruben, M.; Repp, J. Atomic Force Microscopy Reveals Bistable Configurations of Dibenzo[a,h]Thianthrene and Their Interconversion Pathway. *Phys. Rev. Lett.* **2012**, *108* (8), 086101. https://doi.org/10.1103/PhysRevLett.108.086101.

(46)   Kornilovitch, P. E.; Bratkovsky, A. M.; Williams, R. S. Bistable Molecular Conductors with a Field-Switchable Dipole Group. *Phys. Rev. B - Condens. Matter Mater. Phys.* **2002**, *66* (24), 1–7. https://doi.org/10.1103/PhysRevB.66.245413.

(47)   Li, C.; Liu, J.; Zhang, S.; Lefkidis, G.; Huebner, W. Strain Assisted Ultrafast Spin Switching on Co2@C60 Endohedral Fullerenes. *Carbon N. Y.* **2015**, *87* (C), 153–162. https://doi.org/10.1016/j.carbon.2015.02.016.

(48)   Li, C.; Liu, J.; Lefkidis, G.; Hübner, W. Reversible Ultrafast Spin Switching on Ni@B80 Endohedral Fullerene. *Phys. Chem. Chem. Phys.* **2017**, *19* (1), 673–680. https://doi.org/10.1039/C6CP06492B.

(49)   Loth, S.; Baumann, S.; Lutz, C. P.; Eigler, D. M.; Heinrich, A. J. Bistability in Atomic-Scale Antiferromagnets. *Science (80-.).* **2012**, *335*, 196–199. https://doi.org/10.1126/science.1214131.

(50)   Ladenthin, J. N.; Frederiksen, T.; Persson, M.; Sharp, J. C.; Gawinkowski, S.; Waluk, J.; Kumagai, T. Force-Induced Tautomerization in a Single Molecule. *Nat. Chem.* **2016**, *8* (July), 935–940. https://doi.org/10.1038/nchem.2552.

(51)   Qiu, X. H.; Nazin, G. V.; Ho, W. Mechanisms of Reversible Conformational Transitions in a Single Molecule. *Phys. Rev. Lett.* **2004**, *93* (19), 1–4. https://doi.org/10.1103/PhysRevLett.93.196806.

(52)   Collier, C. P.; Mattersteig, G.; Wong, E. W.; Luo, Y.; Beverly, K.; Sampaio, J.; Raymo, F. M.; Stoddart, J. F.; Heath, J. R. A [2]Catenane-Based Solid State Electronically Reconfigurable Switch. *Science (80-.).* **2000**, *289* (5482), 1172–1175. https://doi.org/10.1126/science.289.5482.1172.

(53)   Yasutake, Y.; Shi, Z.; Okazaki, T.; Shinohara, H.; Majima, Y. Single Molecular Orientation Switching of an Endohedral Metallofullerene. *Nano Lett.* **2005**, *5* (6), 1057–1060. https://doi.org/10.1021/nl050490z.

(54)   Simpson, G. J.; Hogan, S. W. L.; Caffio, M.; Adams, C. J.; Früchtl, H.; Van Mourik, T.; Schaub, R. New Class of Metal Bound Molecular Switches Involving H-Tautomerism. *Nano Lett.* **2014**, *14* (2), 634–639. https://doi.org/10.1021/nl4038517.

(55)   Gao, J.; Tang, L.; Holmes, S.; Li, F.; Palmer, R. E.; Guo, Q. Surface-Induced Symmetry Reduction in Molecular Switching: Asymmetric Cis-Trans Switching of CH3S-Au-SCH3 on Au(111). *Nanoscale* **2016**, *8* (47), 19787–19793. https://doi.org/10.1039/c6nr06864b.

(56)   Zhu, K.; Baggi, G.; Loeb, S. J. Ring-through-Ring Molecular Shuttling in a Saturated [3]Rotaxane. *Nat. Chem.* **2018**, *10* (6), 625–630. https://doi.org/10.1038/s41557-018-

0040-9.

(57)   Moresco, F.; Meyer, G.; Rieder, K. H.; Tang, H.; Gourdon, A.; Joachim, C. Conformational Changes of Single Molecules Induced by Scanning Tunneling Microscopy Manipulation: A Route to Molecular Switching. *Phys. Rev. Lett.* **2001**, *86* (4), 672–675. https://doi.org/10.1103/PhysRevLett.86.672.

(58)   Binnig, G.; Rohrer, H.; Gerber, C.; Weibel, E. Tunneling through a Controllable Vacuum Gap. *Appl. Phys. Lett.* **1982**, *40*, 178–180. https://doi.org/10.1063/1.92999.

(59)   Eigler, D. M.; Schweizer, E. K. Positioning Single Atoms with a Scanning Tunneling Microscope. *Nature*. 1990, pp 524–526. https://doi.org/10.1038/344524a0.

(60)   Bandyopadhyay, A.; Pati, R.; Sahu, S.; Peper, F.; Fujita, D. Massively Parallel Computing on an Organic Molecular Layer. *Nat. Phys.* **2010**, *6* (5), 369–375. https://doi.org/10.1038/nphys1636.

(61)   Al Ouahabi, A.; Amalian, J.-A.; Charles, L.; Lutz, J.-F. Mass Spectrometry Sequencing of Long Digital Polymers Facilitated by Programmed Inter-Byte Fragmentation. *Nat. Commun.* **2017**, *8* (1), 967. https://doi.org/10.1038/s41467-017-01104-3.

(62)   Bethune, D. S.; Johnson, R. D.; Salem, J. R.; de Vries, M. S.; Yannoni, C. S. Atoms in Carbon Cages: The Structure and Properties of Endohedral Fullerenes. *Nature* **1993**, *366* (6451), 123–128. https://doi.org/10.1038/366123a0.

(63)   Shinohara, H. Endohedral Metallofullerenes. *Reports Prog. Phys.* **2000**, *63*, 843–892. https://doi.org/10.1088/0034-4885/63/6/201.

(64)   Popov, A. A.; Yang, S.; Dunsch, L. Endohedral Fullerenes. *Chem. Rev.* **2013**, *113*, 5989–6113. https://doi.org/10.1016/B978-0-08-097774-4.00938-4.

(65)   Popov, A. A. *Endohedral Fullerenes: Electron Transfer and Spin*; 2017. https://doi.org/10.1007/978-3-319-47049-8.

(66)   Krachmalnicoff, A.; Bounds, R.; Mamone, S.; Alom, S.; Concistrè, M.; Meier, B.; Kouril, K.; Light, M. E.; Johnson, M. R.; Rols, S.; Horsewill, A. J.; Shugai, A.; Nagel, U.; Rõõm, T.; Carravetta, M.; Levitt, M. H.; Whitby, R. J. The Dipolar Endofullerene HF@C 60. *Nat. Chem.* **2016**, *8* (10), 953–957. https://doi.org/10.1038/nchem.2563.

(67)   Taliani, C.; Ruani, G.; Zamboni, R.; Danieli, R.; Rossini, S.; Denisov, V. N.; Burlakov, V. M.; Negri, F.; Orlandi, G.; Zerbetto, F. Light-Induced Oxygen Incision of C60. *J. Chem. Soc. Chem. Commun.* **1993**, No. 3, 220–222. https://doi.org/10.1039/C39930000220.

(68)   Campbell, E. E. B.; Tellgmann, R.; Krawez, N.; Hertel, I. V. Production and LDMS Characterisation of Endohedral Alkali-Fullerene Films. *J. Phys. Chem. Solids* **1997**, *58* (11), 1763–1769.

(69)   Okada, H.; Komuro, T.; Sakai, T.; Matsuo, Y.; Ono, Y.; Omote, K.; Yokoo, K.; Kawachi, K.; Kasama, Y.; Ono, S.; Hatakeyama, R.; Kaneko, T.; Tobita, H. Preparation of Endohedral Fullerene Containing Lithium (Li@C60) and Isolation as Pure Hexafluorophosphate Salt ([Li+@C60][PF6−]). *RSC Adv.* **2012**, *2* (28), 10624. https://doi.org/10.1039/c2ra21244g.

(70)   Tóth, É.; Bolskar, R. D.; Borel, A.; González, G.; Helm, L.; Merbach, A. E.; Sitharaman, B.; Wilson, L. J. Water-Soluble Gadofullerenes: Toward High-Relaxivity, PH-Responsive MRI Contrast Agents. *J. Am. Chem. Soc.* **2005**, *127* (2), 799–805. https://doi.org/10.1021/ja044688h.

(71)   Guldi, D. M.; Feng, L.; Radhakrishnan, S. G.; Nikawa, H.; Yamada, M.; Mizorogi, N.; Tsuchiya, T.; Akasaka, T.; Nagase, S.; Ángeles Herranz, M.; Martín, N. A Molecular Ce2@ih-C80 Switch-Unprecedented Oxidative Pathway in Photoinduced Charge Transfer

Reactivity. *J. Am. Chem. Soc.* **2010**, *132* (26), 9078–9086.
https://doi.org/10.1021/ja101856j.

(72) Harneit, W. Fullerene-Based Electron-Spin Quantum Computer. *Phys. Rev. A - At. Mol. Opt. Phys.* **2002**, *65* (3), 6. https://doi.org/10.1103/PhysRevA.65.032322.

(73) Kroto, H. W.; Heath, J. R.; O'Brien, S. C.; Curl, R. F.; Smalley, R. E. C60: Buckminsterfullerene. *Nature* **1985**, *318*, 162–163. https://doi.org/10.1038/318162a0.

(74) Krätschmer, W.; Lamb, L. D.; Fostiropoulos, K.; Huffman, D. R. Solid C60: A New Form of Carbon. *Nature* **1990**, *347*, 354–358.

(75) Smalley, R. E. Self-Assembly of the Fullerenes. *Acc. Chem. Res.* **1992**, *25* (3), 98–105. https://doi.org/10.1021/ar00015a001.

(76) Dresselhaus, M. S.; Dresselhaus, G.; Eklund, P. C. Fullerenes. *J. Mater. Res.* **1993**, *8* (8), 2054–2097.

(77) Mirkin, C. A.; Caldwell, W. B. Thin Film, Fullerene-Based Materials. *Tetrahedron* **1996**, *52* (14), 5113–5130.

(78) Sakurai, T.; Wang, X.-D.; Xue, Q. K.; Hasegawa, Y.; Hashizume, T.; Shinohara, H. Scanning Microscopy of Fullerenes Study. *Prog. Surf. Sci.* **1996**, *51* (4), 263–408.

(79) Prato, M. [60]Fullerene Chemistry for Materials Science Applications. *J. Mater. Chem.* **1997**, *7* (7), 1097–1109. https://doi.org/10.1039/a700080d.

(80) Heath, J. R.; O'Brien, S. C.; Liu, Q. Z. Y.; Curl, R. F.; Tittel, F. K.; Smalley, R. E.; Kroto, H. W. Lanthanum Complexes of Spheroidal Carbon Shells. *J. Am. Chem. Soc.* **1985**, *107* (25), 7779–7780. https://doi.org/10.1021/ja00311a102.

(81) Hebard, A. F.; Rosseinsky, M. J.; Haddon, R. C.; Murphy, D. W.; Glarum, S. H.; Palstra, T. T. M.; Ramirez, A. P.; Kortan, A. R. Superconductivity at 18 K in Potassium-Doped C60. *Nature* **1991**, *350*, 600–601. https://doi.org/10.1038/350600a0.

(82) Holczer, K.; Klein, O.; Huang, S.-M.; Kaner, R. B.; Fu, K.-J.; Whetten, R. L.; Diederich, F. Alkali-Fulleride Superconductors: Synthesis, Composition, and Diamagnetic Shielding. *Science (80-.).* **1991**, *252* (5009), 1154–1157.

(83) Ruoff, R. S.; Tse, D. S.; Malhotra, R.; Lorents, D. C. Solubility of C60 in a Variety of Solvents. *J. Phys. Chem.* **1993**, *97*, 3379–3383. https://doi.org/10.1021/j100115a049.

(84) Cami, J.; Bernard-Salas, J.; Peeters, E.; Malek, S. E. Detection of C60 and C70 in a Young Planetary Nebula. *Science (80-.).* **2010**, *329* (5996), 1180–1182.

(85) Sellgren, K.; Werner, M. W.; Ingalls, J. G.; Smith, J. D. T.; Carleton, T. M.; Joblin, C. C60 in Reflection Nebulae. *Astrophys. J. Lett.* **2010**, *722* (1 PART 2), 54–57. https://doi.org/10.1088/2041-8205/722/1/L54.

(86) Acquah, S. F. A.; Penkova, A. V.; Markelov, D. A.; Semisalova, A. S.; Leonhardt, B. E.; Magi, J. M. Review-The Beautiful Molecule: 30 Years of C60 and Its Derivatives. *ECS J. Solid State Sci. Technol.* **2017**, *6* (6), M3155–M3162. https://doi.org/10.1149/2.0271706jss.

(87) Lüthi, H. P.; Almlöf, J. AB Initio Studies on the Thermodynamic Stability of the Icosahedral C60 Molecule "Buckminsterfullerene." *Chem. Phys. Lett.* **1987**, *135* (4–5), 357–360. https://doi.org/10.1016/0009-2614(87)85171-0.

(88) Hare, J. P.; Kroto, H. W.; Taylor, R. Preparation and UV/Visible Spectra of Fullerenes C60 and C70. *Chem. Phys. Lett.* **1991**, *177* (43), 394–398. https://doi.org/10.1016/j.cplett.2013.08.068.

(89)   Haddon, R. C. Chemistry of the Fullerenes: The Manifestation of Strain in a Class of Continuous Aromatic Molecules. *Science (80-.).* **1993**, *261* (5128), 1545–1550. https://doi.org/10.1126/science.261.5128.1545.

(90)   Fleming, R. M.; Siegrist, T.; Marsh, P. M.; Hessen, B.; Kortan, A. R.; Murphy, D. W.; Haddon, R. C.; Tycko, R.; Dabbagh, G.; Mujsce, A. M.; Kaplan, M. L.; Zahurak, S. M. Diffraction Symmetry in Crystalline, Close-Packed C60. *MRS Proc.* **1990**, *206*, 691. https://doi.org/10.1557/PROC-206-691.

(91)   Heiney, P. A.; Fischer, J. E.; McGhie, A. R.; Romanow, W. J.; Denenstein, A. M.; McCauley, J. P.; Smith, A. B.; Cox, D. E. Orientational Ordering Transition in Solid C60. *Phys. Rev. Lett.* **1991**, *66* (22), 2911–2914. https://doi.org/10.1103/PhysRevLett.66.2911.

(92)   Heiney, P. A.; Vaughan, G. B. M.; Fischer, J. E.; Coustel, N.; Cox, D. E.; Copley, J. R. D.; Neumann, D. A.; Kamitakahara, W. A.; Creegan, K. M.; Cox, D. M.; McCauley, J. P.; Smith, A. B. Discontinuous Volume Change at the Orientational-Ordering Transition in Solid C60. *Phys. Rev. B* **1992**, *45* (8), 4544–4547. https://doi.org/10.1103/PhysRevB.45.4544.

(93)   Harshman, D. R.; Fiory, A. T. High-T C Superconductivity in Cs3C60 Compounds Governed by Local Cs-C60 Coulomb Interactions. *J. Phys. Condens. Matter* **2017**, *29* (14). https://doi.org/10.1088/1361-648X/aa5dbd.

(94)   Wang, L.-S.; Conceicao, J.; Jin, C.; Smalley, R. E. Threshold Photodetachment of Cold C-60. *Chem. Phys. Lett.* **1991**, *182*, 5–11. https://doi.org/10.1016/0009-2614(91)80094-E.

(95)   Fleming, R. M.; Ramirez, A. P.; Rosseinsky, M. J.; Murphy, D. W.; Haddon, R. C.; Zahurak, S. M.; Makhija, A. V. Relation of Structure and Superconducting Transition Temperatures in A3C60. *Nature* **1991**, *352* (6338), 787–788. https://doi.org/10.1038/352787a0.

(96)   Torrelles, X.; Pedio, M.; Cepek, C.; Felici, R. (2√3 × 2√3)R30∘ Induced Self-Assembly Ordering by C60 on a Au(111) Surface: X-Ray Diffraction Structure Analysis. *Phys. Rev. B* **2012**, *86* (7), 075461. https://doi.org/10.1103/PhysRevB.86.075461.

(97)   Feng, M.; Zhao, J.; Petek, H. Atomlike, Hollow-Core–Bound Molecular Orbitals of C60. *Science (80-.).* **2008**, *320*, 359–362. https://doi.org/10.1126/science.1155866.

(98)   Dutton, G. J.; Dougherty, D. B.; Jin, W.; Reutt-Robey, J. E.; Robey, S. W. Superatom Orbitals of C60 on Ag(111): Two-Photon Photoemission and Scanning Tunneling Spectroscopy. *Phys. Rev. B - Condens. Matter Mater. Phys.* **2011**, *84* (19), 195435. https://doi.org/10.1103/PhysRevB.84.195435.

(99)   Tang, L.; Zhang, X.; Guo, Q.; Wu, Y.-N.; Wang, L.-L.; Cheng, H.-P. Two Bonding Configurations for Individually Adsorbed C60 Molecules on Au(111). *Phys. Rev. B - Condens. Matter Mater. Phys.* **2010**, *82* (12), 125414. https://doi.org/10.1103/PhysRevB.82.125414.

(100) Rogero, C.; Pascual, J. I.; Gómez-Herrero, J.; Baró, A. M. Resolution of Site-Specific Bonding Properties of C60 Adsorbed on Au(111). *J. Chem. Phys.* **2002**, *116*, 832–836. https://doi.org/10.1063/1.1424291.

(101) Schull, G.; Néel, N.; Becker, M.; Kröger, J.; Berndt, R. Spatially Resolved Conductance of Oriented C60. *New J. Phys.* **2008**, *10* (6), 065012. https://doi.org/10.1088/1367-2630/10/6/065012.

(102) Larsson, J. A.; Elliott, S. D.; Greer, J. C.; Repp, J.; Meyer, G.; Allenspach, R. Orientation of Individual C60 Molecules Adsorbed on Cu(111): Low-Temperature Scanning Tunneling Microscopy and Density Functional Calculations. *Phys. Rev. B - Condens. Matter Mater. Phys.* **2008**, *77* (11), 115434. https://doi.org/10.1103/PhysRevB.77.115434.

(103) Jarvis, S. P.; Rashid, M. A.; Sweetman, A.; Leaf, J.; Taylor, S.; Moriarty, P.; Dunn, J. Intermolecular Artifacts in Probe Microscope Images of C60 Assemblies. *Phys. Rev. B - Condens. Matter Mater. Phys.* **2015**, *92* (24), 241405. https://doi.org/10.1103/PhysRevB.92.241405.

(104) Shin, H.; Schwarze, A.; Diehl, R. D.; Pussi, K.; Colombier, A.; Gaudry, E.; Ledieu, J.; McGuirk, G. M.; Serkovic Loli, L. N.; Fournée, V.; Wang, L. L.; Schull, G.; Berndt, R. Structure and Dynamics of C60 Molecules on Au(111). *Phys. Rev. B - Condens. Matter Mater. Phys.* **2014**, *89* (24), 245428. https://doi.org/10.1103/PhysRevB.89.245428.

(105) Zhang, Y.; Gao, X.; Weaver, M. J. Scanning Tunneling Microscopy of Carbon Molecule (C60 and C70) on Ordered Gold (111) and Gold (110): Molecular Structure and Electron Transmission. *J. Phys. Chem.* **1992**, *96* (2), 510–513. https://doi.org/10.1021/j100181a003.

(106) Lu, X.; Grobis, M.; Khoo, K. H.; Louie, S. G.; Crommie, M. F. Charge Transfer and Screening in Individual C60 Molecules on Metal Substrates: A Scanning Tunneling Spectroscopy and Theoretical Study. *Phys. Rev. B* **2004**, *70* (11), 115418. https://doi.org/10.1103/PhysRevB.70.115418.

(107) Tzeng, C.; Lo, W.; Yuh, J.; Chu, R.; Tsuei, K. Photoemission, near-Edge x-Ray-Absorption Spectroscopy, and Low-Energy Electron-Diffraction Study of C60 on Au(111) Surfaces. *Phys. Rev. B - Condens. Matter Mater. Phys.* **2000**, *61* (3), 2263–2272. https://doi.org/10.1103/PhysRevB.61.2263.

(108) Guo, S.; Nagel, P. M.; Deering, A. L.; Van Lue, S. M.; Kandel, S. A. Scanning Tunneling Microscopy of Surface-Adsorbed Fullerenes: C60, C70, and C84. *Surf. Sci.* **2007**, *601* (4), 994–1000. https://doi.org/10.1016/j.susc.2006.11.042.

(109) Hashizume, T.; Motai, K.; Wang, X. D.; Shinohara, H.; Saito, Y.; Maruyama, Y.; Ohno, K.; Kawazoe, Y.; Nishina, Y.; Pickering, H. W.; Kuk, Y.; Sakurai, T. Intramolecular Structures of C60 Molecules Adsorbed on the Cu(111)-(1×1) Surface. *Phys. Rev. Lett.* **1993**, *71* (18), 2959–2962. https://doi.org/10.1103/PhysRevLett.71.2959.

(110) Tang, L.; Xie, Y.; Guo, Q. Complex Orientational Ordering of C60 Molecules on Au(111). *J. Chem. Phys.* **2011**, *135* (11). https://doi.org/10.1063/1.3639106.

(111) Wilson, R. J.; Meijer, G.; Bethune, D. S.; Johnson, R. D.; Chambliss, D. D.; de Vries, M. S.; Hunziker, H. E.; Wendt, H. R. Imaging C60 Clusters on a Surface Using a Scanning Tunnelling Microscope. *Nature*. 1990, pp 621–622. https://doi.org/10.1038/348621a0.

(112) Liu, L.; Liu, S.; Chen, X.; Li, C.; Ling, J.; Liu, X.; Cai, Y.; Wang, L. Switching Molecular Orientation of Individual Fullerene at Room Temperature. *Sci. Rep.* **2013**, *3* (111), 3062. https://doi.org/10.1038/srep03062.

(113) Joachim, C.; Gimzewski, J. K. An Electromechanical Amplifier Using a Single Molecule. *Chem. Phys. Lett.* **1997**, *265* (3–5), 353–357. https://doi.org/10.1016/S0009-2614(97)00014-6.

(114) Pedersen, M. O.; Murray, P. W.; Laegsgaard, E.; Stensgaard, I.; Besenbacher, F. Carbon-60 Induced Structures on the Clean and Oxygen Covered Cu(110) Surface: Competitive Adsorption. *Surf. Sci.* **1997**, *389*, 300–309.

(115) Reecht, G.; Heinrich, B. W.; Bulou, H.; Scheurer, F.; Limot, L.; Schull, G. Imaging Isodensity Contours of Molecular States with STM. *New J. Phys.* **2017**, *19* (11), 113033. https://doi.org/10.1088/1367-2630/aa969a.

(116) Joachim, C.; Gimzewski, J. K.; Schlittler, R. R.; Chavy, C. Electronic Transparence of a Single C60 Molecule. *Phys. Rev. Lett.* **1995**, *74* (11), 2102–2105.

https://doi.org/10.1103/PhysRevLett.74.2102.

(117)   Paßens, M.; Karthäuser, S. Interfacial and Intermolecular Interactions Determining the Rotational Orientation of C60 Adsorbed on Au(111). *Surf. Sci.* **2015**, *642*, 11–15. https://doi.org/10.1016/j.susc.2015.07.025.

(118)   Altman, E. I.; Colton, R. J. The Interaction of C60 with Noble Metal Surfaces. *Surf. Sci.* **1993**, *295* (1–2), 13–33. https://doi.org/10.1016/0039-6028(93)90181-I.

(119)   Altman, E. I.; Colton, R. J. Nucleation, Growth, and Structure of Fullerene Films on Au(111). *Surf. Sci.* **1992**, *279* (1–2), 49–67. https://doi.org/10.1016/0039-6028(92)90741-N.

(120)   Gimzewski, J. K.; Modesti, S.; Schlittler, R. R. Cooperative Self-Assembly of Au Atoms and C60 on Au(110) Surfaces. *Phys. Rev. Lett.* **1994**, *72* (7), 1036–1039. https://doi.org/10.1103/PhysRevLett.72.1036.

(121)   Pawlak, R.; Kawai, S.; Fremy, S.; Glatzel, T.; Meyer, E. High-Resolution Imaging of C60 Molecules Using Tuning-Fork-Based Non-Contact Atomic Force Microscopy. *J. Phys. Condens. Matter* **2012**, *24* (8), 084005. https://doi.org/10.1088/0953-8984/24/8/084005.

(122)   Fujita, D.; Yakabe, T.; Nejoh, H.; Sato, T.; Iwatsuki, M. Scanning Tunneling Microscopy Study on the Initial Adsorption Behavior of C60 Molecules on a Reconstructed Au(111)-(23 × √3) Surface at Various Temperatures. *Surf. Sci.* **1996**, *366* (1), 93–98. https://doi.org/10.1016/0039-6028(96)00786-8.

(123)   Abel, M.; Dmitriev, A.; Fasel, R.; Lin, N.; Barth, J. V; Kern, K. Scanning Tunneling Microscopy and X-Ray Photoelectron Diffraction Investigation of C60 Films on Cu(100). *Phys. Rev. B* **2003**, *67*, 245407. https://doi.org/10.1103/PhysRevB.67.245407.

(124)   Hauptmann, N.; González, C.; Mohn, F.; Gross, L.; Meyer, G.; Berndt, R. Interactions between Two C60 Molecules Measured by Scanning Probe Microscopies. *Nanotechnology* **2015**, *26* (44), 445703. https://doi.org/10.1088/0957-4484/26/44/445703.

(125)   Zhang, X.; Yin, F.; Palmer, R. E.; Guo, Q. The C60/Au(111) Interface at Room Temperature: A Scanning Tunnelling Microscopy Study. *Surf. Sci.* **2008**, *602* (4), 885–892. https://doi.org/10.1016/j.susc.2007.12.036.

(126)   Barth, J. V. V.; Brune, H.; Ertl, G.; Behm, R. J. Scanning Tunneling Microscopy Observations on the Reconstructed Au(111) Surface: Atomic Structure, Long-Range Superstructure, Rotational Domains, and Surface Defects. *Phys. Rev. B* **1990**, *42* (15), 9307–9318. https://doi.org/10.1103/PhysRevB.42.9307.

(127)   Schull, G.; Berndt, R. Orientationally Ordered (7×7) Superstructure of C60 on Au(111). *Phys. Rev. Lett.* **2007**, *99* (22), 226105. https://doi.org/10.1103/PhysRevLett.99.226105.

(128)   Gimzewski, J. K.; Modesti, S.; Gerber, C.; Schlittler, R. R. Observation of a New Au (111) Reconstruction at the Interface of an Adsorbed C60 Overlayer. *Chem. Phys. Lett.* **1993**, *213* (3–4), 401–406. https://doi.org/10.1016/0009-2614(93)85153-F.

(129)   Gardener, J. A.; Briggs, G. A. D.; Castell, M. R. Scanning Tunnelling Microscopy Studies of C60 Monolayers on Au(111). *Phys. Rev. B - Condens. Matter Mater. Phys.* **2009**, *80* (23), 235434. https://doi.org/10.1103/PhysRevB.80.235434.

(130)   Lu, X.; Grobis, M.; Khoo, K. H.; Louie, S. G.; Crommie, M. F. Spatially Mapping the Spectral Density of a Single C60 Molecule. *Phys. Rev. Lett.* **2003**, *90* (9), 096802. https://doi.org/10.1103/PhysRevLett.90.096802.

(131)   Wang, H.; Zeng, C.; Wang, B.; Hou, J. G.; Li, Q.; Yang, J. Orientational Configurations of the

C60 Molecules in the (2×2) Superlattice on a Solid C60(111) Surface at Low Temperature. *Phys. Rev. B - Condens. Matter Mater. Phys.* **2001**, *63* (8), 085417. https://doi.org/10.1103/PhysRevB.63.085417.

(132)   Villagómez, C. J.; Garzón, I. L.; Paz-Borbón, L. O. A First-Principles DFT Dispersion-Corrected C60/Au(111) Raman Study. *Comput. Mater. Sci.* **2020**, *171* (August 2019), 109208. https://doi.org/10.1016/j.commatsci.2019.109208.

(133)   Wang, L. L.; Cheng, H. P. Density Functional Study of the Adsorption of a C60 Monolayer on Ag(111) and Au(111) Surfaces. *Phys. Rev. B - Condens. Matter Mater. Phys.* **2004**, *69* (16), 165417. https://doi.org/10.1103/PhysRevB.69.165417.

(134)   Wang, L. L.; Cheng, H. P. Erratum: Density Functional Study of the Adsorption of a C60 Monolayer on Ag(111) and Au(111) Surfaces (Physical Review B - Condensed Matter and Materials Physics (2004) 69 (165417)). *Phys. Rev. B - Condens. Matter Mater. Phys.* **2007**, *75* (11), 165417. https://doi.org/10.1103/PhysRevB.75.119901.

(135)   Hamada, I.; Tsukada, M. Adsorption of C60 on Au(111) Revisited: A van Der Waals Density Functional Study. *Phys. Rev. B - Condens. Matter Mater. Phys.* **2011**, *83* (24), 245437. https://doi.org/10.1103/PhysRevB.83.245437.

(136)   Abad, E.; Ortega, J.; Flores, F. Metal/Organic Barrier Formation for a C 60/Au Interface: From the Molecular to the Monolayer Limit. *Phys. Status Solidi Appl. Mater. Sci.* **2012**, *209* (4), 636–646. https://doi.org/10.1002/pssa.201100610.

(137)   Pawlak, R.; Kawai, S.; Fremy, S.; Glatzel, T.; Meyer, E. Atomic-Scale Mechanical Properties of Orientated C60 Molecules Revealed by Noncontact Atomic Force Microscopy. *ACS Nano* **2011**, *5* (8), 6349–6354. https://doi.org/10.1021/nn201462g.

(138)   Li, H. I.; Pussi, K.; Hanna, K. J.; Wang, L. L.; Johnson, D. D.; Cheng, H. P.; Shin, H.; Curtarolo, S.; Moritz, W.; Smerdon, J. A.; McGrath, R.; Diehl, R. D. Surface Geometry of C60 on Ag(111). *Phys. Rev. Lett.* **2009**, *103* (5), 1–4. https://doi.org/10.1103/PhysRevLett.103.056101.

(139)   Pedio, M.; Felici, R.; Torrelles, X.; Rudolf, P.; Capozi, M.; Rius, J.; Ferrer, S. Study of C60/Au(111)-p(6 × 5) Reconstruction from In-Plane X-Ray Diffraction Data. *Phys. Rev. Lett.* **2000**, *85* (5), 1040–1043. https://doi.org/10.1103/PhysRevLett.85.1040.

(140)   Hinterstein, M.; Torrelles, X.; Felici, R.; Rius, J.; Huang, M.; Fabris, S.; Fuess, H.; Pedio, M. Looking underneath Fullerenes on Au(110): Formation of Dimples in the Substrate. *Phys. Rev. B - Condens. Matter Mater. Phys.* **2008**, *77* (15), 1–4. https://doi.org/10.1103/PhysRevB.77.153412.

(141)   Schull, G.; Frederiksen, T.; Brandbyge, M.; Berndt, R. Passing Current through Touching Molecules. *Phys. Rev. Lett.* **2009**, *103* (20), 11–14. https://doi.org/10.1103/PhysRevLett.103.206803.

(142)   Zhao, J.; Feng, M.; Yang, J.; Petek, H. The Superatom States of Fullerenes and Their Hybridization into the Nearly Free Electron Bands of Fullerites. *ACS Nano* **2009**, *3* (4), 853–864. https://doi.org/10.1021/nn800834k.

(143)   Feng, M.; Zhao, J.; Huang, T.; Zhu, X.; Petek, H. The Electronic Properties of Superatom States of Hollow Molecules. *Acc. Chem. Res.* **2011**, *44* (5), 360–368. https://doi.org/10.1021/ar1001445.

(144)   Hu, S.; Zhao, J.; Jin, Y.; Yang, J.; Petek, H.; Hou, J. G. Nearly Free Electron Superatom States of Carbon and Boron Nitride Nanotubes. *Nano Lett.* **2010**, *10* (12), 4830–4838. https://doi.org/10.1021/nl1023854.

(145) Bohl, E.; Mignolet, B.; Johansson, J. O.; Remacle, F.; Campbell, E. E. B. Low-Lying, Rydberg States of Polycyclic Aromatic Hydrocarbons (PAHs) and Cyclic Alkanes. *Phys. Chem. Chem. Phys.* **2017**, *19* (35), 24090–24099. https://doi.org/10.1039/c7cp03913a.

(146) Johansson, J. O.; Bohl, E.; Henderson, G. G.; Mignolet, B.; Dennis, T. J. S.; Remacle, F.; Campbell, E. E. B. Hot Electron Production and Diffuse Excited States in C70, C82, and Sc3N@C80 Characterized by Angular-Resolved Photoelectron Spectroscopy. *J. Chem. Phys.* **2013**, *139*, 084309. https://doi.org/10.1063/1.4818987.

(147) Feng, M.; Shi, Y.; Lin, C.; Zhao, J.; Liu, F.; Yang, S.; Petek, H. Energy Stabilization of the S-Symmetry Superatom Molecular Orbital by Endohedral Doping of C82 Fullerene with a Lanthanum Atom. *Phys. Rev. B - Condens. Matter Mater. Phys.* **2013**, *88* (7), 075417. https://doi.org/10.1103/PhysRevB.88.075417.

(148) Mignolet, B.; Campbell, E. E. B.; Remacle, F. Optical Activity of the Super-Atom Molecular Orbital (SAMO) States in Li@C60+ Conformers. *AIP Conf. Proc.* **2017**, *1906* (November), 030027. https://doi.org/10.1063/1.5012307.

(149) Yang, Y.-F.; Gromov, E. V.; Cederbaum, L. S. Caged-Electron States in Endohedral Li Fullerenes. *J. Phys. Chem. Lett.* **2019**, *10*, 7617–7622. https://doi.org/10.1021/acs.jpclett.9b02934.

(150) Huang, T.; Zhao, J.; Feng, M.; Petek, H.; Yang, S.; Dunsch, L. Superatom Orbitals of Sc3N@C80 and Their Intermolecular Hybridization on Cu(110)-(2x1)-O Surface. *Phys. Rev. B - Condens. Matter Mater. Phys.* **2010**, *81* (8), 085434. https://doi.org/10.1103/PhysRevB.81.085434.

(151) Guo, H.; Zhao, C.; Zheng, Q.; Lan, Z.; Prezhdo, O. V.; Saidi, W. A.; Zhao, J. Superatom Molecular Orbital as an Interfacial Charge Separation State. *J. Phys. Chem. Lett.* **2018**, *9* (12), 3485–3490. https://doi.org/10.1021/acs.jpclett.8b01302.

(152) Srivastava, A. K.; Pandey, S. K.; Pandey, A. K.; Misra, N. C60 as Electron Acceptor and Donor: A Comparative DFT Study of Li@C60 and F@C60. *Aust. J. Chem.* **2018**, *71* (12), 953–956. https://doi.org/10.1071/CH18391.

(153) Dunlap, B. I.; Ballester, J. L.; Schmidt, P. P. Interaction between C60 and Endohedral Alkali Atoms. *J. Phys. Chem.* **1992**, *96* (23), 9781–9787. https://doi.org/10.1021/j100203a038.

(154) Li, Y. S.; Tománek, D. How Free Are Encapsulated Atoms in C60? *Chem. Phys. Lett.* **1994**, *221* (5–6), 453–458. https://doi.org/10.1016/0009-2614(94)00297-5.

(155) Ohno, K.; Maruyama, Y.; Esfarjani, K.; Kawazoe, Y.; Sato, N.; Hatakeyama, R.; Hirata, T.; Niwano, M. Ab Initio Molecular Dynamics Simulations for Collision between C60- and Alkali-Metal Ions: A Possibility of Li@C60. *Phys. Rev. Lett.* **1996**, *76*, 3590–3593. https://doi.org/10.1103/PhysRevLett.76.3590.

(156) Hernández-Rojas, J.; Bretón, J.; Gomez Llorente, J. M. Rotational Spectra for Off-Center Endohedral Atoms at C60 Fullerene. *J. Chem. Phys.* **1996**, *104* (4), 1179–1186. https://doi.org/10.1063/1.470778.

(157) Bakowies, D.; Thiel, W. MNDO Study of Large Carbon Clusters. *J. Am. Chem. Soc.* **1991**, *113* (10), 3704–3714. https://doi.org/10.1021/ja00010a012.

(158) Wan, Z.; Christian, J. F.; Basir, Y.; Anderson, S. L. Collision of Alkali Ions with C60/C70: Insertion, Thermionic Emission, and Fragmentation. *J. Chem. Phys.* **1993**, *99* (8), 5858–5870. https://doi.org/10.1063/1.465939.

(159) Tellgmann, R.; Krawez, N.; Lin, S.-H.; Hertel, I. V.; Campbell, E. E. B. Endohedral Fullerene Production. *Nature* **1996**, *382* (6590), 407–408. https://doi.org/10.1038/382407a0.

(160) Ueno, H.; Aoyagi, S.; Yamazaki, Y.; Ohkubo, K.; Ikuma, N.; Okada, H.; Kato, T.; Matsuo, Y.; Fukuzumi, S.; Kokubo, K. Electrochemical Reduction of Cationic Li+@C60 to Neutral Li+@C60˙−: Isolation and Characterisation of Endohedral [60]Fulleride. *Chem. Sci.* **2016**, *7* (9), 5770–5774. https://doi.org/10.1039/C6SC01209D.

(161) Ueno, H.; Kokubo, K.; Nakamura, Y.; Ohkubo, K.; Ikuma, N.; Moriyama, H.; Fukuzumi, S.; Oshima, T. Ionic Conductivity of [Li+@C60](PF6-) in Organic Solvents and Its Electrochemical Reduction to Li+@C60-. *Chem. Commun.* **2013**, *49* (67), 7376–7378. https://doi.org/10.1039/c3cc43901a.

(162) Jorn, R.; Zhao, J.; Petek, H.; Seideman, T. Current-Driven Dynamics in Molecular Junctions: Endohedral Fullerenes. *ACS Nano* **2011**, *5* (10), 7858–7865. https://doi.org/10.1021/nn202589p.

(163) Srivastava, A. K.; Kumar, A.; Misra, N. Structure and Properties of Li@C60–PF6endofullerene Complex. *Phys. E Low-Dimensional Syst. Nanostructures* **2016**, *84*, 524–529. https://doi.org/10.1016/j.physe.2016.06.021.

(164) Pavanello, M.; Jalbout, A. F.; Trzaskowski, B.; Adamowicz, L. Fullerene as an Electron Buffer: Charge Transfer in Li@C60. *Chem. Phys. Lett.* **2007**, *442*, 339–343. https://doi.org/10.1016/j.cplett.2007.05.096.

(165) Yamada, Y.; Kuklin, A. V.; Sato, S.; Esaka, F.; Sumi, N.; Zhang, C.; Sasaki, M.; Kwon, E.; Kasama, Y.; Avramov, P. V.; Sakai, S. Electronic Structure of Li+@C60: Photoelectron Spectroscopy of the Li+@C60[PF6−] Salt and STM of the Single Li+@C60 Molecules on Cu(111). *Carbon N. Y.* **2018**, *133* (111), 23–30. https://doi.org/10.1016/j.carbon.2018.02.106.

(166) Zhang, M.; Harding, L. B.; Gray, S. K.; Rice, S. A. Quantum States of the Endohedral Fullerene Li@C60. *J. Phys. Chem. A* **2008**, *112*, 5478–5485. https://doi.org/10.1021/jp801083m.

(167) Andreoni, W.; Curioni, A. Ab Initio Approach to the Structure and Dynamics of Metallofullerenes. *Appl. Phys. A Mater. Sci. Process.* **1998**, *66* (3), 299–306. https://doi.org/10.1007/s003390050670.

(168) Aree, T.; Kerdcharoen, T.; Hannongbua, S. Charge Transfer, Polarizability and Stability of Li–C60 Complexes. *Chem. Phys. Lett.* **1998**, *285* (3), 221–225. https://doi.org/10.1016/S0009-2614(98)00031-1.

(169) Campbell, E. E. B.; Fanti, M.; Hertel, I. V.; Mitzner, R.; Zerbetto, F. The Hyperpolarisability of an Endohedral Fullerene: Li@C60. *Chem. Phys. Lett.* **1998**, *288* (1), 131–137. https://doi.org/10.1016/S0009-2614(98)00255-3.

(170) Bernshtein, V.; Oref, I. Surface Migrations of Endohedral Li+ on the Inner Wall of C60. *Phys. Rev. A* **2000**, *62* (February), 033201. https://doi.org/10.1103/PhysRevA.62.033201.

(171) Varganov, S. A.; Avramov, P. V; Ovchinnikov, S. G. Ab Initio Calculations of Endo- and Exohedral C60 Fullerene Complexes with Li+ Ion and the Endohedral C60 Fullerene Complex with Li2 Dimer. *Phys. Solid State* **2000**, *42* (2), 388–392. https://doi.org/10.1134/1.1131218.

(172) Aoyagi, S.; Nishibori, E.; Sawa, H.; Sugimoto, K.; Takata, M.; Miyata, Y.; Kitaura, R.; Shinohara, H.; Okada, H.; Sakai, T.; Ono, Y.; Kawachi, K.; Yokoo, K.; Ono, S.; Omote, K.; Kasama, Y.; Ishikawa, S.; Komuro, T.; Tobita, H. A Layered Ionic Crystal of Polar Li@C(60) Superatoms. *Nat. Chem.* **2010**, *2* (8), 678–683. https://doi.org/10.1038/nchem.698.

(173) Aoyagi, S.; Sado, Y.; Nishibori, E.; Sawa, H.; Okada, H.; Tobita, H.; Kasama, Y.; Kitaura, R.; Shinohara, H. Rock-Salt-Type Crystal of Thermally Contracted C60 with Encapsulated

Lithium Cation. *Angew. Chemie - Int. Ed.* **2012**, *51* (14), 3377–3381.
https://doi.org/10.1002/anie.201108551.

(174) Gromov, A.; Krawez, N.; Lassesson, A.; Ostrovskii, D. I.; Campbell, E. E. B. Optical
Properties of Endohedral Li@C60. *Curr. Appl. Phys.* **2002**, *2* (1), 51–55.
https://doi.org/10.1016/S1567-1739(01)00101-8.

(175) Popok, V. N.; Azarko, I. I.; Gromov, A. V.; Jönsson, M.; Lassesson, A.; Campbell, E. E. B.
Conductance and EPR Study of the Endohedral Fullerene Li@C60. *Solid State Commun.*
2005, *133* (8), 499–503. https://doi.org/10.1016/j.ssc.2004.12.014.

(176) Kwon, E.; Komatsu, K.-I.; Kawachi, K.; Kasama, Y.; Endo, T. Dynamic Behavior of Lithium-
Cation in a C60 Fullerene Cage Elucidated by Terahertz Spectroscopy. *Mol. Cryst. Liq.
Cryst.* **2014**, *598* (1), 28–31. https://doi.org/10.1080/15421406.2014.933294.

(177) Aoyagi, S.; Tokumitu, A.; Sugimoto, K.; Okada, H.; Hoshino, N.; Akutagawa, T. Tunneling
Motion and Antiferroelectric Ordering of Lithium Cations Trapped inside Carbon Cages. *J.
Phys. Soc. Japan* **2016**, *85* (9), 094605. https://doi.org/10.7566/JPSJ.85.094605.

(178) Suzuki, H.; Ishida, M.; Yamashita, M.; Otani, C.; Kawachi, K.; Kasama, Y.; Kwon, E.
Rotational Dynamics of Li+ Ions Encapsulated in C60 Cages at Low Temperatures. *Phys.
Chem. Chem. Phys.* **2016**, *18* (46), 31384–31387. https://doi.org/10.1039/C6CP06949E.

(179) Gromov, A.; Ostrovskii, D.; Lassesson, A.; Jönsson, M.; Campbell, E. E. B. Fourier
Transform Infrared and Raman Spectroscopic Study of Chromatographically Isolated
Li@C60 and Li@C70. *J. Phys. Chem. B* **2003**, *107* (41), 11290–11301.
https://doi.org/10.1021/jp030403w.

(180) Delaney, P.; Greer, J. C. C60 as a Faraday Cage. *Appl. Phys. Lett.* **2004**, *84* (3), 431–433.
https://doi.org/10.1063/1.1640783.

(181) Sabirov, D. S. Rules of Fullerene Polarizability. *Fullerenes, Nanotub. Carbon
Nanostructures* **2020**, *28* (1), 71–77. https://doi.org/10.1080/1536383X.2019.1671369.

(182) Johansson, M. P.; Jusélius, J.; Sundholm, D. Sphere Currents of Buckminsterfullerene.
Angew. Chemie - Int. Ed. **2005**, *44* (12), 1843–1846.
https://doi.org/10.1002/anie.200462348.

(183) Stefanou, M.; Chandler, H. J.; Mignolet, B.; Williams, E.; Nanoh, S. A.; Thompson, J. O. F.;
Remacle, F.; Schaub, R.; Campbell, E. E. B. Angle-Resolved Photoelectron Spectroscopy
and Scanning Tunnelling Spectroscopy Studies of the Endohedral Fullerene Li@C60.
Nanoscale **2019**, *11*, 2668–2678. https://doi.org/10.1039/c8nr07088a.

2 - <u>Methods</u>

The following chapter will describe the STM techniques employed in the analysis of the surface-bound Li@C_{60} system studied during this thesis. Firstly, the scanning tunnelling microscope will be introduced. Followed by a brief introduction to the theory of quantum tunnelling, the phenomenon upon which the microscope relies to investigate surfaces. This will lead to a discussion of the standard types of imaging and spectroscopic analysis available when employing an STM at low temperature. Finally, the concept of single molecule manipulation will be discussed and the specific methods utilised in exploring the activation of Li-migration within a surface-bound Li@C_{60} will be presented.

2.1 - <u>Scanning Tunnelling Microscope (STM)</u>

The scanning tunnelling microscope (see **Fig. 2.1** for example schematic) was invented by Binnig, Rohrer, Gerber and Wiebel in 1981[1] and employs a phenomenon called quantum tunnelling to analyse the surface of a substrate. Very simply, quantum tunnelling occurs when two conductive electrodes are brought close enough for their wavefunctions to overlap. This means that there is a probability that the electrons can leave the surface of one electrode, tunnel through the vacuum and progress into the other. By replacing one electrode with a metallic probe, images of the surface can be attained by raster scanning the probe across a surface and recording the flow of tunnelling electrons. Upon achieving suitable stability within the microscope, images of single atoms can be acquired.

Young *et al.* were the first to experimentally observe the phenomenon of electron tunnelling[2]. They designed a set-up which they named a "topografiner" and appeared very similar to a scanning tunnelling microscope (STM). However, they were plagued by mechanical vibrations which prevented them from achieving the atomic resolution which was observed by Binnig *et al.* after their invention of the STM[3].

The mechanical stability attained by Binnig *et al*. has been further improved upon using common techniques like suspending the STM with springs or using magnetic levitation. Also, separating the microscope housing from the surrounding building by placing it on its own foundations or using air dampening legs. Improvements to the signal to noise ratio have also been achieved by using shielded coaxial cables and converting the very low
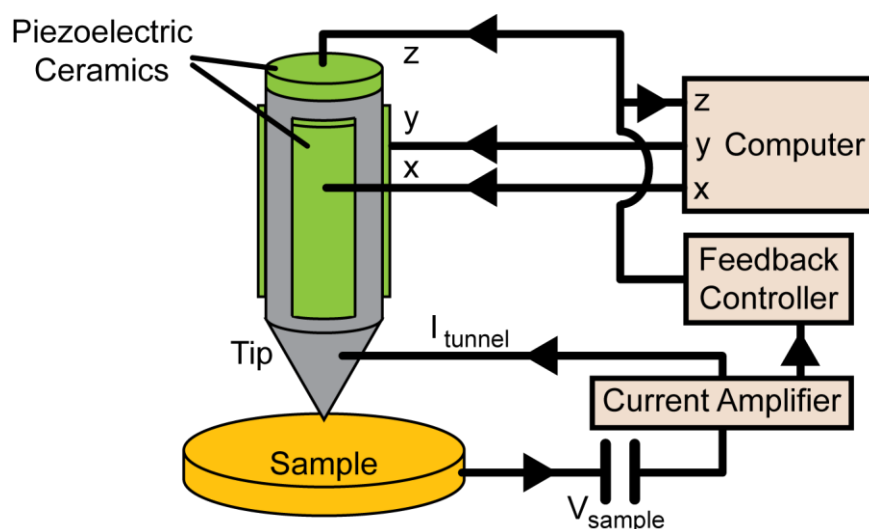
Figure 2.1: *Basic schematic of the STM consisting of a conductive sample, a current amplifier and an STM tip positioned by piezoelectric ceramics which respond to the feedback controller and the computer. Depending on the technique, the signal received by the computer is translated into spectra or 2D images.*

tunnelling current (~nA) to a voltage signal. This converted signal is preferred because it is less susceptible to noise from other electrical interference sources as it travels to the digital signal processing (DSP) board.

It wasn't long before the impact that the STM could have on the progression of surface science was recognised by the scientific world. This is illustrated by the Nobel Prize in Physics that Binnig and Rohrer won in 1986, only 5 years after the invention of the STM. Since then the field of scanning probe microscopy (SPM) has exploded and other revolutionary techniques have also been developed, like atomic force microscopy (AFM) and Kelvin probe force microscopy (KPFM). Further refinements have been made to each probe technique allowing hugely complex measurements to be achieved. For STM these techniques include, for example, scanning with modified tips[4,5], vibrational spectroscopy[6,7] and atomic manipulation[8] under a large range of environmental conditions. All of these STM techniques are based on the concept of quantum tunnelling, therefore an understanding of this must be achieved before any data analysis can be approached.

2.1.1 - <u>Quantum Tunnelling</u>

Quantum mechanics employs the Schrödinger equation (**eq. 1**) to describe the behaviour of elementary particles, like electrons. Wavefunctions are used since the particles exhibit wave-like behaviour as determined by the de Broglie equation (**eq. 2**). A more accurate description considers these particles as wavepackets which have an inherent uncertainty in their position and momentum, as described by the Heisenberg's uncertainty principle (**eq. 3**). However, for the purposes of this introduction to quantum tunnelling, utilising Schrödinger's equation to describe the elementary particles is sufficient to illustrate the phenomenon.

$$\frac{\delta^2 \psi}{dx^2} + \frac{8\pi^2 m}{h^2}(E - V)\psi = 0 \qquad\qquad eq.\ 1$$

$$\lambda = \frac{h}{p} \qquad\qquad eq.\ 2$$

$$\Delta x \cdot \Delta p \geq \frac{\hbar}{2} \qquad\qquad eq.\ 3$$

Where: $\psi =$ wavefunction, $m =$ mass, $h =$ Planck's constant, $E =$ kinetic energy, $V =$ potential energy, $\lambda =$ wavelength, $p =$ momentum, $\Delta x =$ uncertainty in position, $\Delta p =$ uncertainty in momentum, and $\hbar = \frac{h}{2}$

Considering this wave-like behaviour of the particles, the introduction of a potential barrier to the system results in some interesting observations. First, an infinitely high potential barrier will result in reflection of the particle, which agrees with how classical physics would describe the system. However, when one considers a finite potential well the wavefunction of the incidental particle extends beyond the edge of the potential barrier into a region which is forbidden by classical mechanics. This is known as quantum tunnelling.

The simplest description of quantum tunnelling (see **Fig. 2.2**) considers a free particle described by the wavefunction $\psi_1(x)$ with energy E_0. This particle starts in a 1D potential well (region 1) approaching a rectangular potential barrier of energy V (region 2). Since $E_0 < V$, classical mechanics states that the particle cannot progress and is reflected by the potential barrier. However, for small particles like electrons, the solution of the Schrödinger equation for region 2 shows that there is a non-zero probability of the particle progressing beyond the edge of the potential barrier. If the potential barrier, for example
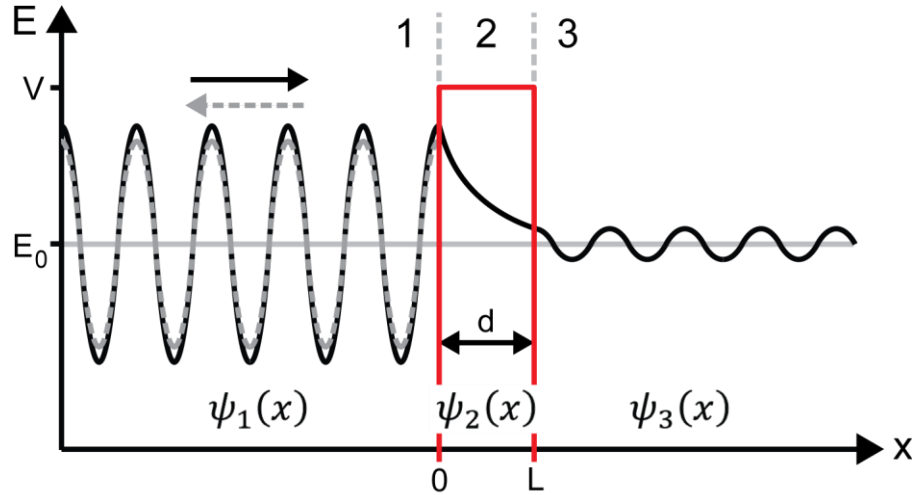
Figure 2.2: *Simplest illustration of quantum tunnelling: a free particle ($\psi_1(x)$, energy of E_0, solid black line, region 1) approaches a rectangular potential barrier (height of V, width of d, region 2). A portion of the wavefunction is reflected at the barrier ($x = 0$) (grey dashed line), but there is also a portion which enters the rectangular barrier (region 2). The wavefunction within the barrier is described by $\psi_2(x)$, the amplitude of which decays exponentially across region 2. Upon exiting the barrier (region 3) the particle acts as a free particle described by $\psi_3(x)$.*

a region of vacuum between two metal electrodes, is finite in length there is a chance that the particle will propagate through to region 3 where it returns to behaving like a free particle. This example of quantum tunnelling (employing two metal electrodes separated by a narrow region of vacuum) was first conceived of more than 90 years ago[9,10] and is the basis for the scanning tunnelling microscope.

The wavefunction for the particle in regions 1, 2 and 3 are represented by **eqs. 4, 5** and **6** respectively:

$$\psi_1(x) = A_I \cdot e^{i \cdot k \cdot x} + A_R \cdot e^{-i \cdot k \cdot x} \qquad\qquad eq.\ 4$$

$$\psi_2(x) = B \cdot e^{-k\prime \cdot x} \qquad\qquad eq.\ 5$$

$$\psi_3(x) = C \cdot e^{i \cdot k \cdot x} \qquad\qquad eq.\ 6$$

Where: A_I = amplitude of incident wavefunction, A_R = amplitude of reflected wavefunction, B = amplitude of tunnelling wavefunction, C = amplitude of transmitted wavefunction, $k = \sqrt{\dfrac{2 \cdot m(E_0 - V)}{\hbar^2}}$ = wavenumber of the

particle, and $k' = \sqrt{\frac{2 \cdot m(V - E_0)}{\hbar^2}}$ which replaces k when $E_0 < V$ (i.e. in region 2) since this would make k imaginary.

The wavefunction for the particle in region 1 of **Fig. 2.2** is composed of two parts: $A_I \cdot e^{i \cdot k \cdot x}$ which represents the incident particle (solid curve), and $A_R \cdot e^{-i \cdot k \cdot x}$ which describes the reflected portion of the wavefunction (dashed curve). Upon breaching the first edge of the potential barrier ($x = 0$ in **Fig. 2.2**) and entering region 2, the wavenumber (k) becomes imaginary because the energy of the particle is less than that of the potential barrier ($E_0 < V$). As such, this wavefunction is instead described with the wavevector k'. This results in the loss of the wave-like nature of the particle propagating through the potential barrier, instead the amplitude of the wavefunction decays exponentially. If the potential barrier is finite in width, the amplitude of the wavefunction upon reaching the terminating edge of the barrier ($x = L$ in **Fig. 2.2**) is non-zero. This results in the particle exiting the barrier, reacquiring its wavelike behaviour and propagating freely again (region 3 in **Fig. 2.2**). The wavefunction for the particle in region 3 exhibits the same wavelength as in region 1 but with a smaller amplitude due to the exponential decay as it progresses through the potential barrier.

The probability of a particle tunnelling through a potential barrier is known as the transmission probability (T) and is described by the following equation:

$$|\psi_2|^2 = T \propto e^{-2 \cdot k' \cdot d} \qquad\qquad \textit{eq. 7}$$

The exponential relationship between the transmission probability and the width of the potential barrier is the behaviour that Binnig *et al.* sought to employ in their design of the STM. It is also what affords the technique such high vertical resolution. This will be discussed further in this chapter.

2.1.2 - <u>Scanning Tunnelling Microscopy (STM)</u>

STM enables the study of the electron density of a surface by replacing one of the electrodes in **Fig. 2.2** with a scanning probe, or "STM tip", and applying a bias between the two electrodes to promote tunnelling in a specific direction (see **Fig. 2.3**).
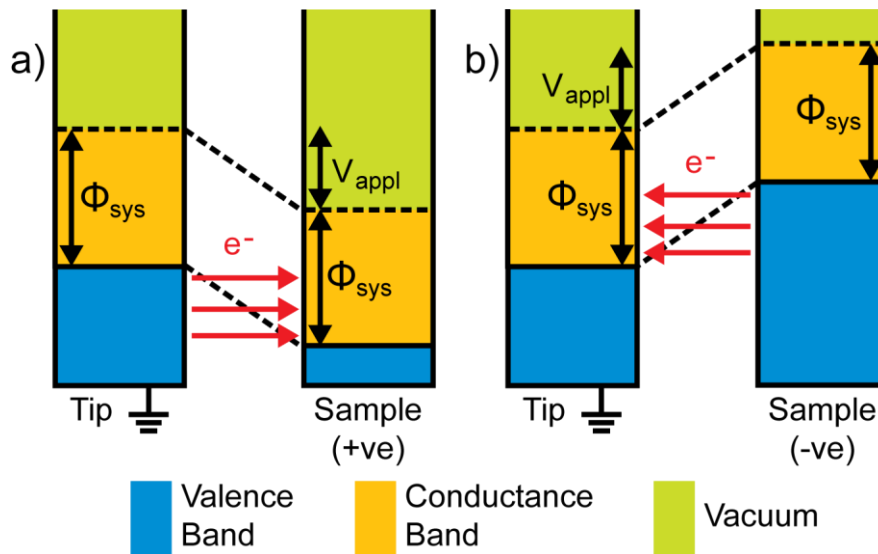
Figure 2.3: *Illustration of the effect of changing the applied bias between two conducting electrodes (i.e. tip and sample). Red arrows indicate the direction of electron tunnelling. **a)** A positive bias of magnitude V$_{appl}$ is applied to the sample. **b)** A negative bias of magnitude V$_{appl}$ is applied to the sample. In this illustration, the STM tip is grounded.*

Fig. 2.3 illustrates the effect of applying a bias across the electrodes in an STM junction. By applying a positive bias to the sample with respect to the tip, the Fermi level of the sample is lowered. Tunnelling is therefore promoted from the valence band of the tip into the conduction band of the sample, providing information on the unfilled states of the sample (**Fig. 2.3 (a)**). Applying a negative bias to the sample reverses this, instead probing its filled states (**Fig. 2.3 (b)**).

Fig. 2.3 is an overly simplified representation of the band structure of a system being studied. However, it does raise one issue which requires refinement of the description of quantum tunnelling utilised in **Fig. 2.2**. The previous description (**Fig. 2.2**) is a reasonable first approximation of quantum tunnelling, but is quickly complicated with the introduction of non-ideal potential barriers, like those exhibited in **Fig. 2.3** (trapezoidal rather than rectangular). Since the height of the potential barrier changes across the width of it (indicated by the slope of the dashed line in the tunnel junction), the value of k' will also change. This alters the decay rate of the particle as it propagates through the barrier. In an attempt to describe the tunnelling current through these potential barriers

an approximation was identified, known as the Wenzel-Kramers-Brillouin (WKB) approximation[11].

The WKB approximation essentially treats a non-ideal potential barrier as if it were an infinite number of consecutive ideal barriers. This allows the varying k' to be accounted for and produces infinite transmission probabilities which can be multiplied together to form the transmission probability for the non-ideal barrier. This is represented by the following equation:

$$T \propto e^{-\frac{2}{\hbar} \int_0^L \sqrt{2 \cdot m(V(x) - E_0)} \delta x} \qquad \textit{eq. 8}$$

The integral represents the combination of the infinite number of ideal barriers that approximate the non-ideal barrier where $V(x)$ is the potential barrier height at x when: $0 < x < L$.

Despite the application of the WKB approximation, the exponential decay exhibited by the wavefunction in the potential barrier is qualitatively similar. As understanding of the phenomenon of quantum tunnelling progressed, however, the WKB approximation was considered overly simple since it treats both electrodes as having featureless density of states (DOS). This is obviously not true when studying real electrodes.

The first success towards describing the tunnelling current more realistically was made by Bardeen[12] but only considered the case where the states being probed were close to the Fermi level (<10 meV). By making two assumptions: a) tunnelling is a single electron process (no interactions within the tunnel junction) and b) that the tip and surface are sufficiently separated to avoid direct interaction, Bardeen produced a definition of the probability of electron tunnelling using time dependent perturbation theory and Fermi's golden rule. This approximation was later expanded upon by Tersoff and Hamann.

Firstly, Tersoff and Hamann explained the exponential dependence of the resolution that is afforded by STM[13], and followed this by recognising that the tunnelling current is proportional to the local density of states (LDOS) of the sample[14]. These conclusions both centre on the assumption that the apex of the STM tip can be considered a spherical s-orbital upon probing a surface at energies close to the Fermi level (see **Fig. 2.4**). As such, the DOS of the tip are considered constant and can therefore be excluded from being responsible for any variation observed in the tunnelling current.
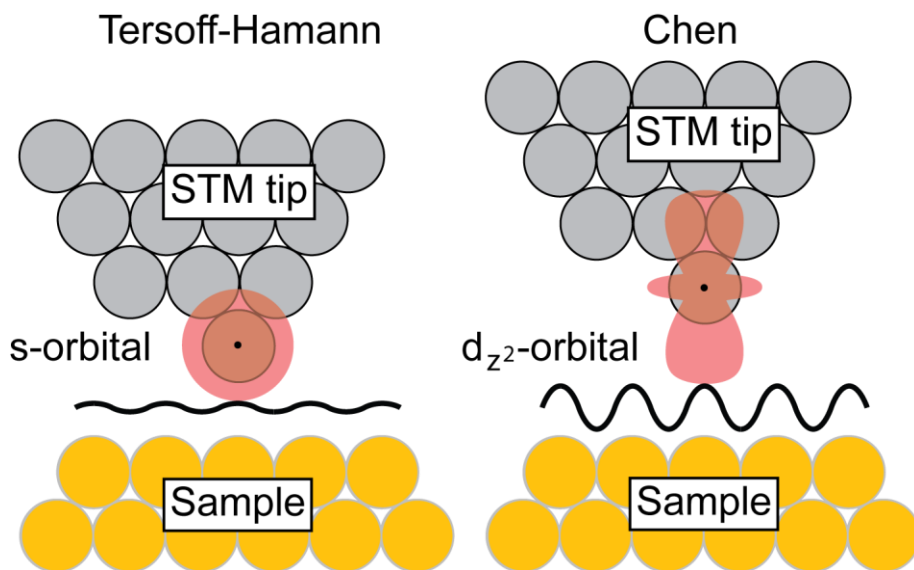
Figure 2.4: *Illustration of the Tersoff-Hamann[13,14] and Chen[15,16] models of the apex of an STM tip during tunnelling when in proximity to the Fermi level.*

The Tersoff-Hamann model of an s-orbital terminated tip also provided an explanation for why atomic corrugation could be achieved in STM imaging[3]. Due to the exponential decay of the tunnelling current in the tunnel junction, 90% of the tunnelling current is transmitted through an apex atom (assuming a tip structure like in **Fig. 2.4**). This allows the tunnel current to be assigned to specific coordinates as the tip is raster-scanned across a surface, and hence an image of the electron density of a region of the surface can be acquired.

Upon considering the corrugation of such experimentally acquired STM images, Chen suggested that the Tersoff-Hamann model of the apex of an STM tip was insufficient since the corrugation was greater than an s-orbital would record[15,16]. Instead they suggested that the d_{z^2}-orbital of the apex atom was responsible for transmitting the tunnelling current. The difference between these two conclusions is illustrated in **Fig. 2.4**. When scanning close to the Fermi level (~meV), the Chen model is considered most accurate. However, at higher scanning bias (~1-3 V) this model proves insufficient and the WKB approximation is used instead. In depth analysis of STM images therefore requires a different model depending on the bias regime in which the images are recorded.
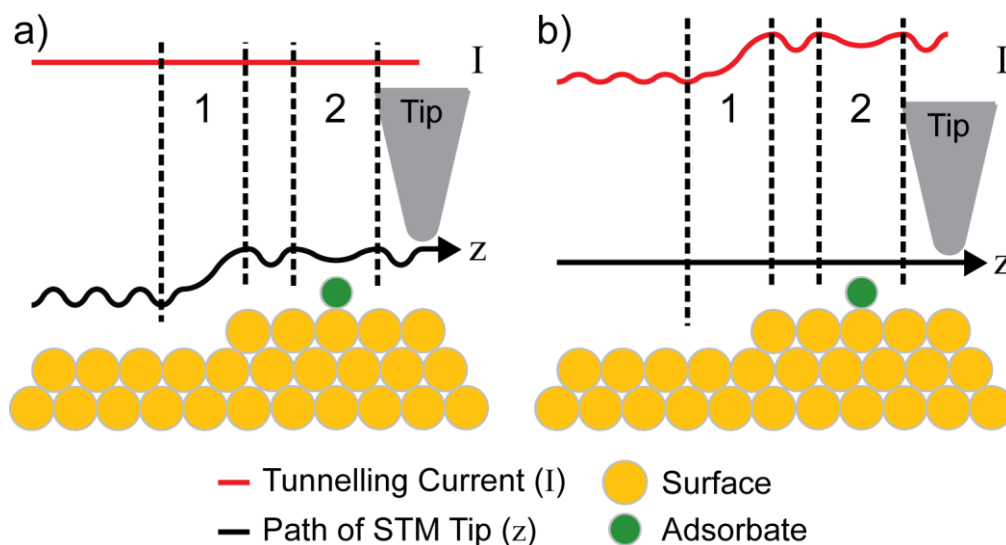
Figure 2.5: *Illustration of the two most common scanning modes for STM: **a)** constant current scanning tunnelling microscopy (c.c. STM) and **b)** constant height scanning tunnelling microscopy (c.h. STM).*

STM images are 3D representations of the electron density of a surface at a selected bias range, the *x* and *y* coordinates of the tip are two of the dimensions and the third is conveyed by the contrast within the images. On a clean, monometallic surface the map of the electronic density is comparable to a topographical map since the atoms all have the same electronic structure. When studying mixed metal surfaces or systems with adsorbates this comparison is no longer reliable since they have different electronic structures (as is shown in **Fig. 2.5**).

Fig. 2.5 illustrates the two most common scanning modes employed by an STM, how they respond to the electronic density as the surface is scanned, and how this signal can differ from the topographic appearance of the surface. The first is constant current scanning tunnelling microscopy (c.c. STM) (see **Fig. 2.5 (a)**). In this scan mode a feedback loop in the electronics of the microscope is employed to ensure the piezoelectric ceramics maintain a constant tunnelling current (*I*) throughout the raster scanning of the probe (see the red line profile in **Fig. 2.5 (a)**). These ceramics moderate the distance between the tip and the surface (see the black line profile in **Fig. 2.5 (a)**, this is the *z*-signal). Throughout the scan the tip can be seen reacting to the atomic corrugation of the substrate. However, in region 1 of the profiles (between the corresponding dashed lines) the tip retracts as the tunnelling current increases due to the proximity of the step edge.

Note that the tip reacts before the step edge is directly below it, this is due to tip convolution. In region 2 of the scan, the tip encounters an adsorbate with a wavefunction that does not extend as far as the bare surface. In order to maintain the required tunnelling current the tip approaches the surface causing a dip in the z-signal. Due to the response of the tip, the variation in the electronic density appears like a height change across an STM scan. However, the interaction with the adsorbate in region 2 highlights that it does not always correspond with topographic variation. As a result, the z-signal in this scan mode is referred to as apparent height.

Fig. 2.5 (b) illustrates the same portion of the surface scanned by the other most commonly used scanning mode; constant height scanning tunnelling microscopy (c.h. STM). In this case, the tip maintains a constant height (z) (see the black line profile in **Fig. 2.5 (b)**) and the varying tunnelling current (I) illustrates the changing electron density of the surface (see the red line profile in **Fig. 2.5 (b)**). In this instance the same data is collected, with respect to the changing electron density of the substrate in regions 1 and 2, but the useful information is instead observed in the tunnelling current profile (I-signal).

There are advantages and disadvantages to both of the above mentioned scanning modes; the requirements of the system and the intended investigations determine which is employed. Over atomically flat planes, c.h. STM is often preferred since raster speeds can be increased because the piezoelectric ceramics do not need to alter the vertical component of the tip trajectory. However, variation in the topography of the substrate, due to multiple terraces or large adsorbates for example, can result in the probe colliding with the sample which is likely to be detrimental for both the tip itself and the substrate. By engaging the feedback loop during data collection, c.c. STM can accommodate for large topographic height variation since the displacement of the tip can be adjusted to maintain a constant tunnelling current. This allows expansive areas of surfaces and large adsorbates to be examined without endangering the scanning probe. During these scans, the sensitivity of the feedback loop is very important as this determines the responsiveness of the piezoelectric ceramics (which control z) to variations in the tunnelling current (I). If the sensitivity is too low the probe responds slowly and features of the image are smoothed out resulting in distortions on the surface. If the sensitivity is too high the signal can cause ripples to appear on the image as the piezoelectric ceramics

overcompensate for the variation in current and oscillate during the scan. The sensitivity of the feedback loop therefore determines the speed at which the scans can be recorded.

For the purpose of the current work, c.c. STM is preferred over c.h. STM for its versatility. The size of the fullerenes (~7 Å[17] diameter, ~10 Å including the π-electron cloud[18]) prevents the simultaneous scanning of molecules and bare surface in constant height mode. Though c.c. STM requires more time to scan the surface, this does not cause issues within the current work since the microscope is cooled to ~5 K which prevents diffusion of adsorbates and limits thermal drift. Cooling the STM allows further techniques to be employed in the study of surfaces. These will be the topic of the next section.

2.2 - Low Temperature Scanning Tunnelling Microscope (LT-STM) Techniques

Operating an STM at low temperatures is commonly achieved by employing cryogenic liquids to cool the microscope (i.e. LN_2 and LHe). This is fairly regularly used with STM studies since it quenches the surface, fixing the substrate and adsorbates in place. Not only does this immobility afford the possibility of identifying specific adsorption sites and orientations of molecules, but also the possibility of manipulating single atoms or molecules. Another benefit of cooling the substrate is that the thermal drift is minimised, the STM tip can therefore be positioned over a single molecule for minutes (even hours) at a time. This allows the study of the electronic structure of the molecule using spectroscopic techniques.

2.2.1 - Scanning Tunnelling Spectroscopy (STS)

Scanning tunnelling spectroscopy (STS) is the most commonly utilised technique to examine the electronic structure of single molecules. Other methods of acquiring this information, such as PES, are incapable of being molecule specific so the results are representative of all species in the system. A standard STS procedure fixes the x and y coordinates of the STM probe such that the transmitted tunnelling current is recorded only through a single point. This leaves three parameters which can be monitored and manipulated to vary the data acquired; tip-sample displacement (z), the tunnelling current (I) and the bias applied to the system (V). There are many different modes of STS

Table 2.1: *Table showing some common types of scanning tunnelling spectroscopy.*

Constant parameter	Varied parameter	Examined signal
z	V	I
z	V	(c.h.) dI/dV
z	V	d^2I/dV^2
I	V	z
I	V	dz/dV
I	V	(c.c.) dI/dV

which can reveal different information about a surface or an adsorbate. By fixing one of the above parameters, controllably varying another and monitoring the response of a third, different properties can be examined. **Table 2.1** shows some of the most commonly employed combinations of this technique.

The first combination in **Table 2.1** is a mode in which the tip-sample displacement (z) is maintained whilst the tunnelling bias (V) is varied over a specific range, and the resulting current (I) is monitored. As a result of these parameter changes, the tunnelling current is expected to increase with the magnitude of the bias since the number of electronic states available for tunnelling also increases. This relationship is more striking when considering the first derivative of this signal (differential conductance [dI/dV]) since these variations are observed as peaks. This dI/dV signal can be acquired by employing either of two methods. The first is numerical differentiation of the I/V signal, however this can result in noisy spectra so more commonly a bias modulation is superimposed onto the bias ramp. This, in turn, induces a modulation in the tunnelling current and the dI/dV signal is then recorded by using a lock-in amplifier. A lock-in amplifier is a device which identifies the portion of the incoming signal which shares the frequency of the superimposed bias modulation and strongly attenuates all other signals in the spectrum. This leaves a much cleaner dI/dV signal for analysis. Though the dI/dV signal is known to be proportional to the LDOS[14,19,20], no compositional data can be directly analysed from this technique so it must be used in conjunction with other analytical methods (e.g. XPS, AES, DFT) in order to identify adsorbates/molecules on a surface.

In the current work, two modes of dI/dV STS are utilised in the analysis of the adsorbed fullerenes. The first is referred to as constant height differential conductance

spectroscopy (c.h. *dI/dV* STS) since the tip-sample displacement is held constant as the variation in the tunnelling current is recorded. The second is referred to as constant current differential conductance spectroscopy (c.c. *dI/dV* STS). As the name suggests, this technique maintains a constant current as a bias with a superimposed modulation is swept across the range of interest. In order to maintain a constant current the tip-sample displacement varies, however, the recorded signal is not this displacement but the small variations in the current as the piezoelectric ceramics readjust. The majority of *dI/dV* spectra discussed in the following chapters are acquired with a bias modulation of 50 mVpp oscillating at 1470 Hz, and the c.c. *dI/dV* spectra have a set point of 0.1 nA.

Both c.h. and c.c. *dI/dV* STS are utilised in the analysis of C_{60} and Li@C_{60} because of the large range of biases that is required during the study of these fullerenes. Due to limitations in the dynamical range of current measurement, the c.h. *dI/dV* STS technique is constrained to sweeping a small bias range. If this range is increased, the preamplifier responsible for current measurement is likely to saturate. This can be circumvented if the gain stage of the preamplifier is reduced, but this comes with a reduction in the sensitivity of the measurement. This behaviour is not observed for c.c. *dI/dV* STS. The resonance peaks in c.c. *dI/dV* spectra can be recorded over a much larger range because the current is moderated by the tip-sample displacement. One drawback of c.c. *dI/dV* STS is that crossing the Fermi level (*V*=0) leads to crashing the tip into the surface as it attempts to maintain a rapidly reducing tunnelling current by approaching the substrate. Another drawback for this technique is that the signal is not proportional to the LDOS of the molecule. More complex correction factors must be applied for the c.c. *dI/dV* signal[21] than for the c.h. *dI/dV* signal[22,23] in order to relate it to the LDOS. Without these corrections quantitative comparisons between the techniques are meaningless since specific resonance peaks will differ in energy.

Beside the single point techniques that are afforded by the above mentioned spectroscopic modes, both c.c. and c.h. *dI/dV* STS can also be applied to complementary imaging modes. By applying a small modulation to the tunnelling bias during a raster scan a small portion of the spectrum is recorded on each point of the image, compiling these spectra results in a 2D map of a portion of the electron density. This technique is known as differential conductance scanning tunnelling microscopy (*dI/dV* STM). Careful selection of the appropriate parameters (scanning bias, modulation and scan speed) can allow

images of specific electronic resonances to be captured. The most common method engages the feedback loop during scanning which results in the simultaneous capture of c.c. STM and c.c. *dI/dV* STM images. The images acquired are a reasonable approximation of a 2D map of a portion of the LDOS and thus lead to useful discussion regarding the distribution of electron density at different energies. These *dI/dV* imaging techniques are time-consuming but provide spatial representation of the orbitals which can be beneficial for the discussion.

2.2.2 - <u>Manipulation of Adsorbates</u>

After the successful utilisation of the STM probe in observing the electron density of single atoms, it wasn't long before the idea of manipulating these atoms was conceived. Though a small hop conceptually, it was no easy feat to accomplish. It wasn't until almost 10 years after the design of the STM that a different team at IBM, this time in California, first achieved controlled atomic manipulation with a cryogenically cooled STM[8]. Since then atomic and molecular manipulations have been studied via various methods resulting in a plethora of responses such as: lifting of single atoms[24] and polymerisation reactions[25]. Most importantly for this project, however, are those responses which are reversible and could be utilised within a molecular switch.

As was introduced in **section 1.2.1**, there are numerous manipulation methods which can be employed using an STM tip. These are controlled very similarly to the various spectroscopic modes detailed above; the three parameters (tip coordinates [*x, y, z*], *I* and *V*) can be varied, monitored and maintained. In this case an alteration of the molecule is desired, not merely an observation of its state. Some previous methods that have been explored include use of the electric field between the tip and the surface[26–29], mechanical manipulation (both vertical and lateral[30–32]) and excitation by inelastic electron collision[33–37].

The method of manipulation predominantly used in this project is similar to a technique employed by Schulze *et al.*[38,39] in their work studying the decomposition of C_{60} on surfaces. In their work, they employ resonant tunnelling to efficiently excite the selected molecule until decomposition of the carbon cage occurs. Resonant tunnelling occurs when the incidental tunnelling electrons share the same energy as one of the molecular orbitals of the adsorbate, as illustrated in **Fig. 2.6**.
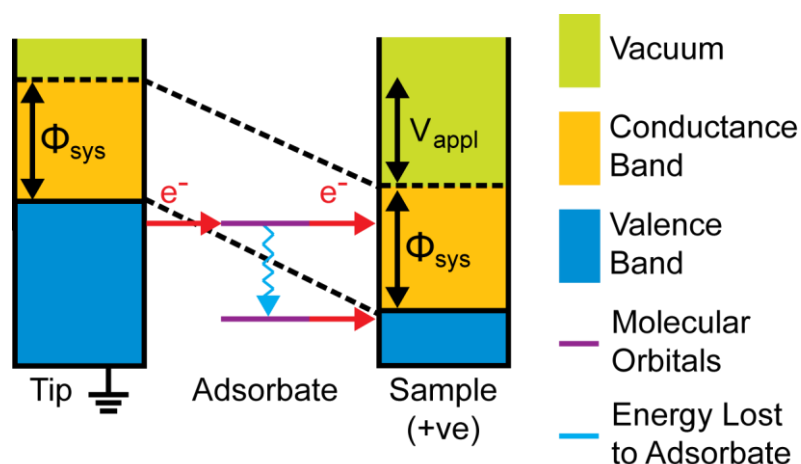
Figure 2.6: *Illustration of how resonant tunnelling occurs when an adsorbate is introduced into a tunnel junction. The adsorbate is represented by the energy levels in the tunnel junction (purple) between the tip (grounded) and the metal sample. Resonant tunnelling electrons can be transmitted to the sample with no energy loss (upper red arrow), or after interacting with the adsorbate and losing energy (lower red arrow).*

Fig. 2.6 is a simple illustration of how resonant tunnelling electrons can interact with molecules inserted into the tunnel junction of an STM. Electrons traversing the tunnel junction can be transmitted to the sample by two methods. Elastic tunnelling electrons lose no energy to the adsorbate before being transmitted to the sample, this is very efficient but requires the incidental electrons to share the energy of a molecular orbital in the adsorbate. The second method is inelastic tunnelling, these electrons lose energy upon interacting with the adsorbate and thus are transmitted to the sample with less energy than when leaving the tip. This excitation of the molecule can result in a variety of responses. Schulze *et al.*[38,39] identified thermal excitation of the C_{60} which resulted in more efficient decomposition of the carbon cage when the incidental electrons coupled with the LUMOs (LUMO, LUMO+1 etc.) of the fullerene. The current work uses resonant tunnelling slightly differently, and thus the manipulation method varies appropriately.

The dominant manipulation technique used during this work involves selecting a tunnelling current set point and disengaging the feedback loop. The manipulation parameters are then chosen such that a constant tunnelling bias is applied to the fullerene and a *z*-offset is utilised to lift the tunnelling current as required. During the application

of these parameters the tunnelling current is monitored for spontaneous changes which denote an alteration to the tunnel junction. Though the parameters vary slightly depending on the manipulation being explored, the standard parameters used throughout this thesis are +5.0 V and ±1.85 µA. Any variation from these is detailed in the relevant text in **Chapter 5**.

The second manipulation technique utilised in this work matches that described by Schulze *et al*. since decomposition of the fullerenes is the intended consequence[38,39]. Instead of selecting and maintaining both parameters throughout the manipulation process (as described above), this second technique involves maintaining a constant tunnel bias as the STM tip is forced closer to the substrate. This increases the tunnelling current, which is monitored, until such a point where a spontaneous reduction is observed indicating an alteration to the tunnel junction. The manipulation parameters are then removed and the STM returned to the set point.

2.3 - References

(1)   Binnig, G.; Rohrer, H.; Gerber, C.; Weibel, E. Tunneling through a Controllable Vacuum Gap. *Appl. Phys. Lett.* **1982**, *40*, 178–180. https://doi.org/10.1063/1.92999.

(2)   Young, R.; Ward, J.; Scire, F. Observation of Metal-Vacuum-Metal Tunneling, Field Emission, and the Transition Region. *Phys. Rev. Lett.* **1971**, *27* (14), 922–924. https://doi.org/10.1103/PhysRevLett.27.922.

(3)   Binnig, G.; Rohrer, H.; Gerber, C.; Weibel, E. 7x7 Reconstruction on Si(111) Resolved in Real Space. *Phys. Rev. Lett.* **1983**, *50* (2), 120–123.

(4)   Temirov, R.; Soubatch, S.; Neucheva, O.; Lassise, A. C.; Tautz, F. S. A Novel Method Achieving Ultra-High Geometrical Resolution in Scanning Tunnelling Microscopy. *New J. Phys.* **2008**, *10*, 053012. https://doi.org/10.1088/1367-2630/10/5/053012.

(5)   Nguyen, G. D.; Tsai, H.-Z.; Omrani, A. A.; Marangoni, T.; Wu, M.; Rizzo, D. J.; Rodgers, G. F.; Cloke, R. R.; Durr, R. A.; Sakai, Y.; Liou, F.; Aikawa, A. S.; Chelikowsky, J. R.; Louie, S. G.; Fischer, F. R.; Crommie, M. F. Atomically Precise Graphene Nanoribbon Heterojunctions from a Single Molecular Precursor. *Nat. Nanotechnol.* **2017**, *12* (September), 1077–1083. https://doi.org/10.1038/nnano.2017.155.

(6)   Stipe, B. C.; Rezaei, M. A.; Ho, W. Single-Molecule Vibrational Spectroscopy and Microscopy. *Science (80-.).* **1998**, *280* (5370), 1732–1735. https://doi.org/10.1126/science.280.5370.1732.

(7)   Bocquet, M.-L.; Lesnard, H.; Lorente, N. Inelastic Spectroscopy Identification of STM-Induced Benzene Dehydrogenation. *Phys. Rev. Lett.* **2006**, *96* (9), 096101. https://doi.org/10.1103/PhysRevLett.96.096101.

(8)   Eigler, D. M.; Schweizer, E. K. Positioning Single Atoms with a Scanning Tunneling Microscope. *Nature*. 1990, pp 524–526. https://doi.org/10.1038/344524a0.

(9)   Fowler, R. H.; Nordheim, L. Electron Emission in Intense Electric Fields. *Proc. R. Soc. London A* **1928**, *119*, 173–181. https://doi.org/10.1098/rspa.1928.0091.

(10)   Frenkel, J. On The Electrical Resistance of Contacts Between Solid Conductors. *Phys. Rev.* **1930**, *36*, 1604–1618. https://doi.org/10.1103/PhysRev.36.1604.

(11)   Bonnell, D. A. *Scanning Probe Microscopy and Spectroscopy: Theory, Techniques, and Applications*, 2nd ed.; Wiley-VCH: New York, 2001.

(12)   Bardeen, J. Tunnelling from a Many-Particle Point of View. *Phys. Rev. Lett.* **1961**, *6* (2), 57–59. https://doi.org/10.1103/PhysRevLett.41.1825.

(13)   Tersoff, J.; Hamann, D. R. Theory and Application for the Scanning Tunneling Microscope. *Phys. Rev. Lett.* **1983**, *50* (25), 1998–2001. https://doi.org/10.1002/ar.1092160117.

(14)   Tersoff, J.; Hamann, D. R. Theory of the Scanning Tunneling Microscope. *Phys. Rev. B* **1985**, *31* (2), 805–813.

(15)   Chen, C. J. Tunneling Matrix Elements in Three-Dimensional Space: The Derivative Rule and the Sum Rule. *Phys. Rev. B* **1990**, *42* (14), 8841–8857. https://doi.org/10.1103/PhysRevB.42.8841.

(16)   Chen, C. J. Effects of M=/=0 Tip States in Scanning Tunneling Microscopy: The Explanations of Corrugation Reversal. *Phys. Rev. Lett.* **1992**, *69* (11), 1656–1659. https://doi.org/10.1103/PhysRevLett.69.1656.

(17)   Kroto, H. W.; Heath, J. R.; O'Brien, S. C.; Curl, R. F.; Smalley, R. E. C60: Buckminsterfullerene. *Nature* **1985**, *318*, 162–163. https://doi.org/10.1038/318162a0.

(18)   Dresselhaus, M. S.; Dresselhaus, G.; Eklund, P. C. Fullerenes. *J. Mater. Res.* **1993**, *8* (8), 2054–2097.

(19)   Stroscio, J. A.; Feenstra, R. M.; Fein, A. P. Electronic Structure of the Si(111) 2x1 Surface by Scanning-Tunneling Microscopy. *Phys. Rev. Lett.* **1986**, *57* (20), 2579–2582. https://doi.org/10.1103/PhysRevLett.57.2579.

(20)   Lang, N. D. Spectroscopy of Single Atoms in the Scanning Tunneling Microscope. *Phys. Rev. B* **1986**, *34* (8), 5947–5950. https://doi.org/10.1103/PhysRevB.34.5947.

(21)   Ziegler, M.; Néel, N.; Sperl, A.; Kröger, J.; Berndt, R. Local Density of States from Constant-Current Tunneling Spectra. *Phys. Rev. B - Condens. Matter Mater. Phys.* **2009**, *80* (12), 125402. https://doi.org/10.1103/PhysRevB.80.125402.

(22)   Koslowski, B.; Dietrich, C.; Tschetschetkin, A.; Ziemann, P. Evaluation of Scanning Tunneling Spectroscopy Data: Approaching a Quantitative Determination of the Electronic Density of States. *Phys. Rev. B - Condens. Matter Mater. Phys.* **2007**, *75* (3), 035421. https://doi.org/10.1103/PhysRevB.75.035421.

(23)   Passoni, M.; Donati, F.; Li Bassi, A.; Casari, C. S.; Bottani, C. E. Recovery of Local Density of States Using Scanning Tunneling Spectroscopy. *Phys. Rev. B - Condens. Matter Mater. Phys.* **2009**, *79* (4), 1–11. https://doi.org/10.1103/PhysRevB.79.045404.

(24)   Eigler, D. M.; Lutz, C. P.; Rudge, W. E. An Atomic Switch Realized with the Scanning Tunnelling Microscope. *Nature*. 1991, pp 600–603. https://doi.org/10.1038/352600a0.

(25)   Okawa, Y.; Akai-Kasaya, M.; Kuwahara, Y.; Mandal, S. K.; Aono, M. Controlled Chain Polymerisation and Chemical Soldering for Single-Molecule Electronics. *Nanoscale* **2012**, *4* (10), 3013–3028. https://doi.org/10.1039/c2nr30245d.

(26)   Alemani, M.; Peters, M. V.; Hecht, S.; Rieder, K. H.; Moresco, F.; Grill, L. Electric Field-

Induced Isomerization of Azobenzene by STM. *J. Am. Chem. Soc.* **2006**, *128* (45), 14446–14447. https://doi.org/10.1021/ja065449s.

(27)   Raggi, G.; Stace, A. J.; Bichoutskaia, E. Polarisation Charge Switching through the Motion of Metal Atoms Trapped in Fullerene Cages. *Phys. Chem. Chem. Phys.* **2014**, *16* (43), 23869–23873. https://doi.org/10.1039/c4cp02672a.

(28)   Leoni, T.; Guillermet, O.; Walch, H.; Langlais, V.; Scheuermann, A.; Bonvoisin, J.; Gauthier, S. Controlling the Charge State of a Single Redox Molecular Switch. *Phys. Rev. Lett.* **2011**, *106* (21), 216103. https://doi.org/10.1103/PhysRevLett.106.216103.

(29)   Foroutan-Nejad, C.; Andrushchenko, V.; Straka, M. Dipolar Molecules inside C70: An Electric Field-Driven Room-Temperature Single-Molecule Switch. *Phys. Chem. Chem. Phys.* **2016**, *18* (48), 32673–32677. https://doi.org/10.1039/C6CP06986J.

(30)   Ladenthin, J. N.; Frederiksen, T.; Persson, M.; Sharp, J. C.; Gawinkowski, S.; Waluk, J.; Kumagai, T. Force-Induced Tautomerization in a Single Molecule. *Nat. Chem.* **2016**, *8* (July), 935–940. https://doi.org/10.1038/nchem.2552.

(31)   Gao, J.; Tang, L.; Holmes, S.; Li, F.; Palmer, R. E.; Guo, Q. Surface-Induced Symmetry Reduction in Molecular Switching: Asymmetric Cis-Trans Switching of CH3S-Au-SCH3 on Au(111). *Nanoscale* **2016**, *8* (47), 19787–19793. https://doi.org/10.1039/c6nr06864b.

(32)   Moresco, F.; Meyer, G.; Rieder, K. H.; Tang, H.; Gourdon, A.; Joachim, C. Conformational Changes of Single Molecules Induced by Scanning Tunneling Microscopy Manipulation: A Route to Molecular Switching. *Phys. Rev. Lett.* **2001**, *86* (4), 672–675. https://doi.org/10.1103/PhysRevLett.86.672.

(33)   Choi, B. Y.; Kahng, S. J.; Kim, S.; Kim, H.; Kim, H. W.; Song, Y. J.; Ihm, J.; Kuk, Y. Conformational Molecular Switch of the Azobenzene Molecule: A Scanning Tunneling Microscopy Study. *Phys. Rev. Lett.* **2006**, *96* (15), 156106. https://doi.org/10.1103/PhysRevLett.96.156106.

(34)   Scheil, K.; Gopakumar, T. G.; Bahrenburg, J.; Temps, F.; Maurer, R. J.; Reuter, K.; Berndt, R. Switching of an Azobenzene-Tripod Molecule on Ag(111). *J. Phys. Chem. Lett.* **2016**, *7* (11), 2080–2084. https://doi.org/10.1021/acs.jpclett.6b01011.

(35)   Pavliček, N.; Fleury, B.; Neu, M.; Niedenführ, J.; Herranz-Lancho, C.; Ruben, M.; Repp, J. Atomic Force Microscopy Reveals Bistable Configurations of Dibenzo[a,h]Thianthrene and Their Interconversion Pathway. *Phys. Rev. Lett.* **2012**, *108* (8), 086101. https://doi.org/10.1103/PhysRevLett.108.086101.

(36)   Simpson, G. J.; Hogan, S. W. L.; Caffio, M.; Adams, C. J.; Früchtl, H.; Van Mourik, T.; Schaub, R. New Class of Metal Bound Molecular Switches Involving H-Tautomerism. *Nano Lett.* **2014**, *14* (2), 634–639. https://doi.org/10.1021/nl4038517.

(37)   Huang, T.; Zhao, J.; Feng, M.; Popov, A. A.; Yang, S.; Dunsch, L.; Petek, H. A Molecular Switch Based on Current-Driven Rotation of an Encapsulated Cluster within a Fullerene Cage. *Nano Lett.* **2011**, *11* (12), 5327–5332. https://doi.org/10.1021/nl2028409.

(38)   Schulze, G.; Franke, K. J.; Gagliardi, A.; Romano, G.; Lin, C. S.; Rosa, A. L.; Niehaus, T. A.; Frauenheim, T.; Di Carlo, A.; Pecchia, A.; Pascual, J. I. Resonant Electron Heating and Molecular Phonon Cooling in Single C60 Junctions. *Phys. Rev. Lett.* **2008**, *100* (13), 136801. https://doi.org/10.1103/PhysRevLett.100.136801.

(39)   Schulze, G.; Franke, K. J.; Pascual, J. I. Resonant Heating and Substrate-Mediated Cooling of a Single C60 Molecule in a Tunnel Junction. *New J. Phys.* **2008**, *10,* 065005. https://doi.org/10.1088/1367-2630/10/6/065005.

3 - <u>Experimental</u>

What follows is an account of the experimental set up and procedures employed during the undertaking of this research.

3.1 - <u>Instrumentation</u>

The system used to acquire all of the STM images and spectroscopy in the following chapters is a CreaTec Low Temperature Scanning Tunnelling Microscope (LT-STM) cooled to ~5 K. Not only does this low temperature prevent spontaneous molecular migration on the surfaces but it minimises both thermal creep and drift of the piezoelectric ceramics, and reduces the z-noise to about 1 pm. CreaTec are a German manufacturer of highly customisable ultra-high vacuum (UHV) systems who work closely with their clients to design systems to suit specific experimental requirements.

For this project the UHV LT-STM system (see the CAD model in **Fig. 3.1**) houses a Besocke beetle-type microscope[1] inside a chamber which can be isolated from the rest of the system using gate valves (**Fig. 3.1 (e)**). The microscope is suspended by springs within a double layered radiation shield and is cooled by two cryostats (15 L outer and 5 L inner, see **Fig. 3.1 (6)**). The whole system is situated on four Newport Dampener Legs (**Fig. 3.1 (g)**) which can be inflated with nitrogen gas to provide added vibrational isolation for the most delicate experiments. These are rarely needed, however, because the housing is situated on a 14 tonne concrete block which acts as its own foundations. This separates the system from the rest of the building minimising the vibrations which could be transmitted to the microscope from elsewhere in the department. A pressure of $<10^{-11}$ mbar is attained in the microscope chamber by a combination of turbo-molecular vacuum pumps and ion pumps (**Fig. 3.1 (b)**). This level of cleanliness and stability are vital for the projects discussed below due to the requirement to study single molecules for days at a time. This complex system (**Fig. 3.1**) can be simplified by considering the 6 distinct sections and discussing the role of each in the process of moving the sample from the workbench and into the microscope for analysis.
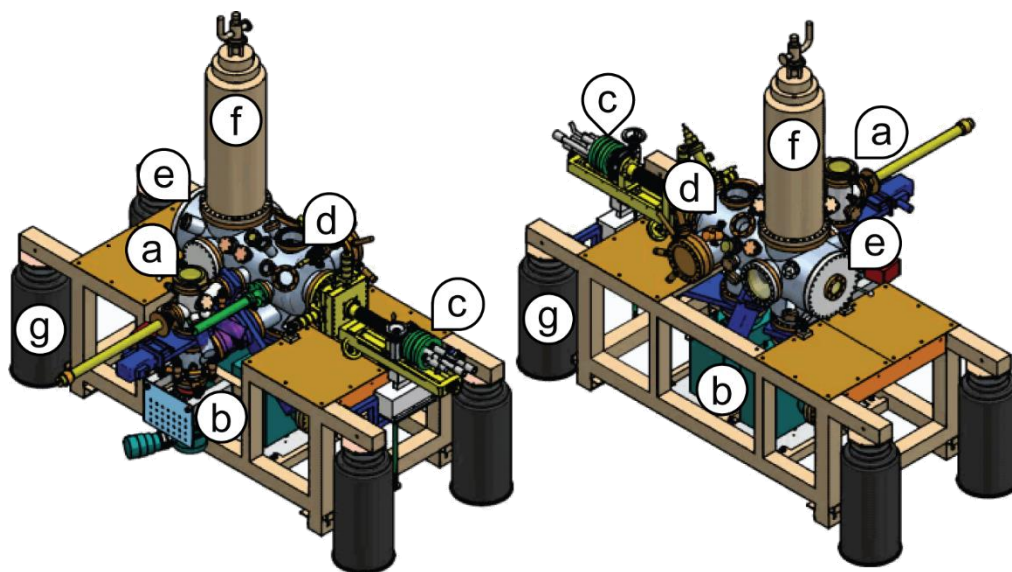
Figure 3.1: *Front and back views of the CAD model (kindly supplied by CreaTec and published with their permission).* ***a)*** *Load lock with magnetic arm.* ***b)*** *Pumping system comprised of turbo-molecular pumps and ion pumps.* ***c)*** *Manipulator arm.* ***d)*** *Preparation chamber.* ***e)*** *STM chamber.* ***f)*** *Cryostats.* ***g)*** *Newport dampener legs.*

3.1.1 - Load Lock

The load lock (**Fig. 3.1 (a)**) is a small chamber that is most often used for easy transfer of samples in and out of the vacuum chambers. The uppermost flange allows for either a copper-gasket sealed permanent view-port (with a base pressure of ~10^{-10} mbar) or a hinged view-port sealed with a Viton ring (with a base pressure of ~10^{-7} mbar). The magnetic arm facilitates quick transfers between the load lock and the preparation chamber. The load lock also has a gate valve allowing direct access to the turbo-molecular pumping system positioned below it. This facilitates removal of the majority of the vacuum from the load lock before introducing the sample to the preparation chamber.

3.1.2 - Pumping System

The pumping system (**Fig. 3.1 (b)**) can be split into three distinct sections: the combination of pumps which remove the bulk of the pressure from the system, the ion pumps and the additional pumps.

The first set of pumps, located beneath the load lock, are responsible for reducing the pressure throughout the system from atmosphere (1 bar) to ~10^{-10} mbar (UHV), and for maintaining sufficient cleanliness in the preparation chamber during sample preparation. This is achieved by a combination of a two-stage membrane pump which reduces the pressure behind a 60 L/s turbo-molecular pump so that it can bring the pressure to ~10^{-6} mbar. This small turbo-pump is responsible for reducing the pressure behind the 240 L/s turbo-molecular pump which achieves the standard operating pressure of ~10^{-10} mbar throughout the UHV system.

The ion pumps are used to achieve the highest levels of cleanliness in the system since turbo-pumps are inefficient when working with lighter species such as hydrogen and helium. The preparation and STM chambers each have an ion pump to ensure they can be isolated from each other whilst maintaining sufficient cleanliness. These pumps are rarely turned off but gate valves can be employed to separate them from their respective chambers in order to maximise the operational lifespan. This is particularly useful during preparation of the samples when employing partial pressures greater than 10^{-9} mbar or gases which can be harmful to the pumps (e.g. Ar for sputtering and O_2 for Cu(110)-(2×1)O reconstruction).

The additional pumps on this system are mostly combination pumps (a singular unit with a 60 L/s turbo-molecular pump backed by a two stage membrane pump). This type of pump is used in two places: the manipulator and gas storage system to maintain the cleanliness of these lines, and during preparation of the molecular evaporator. In the second case an additional 60 L/s turbo-molecular pumping unit is also employed to ensure the evaporator achieves sufficient pressures and cleanliness before introduction to the preparation chamber.

3.1.3 - Manipulator

The manipulator arm (**Fig. 3.1 (c)**) affords control over the sample once it is transferred to the preparation chamber from the load lock. The four-degrees of freedom for the movement of the manipulator (x, y, z and 360° rotation) allow the millimetre precision required when positioning the sample holder for each stage of the preparation, and transferring it in and out of the STM. The temperature of the manipulator can be finely controlled by a combination of resistive heating and cryogenic cooling employing,

respectively, a set of wires and a capillary tube running along its length. Type K thermocouple wires (alumel/chromel) allow accurate temperature reading of both the sample and the manipulator at mid-range temperatures, and at extreme temperatures give an error of only ±50 K. This heating system allows a large range of temperatures to be experimented with (~20 K → >750 K).

3.1.4 - <u>Preparation Chamber</u>

The preparation chamber (see **Fig. 3.1 (d)** and the blue portion of **Fig. 3.2**) is where the majority of surface modification occurs before the sample is transferred into the STM chamber (see **Fig. 3.1 (e)** and the red portion of **Fig. 3.2**). Besides the devices required for preparation of the samples, there are also some analytical techniques available in the preparation chamber. The flanges utilised for these devices are labelled in **Fig. 3.2**.

The Ar$^+$ ion gun (**Fig. 3.2 (a)**) is used to clean the substrates by repeated sputter/anneal cycles to ensure a good quality surface for the deposition of the intended species. Some sample preparations require the introduction of deliberate partial pressures of selected gases, this is achieved by the 2 small reservoirs with needle valves which are connected to the gas inlet (**Fig. 3.2 (b)**). These needle valves allow very fine control over the pressure so that accurate conditions could be repeated in the preparation of specific surfaces, for example the Cu(110)-(2×1)O which will be introduced in **section 3.2.1.2**. These gas reservoirs are connected to the gas storage system, which is mentioned above, but also to an inlet on the STM chamber such that small amounts of gases could be introduced directly into the microscope if desired. This function is not utilised in the following work.

The other components attached to the preparation chamber include: a storage garage for other samples and spare STM tips (**Fig. 3.2 (c)**), an ion pressure gauge (range of 10^{-5}-10^{-12} mbar) (**Fig. 3.2 (d)**), a view-port into the vacuum system (**Fig. 3.2 (e)**), an Auger electron spectroscopy (AES) unit and low energy electron diffraction (LEED) device with fluorescent screen (**Fig. 3.2 (f)**), and a residual gas analyser (RGA) mass spectrometer (range of 0-100 amu) (**Fig. 3.2 (g)**). The final occupied flange on the preparation chamber has a gate valve attached to it allowing the molecular evaporator to be separated from the preparation chamber (**Fig. 3.2 (h)**). This allows for baking and degassing of the molecular samples before introduction to the UHV system ensuring the cleanliness of the system can be maintained.
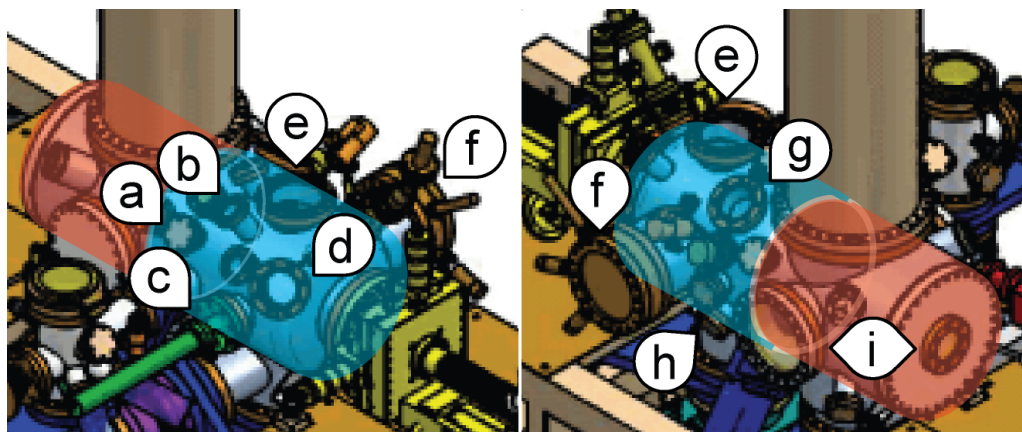
Figure 3.2: *Magnified images of the front and back views of the CAD model in Fig. 3.1. To facilitate identification of the two chambers the preparation chamber is shaded blue and the STM chamber is red. The labelled positions correspond with flanges which accommodate the following devices: **a)** Ar⁺ ion gun, **b)** gas reservoirs, **c)** sample storage garage, **d)** ion pressure gauge, **e)** window, **f)** Low Energy Electron Diffraction (LEED) and Auger Electron Spectroscopy (AES), **g)** residual gas analyser (RGA) mass spectrometer, **h)** gate valve to separate the molecular evaporator from the preparation chamber, **i)** windows for the STM chamber.*

Due to the system of pumps described above, the standby pressure in the preparation chamber is typically <10^{-10} mbar. Maintaining this pressure is important to avoid transfer of pollutants into the STM chamber when placing the sample in the microscope for analysis. This transfer process was delicate since the view-ports on the STM chamber (**Fig. 3.2 (i)**) only allow limited visual access past the radiation shields and into the microscope itself.

3.1.5 - STM Chamber

The STM chamber (**Fig. 3.1 (e)**) houses the microscope which is suspended on springs, further stabilisation is afforded by magnets which dampen any movements induced in the microscope by external vibrations. The microscope is also shielded from radiation to ensure that the cryostats can maintain a constant temperature on the sample. This reduces the thermal drift to ~1 Å/hr in the x and y directions and 1 pm/hr in the z direction. The wiring in the microscope is set up such that the bias is applied to the sample. When

operating at negative biases, therefore, the filled states of the surface are probed and vice versa.

In order to minimise the noise induced in the signal between the tip and the digital signal processing (DSP) unit, the current transmitted to (or from) the tip is converted to a voltage signal by a variable gain, low noise Femto pre-amplifier. Voltage signals are less susceptible to noise than current signals; with the working currents employed in this microscope (~nA) the noise induced in the signal would be significant given the metres of coaxial cabling along which the signal is transmitted. The DSP converts the voltage into a signal which can be processed by the scanning software (detailed in **section 3.3**) into the images and spectra used for analysis.

3.1.6 - Cryostats

The entirety of the following work is achieved at ~5 K by utilising cryostats filled with cryogenic liquids (**Fig. 3.1 (f)**). The inner cryostat (5 L) is regularly filled with liquid helium (LHe) and the outer cryostat (15 L) with liquid nitrogen (LN_2). Since LN_2 is more readily available and reasonably cheap the outer cryostat is used as insulation for the inner cryostat, thus reducing the rate of evaporation of the LHe. This helps maintain stability because top ups are only required every couple of days. We are fortunate that our department has an inbuilt LHe recovery line capable of retaining >95% of the LHe, recompressing it and allowing waste to be minimised.

3.1.7 - Sample Holder

Each of the metal single crystals employed during this project is attached to a sample holder in order to interface with both the manipulator and the STM. An illustration of the sample holder can be seen in **Fig. 3.3**.

The "top hat" single crystal metal samples (**Fig. 3.3 (a)**) (detailed in **section 3.2.1**) are secured with a tantalum clip (**Fig. 3.3 (b)**) to maintain a solid contact between the sample and the button heater oven (**Fig. 3.3 (c)**) ensuring efficient heating of the sample. The oven is held in place by a ceramic collar (**Fig. 3.3 (d)**) allowing the height of the oven to be accurately set whilst the set-up in **Fig. 3.3** is constructed, but more importantly insulating
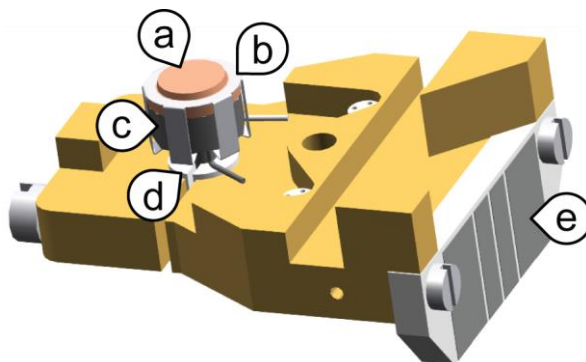
Figure 3.3: *CAD rendered image of the sample holder (kindly supplied by CreaTec and is displayed with their permission). The labels indicate: **a)** the single crystal metal sample, **b)** the tantalum clip, **c)** the button heater oven, **d)** the ceramic collar and **e)** the ceramic backplate.*

it from the sample holder which is predominantly made of copper. Two pairs of wires pass through small ceramic pieces in the sample holder and contact the electrodes on the ceramic backplate (**Fig. 3.3 (e)**). One pair is connected to the button heater supplying both the resistive current for heating the sample and the bias application for STM measurements. The other pair are the Type K thermocouple wires which enable temperature measurements whilst in the STM and during the sample preparation.

3.2 - Preparation

The work of Gardener *et al*. on C_{60} on Au(111)[2] in combination with advice from our collaborators in the Campbell group formed the basis of our preparation process for Li@C_{60}. The preparation of the samples follow general protocols for C_{60} on metal substrates as seen in the literature[2–5]. Once the sample holder is introduced to the vacuum system the metal crystal is cleaned by repeated sputter/anneal cycles and prepared for the molecular deposition. The specific conditions for the surface preparations can be seen in **Table 3.1**, these vary with the metal crystal and the type of surface required. For example, the Au(111) sample is prepared with 2 different molecular structures (large 2D arrays of fullerenes and small islands with some isolated species, see **Chapter 4** for details) but the Cu(110) crystal undergoes a partial oxidation before the fullerenes are deposited. The preparation of these surfaces is the discussion for the following sections.

Table 3.1: *Preparation conditions for each of the three surfaces studied below.*

	Metal Crystal:	Au(111)	Au(111)	Cu(110)
	Ordering of Fullerenes:	Large Islands	Small Islands/ Isolated	Decorated Edges/Isolated
Sputtering:	Temperature (K):	300	300	300
	Beam Energy (eV):	1500	1500	1000
	Ar$^+$ Ion Current (µA):	0.7	0.7	0.7
	Duration (mins):	7.5	7.5	7.5
UHV Annealing:	Temperature (K):	823	823	773
	Duration (mins):	15	15	15
Sputter/Anneal:	Cycles:	2	2	2
Surface Modification:	Treatment:	N/A	N/A	Oxidation (O_2)
	Temperature (K):	N/A	N/A	623
	Pressure (mbar):	N/A	N/A	5×10^{-8}
	Duration (s):	N/A	N/A	45
Sample Deposition:	Molecule:	Li@C_{60}	Li@C_{60}	Li@C_{60}
	Sample Temp. (K):	~290	~320	~320
	Molecule Temp. (K):	~663	~663	~663
	Pressure (mbar):	~1×10^{-7}	~5×10^{-8}	~5×10^{-8}
	Duration (mins):	8	4	4
Post-Adsorption Anneal	Temperature (K):	~570	~320	~320
	Duration (mins):	0.5	60	60

3.2.1 - Metal Single Crystals

3.2.1.1 - Au(111)

Au(111) was selected for this project largely due to the inertness of the surface, as described in **section 1.3.1.2**. Since the spectra obtained are to be compared with gas phase spectra, minimal surface induced perturbations are desired. The cleaning process is fairly simple for Au(111) requiring only 2 sputter/anneal cycles before the molecular deposition (as seen in **Table 3.1**).
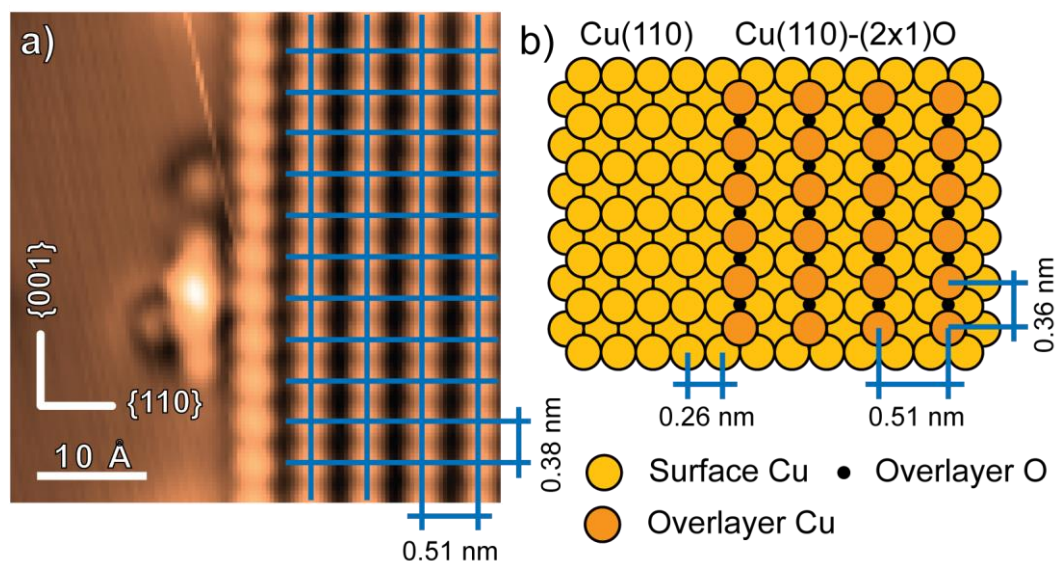
Figure 3.4: *Cu(110)-(2×1)O reconstruction. **a)** STM image (250 mV, 32 pA) of a partially oxidised Cu(110) surface with a small patch of the Cu(110)-(2×1)O reconstruction indicated by the overlay. Image courtesy of the Schaub group. **b)** Ball model of the Cu(110)-(2×1)O reconstruction which illustrates the atomic arrangement of the surface.*

3.2.1.2 - Cu(110)

The purpose for including the Cu(110) crystal in this exploration is to allow direct comparison between our *dI/dV* STM images and those which are observed in literature[6]. The Cu(110) surface is more reactive than Au(111), but oxidation is known to somewhat passivate this reactivity as it results in a reconstructed surface (Cu(110)-(2×1)O) which is commonly used as an alternative to Au(111). The reconstruction, as shown in **Fig. 3.4**, was first identified by Jensen *et al.*[7] and has previously been utilised to study C_{60}[6,8]. This provided some useful background knowledge for the current analysis. **Fig. 3.4 (a)** shows a portion of this reconstruction (with a partial overlay to identify the unit cell) alongside an unaffected region of the Cu(110) surface. **Fig. 3.4 (b)** is a model showing the atomic construction of the overlayer.

Fig. 3.4 (a) is an STM image (250 mV, 32 pA) showing the difference between the reconstructed oxidised-Cu(110) (right side of image) and the unaltered surface (left side). The overlay illustrates the unit cell for the Cu(110)-(2×1)O reconstruction which can be compared to the unit cell in the ball model of the substrate in **Fig. 3.4 (b)**. The rectangular

packing of the reconstructed copper surface may express an anisotropic perturbation on the adsorbates, rather than the hexagonally close-packed Au(111) substrate. However, the passivation as a result of the oxygen is intended to reduce this perturbation effect preventing any strong interactions between the molecular overlayer and the substrate.

3.2.2 - Molecular Sample

The $[Li^+@C_{60}](PF_6)^-$ samples utilised during this project are a product of Idea International Inc. (>99% purity)[9], supplied to us by our collaborators in Edinburgh. These samples are prepared by placing the salt in a homemade molecular evaporator (**Fig. 3.5**). This evaporator is then degassed before the molecular sample is sublimed (~663 K) and the fullerenes are deposited on the substrates. The degas procedure is important because it removes the vast majority of the PF_6^- (which acts as a stabilising ligand for the $Li^+@C_{60}$) from the salt before sample preparation. However, the degas temperature must be carefully monitored because $Li@C_{60}$ begins to decompose when exposed to temperatures in excess of ~570 K[10]. This decomposition results in the ejection of Li from the carbon cage, thus the molecular sample is instead composed of a combination of $Li@C_{60}$ and C_{60}.

The crucible (**Fig. 3.5 (a)**) is composed of a capillary tube with a ceramic insert with two holes. These holes allow the Type K thermocouple wires direct access to the molecular sample affording more accurate temperature measurements during preparation. These thermocouple wires are accessed via the indicated electrodes (**Fig. 3.5 (b)**). The crucible is also wrapped in tungsten wire which is evenly distributed along its length to ensure homogeneous heating of the crucible via resistive heating. Copper rods (**Fig. 3.5 (c)**) allow external power supply access to provide the tungsten wire with the current required for heating the crucible.

Once compiled, the molecular evaporator (**Fig. 3.5**) is attached to the UHV system such that the blue portion of the image above is under vacuum and the red portion is not. This affords access to the thermocouple wires and resistive heating system from outside the vacuum. The molecular samples are subsequently degassed for a number of hours at temperatures between 420 K and 620 K to remove the PF_6^-. This leaves only the $Li^+@C_{60}$ to be deposited on the metal substrates.
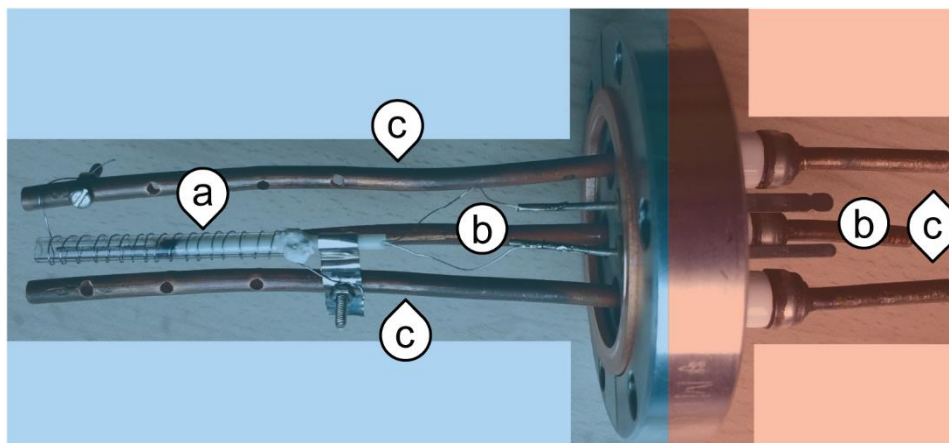
Figure 3.5: *This homemade molecular evaporator is composed of: **a)** crucible, **b)** connections affording accurate measurement of the temperature of the molecular sample, and **c)** copper rods which connect to the external power supply enabling heating of the crucible. Blue represents the portion of the evaporator inside the UHV system, the portion which remains outside is red.*

3.2.3 - Surfaces

Once the metal single crystal samples have been prepared (following the conditions observed in **Table 3.1**) and the molecular evaporator has been degassed, the surfaces can be prepared for observation. Heating the molecular sample to ~663 K results in an effusive beam of $Li^+@C_{60}$. For the Au(111) sample with large 2D arrays of fullerenes, the substrate is maintained at room temperature during the molecular deposition, but for the other Au(111) sample (small islands and isolated fullerenes) and the Cu(110)-(2×1)O sample the metal substrates are maintained at ~320 K.

After the deposition is completed, the first Au sample is subjected to a flash anneal to ~570 K for 30s in order to trigger the mass transport of fullerenes before rapidly quenching the substrate with LN_2 to transfer into the microscope. However, the other two substrates are maintained at ~320 K for an hour after deposition to ensure any remaining pollutants are desorbed from the surface and only minimal diffusion of the fullerenes is observed. These samples are also quenched with LN_2 before being transferred into the microscope for observation.

3.3 - <u>Software</u>

The software used to record the following data is the proprietary software supplied by CreaTec (AFM-STM) and provides sufficient functionality to complete all acquisition measurements required. This includes the bias modulation which allows internal lock-in techniques to directly record differential electronic spectroscopy.

Igor Pro (from Wavemetrics) is predominantly used to analyse the data and relies on a set of useful procedures that have been computed in-house.

The following chapters discuss the observations resulting from the various analyses of the different Au(111) and Cu(110)-(2×1)O substrates described in this chapter.

3.4 - <u>References</u>

(1)   Besocke, K. An Easily Operable Scanning Tunneling Microscope. *Surf. Sci.* **1987**, *181*, 145–153.

(2)   Gardener, J. A.; Briggs, G. A. D.; Castell, M. R. Scanning Tunnelling Microscopy Studies of C60 Monolayers on Au(111). *Phys. Rev. B - Condens. Matter Mater. Phys.* **2009**, *80* (23), 235434. https://doi.org/10.1103/PhysRevB.80.235434.

(3)   Altman, E. I.; Colton, R. J. Nucleation, Growth, and Structure of Fullerene Films on Au(111). *Surf. Sci.* **1992**, *279* (1–2), 49–67. https://doi.org/10.1016/0039-6028(92)90741-N.

(4)   Fujita, D.; Yakabe, T.; Nejoh, H.; Sato, T.; Iwatsuki, M. Scanning Tunneling Microscopy Study on the Initial Adsorption Behavior of C60 Molecules on a Reconstructed Au(111)-(23 × √3) Surface at Various Temperatures. *Surf. Sci.* **1996**, *366* (1), 93–98. https://doi.org/10.1016/0039-6028(96)00786-8.

(5)   Gimzewski, J. K.; Modesti, S.; Gerber, C.; Schlittler, R. R. Observation of a New Au (111) Reconstruction at the Interface of an Adsorbed C60 Overlayer. *Chem. Phys. Lett.* **1993**, *213* (3–4), 401–406. https://doi.org/10.1016/0009-2614(93)85153-F.

(6)   Feng, M.; Zhao, J.; Petek, H. Atomlike, Hollow-Core–Bound Molecular Orbitals of C60. *Science (80-.).* **2008**, *320*, 359–362. https://doi.org/10.1126/science.1155866.

(7)   Jensen, F.; Besenbacher, F.; Laegsgaard, E.; Stensgaard, I. Surface Reconstruction of Cu(110) Induced by Oxygen Chemisorption. *Phys. Rev. B* **1990**, *41* (14), 10233–10236. https://doi.org/10.1103/PhysRevB.41.10233.

(8)   Pedersen, M. O.; Murray, P. W.; Laegsgaard, E.; Stensgaard, I.; Besenbacher, F. Carbon-60 Induced Structures on the Clean and Oxygen Covered Cu(110) Surface: Competitive Adsorption. *Surf. Sci.* **1997**, *389*, 300–309.

(9)   Okada, H.; Komuro, T.; Sakai, T.; Matsuo, Y.; Ono, Y.; Omote, K.; Yokoo, K.; Kawachi, K.; Kasama, Y.; Ono, S.; Hatakeyama, R.; Kaneko, T.; Tobita, H. Preparation of Endohedral Fullerene Containing Lithium (Li@C60) and Isolation as Pure Hexafluorophosphate Salt ([Li+@C60][PF6−]). *RSC Adv.* **2012**, *2* (28), 10624. https://doi.org/10.1039/c2ra21244g.

(10)   Campbell, E. E. B.; Chandler, H. J.; Schaub, R. Sublimation of Li@C60. *Eur. Phys. J. D* **2020**,

74, 122.

4 - Identifying the electronic structures of Li@C$_{60}$ and C$_{60}$ on Au(111) and Cu(110)-(2×1)O substrates

The following chapter aims to identify the electronic structure of Li@C$_{60}$ and compare it with that of C$_{60}$ such that the stabilisation effect of the Li-encapsulation can be determined. The surfaces which will be discussed are composed of a mixture of the fullerene molecules adsorbed on both the Au(111) and Cu(110)-(2×1)O substrates after the preparation cycles described in the previous chapter. Each set of preparation conditions results in a slightly different molecular overlayer due to the varying post-adsorption anneal temperatures. Three systems are studied in total: large 2D islands on the Au(111) surface as a result of extensive molecular diffusion at elevated temperatures (~570 K) (**section 4.1**), small islands on Au(111)with some isolated Li@C$_{60}$ resulting from a lower anneal temperature (320 K) (**section 4.2**), and a system with isolated fullerenes on Cu(110)-(2×1)O (**section 4.3**).

As discussed in **section 1.3.1**, C$_{60}$ has been studied by STM on various substrates with increasingly improving imaging resolution[1–23]. This means there is a wealth of information to refer to and build upon. However, the experimental studies presented here are amongst the first to report on surface-bound Li@C$_{60}$ (Yamada *et al.*[24] published their work on Cu(111) during the data collection of this project). In order to determine the differences between the electronic structures of C$_{60}$ and Li@C$_{60}$, both must first be identified on each of the three surfaces.

4.1 - Identifying the electronic structures of Li@C$_{60}$ and C$_{60}$ on Au(111) after a post-adsorption anneal at ~570 K

The following section will first focus on identifying the fullerene structures on Au(111) which result from the molecular deposition and post-adsorption anneal at ~570 K (**section 4.1.1**). With a focus on the 2D arrays, the adsorption configurations exhibited by both Li@C$_{60}$ and C$_{60}$ will be identified and their population distribution analysed (**section 4.1.2**). Upon differentiating between the Li@C$_{60}$ and C$_{60}$ present on the substrate the electronic structures of each will be explored; firstly by scanning tunnelling spectroscopy (**sections 4.1.3** and **4.1.4**), and subsequently by c.c. *dI/dV* STM imaging (**section 4.1.5**).

4.1.1 - Identifying the 1D and 2D arrays of fullerenes

Au(111) has been selected as a substrate for this exploration due to its chemical inertness. This results in weakly coupled adsorbates allowing for more reliable comparison with the gas phase experiments that were completed by our collaborators. Evaporating the molecular sample onto the Au(111) crystal and subsequently flash annealing it at ~570 K (as detailed in **section 3.2**) results in the surface exhibited by **Fig. 4.1 (a)**. Upon scanning the surface with standard parameters (+1.0 V, 0.1 nA) three different regions are immediately recognised. The first and most apparent is the large hexagonally close-packed 2D island of fullerenes. Each of the small, rounded protrusions within the island on the left of the STM image is a fullerene, irrespective of the various apparent heights. The second region on the surface is the empty terrace with visible herringbone reconstruction (see bottom right corner of **Fig. 4.1 (a)**). The third region of interest is the partially decorated step edge that presents the fullerenes in distinct dashed lines (see top right corner of **Fig. 4.1 (a)**). The behaviour that formed these three regions will be explored further below.

A large hexagonally close-packed island of fullerenes (>100 nm across) dominates the STM image (**Fig. 4.1 (a)**) and is one of many like it across this substrate. The variation in apparent height of the fullerenes within the island is reminiscent of the behaviour of C_{60} on Au(111)[1,2,13,17–20], however there is no obvious indication of the presence of Li@C_{60}. Two explanations are possible: that the Li@C_{60} is indistinguishable from the C_{60} at this scanning bias, or that there are no Li@C_{60} within the island. A refined strategy is therefore required to determine whether Li@C_{60} is present in the 2D array. The random distribution of these apparent heights is also similar to what is observed for some pure C_{60} islands. It is reported that, after low temperature post-adsorption anneals, the islands adopt highly ordered structures with domains of fullerenes assuming identical adsorption orientations[1]. As the anneal temperature is raised, more disorder is introduced into the packing structure and the islands approach closely-packed arrays of fullerenes with a random distribution of adsorption orientations. This results in an island with various apparent heights like that observed in **Fig. 4.1 (a)**.
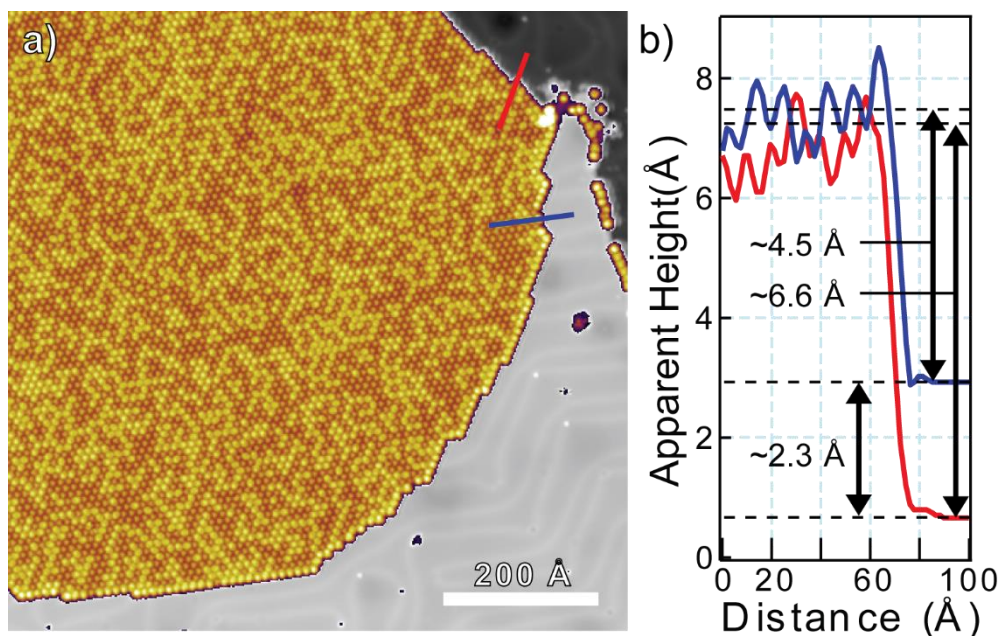
Figure 4.1: *a)* *STM image (+1.0 V, 0.1 nA) of the Au(111) substrate after post-adsorption flash anneal to ~570 K. **b)** Line profiles extracted from the STM image with arrows indicating the step height of Au(111) and the apparent height of the fullerenes with respect to each terrace.*

Inspection of **Fig. 4.1 (a)** does not reveal which terrace the island is adsorbed to; it could, therefore, be stabilised at the top of the step edge or at the bottom, as one might naïvely expect. The line profiles in **Fig. 4.1 (b)** can be used to determine this. The red curve shows the apparent height of the island with respect to the lower terrace is ~6.6 Å ± 0.5 Å, whereas the blue curve shows a height difference of ~4.5 Å ± 0.5 Å between the island and the upper terrace. The difference between the two terraces can be seen as ~2.3 Å which is comparable to the 2.35 Å expected for the separation between (111) planes of the substrate. At these scanning parameters the expected apparent height of the fullerenes is ~7 Å[25] which indicates that the island is adsorbed to the lower terrace. The fullerenes lining the step edge are therefore stabilised by both the lower terrace and the step edge. This increased coordination with the substrate may be responsible for these fullerenes exhibiting a greater apparent height than those within the 2D array which are only stabilised by the terrace (see **Fig. 4.1 (a)**).

Figure 4.2: *STM image (+2.5 V, 0.1 nA) showing a partially decorated step edge on the Au(111) surface after a post-adsorption flash anneal at ~570 K.*

The 1D structures seen along the step edges in the top right corner of **Fig. 4.1 (a)** and in **Fig. 4.2** are secondary fullerene structures th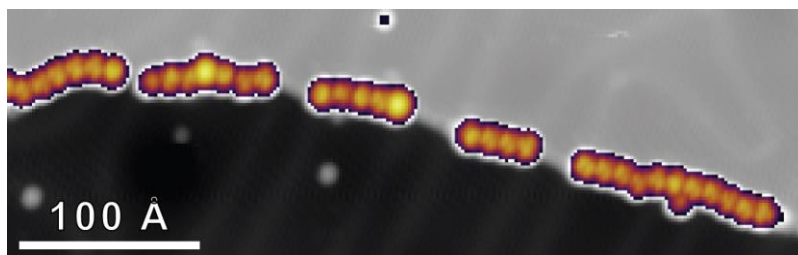at seem to result from molecules which don't condense into 2D arrays during the anneal process[21]. The fullerenes, which are also adsorbed to the bottom terrace, are all limited to the fcc regions of the herringbone reconstruction on both the top and bottom terraces resulting in this "dashed line" effect (see **Fig. 4.2**). This leads to a hypothesis which proposes that fullerenes preferentially stabilise on the fcc regions of the herringbone reconstruction. The majority of the fullerenes on this substrate are found in the 2D arrays suggesting that this structure is preferable over the 1D arrays seen in **Fig. 4.2**. As such, no further analysis of these dashed lines will be discussed. However, the apparent interaction between the fullerenes and the herringbone reconstruction, seen starkly with the 1D arrays, suggests an interaction which does require further analysis.

Two other observations are made regarding the distinctive herringbone reconstruction (seen in the bottom right hand corner of the **Fig. 4.1(a)**). First, the herringbone reconstruction on the substrate terraces is clear of fullerenes. The elbows of the herringbone are known to act as nucleation sites, hence the pollution observed at those sites on the upper terrace in **Fig.4.1 (a)**. The mostly naked Au(111) surface indicates that the anneal temperature is not only sufficient to cause diffusion of the fullerenes, but also to prevent their stabilisation on the terraces. The second observation is the lack of any sign of the herringbone within the island. This also matches the lifting of the Au(111) surface which is reported for 2D C_{60} arrays under appropriate preparation conditions[1], as discussed in **section 1.3.1**. These general behaviours of the molecular system (formation of 1D and 2D arrays, and relaxation of the herringbone reconstruction) are all similar to
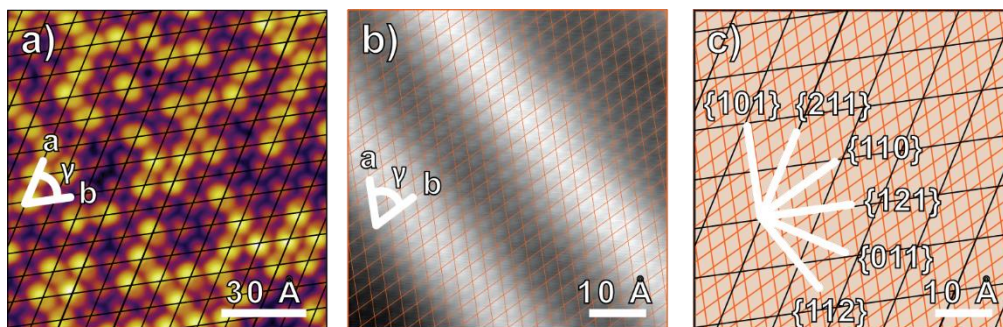
Figure 4.3: *a) STM image (+1.0 V, 0.1 nA) of a large, hexagonally close-packed island of fullerenes. The lattice overlay illustrates a unit cell with the parameters: a = 9.9 Å, b = 10.5 Å and γ = 59.5°. b) STM image (+20 mV, 2.3 nA) of the Au(111) surface. The lattice overlay illustrates a unit cell with the parameters: a = 2.9 Å, b = 2.9 Å and γ = 58.5°. c) By combining the lattices from a) and b) the packing directions of the island are seen to coincide with crystallographic directions of the substrate (as seen by the white compass). Comparing the unit cells identifies the island as a $(2\sqrt{3}\times2\sqrt{3})R30°$ overlayer with a high commensurability.*

what is known for surface-bound C_{60}. Therefore, closer inspection of the large 2D arrays is required to identify any distinction between the current molecular system (expected to contain $Li@C_{60}$) and those observed in literature (pure C_{60}).

By examining the islands at a greater magnification, the molecular appearances of the fullerenes within the island are resolved (see **Fig. 4.3 (a)**) and seen to closely resemble those from previous reports on the C_{60}/Au(111) molecular system[1,2,13,17,18]. The STM image has been overlaid with a lattice in which the vertices are centred on the fullerenes to illustrate the lateral coherence of the island. The overlay on the image shows the island exhibits unit cell parameters of a = 9.9 Å, b = 10.5 Å and $γ$ = 59.5°.

Fig. 4.3 (b) is an STM image of the bare Au(111) surface in which atomic resolution has been achieved across a portion of the herringbone reconstruction (seen in the image as the bright stripes proceeding diagonally across the surface). A similar lattice overlay has been applied to this image and aligned with the Au atoms in the top right corner. In this case the overlay shows the unit cell parameters for the bare Au(111) surface to be: a = 2.9 Å, b = 2.9 Å and $γ$ = 58.5°. These are almost identical to the expected value of 2.88 Å for the distance between closed-packed Au atoms in the (111) plane. By taking the two

lattices and overlapping them (see **Fig. 4.3 (c)**) a direct comparison can be drawn between the island and the surface allowing a partial deduction of their registry.

The high symmetry packing directions within the island are aligned with crystallographic directions of the Au(111) surface ({211}, {121} and {112}, see the white compass in **Fig. 4.3 (c)**). This alignment between the molecular and substrate packing directions, and the lack of Moiré pattern in the molecular overlayer in **Fig. 4.1 (a),** illustrates a high degree of commensurability. Combining this information with the unit cell parameters identifies that the fullerene island is a $\left(2\sqrt{3}\times2\sqrt{3}\right)$R30° overlayer. This is consistent, yet again, with the structures observed for C_{60}/Au(111) and suggests that if Li@C_{60} is present it behaves similarly to the empty fullerene. Other techniques are therefore required to identify Li@C_{60} within the 2D array, this is the topic of the next section.

4.1.2 - Identifying the adsorption configurations of the Li@C_{60} and C_{60}

The adsorption configuration of the fullerenes contains information regarding the adsorption orientation, the azimuthal orientation and the adsorption site of the molecule. The adsorption and azimuthal orientations of the fullerenes can easily be identified with an STM, this is addressed in **section 4.1.2.1** with the statistical distribution of these orientations detailed in **section 4.1.2.2**. However, the adsorption site cannot be directly determined with STM, since it is buried beneath a molecular overlayer. As was introduced in **section 1.3.1.2**, the adsorption site for C_{60} in the $\left(2\sqrt{3}\times2\sqrt{3}\right)$R30° overlayer is a topic of discussion. **Section 4.1.2.3** delves deeper into the evidence from the current molecular system which justifies why the hcp surface site is assumed rather than the proposed nanopit reconstruction.

4.1.2.1 - Determining the adsorption orientation of the fullerenes

It is well known that the adsorption and azimuthal orientations of C_{60} can be determined with STM by imaging the low energy unfilled states of the fullerene[14–16]. The 5:6 bonds are electron-poor which results in the C5-faces appearing as bright segments in each molecular appearance within these STM images, as was illustrated in **section 1.3.1.2**. Directly observing the uppermost C5-faces on the carbon cage, and making an assumption
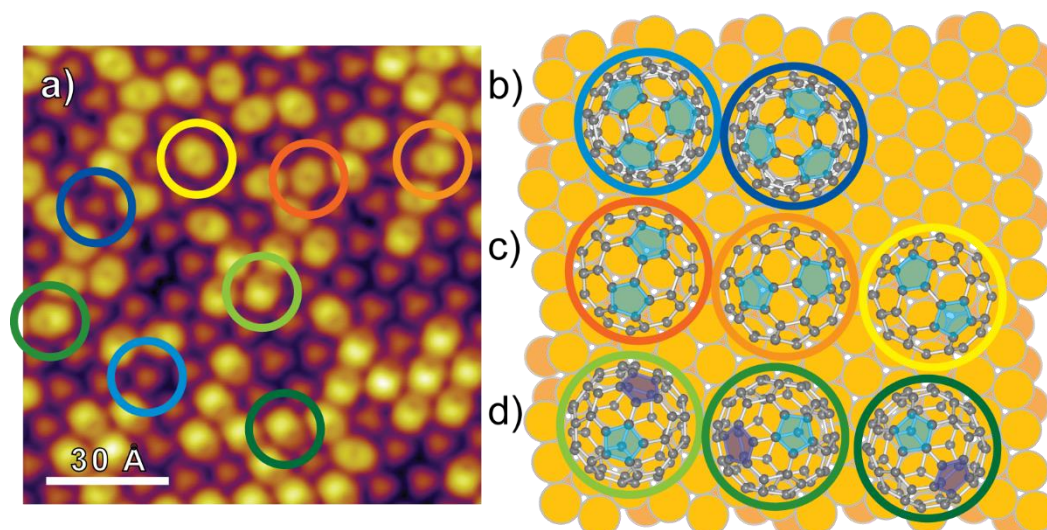
Figure 4.4: *a) Same image as **Fig. 4.3 (a)**. STM image (+1.0 V, 0.1 nA) of a 2D, hexagonally close-packed island of fullerenes. The 8 ringed fullerenes within the island are colour coded to correspond with the ball and stick models. The dominant azimuthal orientations of the three types of C_{60} fullerenes are illustrated on a model of the Au(111) to indicate the alignment of each molecular appearance with respect to the hcp surface site: b) C6-C_{60}, c) 6:6-C_{60}, d) C-C_{60}.*

of the adsorption site based on DFT calculations, allows identification of the adsorption configuration of the fullerenes within an STM image like that depicted in **Fig. 4.4 (a)**. The ball and stick models on the model Au(111) surface (**Fig. 4.4 (b)**) illustrate the dominant adsorption configurations observed in the STM image. The models correspond with the molecular appearances indicated by the coloured rings.

Studying the STM image in **Fig. 4.4 (a)** reveals that there are three different fullerene appearances within the island. With the knowledge of the segments and symmetries mentioned previously (**section 1.3.1.2**), the molecular appearances can be deciphered. The triangular shapes (indicated by the blue rings in **Fig. 4.4 (a)**) are easily identified as C6-C_{60} (**Fig. 4.4 (b)**) because of the three-fold rotational symmetry and two azimuthal orientations which are 180° rotations of each other. The adsorption configuration with the sky blue ring matches the most thermodynamically stable configuration for C_{60} on an hcp site of Au(111) as calculated by Wang *et al*.[26,27].

The other two molecular appearances in the STM image (**Fig. 4.4 (a)**) are described as having two segments and a central axis along their length which acts like a mirror plane.

The first can be described as "coffee-bean" shaped (orange and yellow rings in **Fig. 4.4 (a)**) because its two segments are equally bright. This induces another mirror plane along the short axis of the molecular appearance. The symmetry of this shape therefore denotes it as 6:6-C_{60} (**Fig. 4.4 (c)**). The long axis of this shape is seen to predominantly align with the close packing directions of the island.

The second feature with two segments exhibits an asymmetry in the brightness of the molecular appearance (green rings in **Fig. 4.4 (a)**) which could be the result of two orientations: 5:6-C_{60} and C-C_{60}. However, recalling that the C5-faces of the C_{60} cage coincide with the segments of the molecular appearance in the STM image, this leads to the conclusion that this shape is representative of C-C_{60} (**Fig. 4.4 (d)**). The distinction comes because it has two segments and not three, as would be required for 5:6-C_{60}. The asymmetry in this molecular shape affords the description that the central axis "points" in particular directions. This directionality will become pertinent during the extensive statistical analysis of the molecular appearances later in this section.

Though identifying these three adsorption orientations (C6-C_{60}, 6:6-C_{60} and C-C_{60}) corroborates what is observed in the literature of $\left(2\sqrt{3}\times2\sqrt{3}\right)$R30° overlayers of C_{60} on Au(111), there remains no indication of the presence of Li@C_{60} within the 2D array. This is perplexing because species with different electronic structures are expected to appear different within STM images. These images can be considered a 2D representation of the local density of states (LDOS) integrated from the Fermi level to the scanning bias. Li@C_{60} is electronically distinct from C_{60} due to the additional presence of the Li, so it is anticipated to have its own molecular appearance. Imaging the same portion of the fullerene island shown in **Fig. 4.4** at various scanning biases is one attempt to exploit this variation in the electronic structure. Acquiring such images, as shown in **Fig. 4.5** for -2.5 V, -1.0 V, +1.0 V and +2.5 V, a fourth feature is observed at +2.5 V (red ring in **Fig. 4.5 (d)**). The other three molecular appearances, identified above, are also bias dependent; these have been highlighted in **Fig. 4.5** to illustrate how their appearances change whilst maintaining the same symmetry.

When scanning at -2.5 V (see **Fig. 4.5 (a)**) there are three different molecular shapes possessing distinct symmetries: three-fold rotationally symmetric truncated hexagons (blue and red), two-fold rotationally symmetric dumbbells (orange) and one-fold
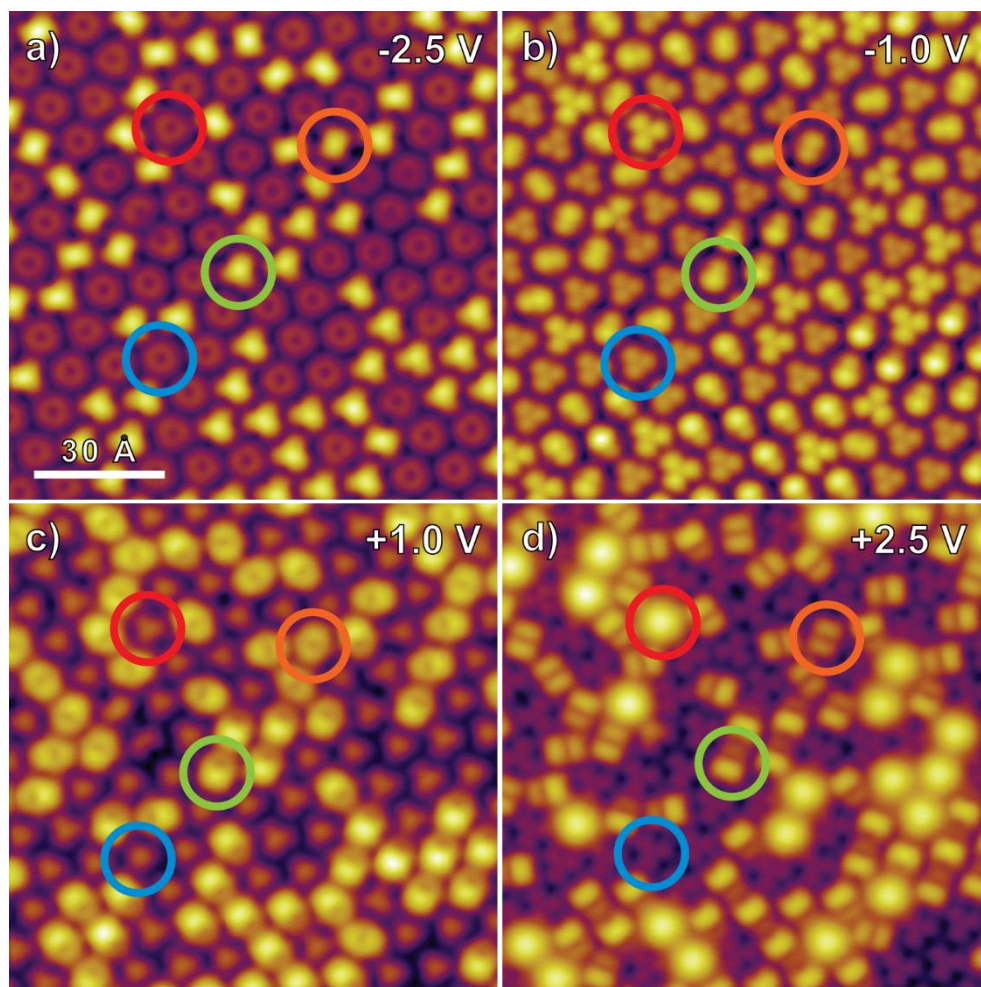
Figure 4.5: *STM images recorded on the same area of a 2D island of fullerenes on Au(111). The four ringed species correspond with C6-C_{60} (blue), C-C_{60} (green), 6:6-C_{60} (orange) and C6-Li@C_{60} (red). **a)** (-2.5 V, 0.1 nA). **b)** (-1.0 V, 0.1 nA). **c)** Same image as **Fig. 4.3 (a)**, (+1.0 V, 0.1 nA). **d)** (+2.5 V, 0.1 nA).*

rotationally symmetric Y-shapes (green). The symmetry of the molecular shapes is maintained throughout the four images but the segment distribution is also maintained for the blue, orange and green fullerenes in the other three images (**Figs. 4.5 (b-d)**). The blue ringed fullerene retains its three-fold rotational symmetry, though the three segments are much more distinct at -1.0 V and +2.5 V than at +1.0 V. The two-segment molecular appearances both retain their general oval shape and symmetric/asymmetric brightness in **Figs. 4.5 (b)** and **(c)**, but the difference between the two adsorption orientations becomes much more distinctive at +2.5 V (see **Fig. 4.5 (d)**).
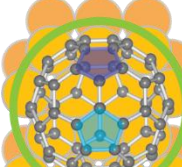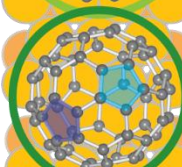
The most apparent difference between **Figs. 4.5 (a-c)** and **(d)** is the emergence of a distinctive fourth molecular appearance (red ring) from amongst the C6-fullerenes (red and blue rings). This "diffuse beacon" no longer exhibits a three-fold rotational symmetry but instead is circular with no sign of internal structure. The similarity of this molecule to C6-C_{60} (blue ring) in all images except **Fig. 4.5 (d)** indicates that there are two types of C6-fullerenes on the surface. This knowledge allows for the differentiation between the C6-fullerenes in **Figs. 4.5 (b)** and **(c)** by observing very slight variations in the shape and brightness of the segments in their respective molecular appearances. In **Fig. 4.5 (a)**, however, the two appearances remain indistinguishable. The factors that differentiate the diffuse beacon from C6-C_{60} lead to the conclusion that the fourth molecular appearance represents C6-Li@C_{60}. This reaffirms that the other three molecular appearances (blue, orange and green rings) are merely different adsorption orientations of C_{60} which can be described by simple rotations of the fullerene around its core.
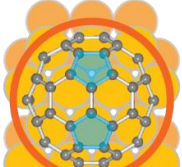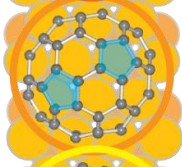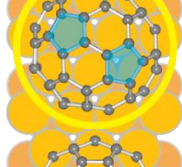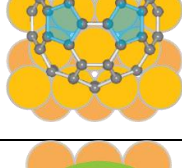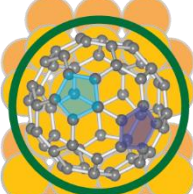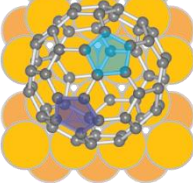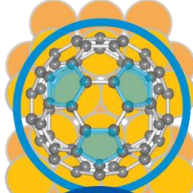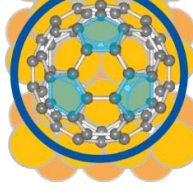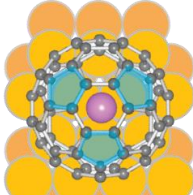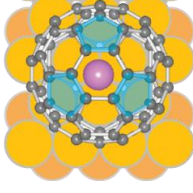
Given the purity of the [Li$^+$@C_{60}](PF$_6^-$) salt that is used during the sample preparation (>99%), the high proportion of C_{60} on the surface is determined to be a result of Li@C_{60} decomposition at the elevated temperatures required for evaporation[28]. In order to properly identify the population density for the Li@C_{60}, and the other adsorption configurations present in the 2D array, an extensive statistical analysis of the surface is achieved. **Table 4.1** summarises the results after analysing 3229 fullerenes and reveals that these largely adopt specific azimuthal orientations. A number of key observations are revealed through this statistical analysis; these are discussed in the next section.

4.1.2.2 - <u>Statistical analysis of the large 2D array of Li@C_{60} and C_{60}</u>

Table 4.1 illustrates the most pertinent information from the statistical analysis of the large 2D array of Li@C_{60} and C_{60}. The first two columns on the far left identify the fullerenes by the specific adsorption configurations that are observed within the large 2D array (see both **Figs. 4.4** and **4.5**). The orientations of 6:6-C_{60} and C-C_{60} without a coloured ring represent all of the non-standard adsorption configurations observed during the analysis. The remaining three columns display different percentages depending on the specific population being considered. The left column of percentages considers the proportion of each fullerene cage orientation. This results in 3 distinct groups: the 6:6-,

Table 4.1: *Statistical analysis of 3229 fullerenes in a mixed 2D array of C_{60} and $Li@C_{60}$ on Au(111). All models are depicted adsorbed to hcp surface sites due to the high commensurability of the large 2D array. The 6:6-C_{60} and C-C_{60} models not highlighted by coloured rings are representative of all other fullerenes which did not match the three orange and green C_{60} respectively. These unlabelled fullerenes adopt various alternative azimuthal orientations but no individual orientation is repeated, hence grouping them and representing them with a single model.*

Adsorption Configuration	Model	% of azimuthal orientation of a single cage orientation	% of adsorption orientation of each molecule (i.e. C_{60} or $Li@C_{60}$)	% of total number of fullerenes analysed
6:6-C_{60}		26.8	6.4	5.6
		32.7	7.9	6.9
		27.0	6.5	5.7
		13.5	3.3	2.8
C-C_{60}		40.2	10.9	9.6
		33.7	9.2	8.0

Adsorption Configuration	Model	% of azimuthal orientation of a single cage orientation	% of adsorption orientation of each molecule (i.e. C_{60} or Li@C_{60})	% of total number of fullerenes analysed
C-C_{60}		25.6	7.0	6.1
		0.5	0.1	0.1
C6-C_{60}		66.4	41.9	36.6
		10.8	6.8	5.9
C6-Li@C_{60}		20.8	90.9	11.5
		2.1	9.1	1.1
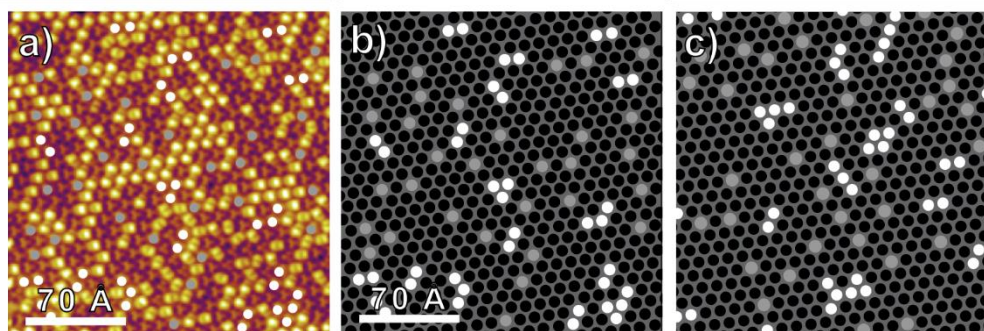
Figure 4.6: *a) STM image (+2.0 V, 0.1 nA) of a 2D array with the Li@C$_{60}$ indicated by dots; grey for monomers and white for "polymers". b) The same fullerene distribution as a) but with the C$_{60}$ indicated by black dots; this facilitates comparison with the simulated image. c) A simulated image showing a statistical distribution of 12.6% Li@C$_{60}$ coverage on a surface. The colour-coding matches that of b) (grey for Li@C$_{60}$ monomers, white for Li@C$_{60}$ "polymers" and black for C$_{60}$).*

the C- and the C6-fullerenes (the C6-C$_{60}$ and C6-Li@C$_{60}$ are combined). The middle column considers the proportion of each molecule; collecting all of the C$_{60}$ and Li@C$_{60}$ separately. The final column considers the proportion of the total number of fullerenes that each configuration represents.

The most striking observations from the statistical analysis are that only 12.6% of the fullerenes are Li@C$_{60}$ and that all of these adopt the C6-Li@C$_{60}$ adsorption orientation. This could indicate a favourable interaction either between the Li@C$_{60}$ and the substrate, or the Li@C$_{60}$ and the neighbouring fullerenes. In previous studies Li@C$_{60}$ has been observed preferentially forming dimers[29–33] so the first test is to identify any evidence of interaction between the Li@C$_{60}$ on the surface; be that attractive or repulsive. A rudimentary exploration of similar interactions in this molecular system is achieved (**Fig. 4.6**).

Firstly, the fullerenes in an STM image of the 2D array (+2.0 V, 0.1 nA) are identified and labelled (**Figs. 4.6 (a)** and **(b)**). This array is subsequently compared with a simulated surface exhibiting a statistical distribution of 12.6% Li@C$_{60}$ to match the proportion observed in the experimental molecular system (**Fig. 4.6 (c)**).

The simulation is achieved by randomly placing 12.6% Li@C$_{60}$ across a surface of C$_{60}$ on the assumption that there is no distinctive interaction (attractive or repulsive) between

two Li@C_{60} compared to a Li@C_{60} and a C_{60}. Upon formation of this 2D array, the neighbouring fullerenes are considered for both the simulated (**Fig. 4.6 (c)**) and the experimental (**Fig. 4.6 (a)**) images. If a Li@C_{60} is isolated from other Li@C_{60} it is labelled a "monomer" (see grey dots in **Fig. 4.6**), but if one or more of its nearest neighbours is also a Li@C_{60} it is labelled a "polymer" (see white dots in **Fig. 4.6**). Analysis of 3229 fullerenes in experimental STM images (like that seen in **Fig. 4.6 (a)**) reveals that 45.7% are monomers. Examining a simulated surface of 3249 fullerenes, and repeating 1000 times to acquire a suitable standard deviation, reveals 45.3 ±4.3% of the Li@C_{60} are observed as monomers. The remarkable agreement between the experimental and theoretical studies is strong evidence that the distribution of Li@C_{60} across the surface is random.

Besides the population of Li@C_{60} compared to C_{60}, the other stark observation from the results in **Table 4.1** is the distinctive preference for each adsorption orientation to adopt specific azimuthal orientations. For example, both 6:6-C_{60} and C-C_{60} are seen, almost entirely, to adopt the 3 azimuthal directions illustrated in **Fig. 4.4**. Only 13.5% and 0.5% of each adsorption orientation, respectively, are observed stabilising in any other alignment (indicated by the C_{60} models not indicated by coloured rings). Secondly, the population of each of these alignments is roughly equal for each adsorption orientation, though 6:6-C_{60} is marginally more evenly split (~30 ±3%) than C-C_{60} (~33 ±8%). In order to explore these surface interactions in greater detail, complex DFT calculations (similar to those conducted by Shin *et al.*[13]) are required. However these are prohibitively expensive so are yet to be completed within the scope of this project.

Complex DFT calculations could also provide evidence to support hypotheses for why these adsorption configurations, with specific azimuthal directions, are observed and others are not. For example, on initial inspection of the directionality of the C-C_{60} ("pointing" in the various directions seen in **Fig. 4.4**) one might naïvely expect 6 different azimuthal orientations: each pointing at one of the nearest neighbours the 2D array. However, as shown in **Table 4.1**, the 3 orientations illustrated in **Fig. 4.4 (d)** are observed to be distinctly dominant. Upon close inspection of these adsorption configurations (as depicted in **Fig. 4.7**) this preference is clearly surface induced, as explained below.

With the bottom C-atom of the C_{60} cage stabilising in the hcp surface site, the 3 adjacent C-atoms (highlighted red in **Fig. 4.7**) are seen to align with two different surface sites. For
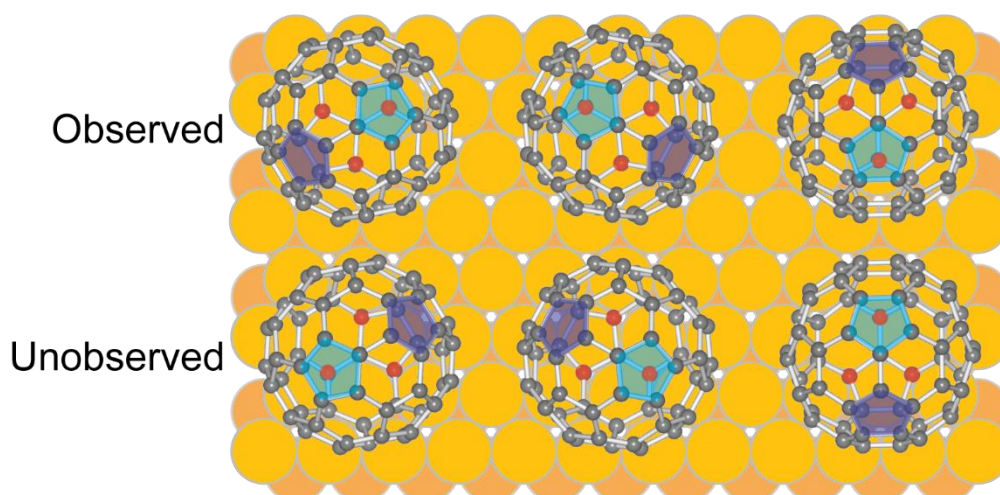
Figure 4.7: *Ball and stick models of the 3 observed azimuthal orientations of C-C$_{60}$ and 3 of the unobserved orientations which also "point" along the high symmetry directions of the island. The atoms adjacent to each surface bound C-atom are highlighted in red to facilitate identification.*

the azimuthal orientations which are observed (top row of **Fig. 4.7**), these adjacent C-atoms align with the Au-atoms which form the hcp surface site. The three unobserved configurations depicted in **Fig. 4.7** illustrate the C-C$_{60}$ "pointing" along the other packing directions within the 2D array. These orientations would result in the three adjacent C-atoms aligning with fcc surface sites. Evidently this configuration is not favourable since these are not observed in an analysis of over 3000 fullerenes in the 2D array. The combination of a 3-fold rotationally symmetric molecule on a 3-fold rotationally symmetric substrate is sufficient to determine favourable adsorption configurations exempt from the effect of neighbouring fullerenes. The detailed DFT calculations suggested above would, no doubt, provide further explanation for why this distinction is observed.

The 3-fold rotational symmetry of the unreconstructed Au(111) surface is also suspected to be responsible for the stark azimuthal preference exhibited by the C6-fullerenes (both C6-C$_{60}$ and C6-Li@C$_{60}$). **Table 4.1** shows that more than half of the fullerenes in the array (55.1%) adopt the C6-fullerene adsorption orientation suggesting it is the most thermodynamically stable orientation. This is in agreement with what is reported in the
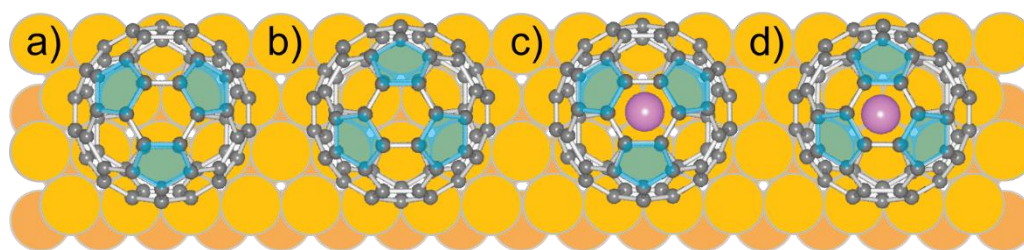
Figure 4.8: *Models illustrating: a) M-C6-C$_{60}$, b) m-C6-C$_{60}$, c) M-C6-Li@C$_{60}$, and d) m-C6-Li@C$_{60}$.*

literature (see **section 1.3.1.2**). 42.5% of the 2D array are C6-C$_{60}$ (48.7% of all C$_{60}$) and the other 12.6% are C6-Li@C$_{60}$ (as discussed above). Importantly, each of these adsorption orientations only adopt 2 azimuthal orientations, and there is a distinct preference for one over the other. C6-C$_{60}$ exhibits a ~6:1 ratio between the two configurations (see **Figs. 4.8 (a)** and **(b)**), and C6-Li@C$_{60}$ exhibits a ~10:1 ratio between similar adsorption configurations (see **Figs. 4.8 (c)** and **(d)**).

Since one of the two C6-adsorption configurations for C$_{60}$ and Li@C$_{60}$ is distinctly favoured over the other, these are denoted the majority (M) and minority (m) species respectively. This affords specific identification of these C6-fullerenes (as illustrated in **Fig. 4.8**) which will become particularly important in **Chapter 5** when exploring the switching capabilities of Li@C$_{60}$. This identification method facilitates discussion of the results of **Table 4.1**. For example, 41.9% of all C$_{60}$ adopt the M-C6-C$_{60}$ configuration (**Fig. 4.8 (a)**) whereas m-C6-C$_{60}$ (**Fig. 4.8 (b)**) only represent 6.8% of the C$_{60}$ in the 2D array, hence the ~6:1 ratio mentioned above. The ~10:1 ratio for Li@C$_{60}$ results from 90.9% adopting the M-C6-Li@C$_{60}$ (**Fig. 4.8 (c)**) configuration and only 9.1% adopting m-C6-Li@C$_{60}$ (**Fig. 4.8 (d)**). The starker ratio between the azimuthal orientations for Li@C$_{60}$ is unsurprising because it couples more strongly with the substrate than C$_{60}$[24] causing an exacerbation of any preference between the adsorption configurations of the fullerenes. The preference for the M-C6-fullerene configuration is strong evidence that this is the most thermodynamically stable orientation for both C$_{60}$ and Li@C$_{60}$.

Close inspection of the models in **Fig. 4.8** provides a suggestion for why this azimuthal preference occurs. In **Figs. 4.8 (a)** and **(c)**, the double bonds between the lowermost C6-face and adjacent C6-faces (6:6-bonds) are located on top of the Au atoms which surround the hcp surface site. As discussed in **section 1.3.1.2**, these 6:6-bonds are electron rich.

Therefore, aligning these with Au-atoms optimises the charge transfer into the surface states strengthening the stabilisation and thus resulting in the preferred azimuthal orientations M-C6-C_{60} and M-C6-Li@C_{60}. For the minority species (m-C6-C_{60} and m-C6-Li@C_{60} depicted by **Figs. 4.8 (b)** and **(d)** respectively) the single bonds between the lowermost C6-face and adjacent C5-faces (5:6-bonds) are located on top of the Au atoms instead. These 5:6-bonds are electron poor resulting in a reduced surface interaction.

The differences between these azimuthal orientations is not something that is frequently considered in great detail when theoretical studies of the C_{60}/Au(111) molecular system are conducted. The specific interactions which lead to these preferences are determined by the adsorption site and its resultant symmetry. The next section discusses the reasons for our adoption of the hcp surface site as the adsorption site for our system and compares this to another that is proposed in the literature; the nanopit.

4.1.2.3 - Identifying the fullerene adsorption site

The distinction between the azimuthal orientations of C6-C_{60} is observed in the calculations of Wang *et al*.[26,27], and resulted in their definition of M-C6-C_{60} on the hcp surface site of Au(111) as the most thermodynamically stable adsorption configuration. Their detailed study of the azimuthal preference of the molecular adsorption, which revealed activation barriers to rotation of the fullerene, and the recent study by Villagómez *et al*.[34] is why the hcp surface site is selected as the assumed adsorption site for the fullerenes studied in this portion of the project. As a result of the fullerene stabilisation, Wang *et al*. report a minor buckling of the Au-atoms around the hcp surface site resulting in a 0.08 Å "dimple" beneath the fullerene[26]. A combination of this minor geometric depression and the increased interaction between the fullerene and the substrate is hypothesised to be responsible for the C6-C_{60} appearing "dim" when compared to the other fullerenes in the STM images.

Gardener *et al*. suggested, however, that this increased interaction was not sufficient to cause this "dimness"; instead they proposed that the C6-C_{60} interaction with the Au(111) is strong enough to create a single atom vacancy. This is the concept of the nanopit which was introduced in **section 1.3.1.2**. Considering the 3-fold rotational symmetry of the substrate, similar azimuthal preference for a C_{60} adsorbed to a nanopit could be expected (as shown in **Fig. 4.9**).
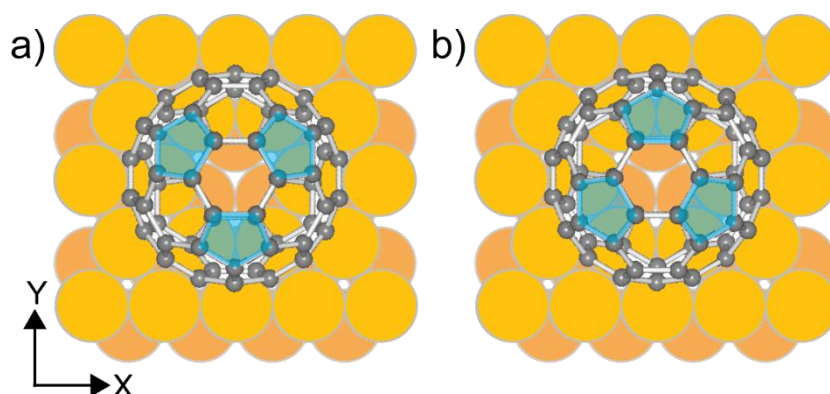
Figure 4.9: *Models illustrating: **a)** M-C6-C$_{60}$, and **b)** m-C6-C$_{60}$ stabilised by nanopits on Au(111).*

Similar to the adsorption configurations seen in **Fig. 4.8**, the difference between the models in **Fig. 4.9** is due to the atoms in the second Au layer. In **Fig. 4.9 (a)**, the electron poor 5:6-bonds are stabilised over the 2nd layer Au atoms, whereas in **Fig. 4.9 (b)** it is the electron-rich 6:6-bonds which adopt these positions. These C6-C$_{60}$ configurations have been explored in detail by Shin *et al.*[13]. By employing DFT and LEED, they identified that a $(2\sqrt{3}\times2\sqrt{3})$R30° overlayer composed of C6-C$_{60}$ on nanopits and 6:6-C$_{60}$ on top sites is the most thermodynamically stable state for the 2D array[13]. The fullerenes adopt slightly altered adsorption sites because C6-C$_{60}$ reportedly interacts strongly enough to form a nanopit, but 6:6-C$_{60}$ does not. The commensurability of the overlayer therefore results in the 6:6-C$_{60}$ adsorbing to a top-site.

The recognition that a mixed layer of C6-C$_{60}$ and 6:6-C$_{60}$ is the most thermodynamically favourable indicated that the preferable state of the 2D array is a compromise between interfacial and intermolecular interactions[13]. Paßens *et al.* sought to understand this balance by employing STM to closely observe the adsorption orientations and identify favourable interactions within the overlayer[18]. They reported that dominance of M-C6-C$_{60}$ is a result of less favourable surface interaction with the nanopit than m-C6-C$_{60}$, which in turn results in stronger Coulomb interactions between neighbouring M-C6-C$_{60}$. These Coulomb interactions result from the alignment of electron-poor pentagonal faces of one fullerene with the electron-rich 6:6-bonds of its neighbour, similar to what is seen in bulk C$_{60}$ (see **section 1.3.1.1**). This intermolecular stabilisation is sufficient to make it more preferable across the 2D arrays. The conclusions that Paßens *et al.* draw regarding the universal favourable interaction (compromising between interactions with the 3-fold

symmetric substrate and nearest neighbours) are made on the assumption that the nanopit concept is correct[18]. However, it is my belief that their observations also appear to be consistent with the C6-C_{60} on the hcp sites.

One argument that is consistent across discussions of nanopits is the origin of the "dimness" of the C6-C_{60} when observed in STM images. Shin *et al.* identified that the adsorption orientation coupled with the nanopit results in a geometric height difference of 0.6 Å between the C6-C_{60} and the 6:6-C_{60}[13]. They conclude that this geometric effect is the reason that C6-C_{60} appears shorter in STM images, arguing that 0.6 Å matches the variation in apparent height. However, geometric and apparent height not synonymous, thus cannot be directly compared.

One suggestion for experiments which would afford direct comparison requires the tip-induced manipulation of C_{60} in the 2D array. By rotating C-C_{60} or 6:6-C_{60} into C6-C_{60}, the apparent height of these induced C6-C_{60} could be directly compared with that of the native C6-C_{60}. Simplistically, the C_{60} would be in the same adsorption orientation but the induced C6-C_{60} would be geometrically taller since it would be stabilised by a top-site rather than a nanopit. The rotation of C_{60} is observed in **Chapter 5**, but the methodical experiments required to explore the apparent heights of each natural and induced adsorption orientation are yet to be achieved. The innate randomness in the rotation of C_{60} results in a technique which is plagued by inconsistencies. Another complication of these experiments could be expected since there would a difference in the charge transfer between the substrate and a C6-C_{60} on a top site or on a nanopit. However, this variation in coupling could be observable in the stabilisation of the electronic structure of the fullerene. Similarly, variation in the stabilisation effect of the nanopit (compared to the hcp surface site) is also expected to be apparent. However, there is no discussion of this variation in the literature.

Shin *et al.* refer to the enhanced strength of the C6-C_{60} interaction with the substrate affording the reconstruction resulting in the nanopits, but there is no comment on how this interaction may affect the charge transfer compared to an hcp surface site. If the C6-C_{60} surface interaction is capable of stabilising vacancies which cover >4% of the Au(111) (i.e. the formation of nanopits for ~50% of fullerenes in the array[13]), one could speculate that the enhanced surface interaction would stabilise the LDOS compared to 6:6-C_{60}. With a mind to identifying this effect, and to unequivocally ascertain that the "beacon"

molecular appearance corresponds with Li@C_{60}, the next section focusses on the examination of the LDOS for the 4 species identified in **Fig. 4.5**.

4.1.3 - <u>Discriminating between Li@C_{60} and C_{60} using scanning tunnelling spectroscopy</u>

Scanning tunnelling spectroscopy (STS) is a common method that allows an STM to record the LDOS within the tunnelling gap. This LDOS arises from complex convolution of the LDOS of the adsorbate, the surface and the tip. The technique does not directly allow for chemical identification of the adsorbed species, but electronic resonances belonging to each contributor to the LDOS can be identified if the surface composition is approximately known. In the case of this work, STS was most useful for determining whether the fullerenes contained Li or not.

Two spectroscopic modes typical to STS are employed and discussed below. The first is constant height differential conductance spectroscopy (c.h. *dI/dV* STS). This mode consists of positioning the STM tip over the selected molecule, removing the feedback loop to ensure a constant tip height, and acquiring the 1st order derivative of the current signal (using an internal lock-in technique) whilst the bias is swept across the desired range with a small superimposed modulation. The c.h. *dI/dV* signal is known to be proportional to the LDOS[35–37] and as a result is most commonly used in literature.

The second spectroscopic mode utilised is constant current differential conductance spectroscopy (c.c. *dI/dV* STS). This mode consists of positioning the STM tip over the selected molecule, leaving the feedback loop engaged to maintain a constant current by varying the tip height with respect to the surface, and acquiring the 1st order derivative of the current signal whilst a small superimposed modulation is applied to the bias as it sweeps the desired range. **Fig. 4.10** exhibits examples of both spectroscopic modes for a C6-C_{60} within the large 2D array.

Resonance peaks can be identified in both spectra and at both polarities (filled and empty states). The difference between the spectroscopy techniques is discussed in greater detail in **section 2.2.1**, but the spectra in **Fig. 4.10** illustrates the requirement for both modes. Since c.h. *dI/dV* spectroscopy maintains the STM tip at a constant height, the spectrum
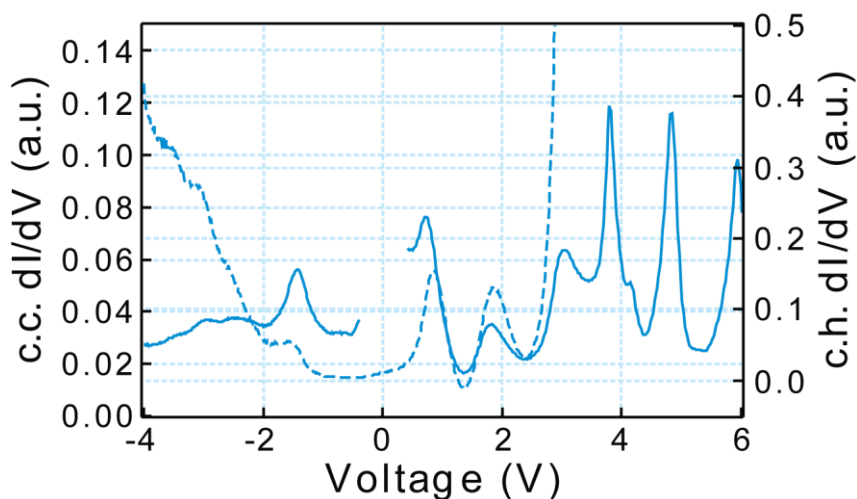
Figure 4.10: *Spectra of C6-C$_{60}$ within a large 2D array. The constant height differential conductance spectrum (c.h. dI/dV STS, with bias modulation of 50 mVpp at 1470 Hz) is represented by the dashed line and the constant current differential conductance spectra (c.c. dI/dV STS, I$_{set}$ = 0.1 nA, with bias modulation of 50 mVpp at 1470 Hz) by the solid lines at positive and negative bias.*

(dashed line in **Fig. 4.10**) can display electronic states close to the Fermi level (0 V). However, the technique is restricted to scanning a smaller range; a limitation which the other spectroscopic mode (c.c. *dI/dV* STS) overcomes by maintaining a constant current. Though this constant current allows a larger range to be examined in a single scan (solid lines in **Fig. 4.10**), it also prevents the technique from being able to cross the Fermi level since this would result in crashing the STM tip into the substrate as the tip attempts to maintain a constant current. The shortcomings of each spectroscopic technique illustrates why both are required to fully explore the bias range observed in **Fig. 4.10**. A second drawback for c.c. *dI/dV* STS is that the signal is not proportional to the LDOS of the molecule, unlike c.h. *dI/dV* STS. A correction factor, described by Ziegler *et al.*[38], must be applied for both spectroscopic techniques to be equivalent, otherwise quantitative comparisons are meaningless since specific resonance peaks will differ slightly in energy.

Close inspection of the two spectra in **Fig. 4.10** reveals the discrepancy between equivalent resonance peaks on c.h. and c.c. *dI/dV* spectra to be on the order of ~100 mV. Though this can be a considerable shift for some molecular systems, it is negligible when considering the magnitude of the energies between the resonance peaks for C$_{60}$. Given that the purpose of the spectroscopy in this study is as a semi-quantitative analysis of the

resonance peaks of fullerenes (i.e. to differentiate between LUMOs and SAMOs of C_{60} and Li@C_{60}), this variation is inconsequential to the overall goal. Therefore, c.c. *dI/dV* STS is sufficiently accurate and selected as the dominant spectroscopic method since it allows a larger energy range to be analysed, and affords better resolution on the high energy resonance peaks.

Fig. 4.11 displays an STM image, ball and stick models, and c.c. *dI/dV* spectra to directly illustrate the variation between the four molecular appearances observed in the $(2\sqrt{3}\times2\sqrt{3})$R30° overlayer discussed above. The STM image (+2.5 V, 0.1 nA, see **Fig. 4.11 (a)**) depicts a small area of a 2D island of fullerenes with colour-coded rings indicating the four fullerenes selected for spectroscopic study. The individual spectra (**Figs. 4.11 (b-e)**) correspond with the molecular appearances in the STM image, and the inset ball and stick models illustrate the adsorption configuration of each of the fullerenes: three adsorption orientations of C_{60} and one of Li@C_{60}. **Fig. 4.11 (f)** collects the c.c. *dI/dV* spectra of the four molecules to directly compare the resonance energies of both the filled (<0 V) and unfilled (>0 V) electronic states.

The negative bias range of the spectra (**Figs. 4.11 (b-f)**) illustrates the filled states (HOMOs) of the fullerenes. The four adsorption configurations appear to be split into pairs by intensity of the HOMO peaks. Despite the difference in the peak heights, these pairs (the C6-fullerenes and the non-C6-fullerenes) exhibit HOMOs which are almost identical in energy (~-1.5 V), regardless of Li-encapsulation. This is why Li@C_{60} is indistinguishable from C6-C_{60} when imaging at negative bias (**Figs. 4.5 (a-b)**); the electronic structure is not sufficiently different to indicate the endohedral fullerenes in the STM images.

The positive bias range of the spectra (**Figs. 4.11 (b-f)**) illustrates the unfilled electronic states of the fullerenes. Literature identifies the low energy unfilled states as LUMOs and the higher energy unfilled states as SAMOs[8]. As mentioned previously, LUMOs are molecular orbitals centred on the cage atoms and are predominantly located on the C5-faces[14]. The small variations in the LUMO peaks for the four fullerenes (~+0.5 V) can therefore be assigned to the various adsorption orientations of each fullerene causing different degrees of coupling with the substrate[2,39]. A similar variation in the energy of the peaks can be observed for the LUMO+1 for C_{60} (~+2 V), though at this stage there is some uncertainty about which of the Li@C_{60} peaks represents the LUMO+1 since there are two
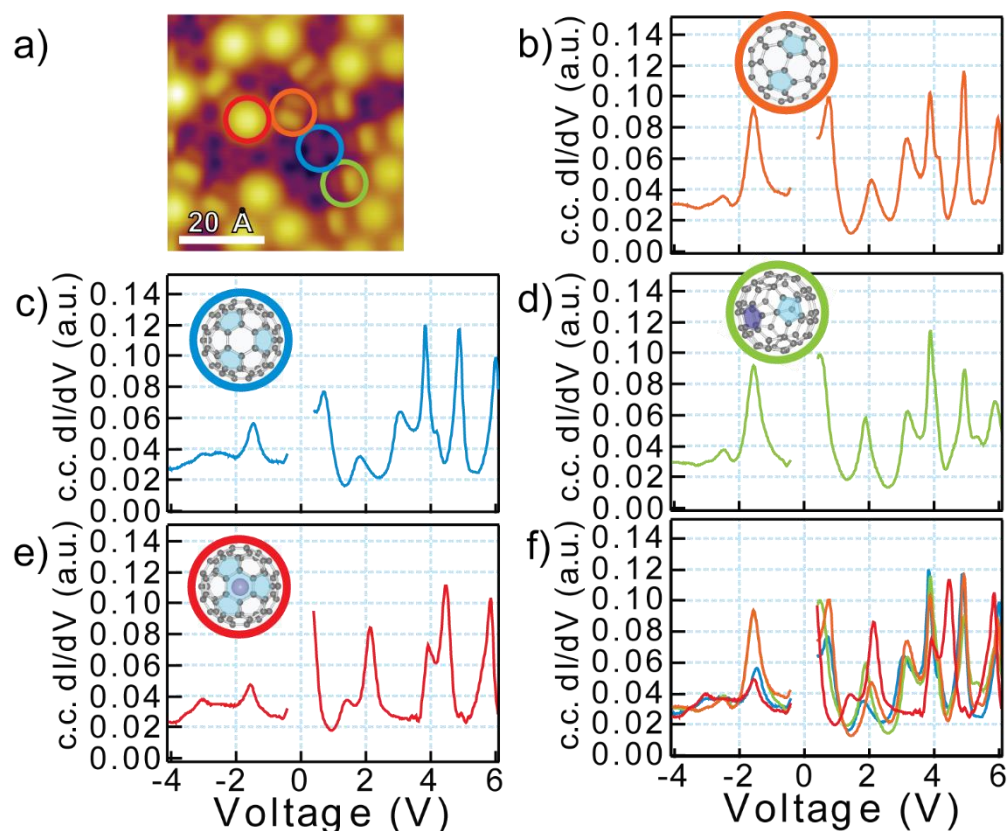
Figure 4.11: *a) STM image (+2.5 V, 0.1 nA) of a small area of a fullerene island. The coloured rings correspond with the STS spectra and the ball and stick models. **b-e)** Each graph contains two c.c. dI/dV spectra (positive and negative voltage ranges). The inset ball and stick models link the adsorption orientations of the molecular appearances in **a)** to the spectra in the following sequence: **b)** 6:6-C_{60}. **c)** M-C6-C_{60}. **d)** C-C_{60}. **e)** M-C6-Li@C_{60}. **f)** Compilation of the c.c. dI/dV spectra depicting the filled (<0 V) and unfilled (>0 V) electronic states for comparison of the four adsorption configurations.*

in close proximity (~+1.5 V and ~+2 V) which are easily observed in the isolated spectrum in **Fig. 4.11 (e)**.

One key point to recognise here is that the LUMO and LUMO+1 of the C6-C_{60} are no more stabilised than those of the non-C6-C_{60} (see **Fig. 4.11 (f)**), contrary to what might be expected for a fullerene adsorbed to a nanopit. This lack of extra stabilisation, combined with the symmetry arguments above, is further evidence that the hcp surface site has been adopted by the fullerenes in this thesis. As mentioned above (see **section 4.1.2.3**), further experimental work could be achieved to provide additional evidence for this

proposed adsorption configuration. However, the assumption that the fullerenes adopt the hcp surface site is sufficient for the purpose of commenting upon the data contained in this thesis since the surface symmetry does not alter the conclusions herein.

Unlike the lower energy peaks, the variation in the orientation of the fullerene is observed to have a negligible effect on the higher energy resonance peaks (see peaks at ~+3 V, ~+4 V, ~+5 V and ~+6 V for **Figs. 4.11 (b-d)**). The latter are suggested to be representative of the SAMOs[8] which are known to be more diffuse and, for C_{60}, centred on the core of the fullerene rather than the cage atoms. Rotation of the C_{60} cage, therefore, would have minimal effect on the SAMOs compared to what is observed on the LUMOs. Upon considering the higher energy resonance peaks, particular attention is drawn to the red spectrum (**Fig. 4.11 (e)**) because the distribution of the SAMOs is markedly different from what is observed on the other three. The altered SAMO structure can only be due to a different electronic structure resulting from a different molecule under the tip. It is with this observation that the red spectrum, and therefore the beacon molecular appearance in STM images like **Fig 4.11 (a)**, can be unambiguously assigned to $Li@C_{60}$.

By combining the unique peak distribution of the red spectrum (**Fig. 4.11 (e)**) and the observations made on the fullerene's changing molecular appearance in **Fig. 4.5**, the adsorption configuration of the fullerene is identified as M-C6-$Li@C_{60}$. This is illustrated by the corresponding ball and stick model in **Fig. 4.11 (e)**. The identification of $Li@C_{60}$ finalises the confident assignment of all four fullerenes on the surface. The next step is to label the resonance peaks, but this requires techniques other than just STM and STS to have any certainty in the identification. This is where the PES data and TDDFT calculations provided by our collaborators from the University of Edinburgh and the University of Liège are required, in combination with DFT from literature.

4.1.4 - <u>Identifying the resonance peak structure for $Li@C_{60}$ and C_{60}</u>

DFT is a powerful tool for simulating the behaviour of complex systems that can be difficult to study experimentally. Many studies of $Li@C_{60}$ have been conducted theoretically with the vast majority exploring the molecule in the gas phase. Some of these results have been confirmed using suitable gas-phase experimental techniques, but this thesis details the first extensive study by STM. The goal of this section is to identify the electronic structure exhibited in the STS data above (see **Fig. 4.11**). This is achieved by

combining four sets of data: the STS data detailed above, DFT calculations completed by Feng *et al.*[8], and experimental photoelectron spectroscopy (PES) data and time-dependent DFT (TDDFT) provided by our collaborators (and detailed in ref[28]). The PES and TDDFT are particularly necessary because understanding the symmetry of the resonance states is a key factor in differentiating between LUMOs and SAMOs. The symmetries of the SAMOs for C_{60} and two configurations of Li@C_{60} are illustrated in **Fig. 4.12**. These were calculated for fullerenes in the gas phase.

Super-atom molecular orbitals (SAMOs) are named as such because the wavefunctions of the SAMOs of C_{60} bear a striking resemblance to atomic orbitals (see **Fig. 4.12 (a)**, adapted from ref[8]) as was first introduced in **section 1.3.1.3**. These SAMO states extend both beyond and inside the C_{60} cage and are centred on the hollow core of the molecule. Upon encapsulation of the Li, however, this hollow core is no longer empty. When positioned centrally within the hollow, the presence of the Li in the cage is reported to stabilise the resonance energies of the SAMOs[8]. This stabilisation is exhibited by the contraction of the SAMOs in **Fig. 4.12 (b)** and the downshift in the energy of the corresponding resonance peaks in **Fig. 4.13 (b)**) (adapted from ref[8]). However, calculations reveal that the most favourable position for the Li is ~1.5 Å off-centre along an axis towards one of the C6 faces[24,40–49]. This results in the SAMO distortions seen in **Fig. 4.12 (c)** illustrating that, even in the gas phase, the SAMOs are strongly affected by the position of the Li within the C_{60}.

The Li@C_{60} ball and stick model in **Fig. 4.12 (c)** illustrates the orientation of the molecule, with the Li closest to the uppermost C6-face, to allow understanding of how the Li affects the SAMOs. As is seen above, the spherical electron density of the *s*-SAMO is strongly shifted away from the side of the C_{60} now occupied by the Li. The *p*-SAMOs lose their degeneracy because the p_z-SAMO aligns with the axis which passes through the Li and the centre of the C_{60}, whereas the p_x- and p_y-SAMOs are orthogonal to it. Since these maintain their degeneracy in the gas phase they will, henceforth, be referred to as the $p_{x,y}$-SAMOs. The electron density of the p_z-SAMO is seen to shift such that the node of the *p*-lobes is positioned on the Li. This results in the C_{60} cage predominantly containing one of the lobes whilst the other extends far beyond it. The $p_{x,y}$-SAMOs also lose their *p*-orbital symmetry though the distortion is less severe; the node is maintained at the centre of the core but the lobes are bent towards the Li causing a loss of their linearity. The *d*-SAMOs (not
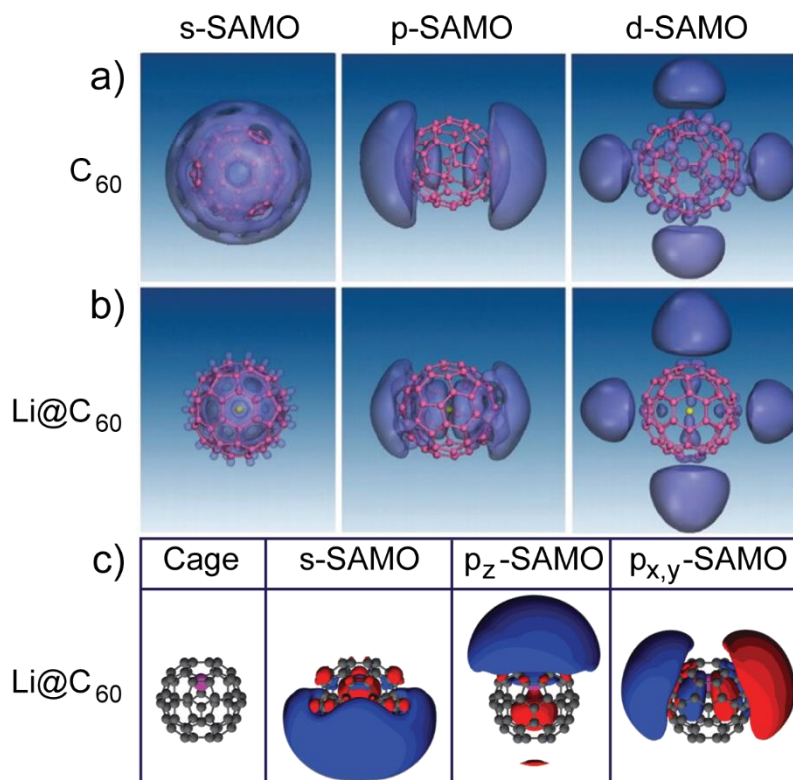
Figure 4.12: *Illustrations of the SAMOs for: **a)** C_{60} and **b)** Li@C_{60} with Li atom centrally located in the C_{60} cage, (adapted from Feng et al. Science 320, 359-362 (2008)[8]. Reprinted with permission from AAAS.), and **c)** Li@C_{60} with Li off-centre by 1.6 Å towards a C6 face (calculated by collaborators at the University of Edinburgh).*

pictured) are more diffuse than the *p*-SAMOs so the distortion of the lobes resulting from the Li encapsulation is suitably minor. This strong dependence on the position of the encapsulated Li is of particular importance when manipulation of the Li is discussed in **Chapter 5**.

The gas phase PES data acquired by our collaborators also reports distortions in the symmetry of the SAMOs[28], but the resonance energies at which these are reported differ from what was expected based on the DFT calculations. This permits no more than a semi-quantitative analysis of the peak structure. The discrepancy in the resonance energies of the PES and DFT data is likely to be due to the averaging nature of the experimental technique. Firstly, the PES analysis was completed on a mixed sample of C_{60}/Li@C_{60} (much like the STM data above); this requires removal of the C_{60} signal before the Li@C_{60} data can be analysed which may affect the results. Secondly, some broadening of the resonance peaks in the PES data is likely to occur because various rotational isomers of

Li@C_{60} will have been observed since there is no method of fixing the axes of the molecule in the gas phase. Both of these reasons justify the use of STS to further analyse the resonance peak energies; the lateral sensitivity of STS allows the study of single fullerenes, and the adsorption to a substrate at ~5 K fixes the axes of the SAMOs in an observable orientation.

The chemical bonding and subsequent charge transfer that results from the surface adsorption of fullerenes varies depending on the substrate selected[7]. The relative inertness of Au(111) is the reason why it was chosen for the initial study of this molecular system. However, regardless of reactivity, surface adsorption of fullerenes is known to cause some stabilisation of the electronic resonances of C_{60} due to the resultant coupling between the molecule and the substrate[7]. This stabilisation is expected to be enhanced for Li@C_{60} since it is known to couple more strongly to surfaces[24] and because the Li will be stationary within the C_{60} cage at ~5 K[50]. Unlike gas phase studies, where the Li is observed rattling around the inside of the cage[46,51,52], the thermally quenched Li is observed preferentially stabilising in an off-centre position towards the uppermost C6-face when adsorbed to a surface[24], as illustrated above. This results in the s- and p_z-SAMOs being orthogonal to the substrate and the $p_{x,y}$-SAMOs being parallel to it, necessarily affecting the energies of the corresponding resonance peaks.

Fig. 4.13 depicts two sets of data presenting the resonance peak structure for both C_{60} and Li@C_{60}. The first data set (**Figs. 4.13 (a)** and **(b)**) is comprised of figures adapted from the seminal paper of Feng *et al.*[8] (reprinted with permission from AAAS) which report calculations of the LDOS of gas phase C_{60} and Li@C_{60} (in which the Li atom is situated in the centre of the cage). The second data set (**Figs. 4.13 (c)** and **(d)**) illustrates the experimental c.h. and c.c. *dI/dV* spectra from the C6-C_{60} and C6-Li@C_{60} on Au(111) described in **Fig. 4.11**. These fullerenes are selected because they adopt the same adsorption orientation and can, within a reasonable approximation, be considered identical except for the encapsulated Li. The presence of the Li, and the resulting distortions of the SAMOs, can therefore be considered the sole reason for any variation in the energy of the resonance peaks.
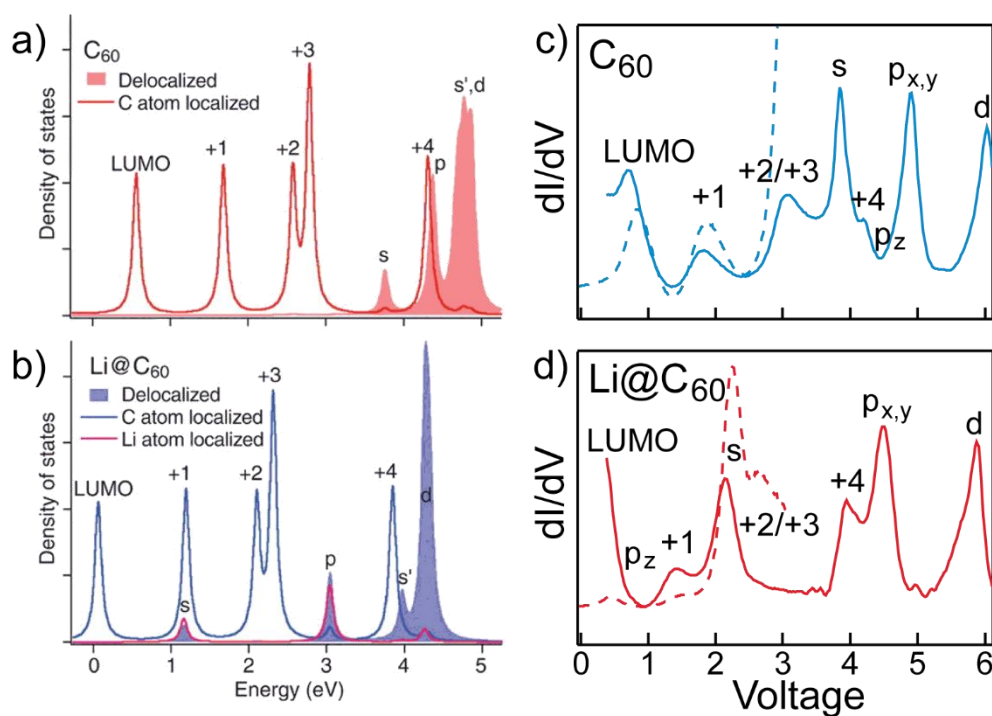
Figure 4.13: *LDOS for a) C_{60} and b) Li@C_{60} with the Li atom in the centre of the cage resulting from gas phase DFT calculations (adapted from Feng et al. Science 320, 359-362 (2008)[8]. Reprinted with permission from AAAS.). Experimental c.h. and c.c. dI/dV spectra (dashed and solid lines, respectively) for c) C6-C_{60} and d) C6-Li@C_{60}. These are the same data as shown in Fig. 4.11.*

The LDOS produced by DFT (**Figs. 4.13 (a)** and **(b)**) illustrates the resonance peaks relating to LUMOs using a solid line and to SAMOs using a block colour graph. The calculated peaks in the C_{60} spectrum (**Fig. 4.13 (a)**) are in the expected order: LUMOs lowest in energy followed by *s*- and *p*-SAMOs with the *d*-SAMOs highest in energy. The encapsulation of the Li atom results in the stabilisation of all resonance peaks (see **Fig. 4.13 (b)**) due to hybridisation effects with the atomic orbitals of the Li atom. The LUMOs exhibit a rigid downward shift of ~0.5 eV but the SAMOs are affected by varying degrees; the *d*-SAMOs are only stabilised by ~0.5 eV, the *p*-SAMOs by ~1.2 eV and the *s*-SAMO by the greatest amount at ~2.5 eV. This brings the *s*-SAMO roughly level with the LUMO+1. Due to the calculations being completed for the fullerenes in the gas phase, and with the Li atom in the centre of the C_{60}, the *p*- and *d*-SAMOs maintain degeneracy and are described by a singular peak.

The experimental spectra (**Figs. 4.13 (c)** and **(d)**) display the resonance peaks observed on C6-C_{60} and C6-Li@C_{60} from within the large 2D array. Both c.h. *dI/dV* spectra (dashed lines) and c.c. *dI/dV* spectra (solid lines) are presented to provide as much information about the peaks as possible. The identification of these resonance peaks for C6-C_{60} (**Fig. 4.13 (c)**) is achieved by semi-quantitative comparison with the DFT calculations. The minor differences are thought to be due to resolution of the spectroscopic technique and splitting of the peaks due to adsorption-induced loss of degeneracy. The LUMO+2/+3 peak, located around +3 V, is the merger of the LUMO+2 and LUMO+3 peaks due to convolution of the signals. The same is observed for the LUMO+4 which appears as a shoulder of the *s*-SAMO. The slight broadening of the peak ~+5 V is likely to be the result of a loss of degeneracy in the *p*-SAMOs because the surface adsorption stabilises the p_z-SAMO further than the $p_{x,y}$-SAMOs.

The stabilisation that results from the Li encapsulation is observed in all of the resonance peaks in **Fig. 4.13 (d)**, but the degree of stabilisation varies between LUMOs and SAMOs (as expected from **Fig. 4.13 (b)**). The distortions to the SAMOs (as seen in **Fig. 4.12 (c)**) will alter the peak energies since coupling of each to the substrate will necessarily change compared to C_{60}. With this knowledge, assignment of all the peaks, except for the p_z-SAMO, is achieved by comparing the spectrum of Li@C_{60} with that of the C_{60} and considering the molecular appearance in the STM images. The p_z-SAMO requires various techniques to identify due to the complexity of the distortion of the SAMO and the resultant coupling with the substrate.

The rigidity of the shift in the LUMOs allows fairly straightforward identification of the corresponding peaks in **Fig. 4.13 (d)**. The LUMO+2/+3 appears lost in the intensity of the peak at ~+2 V in the c.c. *dI/dV* spectrum but is visible in the c.h. *dI/dV* spectrum allowing confirmation of its stabilised position. The LUMO+4 remains at ~+4 V and becomes more pronounced since it is no longer convoluted with the *s*-SAMO.

The beacon molecular appearance of the Li@C_{60} when imaging at +2.5 V is reminiscent of the *s*-SAMO: diffuse and circular. The large peak ~+2 V is clearly a strong contributor to this molecular shape and is therefore determined to be the *s*-SAMO resonance peak. The $p_{x,y}$- and *d*-SAMOs are known to exhibit only minimal stabilisation due to the encapsulated species. The $p_{x,y}$-SAMOs remain roughly parallel to the substrate so added surface

stabilisation is minimal compared to C_{60}, and the *d*-SAMOs are barely affected by the encapsulation of the Li; hence the peak assignments at ~+4.5 V and ~+6 V.

The p_z-SAMO, much like the *s*-SAMO, is strongly affected by the encapsulation of the Li (as seen in **Fig. 4.12**) and is orthogonal to the substrate. Given that Li@C_{60} is more strongly coupled to the substrate than C_{60}, it is expected that the p_z-SAMO will be greatly stabilised. However, there are no immediately obvious unassigned resonance peaks remaining in the spectrum. The symmetries observed in the PES data suggest that the p_z-SAMO is expected to be ~+1 V[28]. After considering the results of the Li-manipulation data (discussed in **Chapter 5**), the p_z-SAMO is identified as having stabilised closer to the Fermi level, and is therefore combined with the signal for the LUMO peak ~+0.5 V.

The combination of DFT, PES and STS data discussed above provides solid evidence for the peak assignment observed in **Figs. 4.13 (c)** and **(d)**. However, capturing the symmetries of the SAMOs with differential conductance scanning tunnelling microscopy (*dI/dV* STM), as seen in the work of Reecht *et al.*[12], would identify these peaks unambiguously. This is the focus of the next section.

4.1.5 - Exploring the electronic states of fullerenes with c.c. *dI/dV* STM imaging

By incrementally sweeping the local voltage range of each resonance peak in a *dI/dV* spectrum, *dI/dV* STM imaging can facilitate the identification of the electronic states. Reecht *et al.* compared calculated symmetries for the various electronic states of C_{60} with experimentally acquired c.c. *dI/dV* STM images of C_{60} on Cu(111) (see **Fig. 4.14**, adapted from ref[12]). As such, they were able to accurately identify the peaks in the corresponding spectra.

Some of the *dI/dV* images in **Fig. 4.14** are slightly distorted compared to the appearance of the DFT-produced isosurfaces, for example the *s*-SAMO. Reecht *et al.* determined that this is because the spectroscopic technique is coupled with a constant current imaging technique[12]. This results in the "single point spectra" which form the 2D image being recorded with varying tunnel junction gaps across the molecule. This in turn causes slight shifts in the energies of the electronic states, and affects the image that is produced such that is not a true reflection of the LDOS. For 3D molecules like C_{60} this is a particular issue

| LUMO E V = 0.1 V | LUMO A V = 0.8 V | LUMO+1 A V = 1.8 V | LUMO+1 E V = 2.2 V | LUMO+2 & +3 V = 3.4 V | $l = 0$ V = 4 V | $l = 1$; $m = 0$ V = 5.4 V | $l = 1$; $m = +/-1$ V = 5.6 V |
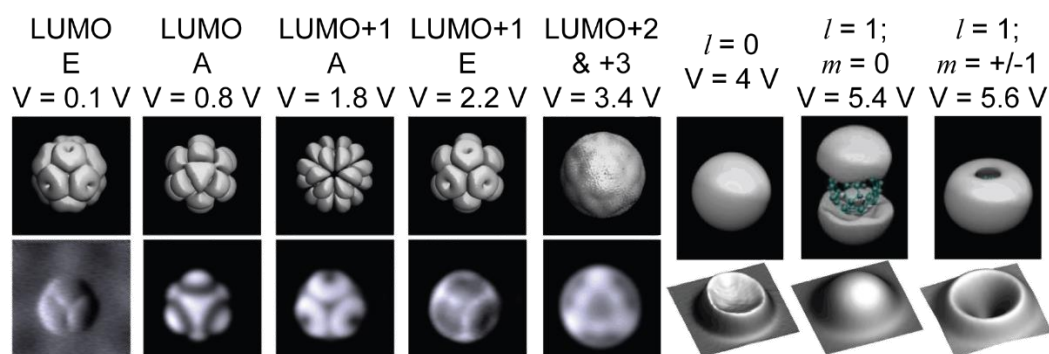
Figure 4.14: *A collection of images of C_{60} wavefunctions calculated with DFT (top row) and experimental c.c. dI/dV STM images of various electronic states of a C6-C_{60} on Cu(111) (bottom row) as reported by Reecht et al.[12]. The c.c. dI/dV STM images of the SAMOs are 3D rendered and labelled with their quantum numbers in place of the SAMO symmetries: from left to right these correspond with the s-, p_z- and $p_{x,y}$-SAMOs. The figure has been adapted from Reecht et al., New Journal of Physics 19, 113033 (2017) courtesy of the CC-BY 3.0 license.*

since the height variation across the image is so dramatic. Despite the approximations required to compare the experimental images to the DFT images, c.c. *dI/dV* STM imaging is shown to provide strong evidence in the identification of the electronic states. Given this capability, similar experiments to those exhibited by Reecht *et al.* (**Fig. 4.14**) are sought on the current system of C_{60} and Li@C_{60} on Au(111) to unambiguously identify the peaks in the spectra observed in **Fig. 4.13**. One example of such measurements is depicted in **Fig. 4.15** which shows a small region of a 2D array simultaneously examined with c.c. STM (**Fig. 4.15 (a)**) and c.c. *dI/dV* STM (**Fig. 4.15 (b)**). Example spectra of the four fullerene configurations seen in these arrays are illustrated in **Fig. 4.15 (c)** to facilitate discussion of which electronic states the images are illustrating.

Figs. 4.15 (a) and **(b)** illustrate the same region of a large, 2D array that is imaged at +2.12 V with a superimposed bias modulation of 100 mVpp at 1470 Hz (this bias scan range is indicated by the thin green stripe on **Fig. 4.15 (c)**). Both the c.c. STM (**Fig. 4.15 (a)**) and c.c. *dI/dV* STM (**Fig. 4.15 (b)**) images are recorded simultaneously allowing for direct identification of the species within the region. This can be used to determine the appearance of each adsorption configuration in the c.c. *dI/dV* STM image.
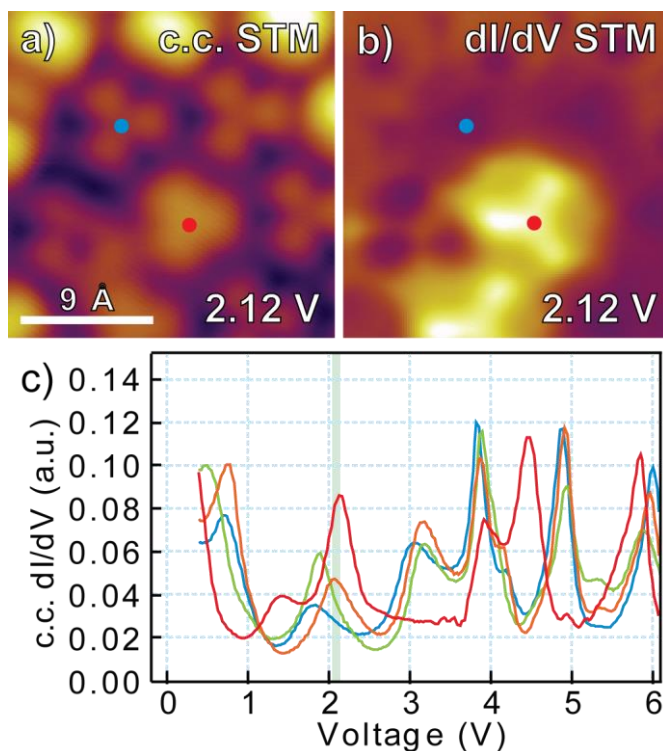
Figure 4.15: *a) c.c. STM image (+2.12 V, 1.1 nA) and b) c.c. dI/dV STM image (+2.12 V, 1.1 nA, 100 mVpp at 1470 Hz) of the same portion of a 2D array composed of C_{60} and Li@C_{60}. A C6-C_{60} (blue) and a C6-Li@C_{60} (red) are highlighted to facilitate identification in both images. c) Example c.c. dI/dV spectra for the molecular configurations observed within the array; C6-C_{60} (blue), C-C_{60} (green), 6:6-C_{60} (orange) and C6-Li@C_{60} (red). The thin green stripe indicates the range over which the bias modulation swept during the capture of the c.c. dI/dV STM image.*

The fullerene highlighted with a blue dot in **Fig. 4.15 (a)** is M-C6-C_{60} and is almost indistinguishable at +2.12 V from what is observed above at +2.5 V (**Fig. 4.5 (d)**). The diffuse appearance of the fullerene highlighted by a red dot in **Fig. 4.15 (a)** is typical of M-C6-Li@C_{60} when imaging at ~+2 V. The three-fold rotational symmetry of the C6-fullerene adsorption orientation is visible but is convoluted with the increased apparent height and loss of internal structure typical of Li@C_{60}. The scan bias for the images in **Figs. 4.15 (a)** and **(b)** is +2.12 V which, by observing the green stripe in **Fig. 4.15 (c)**, is seen to fall on the LUMO+1 peak for C_{60} and the *s*-SAMO peak for Li@C_{60} (as determined in **Figs. 4.13 (c)** and **(d)**). By considering the appearances of these states for C_{60} in **Fig. 4.14**, similar structures could be expected in the experimental c.c. *dI/dV* STM image.

Fig. 4.15 (b) shows the c.c. *dI/dV* STM image of the same region of the 2D array subject to the same STM parameters (+2.12 V with a 1470 Hz bias modulation of 100 mVpp, and 1.1 nA tunnelling current). The M-C6-C_{60} in the region resemble the LUMO+1 A that is depicted in **Fig. 4.14**, however the contrast due to the neighbouring Li@C_{60} signal obscures this making it difficult to observe. This identification matches what is expected with respect to the peak assignment. The M-C6-Li@C_{60}, however, does not match the expected appearance of the *s*-SAMO. The increase in apparent height compared to neighbouring C_{60} is observed, since this is also seen in **Fig. 4.15 (a)**, but with the scanning bias aligned with the *s*-SAMO of the Li@C_{60} the c.c. *dI/dV* STM appearance was expected to be circular and largely featureless. Instead it exhibits the three-fold rotationally symmetric feature of the LUMO+1 E. This suggests that the peak structure of the Li@C_{60} is complex and resonance peaks are representative of the convoluted signals from various electronic states rather than singular ones.

One hypothesis for the convolution of these resonance peaks is linked to the fact that the fullerenes are condensed into 2D arrays. Hybridisation of the higher energy SAMOs has already been observed for C_{60} arrays, with Feng *et al*. noting the NFE band which forms[8]. It is thought that similar effects may be complicating the attempts to image individual electronic states for C_{60} and Li@C_{60} in the current work. As such, c.c. *dI/dV* STM imaging of isolated fullerenes is expected to be more productive.

4.1.6 - <u>Attempting to isolate fullerenes by lateral manipulation of 2D arrays</u>

Lateral manipulation of molecules using an STM probe is a very common technique and would be a simple method of manufacturing isolated fullerenes. Extracting fullerenes from the edges of the large 2D arrays is expected to be the easiest to achieve since the intermolecular interactions between the molecules would be minimised compared to those within the island. As can be seen by the sequential images in **Fig. 4.16** this method is not successful.

Many attempts have been made to push fullerenes away from the edges of islands and step edges using paths similar to that indicated by the blue line in **Fig. 4.16 (a)**. In most cases the STM tip is damaged and the surface unrecognisable. However, very occasionally the fullerenes are successfully manipulated (as seen by the missing fullerenes in **Fig. 4.16**
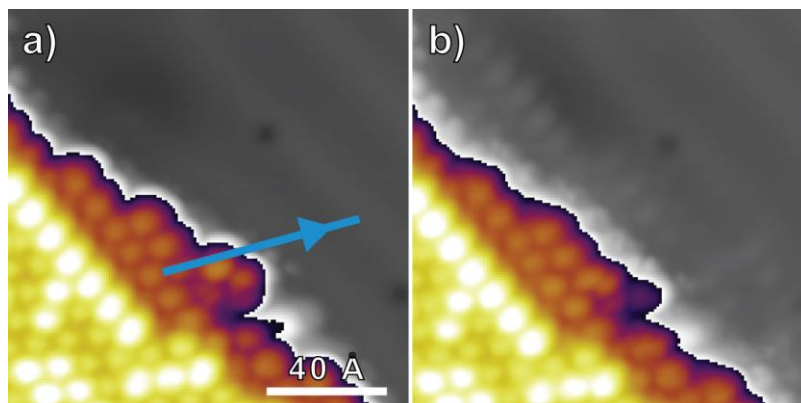
Figure 4.16: *STM images (+1.0 V, 0.1 nA) **a)** before and **b)** after an attempt to push a fullerene away from the edge of a narrow island. The blue line signifies the path taken by the STM probe during the lateral manipulation.*

(b)), but the exact manipulation cannot be determined. Given the state of the tip, as inferred by the artefacts in **Fig. 4.16 (b)**, one suggestion could be an asymmetric adsorption of the C_{60} to the apex of the STM probe. This is unconfirmed, however, because all attempts at subsequently depositing the fullerene resulted in crashing the tip. The failure of this method highlights the requirement for another technique to achieve isolated fullerenes on the Au(111) surface.

4.2 - Identifying the electronic structures of Li@C_{60} and C_{60} on Au(111) after a post-adsorption anneal at 320 K

One method of isolating fullerenes is to reduce the degree of diffusion across the substrate during the preparation stage of the sample. This can be achieved by lowering the temperature of the post-adsorption anneal to avoid exceeding the activation barrier for mass transport of the fullerenes. Given the stronger interaction between the substrate and Li@C_{60}, compared to C_{60}, a degree of segregation can be achieved provided the anneal temperature is appropriately selected. The following section discusses data depicting a surface that has been prepared with the conditions detailed in **section 3.2.1.1** and annealed at 320 K. Similar to **section 4.1**, the following discussion will first utilise a combination of scanning tunnelling microscopy and spectroscopy to differentiate between Li@C_{60} and C_{60} on the Au(111) substrate (**sections 4.2.1-4.2.3**). With the

identification of isolated fullerenes, attempts towards confirming the electronic structure with c.c. *dI/dV* STM imaging will then be discussed (**section 4.2.4**).

4.2.1 - Introducing the fullerene structures on the surface

Upon annealing the Au(111) substrate to 320 K after depositing the fullerene mixture, the surface instead appears like that seen in **Fig. 4.17**. Some diffusion of fullerenes across the Au(111) terrace results in the formation of an island composed of Li@C_{60} (bright, circular molecules) and C_{60} (all other molecular appearances), but isolated molecules are also present (top left corner of the STM image). The final note that pertains to the reduced anneal temperature is the presence of pollution which was previously desorbed from the surface. It is of a relatively small amount but its presence is noteworthy as an illustration of the stability of the elbows of the herringbone reconstruction; a known nucleation site as mentioned previously.

The STM signature of the molecule in the top left corner of the image is ~25 Å in diameter. This is much bigger than the size of the C_{60} in the islands (~10 Å) but is also too narrow to be a cluster of 3 fullerenes. This can be explained simply by tip convolution. The apparent height is similar to the fullerenes in the island and the three-fold rotationally symmetric molecular appearance is very similar to the C6-fullerene orientation described above. The isolated fullerene is adsorbed to the elbow of the herringbone reconstruction. This proves that the stabilisation afforded by this nucleation site is sufficient to prevent further diffusion across the substrate, thus resulting in a non-negligible number of isolated fullerenes. Various other surface sites are also observed stabilising the isolated fullerenes (as seen later in this section), but the majority of the fullerenes are positioned in proximity to the elbows of the herringbone reconstruction.

With respect to the 2D array of fullerenes there are a number of observations that require comment. The first being the location of the island. The large islands (as depicted in **Fig. 4.1 (a)**) are exclusively found along Au(111) step edges whereas islands stabilised on the terraces of the Au(111) surface (like that seen in **Fig. 4.17**) are commonplace after these preparation conditions. Secondly, the islands themselves are often seen to adopt a more elongated shape compared to the larger islands. The lower anneal temperature seems to result in a growth mechanism which is more strongly affected by the uniaxial compression
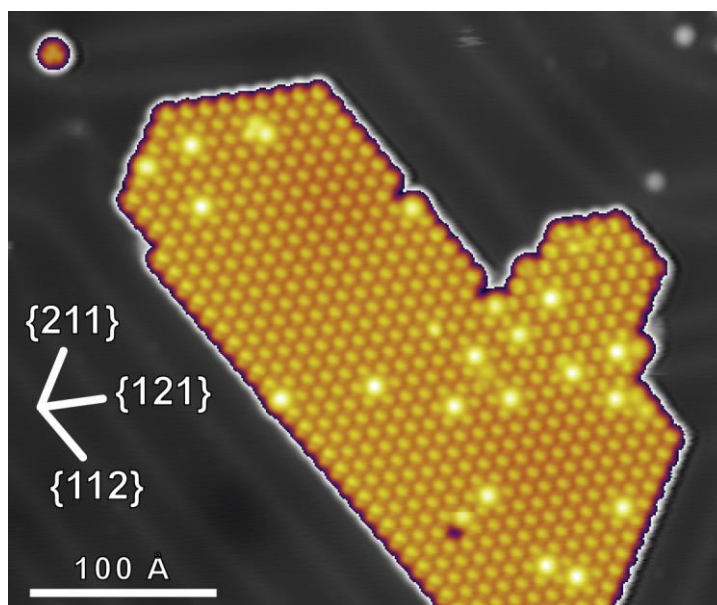
Figure 4.17: *STM image (+2.5 V, 0.1 nA) of the Au(111) surface after a ~1 hr post-adsorption anneal at 320 K. A hexagonally close-packed island of fullerenes is observed with an isolated fullerene in close proximity (top left). The herringbone reconstruction is also visible on the surface, as is some minor pollution (top right). The compass illustrates the crystallographic directions of the substrate which correspond with the packing directions of the island.*

of the Au(111) surface. The axis of elongation of the islands ({112} in **Fig. 4.17**) is orthogonal to this uniaxial compression which is induced by the herringbone reconstruction. It is likely that the resulting anisotropy of the surface alters the interaction between the adsorbate and the substrate, hence apparently promoting growth along particular surface directions. Though the growth of the islands coincides with the herringbone reconstruction, it appears that the relationship is somewhat symbiotic since relaxation of the herringbone reconstruction (as is observed in **Fig. 4.1 (a)**) is also achieved.

Similar to the large islands (as seen in **Fig. 4.1 (a)**), the smaller islands (**Fig. 4.17**) are observed distorting the herringbone reconstruction to ensure that the islands are almost solely located within the fcc regions of the surface. However, unlike for the higher anneal temperature, the lifting of the herringbone reconstruction is not uniformly achieved. For example the appendage on the right of the island (in **Fig. 4.17**) can be seen bridging the herringbone rather than lifting it. Though the characteristic ridges of the reconstruction

are not observed in the contrast of the island, as has been reported in some cases[1,53], there is a noticeable effect on the fullerenes.

Looking closely at the fullerenes within the island reveals that there are two domains largely consisting of fullerenes with identical adsorption configurations. Similar to the disorder of the large 2D array discussed above, these domains of uniformity within the islands are also reported in literature[1]. Within the main portion of the island the vast majority of the C-C$_{60}$ are identically orientated; with the brighter segment making it look like each fullerene is "pointing" in the $[\bar{2}11]$ direction. The C-C$_{60}$ in the small appendage, however, almost solely adopt the $[\bar{1}2\bar{1}]$ orientation. One hypothesis to explain this domain change across the herringbone reconstruction suggests that two islands were nucleated in close proximity with unique adsorption configurations. These configurations were maintained during the growth of each island and subsequent coalescence. However, since the growth was not due to the expansion of a single island, the herringbone reconstruction was not lifted and is trapped beneath the border of the two domains.

Almost none of the C$_{60}$ within the island in **Fig. 4.17** adopt the most thermodynamically stable adsorption configuration, identified above as M-C6-C$_{60}$. As such, it is hypothesised that, at these preparation conditions, the stabilisation gained by the formation of these domains supersedes the preference for individuals to adopt the C6-fullerene adsorption configuration. This "domain stabilisation" aligns with the azimuthal preference discussed above regarding the work of Paßens *et al*.[18]. Their work identified the alignment between electron rich 6:6-bonds and electron poor C5-faces stabilising 2D arrays similar to what is observed in the crystal structure. The extent of this benefit is not fully understood, and DFT calculations to provide such understanding are prohibitively expensive due to the complexity of the molecular system. Some indication of the strength of this effect is gained by considering the effect on the Li@C$_{60}$ adsorption orientation. As has been mentioned numerous times, Li@C$_{60}$ couples more strongly to the substrate than C$_{60}$. If this "domain stabilisation" is capable of causing Li@C$_{60}$ to adopt a different adsorption orientation, that provides a qualitative indication of the strength of the effect. This effect on adsorption orientation can easily be examined using the same technique as detailed in **section 4.1.2**.
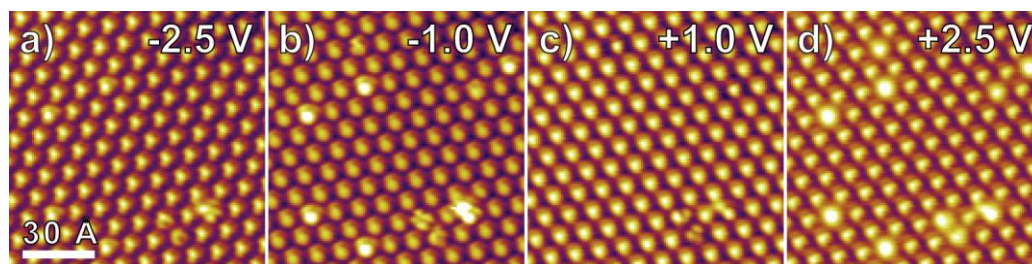
Figure 4.18: *STM images of an island composed of Li@C$_{60}$ and C$_{60}$ on Au(111) after a post-adsorption anneal at 320 K. **a)** (-2.5 V, 0.1 nA) **b)** (-1.0 V, 0.1 nA) **c)** (+1.0 V, 0.1 nA) **d)** (+2.5 V, 0.1 nA).*

4.2.2 - Identifying the adsorption orientations of Li@C$_{60}$ and C$_{60}$

By imaging the surface at various biases, the adsorption orientations of Li@C$_{60}$ in the 2D arrays are identified. **Fig. 4.18** illustrates the bias dependence of the fullerenes in a portion of an island on the Au(111) surface after a post-adsorption anneal at 320 K. Inspection of the STM images reveals that the Li@C$_{60}$ is capable of adopting a non-C6-fullerene adsorption orientation similar to the neighbouring C$_{60}$, unlike what is observed when annealing at 520 K.

The molecular appearances are similar to what is observed on the large 2D arrays (discussed in **section 4.1.2**) allowing for easy recognition of the molecular configurations. All of the C$_{60}$ within the images have adopted the C-C$_{60}$ adsorption orientation represented by the asymmetric two-segment appearance at +2.5 V (**Fig. 4.18 (d)**). The fullerene exhibits a one-fold rotational symmetry which is maintained throughout the four images. All fullerenes that appear different from this are identified as Li@C$_{60}$, confirmed by the beacon appearance at +2.5 V. The majority of these Li@C$_{60}$ adopt a non-C6-fullerene adsorption orientation. This is established at +1.0 V (**Fig. 4.18 (c)**) because most of the Li@C$_{60}$ are indistinguishable from the C-C$_{60}$ indicating these have adopted the C-Li@C$_{60}$ adsorption orientation. This orientation can also be observed at -2.5 V (**Fig. 4.18 (a)**) and -1.0 V (**Fig. 4.18 (b)**). However, in these cases the encapsulation of the Li alters the molecular appearance so it is no longer inconspicuous, unlike in **Fig. 4.5**.

The observation of C-Li@C$_{60}$ supports the argument that there is a stabilisation factor which results from the fullerenes adopting identical adsorption configurations within the islands. However, it also highlights the complexity of this molecular system. It appears to

be a very dynamic system with many factors that alter the behaviour of the adsorbates, therefore nothing can be assumed about the isolated fullerenes.

4.2.3 - Identifying the isolated fullerenes using STM and STS

Isolated fullerenes are reasonably numerous across the terraces of the surface, though are sparsely distributed. The images seen in **Fig. 4.19** are of one area of the surface where the concentration of isolated fullerenes is greater, allowing for direct study of a variety of fullerenes within the same image and with an identical STM tip. The fullerenes ringed green, purple and orange have been deposited at these sites as a result of minor, accidental surface modification during preparation of the STM tip in the vicinity.

The molecular appearances of the three fullerenes deposited by surface modification (green, purple and orange) and the one ringed in light blue retain some structural information throughout the various scanning biases. This suggests that these are representative of isolated C_{60}. The red and dark blue ringed fullerenes are featureless at +2.5 V (**Fig. 4.19 (d)**), implying Li@C_{60}. By employing the same method as for the condensed fullerenes the molecular appearances can be used to tentatively propose the adsorption orientation for each of the molecules.

The green fullerene looks like a distorted ring at -2.5 V (**Fig. 4.19 (a)**) but the three-segment structure with one-fold rotational symmetry seen at +2.5 V (**Fig. 4.19 (d)**) insinuates that it is a 5:6-C_{60}. The purple fullerene has a two-segment appearance in **Figs. 4.19 (b-d)** and the hint of a dumbbell shape in **Fig. 4.19 (a)** which is strong evidence that it is a 6:6-C_{60}. The orange fullerene exhibits a three-fold rotational symmetry in all images suggesting a C6-C_{60}, but is also brighter than any of the other isolated fullerenes on the surface. This behaviour is opposite to that exhibited by C6-C_{60} in the islands which appear dimmer than non-C6 fullerenes. The proximity of the pollution to the fullerene could be affecting the molecular appearance and increasing the apparent height; for example the pollution may extend below the fullerene which is why it appears taller than the others. This would lead to separation from the substrate which could cause the spectrum to appear more similar to that of a gas-phase fullerene. However, the spectrum could also be affected by the pollution so conclusions about this molecule are proposed warily. The light blue fullerene has a distorted three-segment appearance in **Fig. 4.19 (a)** but shares

Figure 4.19: *STM images of six isolated fullerenes on Au(111) after annealing at 320 K.*
a) (-2.5 V, 0.1 nA), b) (-1.0 V, 0.1 nA), c) (+1.0 V, 0.1 nA), and d) (+2.5 V, 0.1 nA).

the symmetry of the green fullerene in **Figs. 4.19 (b-d)** (though it appears brighter than the green fullerene in each). This fullerene is tentatively described as a 5:6-C_{60} though requires STS to identify any differences with the green fullerene.

The red fullerene resembles a ring in **Fig. 4.19 (a)**, exhibits three-fold rotational symmetry in **Figs. 4.19 (b)** and **(c)** and is featureless at +2.5 V (**Fig. 4.19 (d)**) identifying itself as a C6-Li@C_{60}. The final fullerene, dark blue, doesn't exhibit any structure in the STM images. As such it could simply be assigned to a C5-fullerene since this would also be expected to have a round appearance due to the C5-face at its apex. The brightening of the molecule at +2.5 V indicates that the dark blue fullerene is a Li@C_{60}, so it is cautiously labelled as a C5-Li@C_{60}.

The uncertainty in the assignments of molecular orientation highlights the requirement for spectroscopy to confirm the identity of the isolated fullerenes. Upon recording the spectra for the six fullerenes in **Fig. 4.19** (see **Fig. 4.20**), the light blue fullerene is, instead, seen to resemble the Li@C_{60} spectra from the islands more closely than the C_{60} (see **Fig. 4.20 (b)**). As a result, conclusions based on molecular appearance are not considered
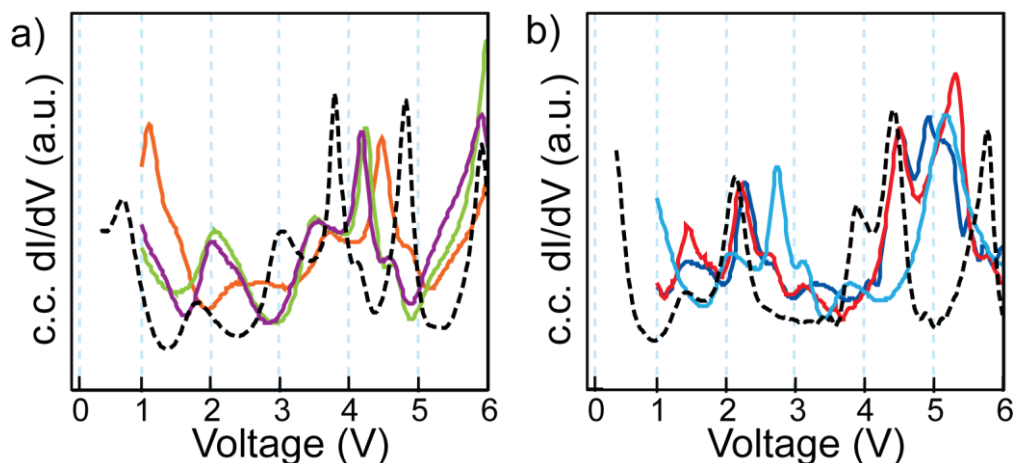
Figure 4.20: *Colour-coded STS data of the isolated fullerenes from Fig. 4.19 with the experimental STS data from Fig. 4.13 of condensed C6-C_{60} and C6-Li@C_{60} (black dashed lines). The spectra are grouped by molecule: **a)** C_{60}, and **b)** Li@C_{60}.*

reliable and future identification of isolated species is only confirmed using spectroscopy. The spectra of the six fullerenes are collected in **Fig. 4.20** and compared with the corresponding species from **Fig. 4.13**.

The spectra exhibited in **Fig. 4.20 (a)** illustrate the electronic structures of various adsorption configurations of C_{60} on Au(111). The black dashed line is the spectrum of C6-C_{60} in the 2D array illustrated in **Fig. 4.13 (c)** and the other three correspond to the isolated fullerenes in **Fig. 4.19**. The similarity between the green and purple spectra illustrates the sensitivity of the spectroscopic method with respect to the adsorption configuration. The very minor variations in resonance peak energies are likely to be due to adsorption orientation as was observed in **Fig. 4.11 (f)** for the C_{60} in the large 2D array. The orange spectrum appears very similar to the green and purple spectra but has been rigidly shifted higher in energy by ~0.25 V. This corresponds with the suggestion that the pollution around, and possibly under, the fullerene has separated the molecule from the substrate thus reducing the stabilising effect resultant from adsorption. This separation cannot be proven, however, so the proposal that the fullerene has been lifted from the substrate is purely conjecture. What can certainly be proven is the relationship between the condensed and isolated forms of C_{60}.

The general peak structure is very similar between the isolated and condensed forms of C_{60}, but each peak undergoes differing degrees of stabilisation as the fullerene is

restrained within a 2D array. The higher energy peaks are more affected by the lack of neighbours than the low energy peaks. For example, the $p_{x,y}$-SAMOs shift >1 V higher in energy between the island C_{60} (~+5 V) and the isolated C_{60} (~+6 V) compared to the LUMO+1 which shifts <0.25 V. As is observed in **Fig. 4.12**, the quasi-degenerate $p_{x,y}$-SAMOs extend parallel to the substrate resulting in extensive overlap with the neighbours in an island forming a nearly free electron (NFE) band[8]. This band links the C_{60} and Li@C_{60} in an island causing further stabilisation. The shift observed in the $p_{x,y}$-SAMOs in **Fig. 4.20 (a)** highlights the extent of this effect.

The stabilisation due to NFE band formation is also observed for Li@C_{60} in **Fig. 4.20 (b)**. The peaks at ~+4 V and ~+4.5 V, corresponding with the LUMO+4 and $p_{x,y}$-SAMOs in the condensed Li@C_{60} spectrum (black dashed line), upshift ≥0.5 V when isolated on the surface. This is exhibited by the red and dark blue spectra. Besides the shift of these resonance peaks, however, the energies of the lower electronic states of the red and dark blue isolated Li@C_{60} are barely altered from the condensed form. Given the strong connection between the position of the Li within the cage and the resulting direction of the SAMOs (illustrated in **Fig. 4.12**), any variation in the adsorption orientation of the Li@C_{60} is expected to greatly affect the p_z- and s-SAMO coupling with the substrate. The fact that the red and dark blue spectra are so similar indicates that the C5-Li@C_{60} adsorption proposed for the dark blue fullerene is likely to be incorrect and it instead adopts the C6-Li@C_{60} configuration.

The correlation between the adsorption orientation and consequent coupling with the substrate is clearly illustrated by the shift in the peaks of the light blue spectrum. The rigid upward shift of ~0.5 V is thought to be due to the non-C6 adsorption orientation of the fullerene, which is more clearly observed for the light blue fullerene compared to the dark blue fullerene in **Fig. 4.19**. This connection between the peak energies and the Li position with respect to the substrate is discussed further with respect to the manipulation of the Li within the cage (see **Chapter 5**).

Despite the occasional stabilisation of Li@C_{60} in non-C6 adsorption orientations, the interaction between the endohedral fullerene and the surface is still stronger than that observed for C_{60}. As expected, this had the effect of segregating the Li@C_{60} from the C_{60} during the 320 K anneal. This is well illustrated because, upon further exploration of the surface, the vast majority of the isolated fullerenes are identified, using STS, as Li@C_{60}. Of

the C_{60} that are observed some are stabilised by pollution and others are the result of accidental surface modification (as seen in **Fig. 4.19**). Very few C_{60} are found natively stabilised on the terrace.

4.2.4 - Exploring the electronic states of fullerenes with c.c. *dI/dV* STM imaging

With the identity of the isolated fullerenes determined by spectroscopic methods, further exploration of the identity of the resonance peaks could be attempted using c.c. *dI/dV* STM imaging. Isolated fullerenes are not expected to exhibit the distorted molecular orbitals which were observed during the analysis of condensed fullerenes. Therefore, c.c. *dI/dV* STM imaging of isolated fullerenes is hoped to reveal the SAMO symmetries affording confirmation of the peak assignment made in **Fig. 4.13**. The analysis which follows discusses these peak identities tentatively due to the minor variation that is known to exist between the energies observed by c.c. *dI/dV* and c.h. *dI/dV* spectroscopic techniques (as detailed in **section 2.2.1**).

One attempt to capture single electronic states of isolated fullerenes by c.c. *dI/dV* STM imaging can be seen in **Fig. 4.21**. The c.c. *dI/dV* spectrum (**Fig. 4.21 (a)**) is of an isolated C_{60} on Au(111); the peak assignments match those suggested in **Fig. 4.13**. The c.c. *dI/dV* STM images (**Figs. 4.21 (b-e)**) illustrate attempts to capture single electronic states by imaging a bias range which straddles the corresponding resonance peaks. The bias ranges are indicated by the green stripes on the spectrum.

The c.c. *dI/dV* spectrum in **Fig. 4.21 (a)** illustrates the electronic structure of the selected C_{60} allowing for identification of the resonance peaks based on the assignment described in **section 4.1.4**. The four dominant peaks are labelled and correspond with the c.c. *dI/dV* STM images illustrated in **Figs. 4.21 (b-e)**. The LUMO+1 resonance peak is broader than the others in the spectrum so the bias range that is employed during the *dI/dV* imaging is also broader (500 mVpp). Since a correction factor is required to quantitatively compare between c.c. *dI/dV* spectra and the LDOS[38], the broad bias range is used in an attempt to ensure the capture of the LUMO+1 regardless of how divergent the electronic state is from the observed resonance peak. Inspection of the resultant c.c. *dI/dV* STM image (**Fig. 4.21 (b)**) does not allow identification of any structure that might be recognisable as the LUMO+1. For example, there are no segments which would be expected if C5-faces were in proximity to the apex of the molecule.

Figure 4.21: *a) c.c. dI/dV spectrum of an isolated C_{60} on Au(111). The green stripes indicate the range swept by the bias modulation for the corresponding c.c. dI/dV STM images. Each image captures a different resonance peak in an attempt to observe the symmetries of the electronic states: b) (+2.10 V, 0.1 nA, 500 mVpp at 1470 Hz), c) (+3.50 V, 0.1 nA, 300 mVpp at 1470 Hz), d) (+4.25 V, 0.1 nA, 300 mVpp at 1470 Hz), and e) (+4.65 V, 0.1 nA, 300 mVpp at 1470 Hz).*

A similar lack of meaningful structure is observed for the images of the LUMO+2/+3 (**Fig. 4.21 (c)**) and the LUMO+4 (**Fig. 4.21 (e)**). The only *dI/dV* image that exhibits any distinctive structure is **Fig. 4.21 (d)**, which corresponds with the peak ~+4.25 V and is expected to represent the *s*-SAMO. The internal structure of the molecular appearance could be identified as a LUMO+1 A for 6:6-C_{60} (rotated accordingly compared to **Fig. 4.14**). However, this is dubious and would disagree with the solid evidence previously discussed which identifies this resonance peak as that of the *s*-SAMO. In general, the c.c. *dI/dV* STM images cannot be deciphered for the C_{60} depicted above because the adsorption orientation of the fullerene is unknown. Unlike in the condensed phase (see **Fig. 4.18**), the adsorption orientation of isolated fullerenes cannot be determined by observing the molecular appearance at various imaging biases. More data would be required to provide further understanding of the behaviour of isolated C_{60} on the Au(111) under these conditions, but these are rare so repeat experiments are limited.

Due to the induced segregation of the fullerenes under the current preparation conditions, isolated Li@C_{60} are more numerous so repeated attempts are easier to achieve. **Fig. 4.22** illustrates the c.c. *dI/dV* spectrum of one such fullerene (**Fig. 4.22 (a)**)
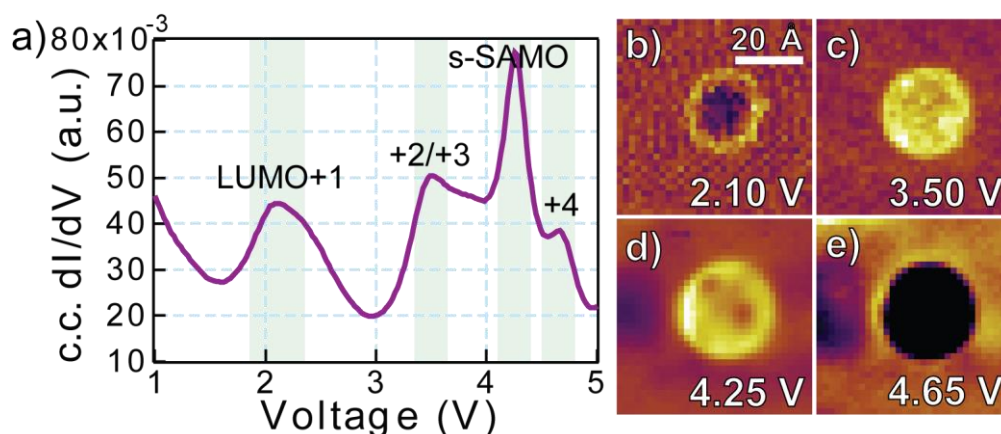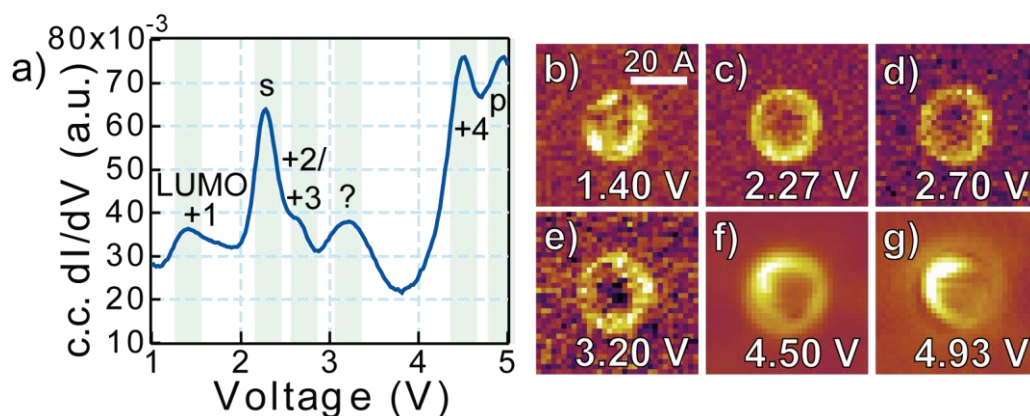
Figure 4.22: *(a) c.c. dI/dV spectrum of an isolated Li@C$_{60}$ on Au(111). The green stripes indicate the 300 mV range swept by the bias modulation for the corresponding c.c. dI/dV STM images. Each image is centred on a different resonance peak, but shares the following scanning parameters: 0.1 nA, 300 mVpp at 1470 Hz. The following indicates the scanning bias represented by each c.c. dI/dV STM image: (b) +1.40 V, (c) +2.27 V, (d) +2.70 V, (e) +3.20 V, (f) +4.50 V, and (g) +4.93 V.*

and the c.c. *dI/dV* STM images (**Figs. 4.22 (b-g)**) utilised to try to identify the spatial distribution of the electronic states.

Fig. 4.22 (a) shows the c.c. *dI/dV* spectrum of an isolated Li@C$_{60}$ on Au(111). By comparing with the spectra which are labelled in **Fig. 4.13**, some of the identities of the resonance peaks are proposed. The peak ~+3.2 V, however, remains a mystery since it does not have an equivalent in the condensed Li@C$_{60}$. The suggestion is that c.c. *dI/dV* STM imaging could reveal the shape of the corresponding electronic state, thus allowing for unambiguous identification.

Though internal structure is visible within the molecular appearance of **Fig. 4.22 (b)**, it does not resemble any adsorption orientation of either of the LUMO+1 symmetries (A or E). It cannot, therefore, be definitively identified. **Fig. 4.22 (c)** looks like a bright ring which is similar to the shape of the *s*-SAMO in **Fig. 4.14**. This could agree with the identification of the peak ~+2.2 V as the *s*-SAMO (as suggested in **section 4.1.4**), however, the subsequent images also resemble rings. These appearances induce an element of uncertainty in the identification of the *dI/dV* images. Though there may be some internal structure on the image at +3.20 V (**Fig. 4.22 (e)**, representing the unlabelled resonance

peak) it is not clear and cannot be further understood by comparing with the images from Reecht *et al.* (**Fig. 4.14**)[12].

The peak at ~+4.5 V in the spectrum is labelled LUMO+4 due to the minimal shift that is observed in the LUMOs despite Li-encapsulation. The corresponding c.c. *dI/dV* STM image (**Fig. 4.22 (f)**) instead appears like an asymmetric ring with very little internal structure which is inconsistent with what would be expected for a LUMO since these are centred on the atoms of carbon cage. Based on the *dI/dV* images in **Fig. 4.14** and the distortions expected in the *p*-SAMOs for Li@C_{60} (see **Fig. 4.12**), the shape in **Fig. 4.22 (f)** could be considered a distorted *p*-SAMO. With a non-C6 adsorption orientation one could expect the $p_{x,y}$-SAMOs to become non-degenerate for Li@C_{60} due to differing degrees of surface interaction. This would result in distinction between the p_x- and p_y-SAMOs. The magnitude of the peak ~+4.5 V in **Fig. 4.22 (a)** is more comparable to the *s*-SAMO than the LUMOs which could be further evidence towards this hypothesis. However, the final image (**Fig. 4.22 (g)**) also appears like an asymmetric ring with the same orientation despite expectations that it represents a different electronic state. Due to the uncertainty in the identification of the c.c. *dI/dV* STM images (**Figs. 4.22 (b-f)**), the accuracy of the labels attributed to each resonance peak is as uncertain as for the isolated C_{60} on Au(111).

Despite the high resolution of the spectra recorded for both condensed and isolated fullerenes on Au(111), the systematic difficulties with identifying the symmetries of the c.c. *dI/dV* STM images prevent any further conclusions to be drawn on the identities of the resonance peaks. The negligible population of isolated C_{60} on the Au(111) surface result in very few opportunities to explore a system that could easily be compared with literature. As a result, a different surface was selected and prepared in another attempt to create a sample which could be thoroughly identified.

4.3 - Identifying the electronic structures of Li@C_{60} and C_{60} on Cu(110)-(2×1)O after post-adsorption anneal at 320 K

Upon starting this project, the work of Reecht *et al.*[12] had yet to be published so the basis for comparison between literature and our studies was the 2008 paper from Feng *et al.* which detailed the seminal identification of SAMOs using c.c. *dI/dV* STM imaging[8]. With the lack of meaningful results on our Au(111) surfaces (as illustrated above) attempts

were made to replicate the work of Feng *et al*. on isolated fullerenes, hence the selection of the Cu(110)-(2×1)O surface.

This Cu(110) reconstruction is often used as an alternative to Au(111). Though copper is a more reactive transition metal than gold, the (2×1)O reconstruction resulting from saturated O_2 exposure at elevated temperatures is known to passivate the metal substrate. The fullerene deposition conditions also become important for maintaining this passivated surface since ordered 2D arrays of C_{60} are known to disrupt the (2×1) reconstruction, favouring adsorption directly to the Cu(110) surface beneath[4]. A surface of isolated fullerenes is therefore desired for two reasons: to avoid disruption of the reconstruction, and to reduce intermolecular interactions which may distort the SAMOs and reduce the effectiveness of c.c. *dI/dV* STM imaging. Similar to the Au(111) surface, the post-adsorption anneal is maintained at 320 K to achieve the desired surface. For more information on the preparation of the Cu(110)-(2×1)O surface see **section 3.2.1.2**.

Similar to **sections 4.1** and **4.2**, the discussion below will first identify the Li@C_{60} and C_{60} on the Cu(110)-(2×1)O substrate with scanning tunnelling microscopy and spectroscopy (**section 4.3.1**). The following section (**section 4.3.2**) will then explore the use of c.c. *dI/dV* STM imaging to identify the symmetries of the LUMOs and SAMOs and thus attempt to confirm the electronic structure of the fullerenes on this surface.

4.3.1 - Differentiating between isolated Li@C_{60} and C_{60} with STM and STS

The low temperature post-adsorption anneal (320 K) achieves a surface with many more isolated fullerenes on Cu(110)-(2×1)O than is exhibited for Au(111) (see **Fig. 4.23 (a)**). This implies that diffusion on the Cu substrate has a higher energy barrier than for the Au. This reduced diffusion could be because the Cu surface interacts more strongly with the fullerenes, a hypothesis that is easily tested since a greater stabilisation would be revealed by a more pronounced shift in the energies of the resonance peaks. Another effect that could reduce diffusion across the surface is linked to the (2×1) reconstruction. Some clustering of fullerenes is observed along the step edges in the {110} direction but almost no fullerenes are adsorbed to the step edges in the {001} direction. This suggests that the diffusion only occurs along the channels of the reconstruction in the {001} direction. This limited diffusion, constrained to only one dimension, may be another reason for the increased proportion of isolated fullerenes compared to the Au(111) surface.
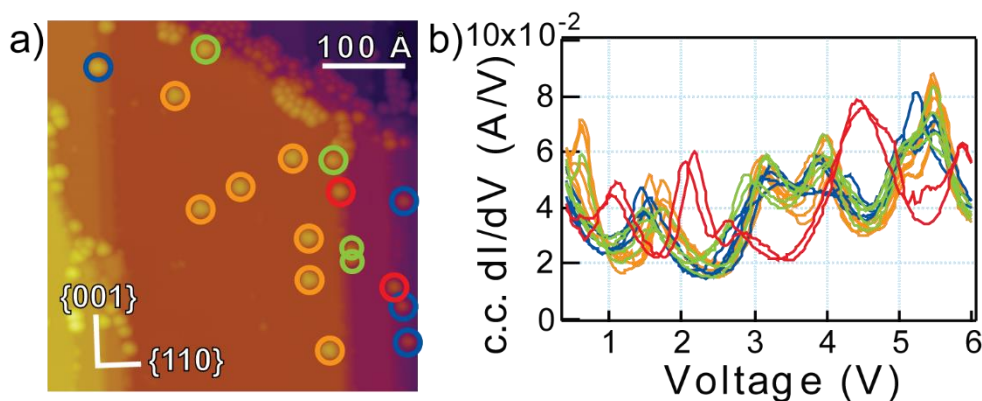
Figure 4.23: *a) STM image (+1.0 V, 0.1 nA) of C$_{60}$ and Li@C$_{60}$ on a Cu(110)-(2×1)O surface which underwent a post-adsorption anneal at 320 K. The red-ringed fullerenes are Li@C$_{60}$ and the orange, blue and green are C$_{60}$ with varying adsorption coordination sites. The c.c. dI/dV spectra in b) are colour-coded to match the fullerenes in a).*

A number of the fullerenes in the STM image below are highlighted by orange, green, red and blue rings. These are colour-coded based on their molecular configuration which is assigned using a mixture of STM and STS data (seen in **Figs. 4.23 (a)** and **(b)**, respectively). The green fullerenes are C$_{60}$ stabilised by neighbours, blue fullerenes are isolated C$_{60}$ on {001} step edges, orange fullerenes are C$_{60}$ on terraces, and red fullerenes are Li@C$_{60}$ (in this case these are also adsorbed to {001} step edges).

Differentiation between C$_{60}$ and Li@C$_{60}$ is only possible using spectroscopy. Much like the isolated fullerenes on Au(111), the bias dependence of the molecular appearance does not result in sufficient "brightening" of the Li@C$_{60}$ at +2.5 V to facilitate unambiguous identification. However, the red spectra are immediately recognised to be distinct from the others in **Fig. 4.23 (b)**. The similarity with the Li@C$_{60}$ spectra on Au(111), in particular the large peak ~+2 V, leads to the assignment of the red spectra to Li@C$_{60}$ on Cu(110)-(2×1)O. This confirms that the orange, blue and green spectra represent the electronic structures of C$_{60}$ adsorbed in the previously described coordination sites across the surface.

The general shape of the C$_{60}$ spectra in **Fig. 4.23 (b)** is consistent regardless of the specific adsorption configuration of C$_{60}$ but even within a single adsorption site the energies of specific resonance peaks vary more than what is observed on Au(111). For example, the

peaks ~+1.5 V in the orange spectra exhibit a variation of >0.2 V across the various spectra. The breadth of variation decreases a little as the energy of the resonance peak increases, possibly indicating that the SAMOs are less susceptible to the observed effect. Similar behaviour is identified for the different adsorption orientations on Au(111) so the same is expected in this case. This is not confirmed, however, because information regarding the orientation of the fullerenes is unreliable on isolated molecules when only examined with c.c. STM imaging. Given that this variation in resonance peak energies does not prevent differentiation between C_{60} and Li@C_{60}, and that analysis of the spectra is semi-quantitative, further exploration of its origin shall not be conducted.

The identification of the fullerenes on the Cu(110)-(2×1)O surface illustrates that the post-adsorption anneal has not segregated the Li@C_{60} from the C_{60} as is observed on the Au(111). Combining this with the Li@C_{60}:C_{60} ratio of ~1:10 makes it much more time-consuming to collect a large amount of data on Li@C_{60}. The quantity of data collected, therefore, is only sufficient to ensure reproducibility of results. The exploration of this substrate is for comparison with two sources. Initially with the work of Feng et al.[8] And secondly with the data from Au(111) in order to unambiguously confirm the identity of the resonance peaks by observing the shapes of the electronic states using c.c. dI/dV STM imaging.

4.3.2 - Exploring the electronic states of fullerenes with c.c. *dI/dV* STM imaging

Similar to the examples above, when studying the electronic states of fullerenes on Au(111), the isolated fullerenes are first selected and identified by STS to determine the presence of endohedral Li. The intention of this section is to improve upon the c.c. dI/dV STM imaging achieved on the Au(111) surfaces (**sections 4.1.5** and **4.2.4**) and definitively identify the electronic structures of C_{60} and Li@C_{60} by observing the symmetries of the LUMOs and SAMOs. Upon identification of the electronic structure the effect of the Li-encapsulation can then be directly observed. **Fig. 4.24** illustrates the c.c. dI/dV spectrum (**Fig. 4.24 (a)**) and corresponding c.c. dI/dV STM images (**Figs. 4.24 (b-f)**) of one such C_{60}.

The resonance peaks in the spectrum in **Fig. 4.24 (a)** are labelled using a combination of two data sources. The general peak distribution for C_{60} on Au(111) (discussed in **section 4.1.4**), and also the appearance of the corresponding *dI/dV* images (**Figs. 4.24 (b-f)**)
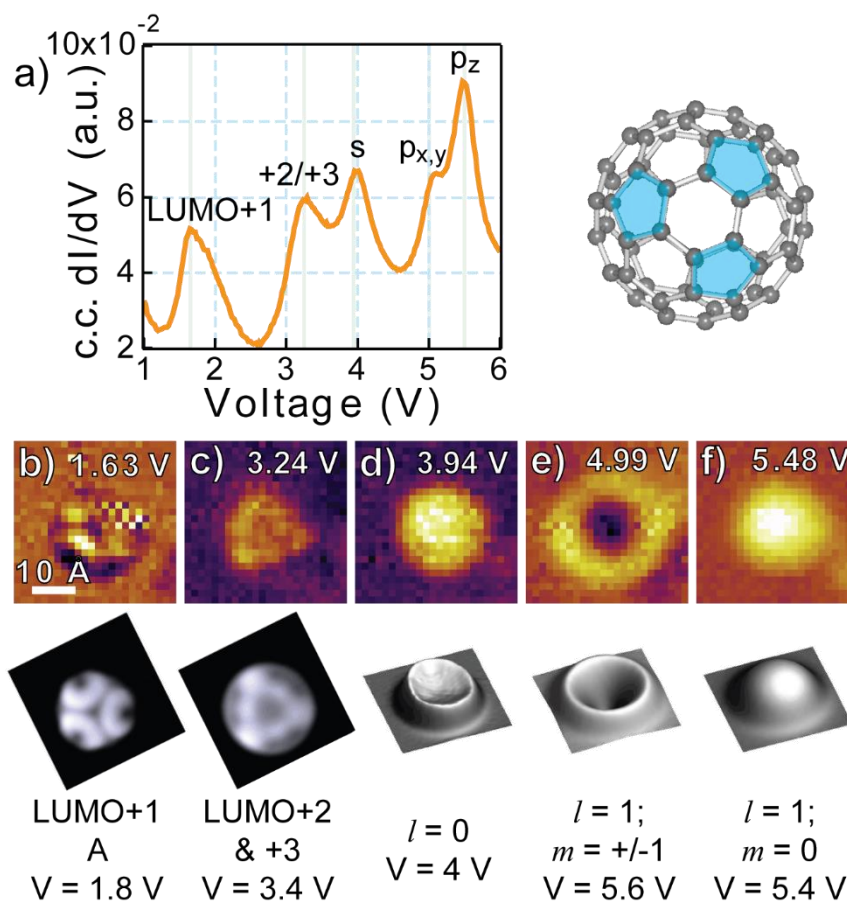
Figure 4.24: *a) c.c. dI/dV spectrum of an isolated C6-C60 on Cu(110)-(2×1)O and model of the adsorption orientation of the C_{60}. The thin green stripes on the spectrum indicate the 20 mV range swept by the bias modulation for the corresponding c.c. dI/dV STM images. Each dI/dV image represents a different resonance peak, in an attempt to illustrate the spatial distribution of the corresponding electronic state. However, the images do share the following scan parameters: 0.1 nA, 20 mVpp at 320 Hz. The images were recorded at the following scanning biases: **b)** +1.63 V, **c)** +3.24 V, **d)** +3.94 V, **e)** +4.99 V, and **f)** +5.48 V. The simulated STM images are repeated from Fig. 4.14, these have been adapted from Reecht et al.[12].*

compared to those from Reecht *et al.*[12] (exhibited in **Fig. 4.14**). **Fig. 4.24 (b)** is recognised as the LUMO+1 A which reveals that the fullerene has adopted the C6-C_{60} adsorption orientation. This symmetry enables more direct comparison between the other *dI/dV* images in **Fig. 4.24** and the images in **Fig. 4.14** since these also represent the appearance of the electronic states for a C6-C_{60}.

Fig. 4.24 (c) closely resembles the c.c. *dI/dV* STM image for the LUMO+2/+3 in **Fig. 4.14** and the energy of the corresponding resonance peak (~+3.2 V) matches where one would expect it based on the electronic structure of the C_{60} on Au(111) (**Fig. 4.13 (c)**). The subsequent peak, and relevant image, are in very slight disagreement with the published results[12]. The energy of the peak is suitably similar (~+4 V) to the observations of Reecht *et al.*. However, where they observe a concave portion of the *dI/dV* image, the fullerene in **Fig. 4.24 (d)** retains its convex appearance. This hemispherical shape is closer to what is expected of the *s*-SAMO, and since the energy of the peak appears consistent with calculations, the molecular appearance and peak are confidently labelled as the *s*-SAMO of the C_{60} on Cu(110)-(2×1)O. Difficulties arise when attempting to identify the higher energy electronic states which combine to form the broad resonance with peaks around +5 V and +5.5 V.

The large ring which encircles a hollow in **Fig. 4.24 (e)** closely resembles the observed shape of the $p_{x,y}$-SAMOs in **Fig. 4.14**. The energy at which it is seen, however, is 0.6 V lower than that reported and falls at a lower energy than the resonance peak which is convincingly identified as coinciding with the p_z-SAMO. The peak at ~+5.5 V matches the literature value for the p_z-SAMO, and the large hemispherical shape (see **Fig. 4.24 (f)**) strongly resembles the spatial distribution of it in **Fig. 4.14**. The p_z-SAMO of a C6-C_{60} is known to be orthogonal to the substrate and is therefore expected to exhibit greater interaction (thus stabilisation) than the $p_{x,y}$-SAMOs. This is opposite to what is observed. The extra stabilisation of the $p_{x,y}$-SAMOs could be due to the rectangular shape of the surface promoting lateral stabilisation over orthogonal stabilisation. However, this cannot be rationalised with the little information provided by the spectrum and images, thus is not considered sufficient evidence to alter the assignment of the peaks for C_{60} on Au(111) from what is discussed in **section 4.1.4**.

With the partial recognition of the electronic states for C_{60} on Cu(110)-(2×1)O, the next step is to consider the electronic structure for the Li@C_{60}. **Fig. 4.25** depicts a data set composed of a c.c. *dI/dV* spectrum (**Fig. 4.25 (a)**) and c.c. *dI/dV* STM images (**Figs. 4.25 (c-g)**) which correspond with the resonance peaks indicated by the thin green stripes. **Fig. 4.25 (b)** illustrates the suggested adsorption orientation of the 6:6-Li@C_{60}, the C6-face to which the Li is thought to be coordinated is highlighted in pink.
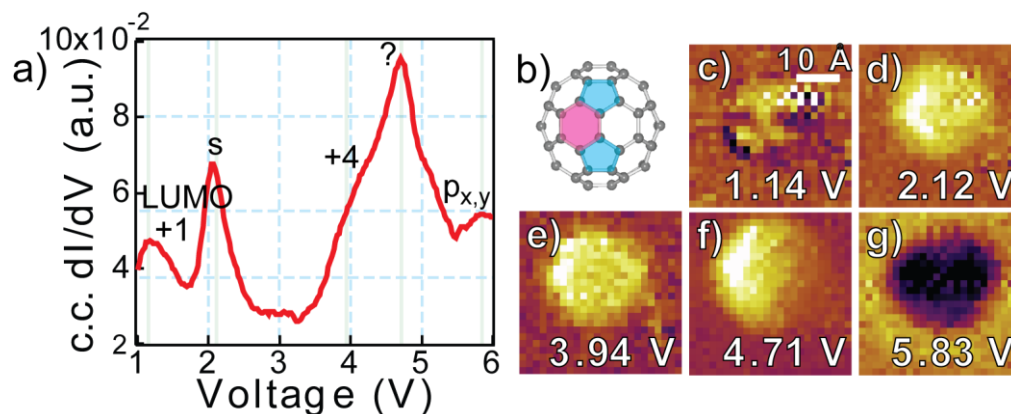
Figure 4.25: *a) c.c. dI/dV spectrum of an isolated Li@C₆₀ on Cu(110)-(2×1)O. The thin green stripes indicate the 20 mV range swept by the bias modulation for the corresponding c.c. dI/dV STM images. b) Ball and stick model indicating the proposed adsorption orientation of the fullerene (6:6-Li@C₆₀). The pink C6-face indicates the one to which the Li is thought to be coordinated. The c.c. dI/dV STM images (c-g) share the following scan parameters: 0.1 nA, 20 mVpp at 320 Hz, but illustrate different scanning biases: c) +1.14 V, d) +2.12 V, e) +3.94 V, f) +4.71 V, g) +5.83 V.*

The peaks in the c.c. *dI/dV* spectrum in **Fig. 4.25 (a)** are less defined than for the Li@C₆₀ on Au(111) (**Fig. 4.13 (d)**). This broadening of the signal is thought to result from coalescence of the resonance peaks due to the non-C6 adsorption orientation of the fullerene. In the case of this data set, the *dI/dV* image at +1.14 V (**Fig. 4.25 (c)**) resembles the LUMO+1 A (see **Fig. 4.14**) with a slight rotation leading to the identification of it as a 6:6-Li@C₆₀ (**Fig. 4.25 (b)**). By acquiring the *dI/dV* image of the LUMO+1, isolated Li@C₆₀ on Cu(110)-(2×1)O are observed adopting more varied orientations than what is observed in the large 2D arrays of the Au(111) surface.

Fig. 4.25 (d) corresponds with the resonance peak that has been confidently assigned to the *s*-SAMO using DFT, STM, STS and PES. However, the c.c. *dI/dV* STM image of the electronic state exhibits internal structure similar to that seen in the LUMO+1 E whilst simultaneously appearing brighter and slightly diffuse. This echoes what was observed in **Fig. 4.15 (b)** for the Li@C₆₀ in the 2D array.

The c.c. *dI/dV* STM image of the shoulder labelled LUMO+4 is similarly non-specific (see **Fig. 4.25 (e)**). The asymmetric brightness in the molecular appearance approximately

coincides with a C6-face, as identified by comparison of **Figs. 4.25 (b)** and **(c)**. This brightness in the *dI/dV* image could suggest that the Li is coordinated to this C6-face (coloured pink in **Fig. 4.25 (b)**) and that there is a minor variation in the LUMO+4 as a result of the Li. However, since there is no distinctive internal structure, this is not a strong argument for justifying the resonance peak assignment. The asymmetry seen in the brightness of the molecular appearance becomes more distinct at +4.71 V (**Fig. 4.25 (f)**) and, since it appears to be aligned with the C6-face proposed to be the location of the Li, this *dI/dV* image could be suggested to represent the p_z-SAMO. However, this bias is much greater than the ~+1 V identified by the PES data as the energy of the Li-stabilised p_z-SAMO. As such, the identity of this resonance peak remains uncertain.

Rotation of the fullerene from a C6-adsorption orientation could be expected to cause a loss of degeneracy in the $p_{x,y}$-SAMOs, since tilting of the *x/y*-plane of the fullerene would result in alterations in the surface overlap, but this is not observed in the *dI/dV* images. Instead the final image in the data set (**Fig. 4.25 (g)**) appears loosely like a bright ring encapsulating a concave region which is suggestive of the $p_{x,y}$-SAMO observed in **Fig. 4.14**. This bright ring, however, is more diffuse and less distinct than that exhibited by C_{60} (**Fig. 4.24 (e)**) and is observed at a higher energy. Since Li-encapsulation is known to stabilise the SAMOs of a C_{60}, this could suggest that *dI/dV* image has captured a *d*-SAMO instead. This would explain the increased diffusivity of the *dI/dV* image but would require strong stabilisation to bring the *d*-SAMO low enough in energy to be observable within the range of the spectrum. This contradicts the proposed reduction in stabilisation which is resultant from the non-C6 adsorption orientation.

The lack of clarity within the c.c. *dI/dV* STM images has not afforded the detailed evidence required to agree with, or refute, the peak assignment previously described (see **section 4.1.4**). This appears to result from the convolution of the LUMOs and SAMOs complicating the *dI/dV* images. With further study this may be resolved, but it is suspected to be a pervasive issue for Li@C_{60}. The strong hybridisation between the encapsulated Li and the C_{60} orbitals, and the variable surface interaction (linked to the adsorption orientation), are expected to affect the c.c. *dI/dV* STM imaging technique regardless of the surface or parameters utilised.

4.4 - Concluding Remarks

In this chapter, the general behaviour of surface-bound Li@C_{60} and C_{60} have been identified for different preparation conditions of both the Au(111) and Cu(110)-(2×1)O surfaces using scanning tunnelling microscopy (STM). Constant current differential conductance scanning tunnelling spectroscopy (c.c. *dI/dV* STS) was employed to determine the effect of both the Li-encapsulation and the adsorption configuration on the energies of the electronic states for C_{60}. By combining these techniques differential conductance scanning tunnelling microscopy (c.c. *dI/dV* STM) was utilised in an attempt to discern the spatial distribution of the electronic states. This was anticipated to provide evidence to unambiguously determine the energies of the electronic states for both C_{60} and Li@C_{60}.

On Au(111), at higher post-adsorption anneal temperatures (~570 K), the C_{60} and Li@C_{60} are observed forming large 2D arrays of mixed composition and are all considered to have adsorbed to the hcp surface site. All of the Li@C_{60} preferentially adopt the C6-fullerene adsorption orientation with two azimuthal orientations, and the C_{60} exhibits three adsorption orientations (C6-C_{60}, C-C_{60} and 6:6-C_{60}) which also express azimuthal preferences. The Li@C_{60} is observed with much stronger coupling to the Au(111) substrate than C_{60}. This is suggested by its sole adsorption orientation and proven by the stabilisation seen in the correlated resonance peaks in the c.c. *dI/dV* spectra.

By lowering the post-adsorption anneal temperature (320 K), some segregation of the fullerenes is observed. Li@C_{60} is capable of stabilising isolated from other species on Au(111) terraces, whereas C_{60} almost solely condenses into highly ordered, often elongated, 2D arrays. The isolated Li@C_{60} exhibit reduced stabilisation of the higher energy SAMOs, as is deduced from the spectra above (see **Fig. 4.20**). This indicates that the diffuse nature of the SAMOs results in hybridisation between neighbouring fullerenes in the condensed arrays which, in turn, stabilises the SAMOs further. The c.c. *dI/dV* STM imaging attempted on both the condensed and isolated fullerenes on Au(111) failed to resolve the SAMOs as intended so further proof of the peak assignment was not forthcoming. Since the initial literature which our analysis was hoping to emphasise was conducted on the Cu(110)-(2×1)O surface[8], another sample was prepared.
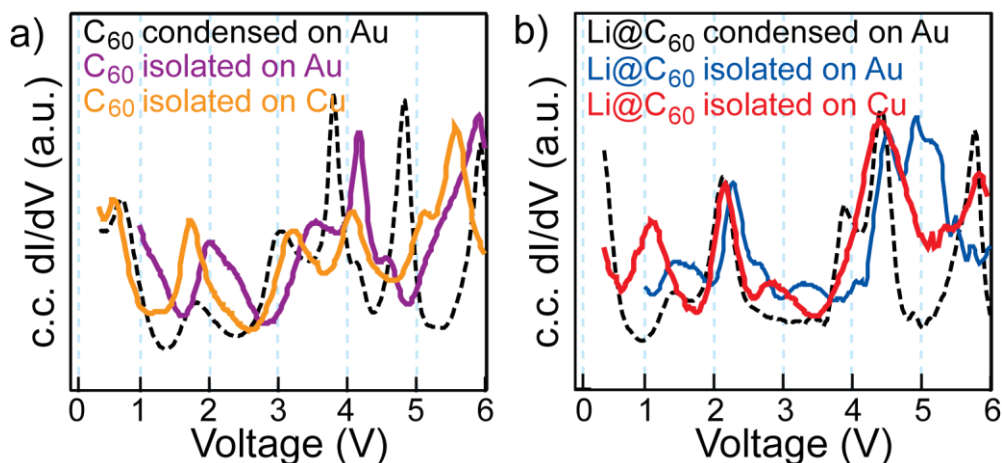
Figure 4.26: *Compilations of c.c. dI/dV spectra of both **a)** C_{60} and **b)** Li@C$_{60}$ on the Cu(110)-(2×1)O and Au(111) surfaces. The black dashed lines in each graph are the same spectra as **Fig. 4.13 (c)** and **(d)**. The isolated C_{60} on Au(111) (purple) is the same as **Fig. 4.20 (a)**, and the isolated Li@C$_{60}$ on Au(111) (dark blue) is from **Fig. 4.20 (b)**. The spectra on Cu(110)-(2×1)O also maintain their colour from **Fig. 4.23 (b)**.*

Upon studying the fullerenes on the Cu(110)-(2×1)O surface, however, it became apparent that there was more stabilisation afforded to the molecules than on the Au(111). **Fig. 4.26** compiles the c.c. *dI/dV* spectra from both molecular systems on Au(111) and the isolated fullerenes on Cu(110)-(2×1)O. This allows direct comparisons to be drawn and conclusions proposed to explain the differing behaviours of each molecule for each surface (**Fig. 4.26 (a)** for C_{60} and **Fig. 4.26 (b)** for Li@C$_{60}$). In both cases, however, the c.c. *dI/dV* STM imaging only revealed useful information regarding the LUMOs of the fullerenes. The stabilisation effect of the Li-encapsulation on the energies of the SAMOs, therefore, remains unconfirmed but parallels between the spectra can allow some hypotheses to be discussed.

For isolated C_{60} (purple and orange spectra in **Fig. 4.26 (a)**) the stabilisation gained by adsorption to the Cu(110)-(2×1)O substrate rather than Au shows a consistent reduction in each of the resonance peak energies of ≤~0.25 V. In the case of the LUMO and LUMO+1 this results in them bearing a much stronger resemblance to the condensed C_{60} on Au(111) (black dashed line in **Fig. 4.26 (a)**). However for the higher energy peaks, especially the $p_{x,y}$-SAMOs, the stabilisation is minimal and these are much more similar to

the peaks in the spectrum of the isolated C_{60} on Au(111). This stabilisation could be a result of a more favourable adsorption orientation of the fullerene on Cu, but an argument could also be made for it exhibiting increased coupling with the substrate. This increased coupling would substantiate the hypothesis that was proposed due to the reduced diffusion seen across the Cu(110)-(2×1)O. However, further experimentation and DFT calculations are required before anything can be stated with more conviction.

The graph compiling Li@C_{60} in various molecular configurations (**Fig. 4.26 (b)**) is more evidence for the suggestion of increased surface interaction on the Cu(110)-(2×1)O substrate. The resonance peak structure is more similar to the condensed Li@C_{60} on Au(111) than that of the isolated fullerene. In some cases the stabilisation is even stronger for the Cu(110)-(2×1)O sample than for the condensed fullerenes (see the red peak ~+1 V in **Fig. 4.26 (b)**). In all cases, except for the *s*-SAMO (~+2 V), the peaks in the spectrum from the isolated Li@C_{60} on Cu(110)-(2×1)O are stabilised by ~0.5 V when compared to those of the isolated Li@C_{60} on Au(111). Why this stabilisation appears not to affect the *s*-SAMO is a little perplexing, but its similarity with the other two *s*-SAMOs featured in **Fig. 4.26 (b)** could simply mean the adsorption orientation is the same. The only example of a shift in this peak (seen in **Fig. 4.20 (b)**) is as a result of the non-C6 adsorption orientation of Li@C_{60} (observed in **Fig. 4.19**). This behaviour of the *s*-SAMO will be explored further during **Chapter 5** when the Li@C_{60} is explored for potential use as a molecular switch.

4.5 - <u>References</u>

(1)   Gardener, J. A.; Briggs, G. A. D.; Castell, M. R. Scanning Tunnelling Microscopy Studies of C60 Monolayers on Au(111). *Phys. Rev. B - Condens. Matter Mater. Phys.* **2009**, *80* (23), 235434. https://doi.org/10.1103/PhysRevB.80.235434.

(2)   Schull, G.; Néel, N.; Becker, M.; Kröger, J.; Berndt, R. Spatially Resolved Conductance of Oriented C60. *New J. Phys.* **2008**, *10* (6), 065012. https://doi.org/10.1088/1367-2630/10/6/065012.

(3)   Sakurai, T.; Wang, X.-D.; Xue, Q. K.; Hasegawa, Y.; Hashizume, T.; Shinohara, H. Scanning Microscopy of Fullerenes Study. *Prog. Surf. Sci.* **1996**, *51* (4), 263–408.

(4)   Pedersen, M. O.; Murray, P. W.; Laegsgaard, E.; Stensgaard, I.; Besenbacher, F. Carbon-60 Induced Structures on the Clean and Oxygen Covered Cu(110) Surface: Competitive Adsorption. *Surf. Sci.* **1997**, *389*, 300–309.

(5)   Rogero, C.; Pascual, J. I.; Gómez-Herrero, J.; Baró, A. M. Resolution of Site-Specific Bonding Properties of C60 Adsorbed on Au(111). *J. Chem. Phys.* **2002**, *116*, 832–836. https://doi.org/10.1063/1.1424291.

(6)   Abel, M.; Dmitriev, A.; Fasel, R.; Lin, N.; Barth, J. V; Kern, K. Scanning Tunneling Microscopy and X-Ray Photoelectron Diffraction Investigation of C60 Films on Cu(100). *Phys. Rev. B* **2003**, *67*, 245407. https://doi.org/10.1103/PhysRevB.67.245407.

(7)   Lu, X.; Grobis, M.; Khoo, K. H.; Louie, S. G.; Crommie, M. F. Charge Transfer and Screening in Individual C60 Molecules on Metal Substrates: A Scanning Tunneling Spectroscopy and Theoretical Study. *Phys. Rev. B* **2004**, *70* (11), 115418. https://doi.org/10.1103/PhysRevB.70.115418.

(8)   Feng, M.; Zhao, J.; Petek, H. Atomlike, Hollow-Core–Bound Molecular Orbitals of C60. *Science (80-.).* **2008**, *320*, 359–362. https://doi.org/10.1126/science.1155866.

(9)   Larsson, J. A.; Elliott, S. D.; Greer, J. C.; Repp, J.; Meyer, G.; Allenspach, R. Orientation of Individual C60 Molecules Adsorbed on Cu(111): Low-Temperature Scanning Tunneling Microscopy and Density Functional Calculations. *Phys. Rev. B - Condens. Matter Mater. Phys.* **2008**, *77* (11), 115434. https://doi.org/10.1103/PhysRevB.77.115434.

(10)   Tang, L.; Zhang, X.; Guo, Q.; Wu, Y.-N.; Wang, L.-L.; Cheng, H.-P. Two Bonding Configurations for Individually Adsorbed C60 Molecules on Au(111). *Phys. Rev. B - Condens. Matter Mater. Phys.* **2010**, *82* (12), 125414. https://doi.org/10.1103/PhysRevB.82.125414.

(11)   Dutton, G. J.; Dougherty, D. B.; Jin, W.; Reutt-Robey, J. E.; Robey, S. W. Superatom Orbitals of C60 on Ag(111): Two-Photon Photoemission and Scanning Tunneling Spectroscopy. *Phys. Rev. B - Condens. Matter Mater. Phys.* **2011**, *84* (19), 195435. https://doi.org/10.1103/PhysRevB.84.195435.

(12)   Reecht, G.; Heinrich, B. W.; Bulou, H.; Scheurer, F.; Limot, L.; Schull, G. Imaging Isodensity Contours of Molecular States with STM. *New J. Phys.* **2017**, *19* (11), 113033. https://doi.org/10.1088/1367-2630/aa969a.

(13)   Shin, H.; Schwarze, A.; Diehl, R. D.; Pussi, K.; Colombier, A.; Gaudry, E.; Ledieu, J.; McGuirk, G. M.; Serkovic Loli, L. N.; Fournée, V.; Wang, L. L.; Schull, G.; Berndt, R. Structure and Dynamics of C60 Molecules on Au(111). *Phys. Rev. B - Condens. Matter Mater. Phys.* **2014**, *89* (24), 245428. https://doi.org/10.1103/PhysRevB.89.245428.

(14)   Lu, X.; Grobis, M.; Khoo, K. H.; Louie, S. G.; Crommie, M. F. Spatially Mapping the Spectral Density of a Single C60 Molecule. *Phys. Rev. Lett.* **2003**, *90* (9), 096802. https://doi.org/10.1103/PhysRevLett.90.096802.

(15)   Wang, H.; Zeng, C.; Wang, B.; Hou, J. G.; Li, Q.; Yang, J. Orientational Configurations of the C60 Molecules in the (2×2) Superlattice on a Solid C60(111) Surface at Low Temperature. *Phys. Rev. B - Condens. Matter Mater. Phys.* **2001**, *63* (8), 085417. https://doi.org/10.1103/PhysRevB.63.085417.

(16)   Hashizume, T.; Motai, K.; Wang, X. D.; Shinohara, H.; Saito, Y.; Maruyama, Y.; Ohno, K.; Kawazoe, Y.; Nishina, Y.; Pickering, H. W.; Kuk, Y.; Sakurai, T. Intramolecular Structures of C60 Molecules Adsorbed on the Cu(111)-(1×1) Surface. *Phys. Rev. Lett.* **1993**, *71* (18), 2959–2962. https://doi.org/10.1103/PhysRevLett.71.2959.

(17)   Tang, L.; Xie, Y.; Guo, Q. Complex Orientational Ordering of C60 Molecules on Au(111). *J. Chem. Phys.* **2011**, *135* (11). https://doi.org/10.1063/1.3639106.

(18)   Paßens, M.; Karthäuser, S. Interfacial and Intermolecular Interactions Determining the Rotational Orientation of C60 Adsorbed on Au(111). *Surf. Sci.* **2015**, *642*, 11–15. https://doi.org/10.1016/j.susc.2015.07.025.

(19)   Altman, E. I.; Colton, R. J. Determination of the Orientation of C60 Adsorbed on Au(111) and Ag(111). *Phys. Rev. B* **1993**, *48* (24), 18244.

https://doi.org/10.1103/PhysRevB.48.18244.

(20)   Wilson, R. J.; Meijer, G.; Bethune, D. S.; Johnson, R. D.; Chambliss, D. D.; de Vries, M. S.;
        Hunziker, H. E.; Wendt, H. R. Imaging C60 Clusters on a Surface Using a Scanning
        Tunnelling Microscope. *Nature*. 1990, pp 621–622. https://doi.org/10.1038/348621a0.

(21)   Altman, E. I.; Colton, R. J. Nucleation, Growth, and Structure of Fullerene Films on
        Au(111). *Surf. Sci.* **1992**, *279* (1–2), 49–67. https://doi.org/10.1016/0039-6028(92)90741-
        N.

(22)   Zhang, Y.; Gao, X.; Weaver, M. J. Scanning Tunneling Microscopy of Carbon Molecule (C60
        and C70) on Ordered Gold (111) and Gold (110): Molecular Structure and Electron
        Transmission. *J. Phys. Chem.* **1992**, *96* (2), 510–513.
        https://doi.org/10.1021/j100181a003.

(23)   Fujita, D.; Yakabe, T.; Nejoh, H.; Sato, T.; Iwatsuki, M. Scanning Tunneling Microscopy
        Study on the Initial Adsorption Behavior of C60 Molecules on a Reconstructed Au(111)-
        (23 × √3) Surface at Various Temperatures. *Surf. Sci.* **1996**, *366* (1), 93–98.
        https://doi.org/10.1016/0039-6028(96)00786-8.

(24)   Yamada, Y.; Kuklin, A. V.; Sato, S.; Esaka, F.; Sumi, N.; Zhang, C.; Sasaki, M.; Kwon, E.;
        Kasama, Y.; Avramov, P. V.; Sakai, S. Electronic Structure of Li+@C60: Photoelectron
        Spectroscopy of the Li+@C60[PF6−] Salt and STM of the Single Li+@C60 Molecules on
        Cu(111). *Carbon N. Y.* **2018**, *133* (111), 23–30.
        https://doi.org/10.1016/j.carbon.2018.02.106.

(25)   Kroto, H. W.; Heath, J. R.; O'Brien, S. C.; Curl, R. F.; Smalley, R. E. C60:
        Buckminsterfullerene. *Nature* **1985**, *318*, 162–163. https://doi.org/10.1038/318162a0.

(26)   Wang, L. L.; Cheng, H. P. Density Functional Study of the Adsorption of a C60 Monolayer
        on Ag(111) and Au(111) Surfaces. *Phys. Rev. B - Condens. Matter Mater. Phys.* **2004**, *69*
        (16), 165417. https://doi.org/10.1103/PhysRevB.69.165417.

(27)   Wang, L. L.; Cheng, H. P. Erratum: Density Functional Study of the Adsorption of a C60
        Monolayer on Ag(111) and Au(111) Surfaces (Physical Review B - Condensed Matter and
        Materials Physics (2004) 69 (165417)). *Phys. Rev. B - Condens. Matter Mater. Phys.* **2007**,
        75 (11), 165417. https://doi.org/10.1103/PhysRevB.75.119901.

(28)   Stefanou, M.; Chandler, H. J.; Mignolet, B.; Williams, E.; Nanoh, S. A.; Thompson, J. O. F.;
        Remacle, F.; Schaub, R.; Campbell, E. E. B. Angle-Resolved Photoelectron Spectroscopy
        and Scanning Tunnelling Spectroscopy Studies of the Endohedral Fullerene Li@C60.
        Nanoscale **2019**, *11*, 2668–2678. https://doi.org/10.1039/c8nr07088a.

(29)   Gromov, A.; Krawez, N.; Lassesson, A.; Ostrovskii, D. I.; Campbell, E. E. B. Optical
        Properties of Endohedral Li@C60. *Curr. Appl. Phys.* **2002**, *2* (1), 51–55.
        https://doi.org/10.1016/S1567-1739(01)00101-8.

(30)   Gromov, A.; Ostrovskii, D.; Lassesson, A.; Jönsson, M.; Campbell, E. E. B. Fourier
        Transform Infrared and Raman Spectroscopic Study of Chromatographically Isolated
        Li@C60 and Li@C70. *J. Phys. Chem. B* **2003**, *107* (41), 11290–11301.
        https://doi.org/10.1021/jp030403w.

(31)   Ueno, H.; Aoyagi, S.; Yamazaki, Y.; Ohkubo, K.; Ikuma, N.; Okada, H.; Kato, T.; Matsuo, Y.;
        Fukuzumi, S.; Kokubo, K. Electrochemical Reduction of Cationic Li+@C60 to Neutral
        Li+@C60˙−: Isolation and Characterisation of Endohedral [60]Fulleride. *Chem. Sci.* **2016**, *7*
        (9), 5770–5774. https://doi.org/10.1039/C6SC01209D.

(32)   Zhao, P.; Liu, D. S.; Zhang, Y.; Su, Y.; Liu, H. Y.; Li, S. J.; Chen, G. Large Low Bias Negative
        Differential Resistance in an Endohedral Li@C60 Dimer Junction. *J. Phys. Chem. C* **2012**,

116 (14), 7968–7974. https://doi.org/10.1021/jp210880j.

(33)   Kusch, C.; Krawez, N.; Tellgmann, R.; Winter, B.; Campbell, E. E. B. Thermal Desorption Spectroscopy of Fullerene Films Containing Endohedral Li@C60. *Appl. Phys. A Mater. Sci. Process.* **1998**, *66* (3), 293–298. https://doi.org/10.1007/s003390050669.

(34)   Villagómez, C. J.; Garzón, I. L.; Paz-Borbón, L. O. A First-Principles DFT Dispersion-Corrected C60/Au(111) Raman Study. *Comput. Mater. Sci.* **2020**, *171* (August 2019), 109208. https://doi.org/10.1016/j.commatsci.2019.109208.

(35)   Stroscio, J. A.; Feenstra, R. M.; Fein, A. P. Electronic Structure of the Si(111) 2x1 Surface by Scanning-Tunneling Microscopy. *Phys. Rev. Lett.* **1986**, *57* (20), 2579–2582. https://doi.org/10.1103/PhysRevLett.57.2579.

(36)   Lang, N. D. Spectroscopy of Single Atoms in the Scanning Tunneling Microscope. *Phys. Rev. B* **1986**, *34* (8), 5947–5950. https://doi.org/10.1103/PhysRevB.34.5947.

(37)   Tersoff, J.; Hamann, D. R. Theory of the Scanning Tunneling Microscope. *Phys. Rev. B* **1985**, *31* (2), 805–813.

(38)   Ziegler, M.; Néel, N.; Sperl, A.; Kröger, J.; Berndt, R. Local Density of States from Constant-Current Tunneling Spectra. *Phys. Rev. B - Condens. Matter Mater. Phys.* **2009**, *80* (12), 125402. https://doi.org/10.1103/PhysRevB.80.125402.

(39)   Daughton, D. R.; Gupta, J. A. Orientation Dependence of Charge Transfer for C60 on Cu(100). *Appl. Phys. Lett.* **2011**, *98* (13), 133303. https://doi.org/10.1063/1.3569719.

(40)   Bakowies, D.; Thiel, W. MNDO Study of Large Carbon Clusters. *J. Am. Chem. Soc.* **1991**, *113* (10), 3704–3714. https://doi.org/10.1021/ja00010a012.

(41)   Srivastava, A. K.; Kumar, A.; Misra, N. Structure and Properties of Li@C60–PF6endofullerene Complex. *Phys. E Low-Dimensional Syst. Nanostructures* **2016**, *84*, 524–529. https://doi.org/10.1016/j.physe.2016.06.021.

(42)   Dunlap, B. I.; Ballester, J. L.; Schmidt, P. P. Interaction between C60 and Endohedral Alkali Atoms. *J. Phys. Chem.* **1992**, *96* (23), 9781–9787. https://doi.org/10.1021/j100203a038.

(43)   Andreoni, W.; Curioni, A. Ab Initio Approach to the Structure and Dynamics of Metallofullerenes. *Appl. Phys. A Mater. Sci. Process.* **1998**, *66* (3), 299–306. https://doi.org/10.1007/s003390050670.

(44)   Aree, T.; Kerdcharoen, T.; Hannongbua, S. Charge Transfer, Polarizability and Stability of Li–C60 Complexes. *Chem. Phys. Lett.* **1998**, *285* (3), 221–225. https://doi.org/10.1016/S0009-2614(98)00031-1.

(45)   Campbell, E. E. B.; Fanti, M.; Hertel, I. V.; Mitzner, R.; Zerbetto, F. The Hyperpolarisability of an Endohedral Fullerene: Li@C60. *Chem. Phys. Lett.* **1998**, *288* (1), 131–137. https://doi.org/10.1016/S0009-2614(98)00255-3.

(46)   Bernshtein, V.; Oref, I. Surface Migrations of Endohedral Li+ on the Inner Wall of C60. *Phys. Rev. A* **2000**, *62* (February), 033201. https://doi.org/10.1103/PhysRevA.62.033201.

(47)   Varganov, S. A.; Avramov, P. V; Ovchinnikov, S. G. Ab Initio Calculations of Endo- and Exohedral C60 Fullerene Complexes with Li+ Ion and the Endohedral C60 Fullerene Complex with Li2 Dimer. *Phys. Solid State* **2000**, *42* (2), 388–392. https://doi.org/10.1134/1.1131218.

(48)   Zhang, M.; Harding, L. B.; Gray, S. K.; Rice, S. A. Quantum States of the Endohedral Fullerene Li@C60. *J. Phys. Chem. A* **2008**, *112*, 5478–5485. https://doi.org/10.1021/jp801083m.

(49)   Jorn, R.; Zhao, J.; Petek, H.; Seideman, T. Current-Driven Dynamics in Molecular Junctions: Endohedral Fullerenes. *ACS Nano* **2011**, *5* (10), 7858–7865. https://doi.org/10.1021/nn202589p.

(50)   Aoyagi, S.; Sado, Y.; Nishibori, E.; Sawa, H.; Okada, H.; Tobita, H.; Kasama, Y.; Kitaura, R.; Shinohara, H. Rock-Salt-Type Crystal of Thermally Contracted C60 with Encapsulated Lithium Cation. *Angew. Chemie - Int. Ed.* **2012**, *51* (14), 3377–3381. https://doi.org/10.1002/anie.201108551.

(51)   Hernández-Rojas, J.; Bretón, J.; Gomez Llorente, J. M. Rotational Spectra for Off-Center Endohedral Atoms at C60 Fullerene. *J. Chem. Phys.* **1996**, *104* (4), 1179–1186. https://doi.org/10.1063/1.470778.

(52)   Li, Y. S.; Tománek, D. How Free Are Encapsulated Atoms in C60? *Chem. Phys. Lett.* **1994**, *221* (5–6), 453–458. https://doi.org/10.1016/0009-2614(94)00297-5.

(53)   Gimzewski, J. K.; Modesti, S.; Gerber, C.; Schlittler, R. R. Observation of a New Au (111) Reconstruction at the Interface of an Adsorbed C60 Overlayer. *Chem. Phys. Lett.* **1993**, *213* (3–4), 401–406. https://doi.org/10.1016/0009-2614(93)85153-F.

5 - <u>Exploring the potential for Li@C$_{60}$ to act as a multi-state molecular switch</u>

The following chapter will describe the experimental exploration of a concept which has been considered for almost 30 years[1]: the potential for Li@C$_{60}$ to act as a single molecule switch. Firstly, the adsorption orientation of the Li@C$_{60}$ will be discussed, recalling the observations from **Chapter 4** and applying these to describe the distribution of its SAMOs with respect to the substrate. Secondly, the experimental techniques and results employed in the identification of the molecular switch will be detailed. Through a combination of STM and STS, 14 discrete ion-cage coordinations will be rationalised as the result of the Li migrating between different positions in the C$_{60}$ cage. Finally, a mechanism for this Li-migration will be proposed based on a combination of the work of Schulze *et al.*[2,3] and Jorn *et al.*[4] regarding vibrational excitation of fullerenes by resonant tunnelling.

5.1 - <u>Expectations for Li@C$_{60}$ manipulation</u>

Chapter 4 confirmed both the presence of Li@C$_{60}$ on the Au(111) surface, and that the adsorption configuration which was predominantly adopted matched that which had been calculated[5] as the most thermodynamically favourable adsorption orientation: M-C6-Li@C$_{60}$ on the hcp site. The encapsulated Li is known to preferentially stabilise off-centre towards one of the C6-faces on the carbon cage (as discussed in **section 1.3.2.1**), but this ion-cage coordination cannot be directly determined from the experimental data in **Chapter 4**. For Cu(111), as is detailed in the work of Yamada *et al.*, Li@C$_{60}$ is calculated to adsorb to the surface such that the Li is displaced from the centre of the cage towards the uppermost C6-face by ~1.5 Å[5]. Initially this was assumed to be consistent on Au(111), hence the depiction in **Fig. 5.1 (a)**, and is consequently proven to be true during the manipulation experiments detailed later in this chapter (see **section 5.2**). Since this is the adsorption orientation adopted by all of the Li@C$_{60}$ on the substrate (split between the two azimuthal orientations discussed in **section 4.1.2**), this Li-cage coordination is henceforth referred to as the native state of Li@C$_{60}$ on Au(111). Upon adsorption to the substrate, the inversion symmetry of the icosahedral carbon cage (discussed in detail in **section 1.3.1.2**) is broken since the surface introduces a frame of reference to the
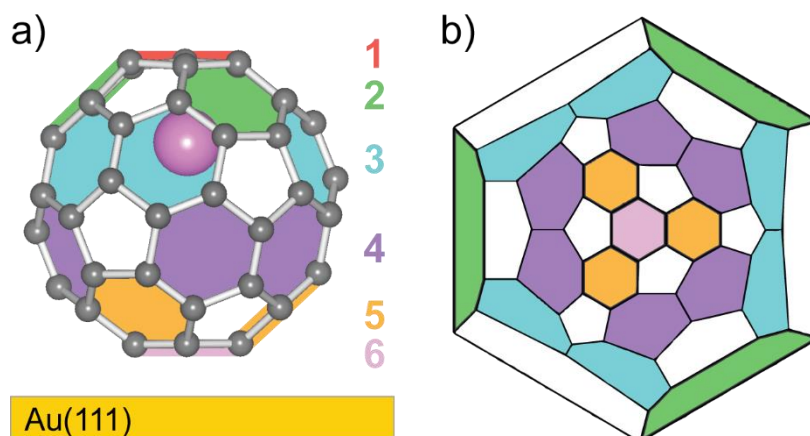
Figure 5.1: *a) Ball and stick model of Li@C$_{60}$, and b) Schlegel diagram of C$_{60}$ illustrating the distribution of the 20 C6-faces around the surface of the C$_{60}$ cage. The colours indicate the level of the C6-faces with respect to their displacement from the substrate. The Schlegel diagram is viewed through level 1 with the Li removed to facilitate identification of the remaining 19 faces.*

molecular system. When adopting the C6-fullerene orientation, this loss of symmetry results in the recognition of 6 "levels" of faces within the C$_{60}$ (as labelled in **Fig. 5.1 (a)**). Since the native state of Li@C$_{60}$ exhibits the Li preferentially stabilising in proximity to the uppermost C6-face, this has been labelled level 1. The C6-faces in both the ball and stick model and Schlegel diagram in **Fig. 5.1** are colour-coded to facilitate identification of the 6 levels of the carbon cage.

As the diagrams show, some of the levels have multiple C6-faces which are distributed around the surface of the C$_{60}$. The number of faces in each level is as follows: 1:3:6:6:3:1 for levels 1 to 6 resulting in a total of 20 C6-faces. Levels 1 and 6 have only 1 C6-face each which share bonds with 3 C6-faces in levels 2 and 5, respectively. Levels 3 and 4 each have 6 C6-faces which appear in 3 pairs that are evenly distributed around the equatorial circumference of the C$_{60}$ cage. Since the point of inversion is in the centre of the C$_{60}$ core, levels 1-3 share the same distribution of C6-faces as levels 4-6 but with a 180° rotation around the *z*-axis (orthogonal to the substrate). The Schlegel diagram (**Fig. 5.1 (b)**) specifically demonstrates that each C6-face has a unique vector from the centre of the molecule when projected onto a 2D plane. It is thought that the 2D projections of these vectors could allow for the visual recognition of the Li-cage coordination in STM images.
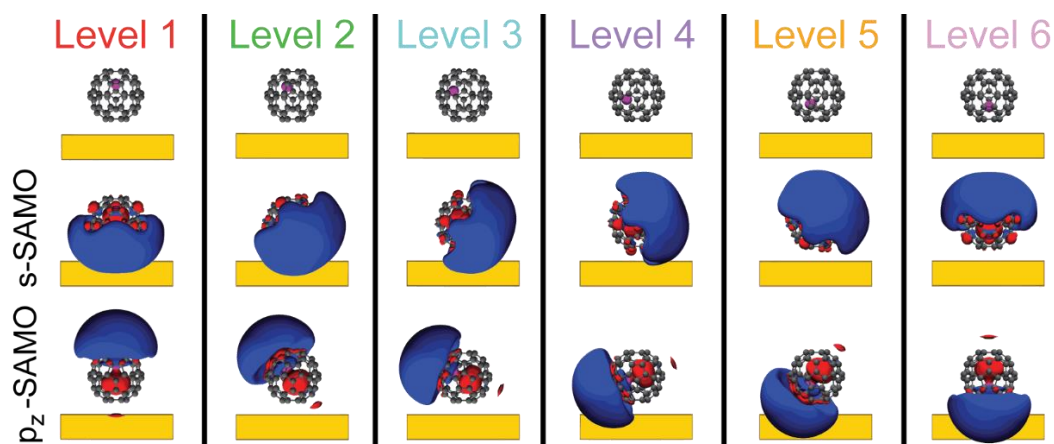
Figure 5.2: *Graphic indicating the s- and p_z-SAMOs for Li@C_{60} in the gas phase as calculated by our collaborators at the University of Edinburgh. The surface is merely to provide reference to the changing orientation of the Li@C_{60} and approximate 6 different ion-cage coordinations.*

The visual recognition of the changing Li position is expected to result from the alterations in the SAMOs of the Li@C_{60}. As is introduced in **section 1.3**, the encapsulation of Li distorts the SAMOs of the C_{60} such that these are closely dependent on the position of the Li within the cage. **Fig. 5.2** illustrates the DFT-calculated isosurfaces of the *s*- and p_z-SAMOs (the most strongly affected by the Li) for 6 hypothetical Li-cage coordinations to indicate the expected effect of Li-migration between the C6-faces of a stationary C_{60}. The DFT calculations, provided by our collaborators at the University of Edinburgh, do not include the Au(111) surface due to the prohibitive computational expense this would require. The surface has been added as a qualitative indication of the degree of surface interaction that could be expected for these 6 ion-cage coordinations.

Fig. 5.2 shows the strong dependence that both the *s*- and p_z-SAMOs possess with respect to the internal position of the Li. Movement of the Li, therefore, is expected to result in a re-orientation of these SAMOs. Since the SAMOs extend far beyond the confines of the carbon cage, the degree of overlap with the surface states will vary as the orientation of the SAMOs changes. This, in turn, will alter the energies of the corresponding resonance peaks in the c.c. *dI/dV* spectra. Before now this behaviour has not been explored by STM.

The various Li-cage coordinations and the energy barriers for migration have been studied both theoretically[4,6] and experimentally[7–10]. The preference that Li exhibits for the C6-

faces has been observed to cause 20 different Li-cage coordinations when examined in the bulk $(Li^+@C_{60})[PF_6]^-$ salt at temperatures greater than 100 K[7]. At temperatures between 100 K and 24 K, Aoyagi *et al*. identified two equally stable states in which the Li is in proximity to opposite C6-faces (i.e. level 1 and 6) and is capable of tunnelling between them[7]. However, below 24 K these two positions are reported to become asymmetrically favoured resulting in greater population of one of the two states. Which of the two states is favoured cannot be determined since the experimental technique is incapable of studying single molecules.

Though Li-migration has been observed experimentally, these previous experiments applied temperature[7,10] or terahertz radiation[8,9] to the $(Li^+@C_{60})[PF_6]^-$ salt in order to actuate the migration. Neither of these manipulation techniques afford control over, or allow identification of, single molecules. By employing low temperature STM to study surface-bound $Li@C_{60}$ not only are single molecules observable but these can be selectively activated with atomic precision. If the Li can be located and controllably moved between the C6-faces on the C_{60} cage, that could result in a single molecule switch with 20 discrete states which may be discernible with STM imaging. The next section discusses the experimental process utilised to actuate the manipulation of $Li@C_{60}$ and identify the resulting molecular configurations.

5.2 - Exploring the manipulation of $Li@C_{60}$ in a 2D array on Au(111)

Manipulations of single molecules using an STM can result in various changes which depend on the molecule's structure and the parameters applied to it by the probe (as discussed in **section 1.2.1**). A typical STM manipulation procedure consists of selecting the coordinates for the manipulation, disabling the feedback loop, and monitoring the current through the selected species as a constant tunnelling bias is applied to it. Typical parameters for such manipulations are on the order of magnitude of 0.1-0.4 V and 1 nA[11,12]. Spontaneous changes in the tunnelling current indicate an alteration to the conductance of the species beneath the STM probe. This signifies a manipulation of the molecule.

By conducting experiments at ~5 K, not only is molecular selectivity achieved but the fullerene is stationary i.e. no spontaneous movement of either the Li or the $Li@C_{60}$, and requires external stimuli to cause any variation as has been observed for C_{60}[13,14]. In the

case of Li@C_{60} the available manipulations include: Li-migration with respect to the C_{60} cage, rotation or translation of the molecule and alterations to the molecular structure (i.e. decomposition of the C_{60}). Since the goal is to study the migration of the Li within a stationary C_{60} cage, a method of minimising these unwanted manipulations is required. As identified in **section 4.1.6**, the intermolecular interactions within the 2D arrays are sufficient to prevent lateral manipulation of the fullerenes. It is therefore hypothesised that by restraining the endohedral fullerenes within a 2D array, these interactions will be strong enough to resist movement of the fullerene resulting in only Li-migration being observed. The first requirement, however, is to determine the manipulation parameters required to trigger a response in the Li@C_{60}.

5.2.1 - <u>Determining the technique required to manipulate Li@C_{60}</u>

For the majority of this chapter the manipulation technique is consistent, though the specific parameters occasionally vary depending on the intended outcome. The basics of the technique were introduced in **section 2.2.2** but a detailed description of the process is as follows. Upon imaging the surface at various biases, as described in **section 4.1.2**, a Li-containing fullerene is identified and selected for manipulation. A tunnelling current set point is selected and the feedback loop disengaged, whereupon the manipulation parameters are then chosen such that a constant tunnelling bias is applied to the fullerene. During the application of these parameters the tunnelling current is monitored for spontaneous changes which denote an alteration to the tunnel junction. **Fig. 5.3** depicts one example of an I(t) spectrum illustrating changes in the tunnelling current upon application of +5.0 V and ~2.0 μA to a Li@C_{60}. Since the applied parameters are constant, these changes in current indicate alterations to the conductance of the tunnel junction.

The tunnelling current in **Fig. 5.3**, which is initially stable at ~2.0 μA, rapidly changes between 6 discrete current levels (grey dashed lines) indicating changes in the conductance of the selected Li@C_{60}. The number of levels is reminiscent of the 6 C6-levels on the carbon cage (as shown in **Fig. 5.1**) which could suggest that the 6 conductance states are indicative of Li-migration between these levels. Detailed analysis discussed later in this chapter proves that it is not as simple as this.
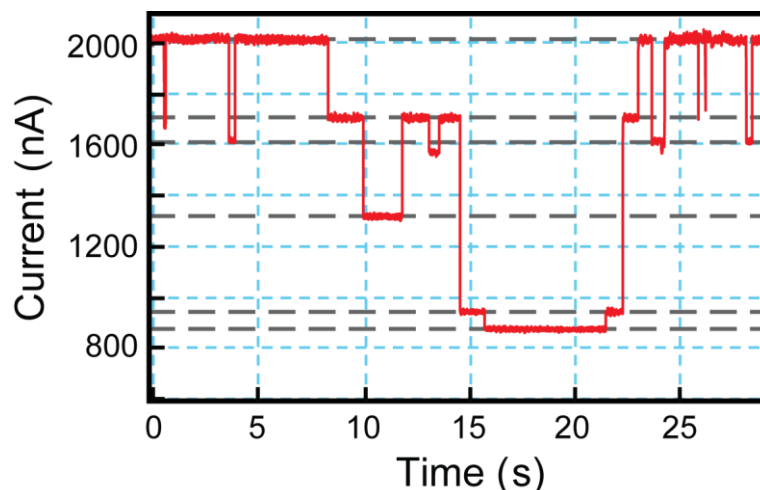
Figure 5.3: *I(t) spectrum illustrating the tunnelling current recorded on a Li@C$_{60}$ in a 2D array on Au(111) during an STM-induced manipulation with parameters of +5.0 V and ~2.0 µA.*

The parameters applied during the above illustrated manipulation (+5.0 V and ~2.0 µA) are the result of exploring the effect of incremental increases in both the tunnelling bias and the tunnelling current. This method revealed that the lowest tunnelling bias capable of causing the sudden changes in the conductance is +3.0 V. However, the tunnelling current required to achieve this within an observable timeframe (more than ~0.02 Hz or ~1 per minute) is very large (~3.7 µA) and often results instead in the collapse of the tunnel junction or decomposition of the fullerene. As the tunnelling bias is further increased, the current required to actuate the conductance changes reduces. Though a thorough understanding of this relationship is not achieved during the current work, brief exploration resulted in the identification of the parameters utilised for the majority of the following experimental exploration (+5.0 V, 1.85 ±0.15 µA). These parameters are many magnitudes greater than standard manipulation parameters (0.1-0.4 V and 1 nA, as mentioned above). This is because proposed mechanism requires the energy of the tunnelling electrons to coincide with $p_{x,y}$-SAMOs for the manipulation to be activated. A more detailed explanation of this mechanism is discussed in **section 5.2.5**.

The extreme parameters required to alter the conductance state of the Li@C$_{60}$ and the fact that there are 6 of them as shown in **Fig. 5.3** (grey dashed lines) are two behaviours exhibited within the *I*(t) spectrum. There is also a third and arguably more directly interesting facet of the data that is apparent; the seeming reversibility of the conductance

changes. The tunnelling current returns to the initial value (~2.0 µA) a number of times throughout the spectrum and also happens to end in that state. The analysis of this reversibility is the focus of the next section.

5.2.2 - Exploring the reversibility of the conductance changes exhibited during Li@C$_{60}$ manipulation

To decipher the origin of the reversibility in the conductance changes exhibited in **Fig. 5.3**, the Li@C$_{60}$ must be identified before and after each alteration in the conductance state. As such, c.c. STM images at +2.5 V and -2.5 V, and c.c. *dI/dV* spectra are acquired before and after each manipulation attempt. The selected Li@C$_{60}$ (highlighted by a solid white ring) is identified by the c.c. STM images in **Fig. 5.4 (a)** and one of the red c.c. *dI/dV* spectra in **Fig. 5.4 (j)**. This fullerene undergoes multiple manipulation procedures and the subsequent STM images (**Fig. 5.4 (b-i)**) illustrate the molecular appearance of each of the resulting conductance states. **Fig. 5.4** illustrates 8 different manipulations to show the reversibility and reproducibility of the procedure.

The first set of STM images (**Fig. 5.4 (a)**) identify the fullerene as a C6-Li@C$_{60}$ in the native state (ring shape at -2.5 V and beacon at +2.5 V). Between each adjacent image set (i.e. between **(a)** & **(b)**, **(b)** & **(c)** etc.) manipulation parameters are applied which cause the changes in the subsequent images. **Figs. 5.4 (c, e, g** and **i)** all appear the same as **Fig. 5.4 (a)** suggesting that the Li@C$_{60}$ is repeatedly returned to its native state. However, the remaining STM images (**Figs. 5.4 (b, d, f** and **h)**) adopt different molecular appearances as a result of the manipulation.

Looking closely at the -2.5 V STM images of the altered Li@C$_{60}$ (top row of **Figs. 5.4 (b, d, f** and **h)**), three different molecular appearances are observed that all exhibit an induced asymmetry in their topographic signatures. **Figs. 5.4 (b)** and **(f)** both appear like ring shapes with an asymmetric brightness on a portion of the ring. **Fig. 5.4 (d)** has the appearance of a kidney bean the asymmetry caused by one end appearing brighter than the other. **Fig. 5.4 (h)** exhibits an asymmetry due to a portion that is darker than the rest, resulting in the ring shape resembling a crescent instead. Upon initial observation it might be assumed that this final appearance actually represents a fullerene after
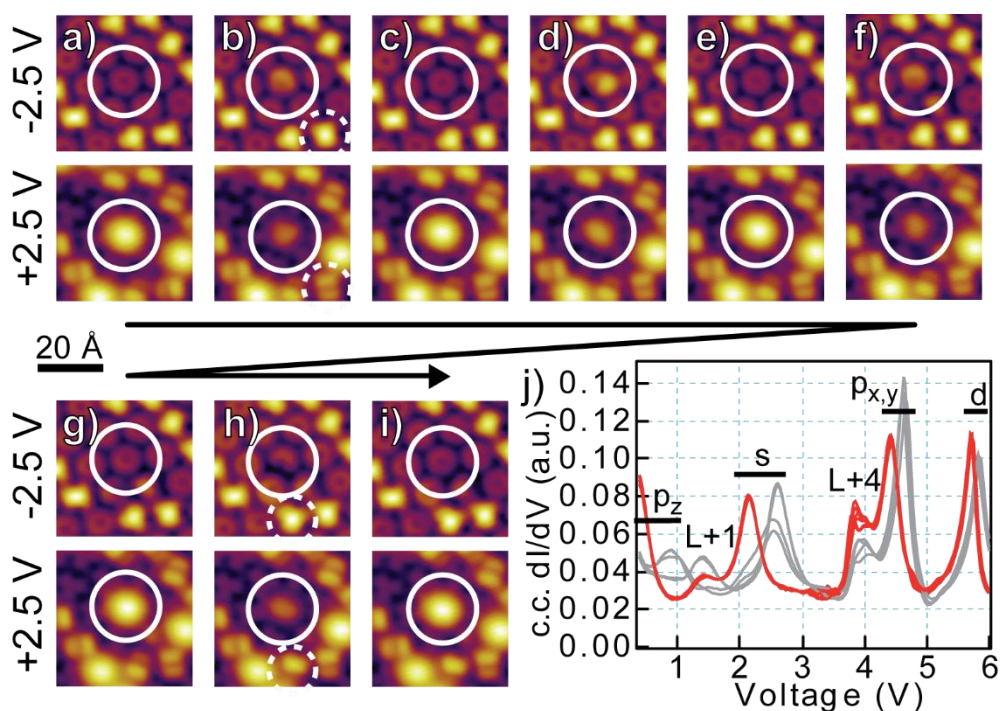
Figure 5.4: *a-i)* *Sequential STM images (-2.5 V, 0.1 nA [top row]; +2.5 V, 0.1 nA [bottom*
row]) of a Li@C$_{60}$ (solid white ring) used to illustrate the reversibility of the Li-switch.
a), c), e), g) *and* *i)* *are data sets for the native state of the Li@C$_{60}$.* *b), d), f)* *and* *h)*
are data sets that represent three different switched states of the Li@C$_{60}$. Dashed
white circles indicate neighbouring C$_{60}$ that have undergone rotations as a result of
the manipulation of the Li@C$_{60}$. *j)* *c.c. dI/dV spectra for each of the data sets with*
the distinct LUMOs (+1 & +4) and the shift of each SAMO labelled. The red spectra
correspond with images a), c), e), g) *and* *i)* *and the grey spectra with* *b), d), f)* *and*
h).

decomposition, however, this is disregarded upon observing that the final STM image of
the figure (**Fig. 5.4 (i)**) shows the Li@C$_{60}$ returned to the native state. Additional evidence
proving the integrity of all of the fullerene appearances in **Fig. 5.4 (b-i)** is illustrated by the
c.c. *dI/dV* spectra in **Fig. 5.4 (j)**.

The red spectra in **Fig. 5.4 (j)** correspond to the Li@C$_{60}$ in the native state (**Figs. 5.4 (a, c,
e, g** and **i)**) and the grey spectra to those in the 3 other states (**Figs. 5.4 (b, d, f** and **h)**).
The almost identical electronic structure seen in the red spectra proves the Li@C$_{60}$ is
observed in the same state for these 5 data sets. Studying **Fig. 5.4 (j)** shows that when
Li@C$_{60}$ is switched out of the native state (red to grey spectra) there is an upshift in all

SAMO resonance energies, which varies for each specific SAMO, but no shift in the energies of the visible LUMOs. The LUMO+1 (~+1.5 V) and the LUMO+4 (~+4 V) exhibit altered intensity but the reason for this is not currently understood. The major observation from the spectra is the proof that, regardless of the appearance of the STM images, the integrity of the $Li@C_{60}$ is maintained for each state. As such, the process of converting between any of the states illustrated in **Fig. 5.4** will simply be known as a Li-switch and all states, besides the native state, will be referred to as switched states.

The manipulation parameters required to return the switched states to the native state are less extreme than those for the initial switch (from native into any of the others). Despite this observation, the switched states exhibit a qualitatively similar stability to the native state i.e. no spontaneous switching of any $Li@C_{60}$ is observed during STM imaging or manipulation of neighbours. This is not the case for C_{60}. As is indicated by the dashed white circles in **Figs. 5.4 (b)** and **(h)**, spontaneous re-orientation of neighbouring C_{60} is quite common during the manipulation of $Li@C_{60}$ and has been recorded on C_{60} up to 5 nm from the selected $Li@C_{60}$. A suggestion for the origin of this behaviour is discussed later in this chapter when proposing a mechanism for the Li-switch (**section 5.2.5**).

The microscopic and spectroscopic identification of the reversibility of the Li-switch is strong evidence that the manipulation is activating a movement of the Li with respect to the substrate. The next sections will attempt to identify this movement and characterise each of the possible switched states.

5.2.3 - Identifying the $Li@C_{60}$ switched states

In order to properly identify the switched states exhibited by $Li@C_{60}$ upon application of the manipulation parameters (+5.0 V, 1.85 ±0.15 µA), a methodical approach to the characterisation before and after each manipulation is required. Since the endohedral fullerenes all adopt the native state naturally, each $Li@C_{60}$ is to be switched only once from the native state into one of the switched states. This allows direct comparison between the data sets for identical $Li@C_{60}$. To provide enough information to fully identify the manipulation process a standardised data set (**Fig. 5.5**) is suggested. Before each manipulation attempt, the starting configuration of the selected $Li@C_{60}$ (i.e. M- or m-C6-$Li@C_{60}$) must be identified to ensure only identical fullerenes are directly compared. As
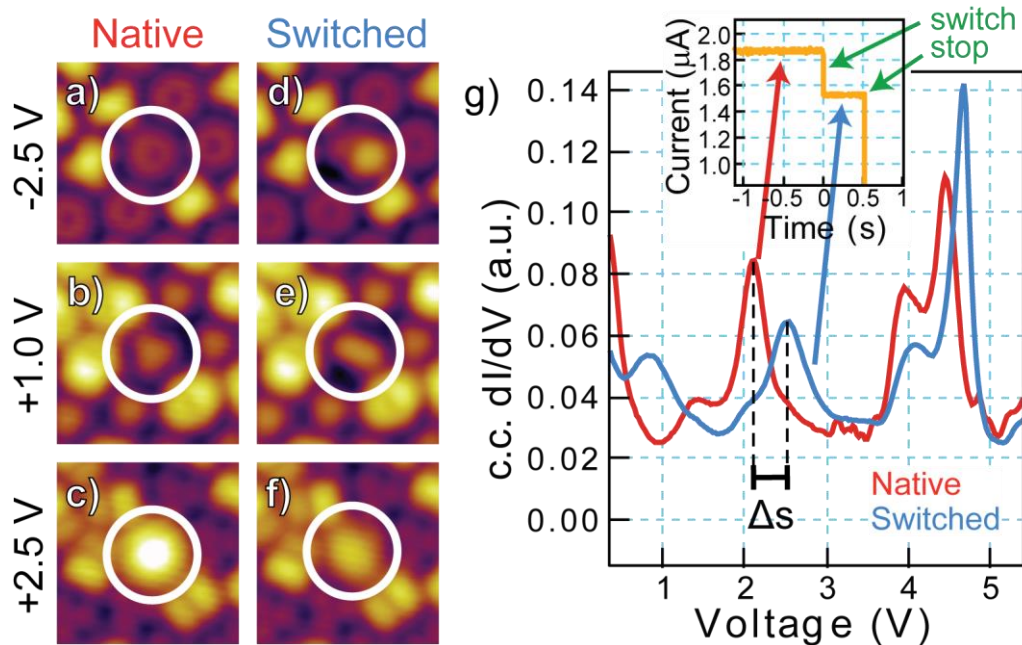
Figure 5.5: *Typical data set for analysis of the Li@C$_{60}$ switch process. STM images prior to the switch prove this fullerene to be M-C6-Li@C$_{60}$ by imaging at the following parameters: **a)** (-2.5 V, 0.1 nA), **b)** (+1.0 V, 0.1 nA) and **c)** (+2.5 V, 0.1 nA). STM images after the manipulation are used to identify the switched state of the Li@C$_{60}$ by imaging at the same parameters: **d)** (-2.5 V, 0.1 nA), **e)** (+1.0 V, 0.1 nA) and **f)** (+2.5 V, 0.1 nA). **g)** c.c. dI/dV spectra of the M-C6-Li@C$_{60}$ from before (red) and after (blue) the switch event. The inset I(t) curve illustrates the tunnelling current during the application of the manipulation parameters (+5.0 V, 1.85 µA).*

such, the data set contains 3 STM images of the Li@C$_{60}$ at various scanning biases (**Figs. 5.5 (a)** -2.5 V, **(b)** +1.0 V, and **(c)** +2.5 V) and a c.c. *dI/dV* spectrum (red curve in **Fig. 5.5 (g)**) proving that the fullerene is in its native state. After the switch procedure, depicted by the inset *I*(t) spectrum in **Fig. 5.5 (g)**, the acquisition of these data is repeated (**Figs. 5.5 (d-f)** and blue curve in **(g)**). Each data set can then be discussed in an attempt to identify the changes which the native state undergoes to result in the various switched states.

The STM images of the selected Li@C$_{60}$ in its native state show the ring shape familiar to C6-fullerenes at -2.5 V (**Fig. 5.5 (a)**), and the orientation of the triangular shape at +1.0 V (**Fig. 6.5 (b)**) identifies it as specifically an M-C6-fullerene. The beacon molecular appearance at +2.5 V visually differentiates the Li@C$_{60}$ from neighbouring C$_{60}$ (**Fig. 5.5 (c)**) and the red c.c. *dI/dV* spectrum (see **Fig. 5.5 (g)**) confirms the characterisation. Each of

these pieces of data are required to fully identify the fullerene before the manipulation procedure, which is represented by the inset I(t) graph in **Fig. 5.5 (g)**. Initially the I(t) graph shows a stable tunnelling current after the manipulation parameters (+5.0 V, 1.85 µA) are applied. A sudden drop in the current (~350 nA, labelled "switch") indicates a spontaneous change in the conductance of the fullerene, after which the parameters are manually removed (current change labelled "stop"). This then allows the remaining data to be recorded in order to complete the data set.

The same image parameters are repeated after the manipulation to provide information on the final state of the Li@C_{60}. The STM image of the switched state at -2.5 V (**Fig. 5.5 (d)**) is arguably the most useful since it provides information on the topographic asymmetry induced by the manipulation. In this case the Li@C_{60} has adopted the kidney bean shape similar to **Fig. 5.4 (d)**. On initial observation this asymmetry is reminiscent of the radial distribution of the C6-faces as described by the Schlegel diagram in **Fig. 5.1 (b)**, this shall be explored further shortly. The STM image at +1.0 V (**Fig. 5.5 (e)**) can be useful for checking the orientation of the molecular appearance with respect to the 2D array. The amorphous shape of the molecular appearance at +2.5 V (**Fig. 5.5 (f)**) is dimmer for the switched state. Though this does not provide any information on the symmetry of the switched state of the fullerene, it can be understood by observing the shift in the s-SAMO peak (indicated by Δs in **Fig. 5.5 (g)**). The c.c. dI/dV spectrum of the Li@C_{60} in the switched state (blue curve in **Fig. 5.5 (g)**) is one of the most important pieces of data since it proves the integrity of the fullerene regardless of the appearance in the STM images. By comparing between the spectra, any shifts in the resonance peak energies can be easily identified and directly associated with the manipulation. This data set can be repeated to suitably analyse the behaviour of the Li@C_{60} when subjected to these manipulation parameters. For the current work, for example, a total of 307 Li@C_{60} have been manipulated and analysed to determine the identity of the possible switched states.

5.2.3.1 - Characterising the Li@C_{60} switched states with STM and STS

After analysis of more than 300 discrete switch procedures, 5 molecular appearances are observed repeatedly, 3 of which exhibit numerous equivalents that adopt different azimuthal orientations with respect to the 2D array. **Fig. 5.6** shows the STM images of the
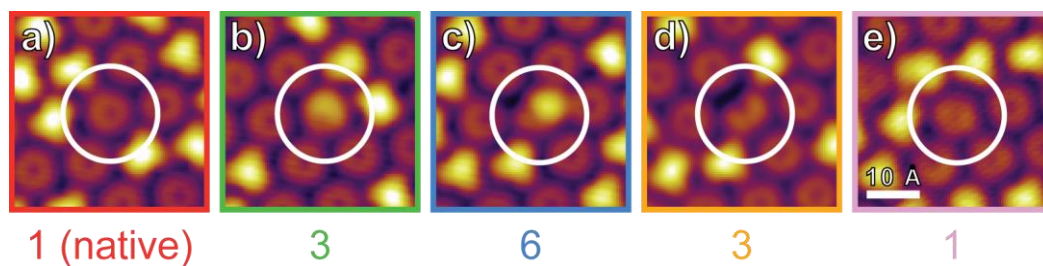
Figure 5.6: *STM images (-2.5 V, 0.1 nA) of the 5 discrete states of M-C6-Li@C$_{60}$ labelled with the corresponding number of azimuthal orientations observed for each molecular appearance.*

5 discrete molecular appearances for the Li@C$_{60}$ with the number of azimuthal orientations observed for each indicated below the image (totalling 14). There is a 15th state which is also identified, but this is very rarely seen and will be identified as a Li-ejection event in **section 5.2.4**. The following analysis only illustrates the results from the M-C6-Li@C$_{60}$ selected for manipulation, however all conclusions formed are also consistent for the m-C6-Li@C$_{60}$ configuration.

Fig. 5.6 (a) is presented as an example of the native state for reference in the comparison with the switched states of M-C6-Li@C$_{60}$ (**Figs. 5.6 (b-e)**). The ring with an asymmetric brightness seen in **Fig. 5.6 (b)** (similar to those in **Figs. 5.4 ((b)** and **(f)**)) is observed adopting 3 azimuthal orientations at 120° intervals. **Fig. 5.6 (c)** depicts a kidney bean shaped molecular appearance with an asymmetric brightness which can be described as "pointing" between two close-packing directions in the 2D array (similar to that in **Fig. 5.4 (d)**). This switched state is observed adopting 6 different azimuthal orientations. Similar to **Fig. 5.6 (b)**, the crescent shaped molecular appearance in **Fig. 5.6 (d)** (reminiscent of that seen in **Fig. 5.4 (h)**) also adopts 3 azimuthal orientations at 120° intervals. The final, discrete molecular appearance (seen in **Figs. 5.6 (e)** and **5.7 (a)**) bears a striking resemblance to the native state due to its symmetrical ring shape. Only by also considering the corresponding c.c. *dI/dV* spectrum can the switched state be proven distinct from the native state (see **Fig. 5.7**).

The number of azimuthal orientations exhibited by the 5 discrete molecular appearances (1:3:6:3:1) is comparable to the distribution of the C6-faces between the levels of the C$_{60}$ cage (1:3:6:6:3:1, as illustrated in **Fig. 5.1**). The migration of the Li resulting in different Li-
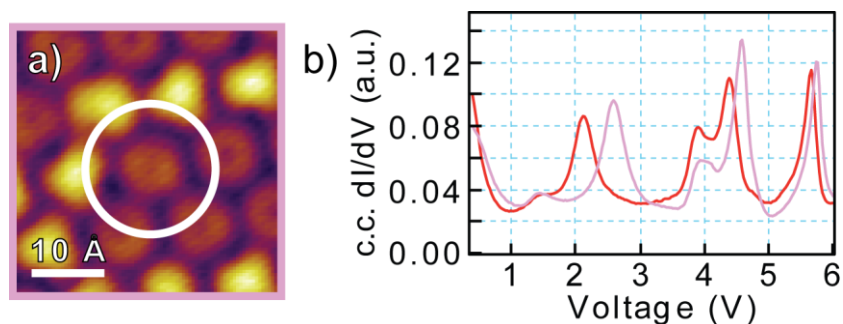
Figure 5.7: *(a) STM image (-2.5 V, 0.1 nA) of M-C6-Li@C$_{60}$ with the Li in level 6 (same image as in Fig. 5.6 (e)). (b) c.c. dI/dV spectra of the white-ringed fullerene in (a) (pink) and a Li@C$_{60}$ in the native state (red).*

cage coordinations is hypothesised to be the source of the induced asymmetry in the molecular appearances in **Fig. 5.6 (b-d)**. In order to explore this, the symmetries of the 5 discrete molecular appearances and the corresponding c.c. *dI/dV* spectra will now be analysed.

Besides the native state of Li@C$_{60}$ (**Fig. 5.6 (a)**), which has already been discussed extensively in **Chapter 4**, the molecular appearance seen in **Figs. 5.6 (e)** and **5.7 (a)** is the simplest to identify because it is symmetrical. **Fig. 5.7 (b)** depicts the c.c. *dI/dV* spectra for this switched state (pink) and an example of the native state (red) to facilitate comparison between the two.

Upon initial observation, the fullerene in **Fig. 5.7 (a)** is barely distinct from the familiar ring shape of Li@C$_{60}$ in the native state. However, by examining the c.c. *dI/dV* spectra in **Fig. 5.7 (b)** it is determined that the symmetrical molecular appearance does represent a fullerene in a switched state. The pink spectrum in **Fig. 5.7 (b)** exhibits an upshift in the energies of the SAMO peaks and negligible response from the visible LUMOs. These changes in the resonance peak energies confirm the spectrum as representing a Li@C$_{60}$ in a switched state; similar to those seen in **Fig. 5.4 (j)**. In order to maintain the same symmetry as the native state (hence the molecular appearance) but with a different Li-cage coordination, the Li must be located in proximity to the single C6-face adsorbed to the substrate. This configuration is, therefore, referred to as M-C6-Li@C$_{60}$ with the Li in level 6.

Figure 5.8: *a) STM images (-2.5 V, 0.1 nA) of 3 examples of M-C6-Li@C$_{60}$ with the Li in the level 2. These images are positioned around a ball and stick model of M-C6-Li@C$_{60}$ to illustrate which of the C6-faces the brightness in each image aligns with. b) c.c. dI/dV spectra of the white-ringed fullerenes in a) (green) and a Li@C$_{60}$ in the native state (red).*

Continuing the analysis of the symmetry of the switched states in **Fig. 5.6**, consider the ring with an asymmetric brightness and 3 azimuthal orientations (see **Figs. 5.6 (b)** and **5.8 (a)**). The ball and stick model below illustrates the adsorption configuration of the M-C6-Li@C$_{60}$ in its native state. The c.c. *dI/dV* spectra in **Fig. 5.8 (b)** represent the electronic structures of the fullerenes indicated in the STM images in **Fig. 5.8 (a)** and a Li@C$_{60}$ in the native state, these are green and red respectively.

Each of the three white-ringed fullerenes in the STM images in **Fig. 5.8 (a)** align with one of the high symmetry packing directions of the 2D array. Comparing this with the ball and stick model, the bright portion of each molecular appearance is observed coinciding with a C6-face in level 2 of the C$_{60}$ cage. This agrees with the hypothesis that the induced asymmetry is related to the Li-cage coordination. The consistency between the corresponding spectra (green in **Fig. 5.8 (b)**) is further evidence that these switched states
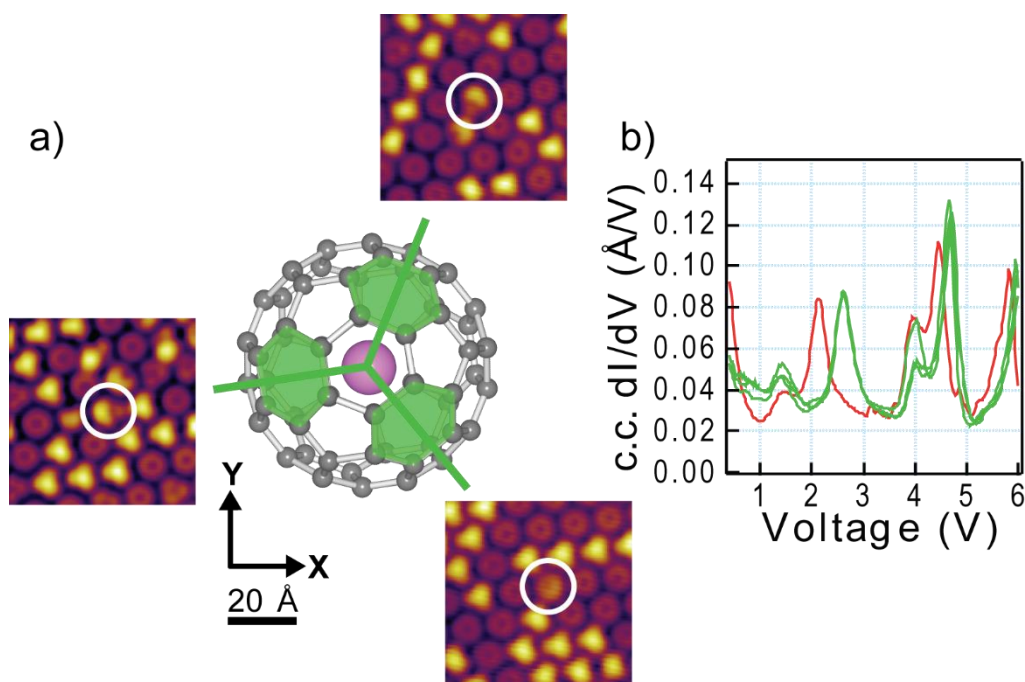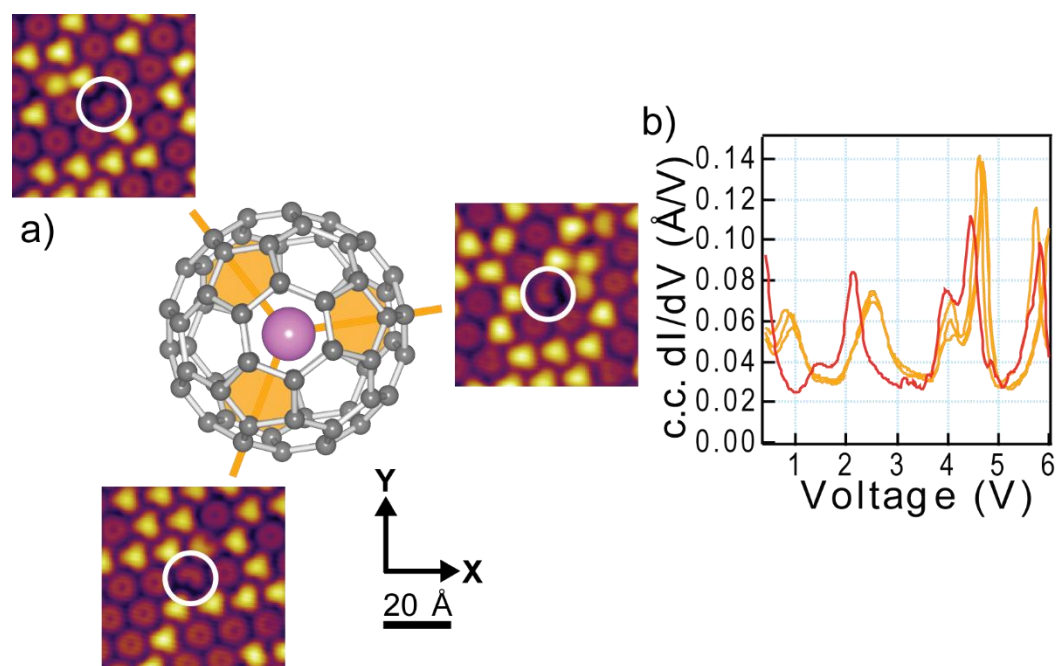
Figure 5.9: *a)* *STM images (-2.5 V, 0.1 nA) of 3 examples of M-C6-Li@C₆₀ with the Li in*
level 5. These images are positioned around a ball and stick model of M-C6-Li@C₆₀
to illustrate which of the C6-faces align with the dark region in each molecular
appearances. ***b)*** *c.c. dI/dV spectra of the white-ringed fullerenes in **a)** (orange) and*
a Li@C₆₀ in the native state (red).

are of similar Li-cage coordinations, merely adopting different azimuthal orientations. This
consistency also indicates the negligible effect that variation in the neighbouring
fullerenes imparts on the electronic structure of Li@C$_{60}$.

The second switched state that exhibits an asymmetric molecular appearance with 3
azimuthal orientations is the crescent shaped molecular appearance seen in **Figs. 5.6 (d)**.
In this case, however, the asymmetry of the shape is a dark region which aligns with the
3 high symmetry packing directions opposite to those adopted by the bright regions of
the level 2 M-C6- Li@C$_{60}$ shapes. These 3 azimuthal orientations are indicated in the STM
images surrounding the ball and stick model of M-C6-Li@C$_{60}$ in **Fig. 5.9 (a)**. The orange c.c.
dI/dV spectra in **Fig. 5.9 (b)** correspond with these molecular appearances and show the
electronic structure of the switched Li@C$_{60}$. The red spectrum is an example of the
electronic structure of Li@C$_{60}$ in the native state.

Direct comparison with the M-C6-Li@C_{60} model shows that the asymmetry in the images aligns with the C5-faces on level 2. However, due to the inversion symmetry of the C_{60} cage this also coincides with the C6-faces in level 5 (as highlighted by the ball and stick model in **Fig. 5.9 (a)**). The known preference for the Li to stabilise in the proximity of C6-faces leads to the conclusion that this molecular appearance corresponds with M-C6-Li@C_{60} with the Li in level 5 of the cage.

Similar to the spectra seen for the level 2 switched state of M-C6-Li@C_{60} (**Fig. 5.8 (b)**), the orange spectra in **Fig. 5.9 (b)** are very consistent in their peak distribution. One difference between the spectra in **Figs. 5.8 (b)** and **5.9 (b)**, however, is the clearly identifiable p_z-SAMO (~+1.0 V) for the level 5 switched state. Why this peak is more distinct for this molecular configuration than for Li@C_{60} in level 2 is, as yet, undetermined.

The p_z-SAMO peak is also apparent in the spectra associated with the final molecular appearance; the kidney bean shape depicted in **Figs. 5.6 (c)** and **5.10**. This final switched state also exhibits an asymmetry due to a portion of the molecular appearance which is brighter than the rest. Similar to the other switched states, this allows the molecule to be identified by the direction it "points" (see the arrows on the STM images in **Fig. 5.10 (a)**). Similar to the previous figures describing the levels 2 and 5 switched states, these STM images surround a ball and stick model of M-C6-Li@C_{60}. The blue c.c. dI/dV spectra exhibited in **Fig. 5.10 (b)** illustrate the electronic structures of the fullerenes indicated by the white and blue rings in **Fig. 5.10 (a)**, and the red spectrum represents the electronic structure of a Li@C_{60} in the native state.

Close observation of the molecular appearances in the STM images in **Fig.5.10 (a)** reveals that instead of 6 azimuthal orientations of the same shape, there are 2 slightly different sets of 3. On initial observation the molecules appear similar but, as is accentuated by the adjacent apostrophe shapes, the direction of the curve differs. This could suggest that two different switched states are present, however the consistency of the electronic spectra for the 6 fullerenes (see **Fig. 5.10 (b)**) disagrees with this proposal. Considering the alignment of the asymmetry in the molecular appearance, as has been used to identify levels 2 and 5, the axes of the azimuthal orientations all fall between the 6 close-packed directions of the 2D array (illustrated by the arrows in **Fig. 5.10 (b)**). Secondly, the axes of these molecular appearances do not align with those of the C6-faces in either levels 3
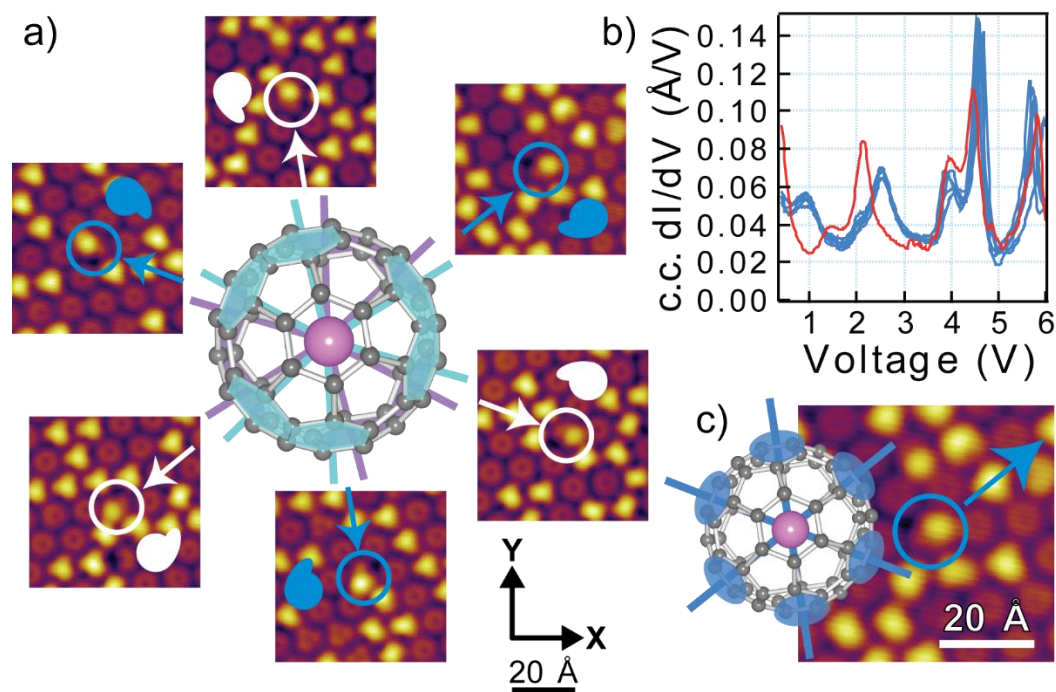
Figure 5.10: *a) STM images (-2.5 V, 0.1 nA) of 6 examples of the kidney bean shaped molecular appearance that are often seen after switching M-C6-Li@C_{60}. These are positioned around a ball and stick model to illustrate that the axes of the C6-faces in levels 3 (turquoise) and 4 (purple) do not align with those of the kidney beans (indicated by the arrows). b) c.c. dI/dV spectra of the 6 ringed fullerenes in a) (blue) and an M-C6-Li@C_{60} in the native state (red). c) Ball and stick model illustrating the alignment between the axis of an STM image from a) and those of the proposed level 3/4 switched state of M-C6-Li@C_{60}.*

(turquoise) or 4 (purple), but instead bisect them. Due to this misalignment of the axes, this switched state proves less trivial to identify than the previous states. The fact that there are only 6 azimuthal orientations (3 for each set) instead of 12 (6 for each of levels 3 and 4) adds further complication to the identification of the switched state represented by the kidney bean shape. Three hypotheses are presented in an attempt to determine the true nature of this switched state.

The first suggestion states that only one of either levels 3 or 4 is observed, with no Li@C_{60} stabilising in the remaining level. Simply put, a rational energetic argument cannot be made for this suggestion so it is dismissed. A second hypothesis proposes that Li@C_{60} adopting both levels 3 and 4 are present in the data, but that the molecular appearance

is too similar and the resolution of the STM images is insufficient to determine the difference. This hypothesis is also dismissed. Firstly, because the 15° angle between adjacent C6-faces in levels 3 (turquoise) and 4 (purple) (see ball and stick model in **Fig. 5.10 (a)**) would be easily observable in the achieved resolution of the STM images. Secondly, each level would be expected to have a unique electronic structure (noticeable in the p_z- and s-SAMO peaks) since the Li-cage coordination would differ. As mentioned above, however, on examining the spectra closely there is only one set of peaks which all exhibit similar resonance peak structures (see **Fig. 5.10 (b)**).

The final hypothesis suggests that the proximity of the neighbouring fullerenes in the 2D array alters the internal potential energy landscape that the Li experiences in the carbon cage. Instead of stabilising close to the C6-faces in levels 3 or 4, the Li adopts a position in proximity to the double bond between the two C6-faces. This reduces the 12 possible stabilisation sites (6 C6-faces in each of levels 3 and 4) to only 6 in an equatorial position henceforth referred to as level 3/4 due to its hybrid nature. The axes that align with these equatorial positions are illustrated on the ball and stick model in **Fig. 5.10 (c)** and coincide with those of the kidney bean shapes (as seen in the corresponding STM image).

Not only do the proposed level 3/4 Li-coordination sites match the 6 axes observed in the STM images, but the plane of the double bond to which the Li stabilises appears to be linked to the curve of the kidney bean shape. **Fig. 5.11** places two examples of the level 3/4 switched state of M-C6-Li@C_{60} from **Fig. 5.10 (a)** alongside ball and stick models to illustrate this connection between the double bond and the shape of the molecular appearance.

The ball and stick models in **Fig. 5.11** are orientated such that the highlighted bond (between the C6-faces of levels 3 and 4) is the stabilisation site for the Li. The models are viewed as if observing the fullerenes along the axis of the arrows on the corresponding STM images. The highlighted bonds can be seen adopting mirror symmetric angles with respect to the substrate (see the difference between the models in **Figs. 5.11 (a)** and **(b)**). The angle adopted by this bond alternates around the equator of the carbon cage and therefore is consistent with the alternating orientation of the kidney bean shapes in the STM images in **Fig. 5.10 (a)**.
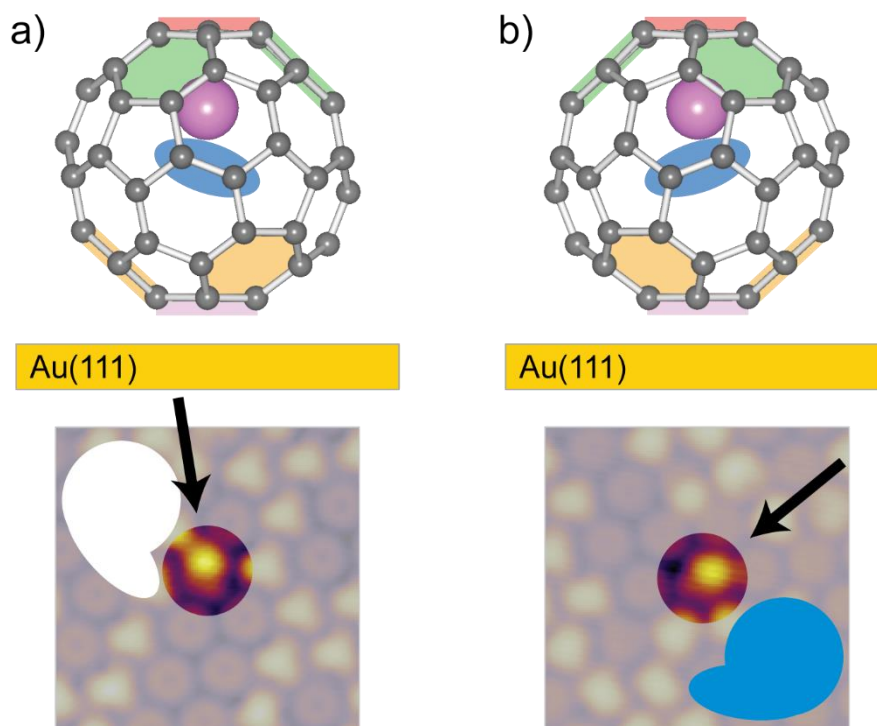
Figure 5.11: *Ball and stick models indicating the stabilisation sites for the Li in the corresponding level 3/4 M-C6-Li@C_{60} switched state (deep blue). These models are orientated as if viewing the Li@C_{60} in the appropriate STM image (-2.5 V, 0.1 nA) along the axis of the arrow. The shape of each molecular appearance is emphasised by the adjacent white and blue apostrophe shapes.*

The proposed bond-coordinated Li-stabilisation site for the level 3/4 switched state of Li@C_{60} agrees with the axes observed in the STM images (**Fig. 5.10 (c)**), and suggests an origin for the alternating orientation of the kidney bean shape. However, the strongest argument for this proposed coordination site is revealed upon a statistical analysis of the population density for each of the four switched states observed (**Fig. 5.6 (b-e)**). These results are presented in **Table 5.1**.

Of the 307 Li@C_{60} which underwent manipulation 270 are identified as switched states, 3 adopted an irreversible but reproducible state (discussed in **section 5.2.4**) and 34 are disregarded as these were irregular and irreproducible. This latter group are suggested to be the result of Li@C_{60} decomposition but are not discussed further due to the lack of identifiable symmetries. The "observed" values in **Table 5.1** are representative of the proportion of the 270 Li@C_{60} which adopt each of the identified switched states. The

Table 5.1: *Statistical analysis of the distribution of the switched states adopted by M-C6-Li@C$_{60}$.*

Ratios	Level 2	Level 3/4	Level 5	Level 6
Observed	20.4%	52.2%	26.3%	1.1%
Expected	23 ± 3%	46 ± 3%	23 ± 3%	8 ± 2%

"expected" values in the table are the result of a random distribution between the four switched states with weighted probabilities of 3:6:3:1 to match the distribution of the C6-faces through the proposed levels of Li-cage coordination. The errors are standard deviations which result from repeating the distribution 270 times, to match the experimental number of identified switched states. As can be seen in **Table 5.1**, the observed population values for levels 2 and 5 fall within the range of expected values for those switched states, but the population of levels 3/4 and 6 fall slightly outwith these ranges. This could suggest that there is a minor avoidance of the level 6 states due to the orientation of its SAMOs and subsequent interaction with the surface states (discussed shortly below). Alternatively, the Li may exhibit some preference for the equatorial sites of level 3/4. These minor variations may be evidence of external factors (i.e. substrate and neighbouring fullerenes) modifying the internal surface potential that the Li experiences, suggesting some preference for certain switched states. However, the discrepancy between expected and observed values in **Table 5.1** is only a few % and, for the size of this study, this can be considered sufficiently small to consider the values the same. Hence, the Li-migration mechanism is determined to be a random process, i.e. there is no preference between the 13 switched states.

Naïvely, one might expect that the proximity of the Li to the surface would induce some preference between the C6-levels within the C$_{60}$ cage due to interactions between the SAMOs and empty surface states. Similar to the native state being considerably preferred over the switched states, one could assume that level 2, for example, would be more preferable than level 5 due to the reduced overlap between the orbitals of the Li and the empty states of the Au. One suggestion as to why this preference is not observed is linked to the Faraday cage-like effect that was reported by Delaney *et al.* in 2004[15]. The shielding afforded to the encapsulated species by this proposed effect may prevent any surface-

induced preference for certain Li-cage coordination sites. However, it could also be expected that this shielding would protect the internal surface potential from the intermolecular interactions of neighbours too. This would obviously disagree with the suggested formation of the level 3/4 switched state. The proposed Faraday cage-like effect, therefore, requires in depth calculations and discussion before any effects on the surface-bound endohedral fullerene can be confirmed. These calculations are beyond the scope of this thesis so have not yet been attempted.

A statistical analysis to explore any effect between nearest neighbours and the adopted Li-cage coordination site may reveal greater insight on interactions within the 2D array. However, the sheer complexity of such a process is also beyond the scope of the current work. In an attempt to ensure the selected Li@C_{60} were as close to identical as possible each was surrounded by 6 C_{60} as nearest neighbours. However, to achieve truly identical conditions the orientation of these neighbours would also have to have been the same. This is impractical for two reasons: firstly the variation in the C_{60} adsorption configurations resulted in a vast number of possible combinations for the 6 neighbours surrounding a Li@C_{60}. Secondly, the frequency with which neighbouring C_{60} rotate under the Li-manipulation parameters would result in the dismissal of the majority of the data collected. Due to these unrealistic requirements for an ideal system the above analysis of STM images is the sum of the quantitative analysis for the distribution of the switched states.

As a result of these 14 proposed Li-cage coordination sites, the diagrams indicating 20 possible states (**Figs. 5.1** and **5.2**) are refined and presented in **Fig. 5.12**. The ball and stick model and the Schlegel diagram identify the 14 suggested Li-cage coordination sites (**Figs. 5.12 (a)** and **(b)**). The s- and p_z-SAMOs depicted in **Fig. 5.12 (c)** are an approximate representation of how the SAMO orientations of the 4 switched states may compare to those of the native state.

Similar to the previous examples of these figures (see **Figs. 5.1** and **5.2**), the highlighted coordination sites of the ball and stick model and Schlegel diagram are colour-coded (see **Figs. 5.12 (a)** and **(b)**, respectively). Similar to **Fig. 5.1 (b)**, the uppermost C6-face and Li are removed from the Schlegel diagram to aid identification of the radial distribution of the 13 switched states. The SAMOs depicted in **Fig. 5.12 (c)** are the result of DFT
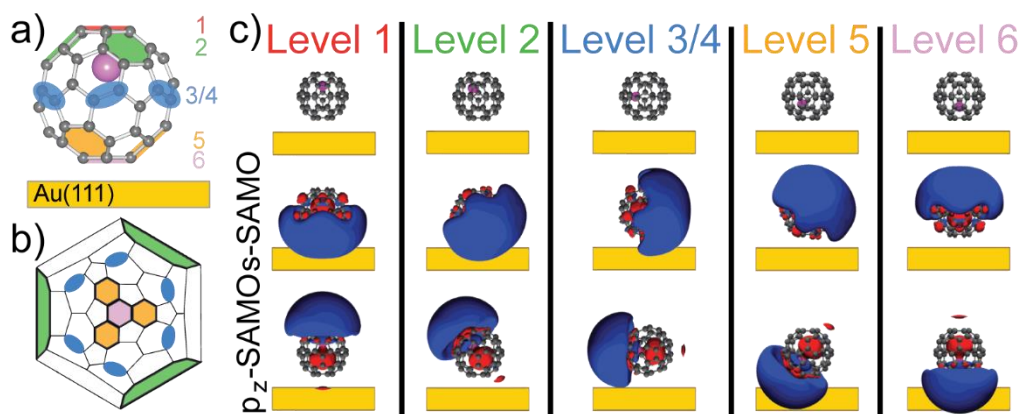
Figure 5.12: *Illustrations of the 14 proposed Li-coordination sites of C6-Li@C$_{60}$ when adsorbed to Au(111). The 14 sites are highlighted on **a)** a ball and stick model, and **b)** a Schlegel diagram. **c)** Approximated s- and p$_z$-SAMOs are presented for the native state and the 4 proposed switched states of Li@C$_{60}$. These SAMOs are the result of gas phase DFT calculations for Li@C$_{60}$ with Li coordinated to a C6-face, the orientations presented are merely to facilitate discussion.*

calculations for Li@C$_{60}$ in the gas phase (see details in **section 4.1.4**) in which the Li is coordinated to a C6-face. The orientation of the *s-* and *p$_z$*-SAMOs is merely intended to illustrate what could be expected if the same SAMO distribution was rotated to approximate the position of the Li with respect to the substrate for the 4 proposed switched states. Such variation in the coupling between the substrate and the SAMOs could be expected to allow for some differentiation between the switched states based on the energies of corresponding resonance peaks. In an attempt to facilitate such a comparison **Fig. 5.13** depicts the c.c. *dI/dV* spectra from **Figs. 5.7-5.10**.

Collecting the c.c. *dI/dV* spectra from the above examples of each switched state (**Figs. 5.7-5.10**) affords a direct comparison of the corresponding resonance peak structures. The first point to make is that the consistency of the energies at which the visible LUMOs (labelled L+1 and L+4 in **Fig. 5.13**) are observed indicates that the switched states are not merely unidentified Li@C$_{60}$ adsorption orientations. As was reported in **section 4.1.3** and refs [16] and [17], rotation of the carbon cage alters the energy at which the LUMOs are measured, so the C6-Li@C$_{60}$ identified before the manipulation all retain the C6-
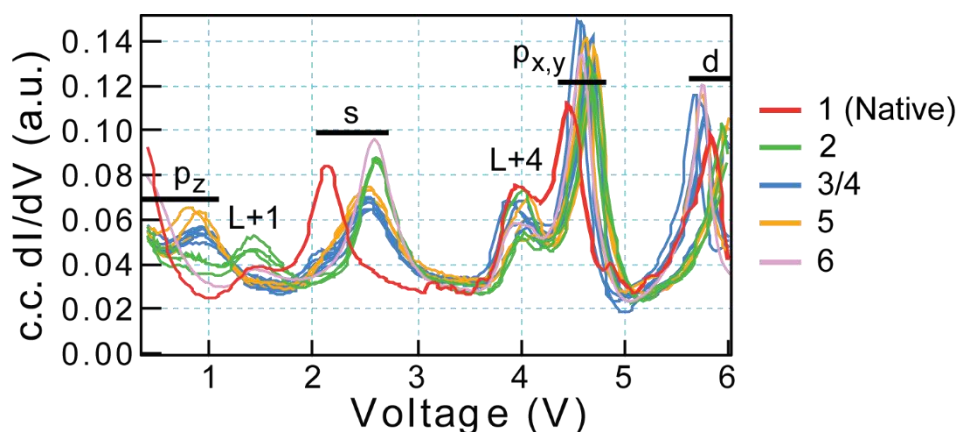
Figure 5.13: *c.c. dI/dV spectra of the various M-C6-Li@C_{60} switched states from **Figs.**
5.7-5.10.*

adsorption orientation after the manipulation too. Further still, the distinct azimuthal
orientations adopted by each switched state described above identify, without exception,
that the Li-cage coordination matches a C6-face on an M-C6-Li@C_{60}, never swapping to
an m-C6-C_{60}. Considering both the consistency in the LUMO peak energies and the cage
orientation, it is concluded that the manipulation involves the migration of Li around the
internal surface of a stationary C_{60}. As such, the manipulation will henceforth be referred
to as Li-migration.

Upon further examination of the spectra in **Fig. 5.13**, the other peaks all exhibit a shift in
energy compared to the corresponding peaks in the spectrum of the Li@C_{60} in the native
state (red). With the knowledge of the resonance peak identities for the native state (as
discussed in **section 4.1.4**), the *s*-, $p_{x,y}$- and *d*-SAMOs are easily labelled for the Li@C_{60}
switched states. Additionally, the upshift of the *s*- and $p_{x,y}$-SAMOs allows the assumption
that the switched state peaks ~+1 V have also been upshifted from a peak with a lower
energy in the native state. According to the PES data acquired by our collaborators (and
detailed in ref [18]), these peaks ~+1 V match the expected value for the resonance peak of
the p_z-SAMO of Li@C_{60}. This connection between the expected p_z-SAMO peak energy and
the general upshift observed for the other SAMOs is the method by which the p_z-SAMO
for the native state was confidently identified at ~+0.5 V (as detailed in **section 4.1.4**).
Given the general trend for upshifting in all switched state SAMOs, except for the *d*-SAMO,
it is apparent that the native state couples with the substrate considerably more strongly
than the switched states. A close inspection of the shift in the peaks of each switched

state may reveal information regarding the corresponding strength of the coupling with the substrate.

The range of the shift exhibited by each SAMO peak is indicated by the black bars in **Fig. 5.13**. The higher energy SAMOs ($p_{x,y}$- and d-SAMOs) appear to be less affected by the Li-migration with the range of each being less than ~500 mV, and in the case of the d-SAMO not solely upshifted. This is likely to be a combination of two effects. Firstly, the increased diffusivity of these SAMOs weakens the dependence on the position of the Li within the C_{60} (see **section 1.3.1.3**) minimising the energetic stabilisation. Secondly, the noise inherent in the c.c. dI/dV signal is exacerbated at higher energies which can lead to greater error in the recorded energy of the resonance peak. For the d-SAMO, for example, the shift in the resonance peak is seen to vary both up and down in energy from that of the native state. The p_z- and s-SAMOs, however, are highly directional and closely dependent on the Li-cage coordination (as proposed in **Fig. 5.12 (c)**). The interaction between these SAMOs and the empty states of the substrate will therefore be strongly altered by any movement of the Li with respect to that substrate, hence the larger upshift (more than 500 mV) for the p_z- and s-SAMO resonance peaks in **Fig. 5.13**.

Despite the proposed variation in the coupling between the SAMOs and the surface states (**Fig. 5.12 (c)**), there is an approximately uniform upshift for each of the p_z-, s- and $p_{x,y}$-SAMOs for the switched states. Though the energy of each of the resonance peaks is similar, the width of the p_z- and s-SAMO peaks and the general shape of the spectra allows each switched state to be differentiated from the others purely by observing the c.c. dI/dV spectrum of the fullerene. For example, level 2 exhibits a less distinctive p_z-SAMO, more distinctive LUMO+1 and a sharper s-SAMO peak compared to the distinctive p_z-SAMO, negligible LUMO+1 and a squatter s-SAMO peak of level 5. However, the differences in peak distribution are less distinctive than what could be expected for the various SAMO distributions proposed in **Fig. 5.12 (c)**. By considering the final piece of information acquired for each data set (I(t) measurements), it is hoped that further differentiation will be revealed, this is discussed in the following section.

5.2.3.2 - Analysing the variation in conductance between the Li@C_{60} switched states

The upshift in the p_z-, s- and $p_{x,y}$-SAMO resonance peaks discussed in **section 5.2.3.1** indicates that the stabilisation of these SAMOs reduces upon switching the Li@C_{60} out of

the native state. This is expected to be due to the proposed reorientation of the SAMOs as the Li-cage coordination changes. However, the analysis of the c.c. dI/dV spectra does not reveal a hierarchy for the resulting substrate-coupling strength of the switched state SAMOs. Since, discrete conductance levels are discernible in the I(t) curve in **Fig. 5.3**, further analysis of the conductance may afford greater understanding of the differences between the switched states. One might expect, for example, that the conductivity of the Li@C$_{60}$ is closely related to the overlap between the SAMOs and the substrate. **Fig. 5.14** collects a number of the I(t) curves recorded during the +5.0 V manipulations of various Li@C$_{60}$. Due to the process by which the manipulation is achieved, the initial tunnelling current exhibits minor variations. As such, the spectra in **Fig. 5.14** have been graphically normalised in order to directly compare the I(t) curves from a number of data sets.

The normalised I(t) traces are colour-coded as a function of the switched state, as indicated by the inset legend, with the conductance of the irreversible 15th state (discussed in **section 5.2.4**) highlighted in grey. Within **Fig. 5.14** bands of colour are utilised to emphasise the limited grouping of the switched states.

The Li@C$_{60}$ in the native state has the highest conductance, and the irreversible switched state exhibits the lowest conductance at ~35% of the native state. The grouping seen in **Fig. 5.14** of the conductance of the switched states around 80% (±10%) is similar to the fairly consistent shift of the SAMOs observed in the c.c. dI/dV spectra in **Fig. 5.13**. However, within this grouping there is a degree of differentiation which could allow for identification of a hierarchy in the strength of the switched state SAMO-substrate coupling. The conductance of the levels 2 and 3/4 switched states are almost identical, both observed at ~85%. The narrow band exhibiting the conductance of the level 6 switched state shows that it has a conductance of ~80%. The conductance of the level 5 switched state is the most reduced of the 13 reversible Li-switched states, seen at ~75%.
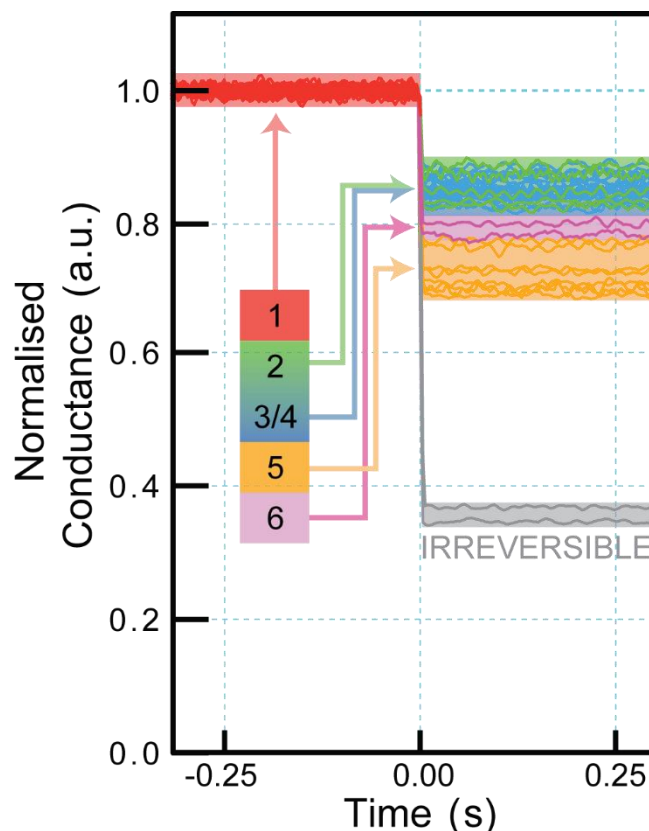
Figure 5.14: *Conductance curves from a selection of Li-manipulation processes at +5.0 V. These have been graphically normalised to allow for the ratio of the conductance change to be identified with respect to the starting conductance. Bands are formed which show that some of the switched states can be identified by the resulting conductance. Both the bands and the conductance graphs are coloured to match the inset legend.*

This differentiation between the conductance states in **Fig. 5.14** suggests minor variations in the strength of the surface coupling. However, the order of conductivity does not directly relate to the displacement of the Li from the substrate or the proposed degree of overlap of the p_z- and s-SAMOs with the surface states as shown in **Fig. 5.12 (c)**. Level 5 is the least conductive of the reversible switched states (suggesting weakest surface coupling) despite the expectation that level 3/4 would be the least coupled since both the p_z- and s-SAMOs are expected to be roughly parallel to the substrate. The unexpected change in the conductance of the fullerene between the switched states could suggest that these SAMOs (p_z- and s-) are not equally responsible for the degree of coupling between the Li@C_{60} and the substrate. For example, if the s-SAMO couples more strongly

than the p_z-SAMO, the greater overlap for the s-SAMO of levels 1, 2 and 3/4 would explain the greater conductivity compared to that of levels 5 and 6 which exhibit predominantly p_z-SAMO coupling. The observation that level 6 couples more strongly than level 5 (higher conductance) can also be explained since the coupling between the p_z-SAMO and the substrate is at its greatest. However, the comparable conductance for levels 2 and 3/4 requires additional discussion since the SAMOs of level 2 clearly exhibit greater overlap with the substrate than those of level 3/4.

The suggestion for the enhanced conductivity of level 3/4, compared to what would be expected based on the SAMO-substrate overlap, is linked to the neighbouring fullerenes. Since the p_z- and s-SAMOs are proposed to be parallel to the substrate the overlap with the SAMOs of the nearest neighbours will be maximised. The interaction with neighbouring C_{60} is hypothesised to be sufficiently strong to alter the internal potential surface of the carbon cage, hence the formation of level 3/4 (as discussed in **section 5.2.3.1**). It is suggested, therefore, that this intermolecular interaction is also responsible for enhancing the conductivity of the level 3/4 switched state. The SAMOs of C_{60} are known to form NFE bands when observed in 2D arrays. Conductance through the interaction of the p_z- and s-SAMOs with this NFE band is therefore proposed as the additional effect which affords the level 3/4 switched state similar conductivity to level 2. Unfortunately, these conclusions are purely conjecture and require considerable theoretical exploration before any certainty can be determined. Especially since the bands identified in **Fig. 5.14** are broad and exhibit some overlap at the boundaries of different switched states.

Similar to the variation in the exact position of the high energy SAMOs in the c.c. dI/dV spectra (as seen in **Fig. 5.13**), the broadness of these bands is suspected to result from the slight differences in the local environment of the selected Li@C_{60}. The effect of the nearest neighbours on the conductance of the Li@C_{60} can be identified by comparing an I(t) curve resulting from the rotation of a neighbour with those of successful Li-migrations, as depicted in **Fig. 5.15**. The 3 spectra correspond with the tunnelling current measured through different Li@C_{60} during manipulations which result in: neighbour rotations (red) and Li-switches into level 2 (green) and level 5 (orange).
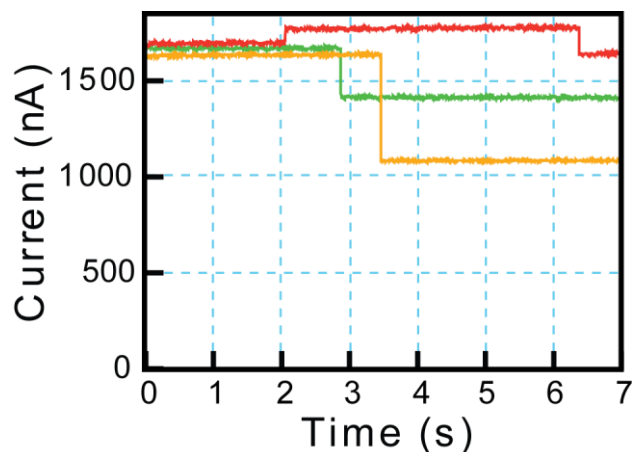
Figure 5.15: *I(t) curves depicting current changes observed during the manipulation of 3 different Li@C$_{60}$. The curves correspond with: a Li@C$_{60}$ remaining in the native state during neighbour rotations (red), and Li-switches into levels 2 (green) and 5 (orange).*

The red curve in **Fig. 5.15** exhibits two current changes (positive and negative) which result from rotations of C$_{60}$ adjacent to the selected Li@C$_{60}$ which remains in its native state. The magnitudes of these current changes (<200 nA) are typical of those resulting from the rotation of neighbouring C$_{60}$ and are noticeably smaller than the changes in the other two *I*(t) curves. The green curve illustrates a reduction in tunnelling current of ~300 nA which correlates with a migration of the Li into the level 2 switched state. The orange curve represents a switch of Li@C$_{60}$ into the level 5 switched state and exhibits a current change >500 nA.

Since these neighbour rotations are observed despite the atomic precision of the STM manipulation, it can be concluded that the energy required to activate these manipulations is minimal compared to the movement of the Li. The parameters utilised in this section (+5.0 V and 1.85 ±0.15 μA) result in the injection of a large amount of energy to the Li@C$_{60}$. As mentioned previously, this results in the occasional observation of irreversible modifications to the Li@C$_{60}$. 37 of the 307 fullerenes manipulated in the current study resulted in such modifications. The majority of these have been dismissed from the analysis since the specific molecular appearances were irreproducible and are concluded to be the result of a Li@C$_{60}$ decomposition. However, there are a rare few data sets which resulted in irreversible but reproducible manipulations. These are the topic of the next section.

5.2.4 - Identifying the ejection of Li from within the Li@C$_{60}$

1.0% of the Li@C$_{60}$ selected for manipulation produced a data set like that seen in **Fig. 5.16** which shows **(a)** STM images and **(b)** c.c. *dI/dV* spectra of a Li@C$_{60}$ before and after manipulation.

The STM images seen in **Fig. 5.16 (a)** show the familiar ring shape (at -2.5 V) and the diffuse beacon (at +2.5 V) identifying the selected fullerene (white ring) as a C6-Li@C$_{60}$. The STM images acquired after manipulation (**Fig. 5.16 (b)**) depict the same fullerene as revealed by inspection of the neighbouring fullerenes. However, these images depict a ring shape (at -2.5 V) and the segmented, 3-fold rotationally symmetric shape (+2.5 V) which is identical to those identified as C6-C$_{60}$ in **Chapter 4**. This suggests that the STM images in **Figs. 5.16 (a)** and **(b)** illustrate a successful Li-ejection which avoids destruction of the carbon cage. This Li-ejection is confirmed by the c.c. *dI/dV* spectra in **Fig. 5.16 (c)**. The red spectrum depicts the electronic structure of the fullerene before the manipulation, clearly that of a Li@C$_{60}$, and the grey spectrum shows the structure of the fullerene after the manipulation. The blue spectrum seen in **Fig. 5.16 (c)** is the c.c. *dI/dV* spectrum taken from **Fig. 4.13** and represents the electronic structure of C6-C$_{60}$ in a 2D array. The remarkable similarity between the grey and blue spectra in **Fig. 5.16 (c)** is the most compelling evidence that the Li has been ejected from the fullerene and that the selected Li@C$_{60}$ is now simply C$_{60}$. No further trace of the Li is observed on the surface, so it is determined that it has been fully ejected from the tunnelling junction, likely into the vacuum.

A number of techniques are available for producing Li@C$_{60}$ but the one most pertinent to these experiments involves the ballistic injection of Li$^+$ ions into C$_{60}$ within a target[19–22]. The minimum energy required is reported as 5 eV[19], which matches the working energy used to collect the Li-switch data detailed in **section 5.2.3**. By applying these manipulation parameters to Li@C$_{60}$ on the Au(111) surface it appears that the ballistic injection of Li$^+$ can be reversed. With a mind to this observation, the following section proposes a mechanism for the Li-migration.
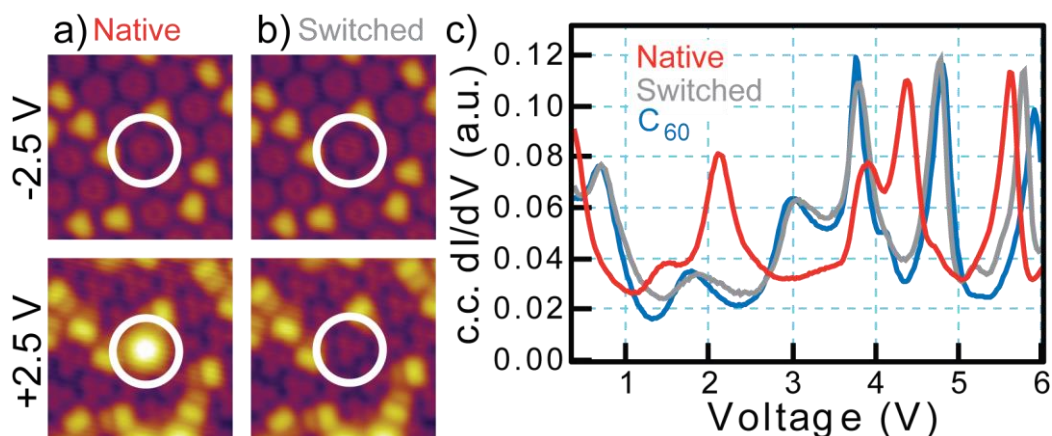
Figure 5.16: *STM images (-2.5 V, 0.1 nA and +2.5 V, 0.1 nA) depict a selected fullerene (white ring) **a)** before and **b)** after manipulation by application of +5.0 V and 1.8 µA. **c)** c.c. dI/dV spectra corresponding with the STM images in **a)** (red) and **b)** (grey), and an example of C6-C$_{60}$ (blue).*

5.2.5 - Proposing a mechanism for the STM-induced migration of Li within Li@C$_{60}$

Some elementary testing during the exploration of the Li@C$_{60}$ switch identifies that certain parameters must be met before the manipulation is observed within a workable timeframe (more than ~1 per minute, or ~0.02 Hz). **Fig. 5.17 (a)** shows an example of a c.c. *dI/dV* spectrum of Li@C$_{60}$ in the native state and the energies at which the Li-switch is observed are encapsulated by the grey region of the graph. The DFT-calculated isosurfaces of the p_z-, *s*-and $p_{x,y}$-SAMOs for Li@C$_{60}$ are presented again in **Fig. 5.17 (b)** to facilitate the discussion regarding the excitation mechanism for the Li-migration.

Fig. 5.17 (a) illustrates that the Li-migration is only observed at manipulation biases of +3.0 V and higher. As was mentioned briefly in **section 5.2.1**, at the lower boundary of this bias range extremely high currents are required before the switch is observed. As the switch bias is increased the current required to activate the Li-migration with a similar frequency reduces though remains high. However, as the bias is increased further, and especially if the current remains high, the frequency with which undesirable effects occur also increases, these effects include fullerene decomposition, collapse of the tunnel junction etc. The identification of these required parameters (≥+3.0 V and high tunnelling current) allows discussion of two common activation methods that are often employed in
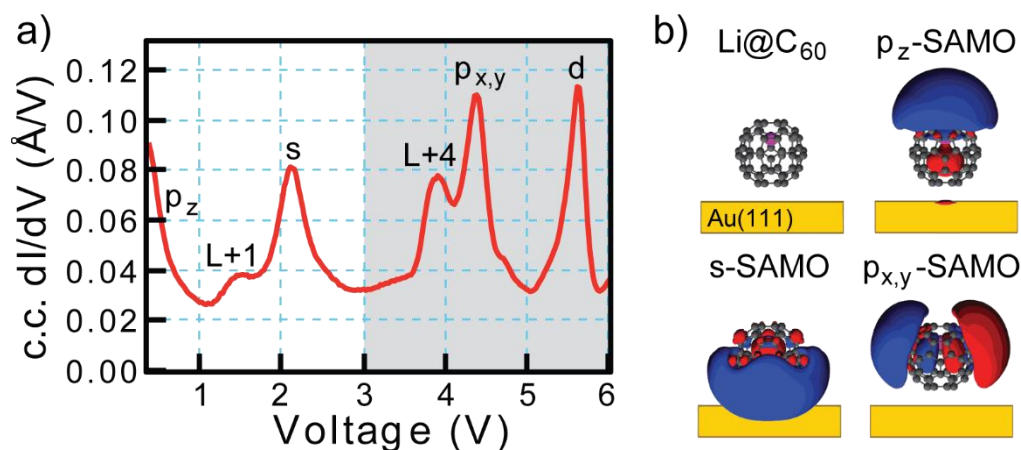
Figure 5.17: *a) c.c. dI/dV spectrum of a native state Li@C$_{60}$ on Au(111). The grey region extends upwards from +3.0 V and illustrates the energies at which the Li-migration is achieved. b) Ball and stick models illustrating the isosurfaces of p$_z$-, s- and p$_{x,y}$-SAMOs of Li@C$_{60}$ as calculated by DFT for gas phase fullerenes. As for Figs. 5.2 and 5.12, the substrate was not included in the calculations but is illustrated to aid discussion.*

the use of single molecule switches: electric fields (EF)[23–29] and inelastic electron tunnelling (IET)[30–33]. Both switch methods exhibit similar behaviour to the Li-migration: EF switches are bias dependent, and IETs mechanisms are closely related to the tunnelling current. However, neither of these mechanisms are quite sufficient to explain the Li-switch. The reasons why are discussed presently.

In order for an EF-induced molecular switch to be reversed, the bias polarity must be inverted. The reversible switching which is observed at a constant bias (see the positive and negative current changes in **Fig. 5.3**) illustrates that this clearly isn't the case for the Li-migration. Conversely, IET-mediated switch processes are polarity independent. However, attempts to activate the Li-migration with comparable parameters of the opposite polarity (-5.0 V, ~2 μA) instead result systematically in catastrophic collapse of the tunnel junction. A second reason that disproves the suggestion that the Li-migration is an IET-induced process is the magnitude of the bias required for activation.

IET-mediated molecular switches typically couple with vibronic states of the molecule. This behaviour is beautifully illustrated by Huang *et al.* in their experiments switching Sc$_3$N@C$_{80}$ by vibrational excitation of a bond stretch in the encapsulated molecule[11,12]. If

a similar process is responsible for the Li-migration, then the energy required would correlate with an internal excitation. However, the energy barriers for migration between potential wells in the C_{60} cage and intramolecular vibronic excitation fall within the range of 40-110 meV[6,34], a fraction of the +3 V which is observed as the lower limit for activation. For the above reasons, the Li-migration cannot be justified as either an inelastic electron tunnelling mediated manipulation or the response of an applied electric field. Another mechanism must be responsible.

Initially proposed by Jorn *et al*.[4], a third manipulation mechanism employs the concept of resonant tunnelling to activate a manipulation of the Li@C_{60}. Resonant tunnelling is the process by which incidental electrons couple with the molecular resonances of the fullerene in order to actuate a molecular manipulation. This mechanism was first identified for C_{60} in the work of Schulze *et al*. wherein they explored the decomposition of the fullerene by electronic excitation with an STM probe[2,3]. The details of their work are elaborated on in **section 5.3**, but essentially they observed a coupling between the energies of the incidental electrons and the LUMOs of the C_{60} which affected the current required to cause molecular decomposition. Subsequently Jorn *et al*., in their theoretical paper considering Li@C_{60} manipulation in a Au junction, briefly mention that resonant tunnelling through the SAMOs could allow excitation of the encapsulated Li[4]. It is well known that LUMOs couple strongly to the C_{60} cage so any attempts to excite the encapsulated Li by tunnelling into these orbitals are expected to result in the vibrational excitation of the fullerene (as observed by Schulze *et al*. [2,3]). However, SAMOs extend both beyond and inside the carbon cage. It is this access to the core of the fullerene which is proposed here to allow the tunnelling electrons to bypass the C_{60} cage and interact with the encapsulated Li directly.

The energy requirement to induce Li-migration (exhibited by the grey region of **Fig. 5.17 (a)**) suggests that only resonant tunnelling into the high energy electronic states results in a manipulation. This partially agrees with the proposal made by Jorn *et al*. since the SAMOs are typically high energy resonance states. For Li@C_{60}, however, this is an incomplete explanation since the *s*- and *p$_z$*-SAMOs are so drastically stabilised compared to those of C_{60}. By considering the isosurfaces in **Fig. 5.17 (b)** and the respective resonance peak labels in **Fig. 5.17 (a)**, further explanations for the switch parameters can be proposed.

The lower limit of the switch parameters (+3.0 V) coincides with the earliest onset for the convoluted signal for the LUMO+4 and $p_{x,y}$-SAMOs which means that both the p_z- and s-SAMOs are inactive with respect to the Li-switch. As discussed above and depicted in **Fig. 5.17 (b)**, a large overlap between the surface states and these inactive SAMOs is expected which would result in strong coupling and explain the degree of stabilisation compared to the SAMOs of C_{60}. This coupling with the surface is also hypothesised to be the reason that the p_z- and s-SAMOs are incapable of activating the Li-migration. In their theoretical studies of C_{60} on a MoS_2 support, Guo *et al*. observed that the "cooling" of "hot" (energetic) electrons in the SAMOs is far quicker by conduction into the surface states than by electron-phonon coupling which would result in vibrational excitation of the LUMOs[35]. The inactivity observed for the p_z- and s-SAMOs with respect to the Li-migration could be considered experimental confirmation of this theoretical observation. On the other hand, the $p_{x,y}$-SAMOs (as seen in **Fig. 5.17 (b)**) remain active for the manipulation because of negligible coupling with the substrate since these extend laterally from the fullerene, almost parallel to the surface.

With surface coupling minimised for $p_{x,y}$-SAMOs, electron conduction into the substrate will be reduced. This is expected to result in other behaviour becoming more prominent in the cooling of hot electrons since the lifetime of the electrons in the SAMOs is expected to increase. Arguably the most important behaviour for the current work is that the electrons in the $p_{x,y}$-SAMOs are now capable of penetrating the carbon cage and exciting the encapsulated Li rather than merely circumventing it like those in the p_z- and s-SAMOs. This is the mechanism by which the Li-migration is actuated, hence the onset of the switch parameters (grey region in **Fig. 5.17 (a)**) matching the low energy edge of the $p_{x,y}$-SAMOs resonance peak. This coincidence of the switch parameters and the resonance peak is the first evidence that the $p_{x,y}$-SAMOs are of significance for the Li-migration mechanism.

Another indication that the $p_{x,y}$-SAMOs are involved in the activation process is the observation of rotating C_{60} up to ~5nm from the Li@C_{60} selected for manipulation. This behaviour is thought to be linked to the NFE band formed by the hybridisation of the quasi-degenerate $p_{x,y}$-SAMOs of Li@C_{60} and C_{60} (as discussed in **Chapter 4**). Conduction of hot electrons through this NFE band could allow excitation of neighbouring C_{60}, hence the occasional rotations observed throughout the data collection for **section 5.2**. Though this hypothesis predominantly aids the discussion in favour of the $p_{x,y}$-SAMOs as the activation

pathway, it also provides a suggestion for the requirement for the large tunnelling current. With conduction through the NFE band removing hot electrons from the selected Li@C_{60} fewer electrons are available to penetrate the carbon cage therefore reducing the chance of Li-excitation.

A second suggestion for the requirement of a large tunnelling current is related to the low probability of Li activation. Upon successful penetration of the carbon cage, sufficient energy transfer to the Li is required before the migration can occur but this is only expected to occur for a small number of electrons which enter the fullerene. Increasing the tunnelling current provides more electrons which will increase the probability of an electron remaining in the $p_{x,y}$-SAMOs of the Li@C_{60} instead of dispersing through the NFE band. This increased population of the SAMO is then expected to increase the probability that an electron will penetrate the carbon cage and excite the Li. As this probability increases, the time between Li-migrations reduces resulting in the switch occurring more regularly. The combination of conduction through the NFE band and the low probability of sufficiently exciting the Li are proposed as the reasons that such high tunnelling currents were required during the data collection stage of this project.

The parameters capable of activating the Li-migration have only been identified to illustrate that the manipulation is possible. With further exploration, which is beyond the scope of the current study, specific behaviour could be tracked to identify if there is a connection between the manipulation bias and the tunnelling current required to activate the Li-migration. Schulze *et al*. recognised that the tunnelling current required for decomposition is dependent on whether the manipulation bias couples with LUMOs[2,3], so closer observation of the Li-migration may reveal a similar connection between the manipulation parameters. For example, we may observe that if the manipulation bias couples directly with the $p_{x,y}$-SAMOs the tunnelling current required to activate the Li-migration within a workable timeframe would reduce. Without additional study of this behaviour, however, such suggestions are merely conjecture.

5.3 - Exploring decomposition of C_{60} with resonant tunnelling electrons

As mentioned in the previous section, experiments completed by Schulze *et al*.[2,3] identified that the current required to decompose C_{60} by vibrational excitation varies depending on the tunnelling bias. At low energies (<3.25 V), Schulze *et al.* report that C_{60}

exhibits a large capacity for thermal excitation before the molecule decomposes. This behaviour results from heat dissipation across the surface of the C_{60} cage due to the molecular structure effectively conducting the incidental electrons away from the bond upon which they impinge. The dispersion of these hot electrons therefore requires a much greater tunnelling current to cause decomposition, since it must thermally excite the whole molecule instead of a single bond. As the efficacy of this dispersion alters, so too does the tunnelling current required for decomposition (I_{dec}). For example, stronger surface coupling is observed to increase dispersion of the hot electrons because the surface is also capable of cooling the fullerene which results in a higher I_{dec}. Schulze *et al.* observed this when studying the difference between C_{60} adsorbed on Cu(110), Pb(111) and Au(111)[3] but since the Li@C_{60} couples more strongly to the Au(111) surface than C_{60}, a qualitatively similar increase in the I_{dec} could be expected.

It is noted in the above mentioned work that, as the energy of the incidental electrons increases, the I_{dec} gradually decreases. This is understandable since each electron has more energy thus the energy lost to the fullerene is greater and the molecule is excited more efficiently. However, when the electron energy coincides with a LUMO resonance, the I_{dec} decreases more drastically. The LUMOs are carbon-centred orbitals which couple to the vibrational modes of the C_{60}. Excitation of the LUMOs, therefore, leads to more efficient activation of the fullerene since each incidental electron is capable of directly exciting a vibrational mode. This effect is referred to as resonant tunnelling.

The published work does not report on vibrational excitation by resonant tunnelling at energies higher than +3.25 V on the C_{60}/Au(111) system[2,3]. Coincidentally, this is approximately the onset of the *s*-SAMO resonance peak for C_{60} on Au(111). Thus, the behaviour of the molecular system when the resonant tunnelling couples with the SAMOs is, as yet, unexplored. The diffuse and conductive nature of the core-centred SAMOs leads to the prediction that a much greater I_{dec} will be required since a large portion of the incidental electrons will simply be conducted directly to the substrate without exciting the fullerene. Though no comprehensive study is explored in the current work, some attempt was made to emulate the experiments of Schulze *et al*. with the intention of determining the effect of the SAMOs, and repeating the experiments for Li@C_{60}.

5.3.1 - Exploring the decomposition of C_{60} when resonant tunnelling into SAMOs

The manipulation technique employed in decomposition experiments differs slightly from that required for Li-migration. Where the Li-migration method maintains constant parameters during a manipulation attempt, the decomposition technique fixes the bias but increases the tunnelling current until a reduction in the conductance is observed. Upon such an alteration, the parameters are removed and the effect of the manipulation is determined with STM imaging and spectroscopy, for example whether simple rotation or decomposition of the fullerene has been induced. For this exploration, consistency between selected fullerenes is important to ensure that any data collected can be reliably compared with those reported. As such, C6-C_{60} are predominantly selected for manipulation since these are easily identified (see analysis in **Chapter 4**), and are rarely observed rotating during the above reported Li-migration experiments (see **section 5.2**). This resistance to rotation is thought to be beneficial to the decomposition experiments since it reduces the potential for false signals i.e. recording a conductance change as decomposition, when it only corresponds with a C_{60} rotation.

Initial experiments selected the C6-C_{60} within C_{60}/Li@C_{60} mixed islands, as detailed in **Chapter 4**, since these samples are thoroughly discussed and analysed in this thesis. After numerous attempts to reproduce what was reported by Schulze *et al*.[2,3], two issues are observed which prevent successful analysis of this molecular system. Firstly, the process is less reliable than what was reported, the vast majority of experiments result in the collapse of the tunnel junction rather than decomposition of the selected C_{60}. Secondly, the few successful I_{dec} which are recorded are significantly larger than those reported by Schulze *et al*. One suggestion for the origin of this behaviour is the greater surface coupling of Li@C_{60}. The higher conductivity of these endohedral fullerenes[36,37] may allow them to act as current sinks in the NFE band which could result in a drastic reduction in the tunnelling electrons effectively exciting the selected C6-C_{60}. In an attempt to avoid such an issue a new surface composed of pure C_{60} islands is prepared.

Despite attempts to remedy the issues described above by preparing a surface of purely C_{60} 2D arrays, the results remain inconsistent with what is reported. The greatest departure from literature is that alterations to the molecule do not always correspond with a change in conductance. For example, many occasions of a fullerene rupturing were only realised upon imaging the molecules after spontaneously removing the manipulation

parameters. These instances had to be discarded from the analysis because there could be no certainty in the reported I_{dec}.

In a final attempt to compare results with the work of Schulze *et al.*, non-C6-C_{60} are selected for decomposition from within the pure C_{60} arrays. These tests are intended to determine whether the stability gained by the C6-adsorption orientation is the reason for the present failure to acquire comparative results. Once again, however, the data acquired is of minimal use. The majority of attempts merely result in rotations of the C_{60} or collapse of the tunnel junction instead of decomposition, and any results which are successful do not corroborate the observations made by Schulze *et al.*[2,3].

Though no experiments afforded confirmation, or further exploration, of the landscape of the decomposition of C_{60} some hypotheses regarding the effect of resonant tunnelling into the SAMOs can be discussed. The diffuse nature of the C_{60} SAMOs is expected to be capable of conducting incidental electrons such that the majority of resonant tunnelling electrons circumvent the fullerene and are lost to the surface states or the NFE band which forms between condensed fullerenes. This conductance away from the selected C_{60} would result in the I_{dec} dramatically increasing since far more electrons would be required to sufficiently excite the vibronic states in order to cause a decomposition of the C_{60}. Similar behaviour would be expected for Li@C_{60} but the encapsulated Li complicates the electronic structure. Whereas the low energy electrons which couple with the LUMOs for C_{60} result in a reduced I_{dec}, the Li stabilises the p_z- and s-SAMOs sufficiently that these are at similar energies to the LUMO and LUMO+1. As such these SAMOs may act as conduction pathways even for low energy electrons which would drastically increase the I_{dec} compared to C_{60} at similar energies. This hypothesis can, somewhat, be supported by the observations made during the Li-migration experiments. Despite the inability to activate the Li-switch below +3 V, Li@C_{60} frequently withstood extreme currents (>3.5 µA) without exhibiting adverse effects. This behaviour indicates an increased capacity for avoiding decomposition and it is suggested that the conductivity of the SAMOs is the root cause. Further experimentation is beyond the scope of this project, but successful exploration of both C_{60} and Li@C_{60} would be particularly useful to aid the discussion in the role of SAMOs in the conduction of electrons through molecular systems.

5.4 - Concluding remarks

This chapter identifies that Li@C$_{60}$ can be reversibly switched between 14 distinct states by applying suitable manipulation parameters (≥+3.0 V, ≥~1.5 μA) with an STM probe. The Li@C$_{60}$ are identified as adopting the same starting state, referred to as the native state. In this state the Li is coordinated to the uppermost C6-face whilst the molecule is constrained within a 2D array of fullerenes on a Au(111) surface. The experimental data detailed above simultaneously proves decades of speculation migration of Li within that Li@C$_{60}$ can be selectively activated[1,4,6–10,34,38–42] and identifies it as a molecule with a significantly higher number of stable states than other multi-state molecular switches[11,12,43]. The states are determined by a mixture of STM imaging and spectroscopy. 8 of the 14 reversible states correspond with Li-cage coordinations where the Li is located nearest to the C6-faces on levels 1, 2, 5 and 6 of a C6-C$_{60}$ (see **Figs. 5.12 (a)** and **(b)**). The remaining 6 adopt an equatorial position which appears to be a hybridisation of the C6-faces in levels 3 and 4. These proposed level 3/4 coordination sites are formed by interactions with the neighbouring fullerenes altering the internal surface potential of the carbon cage.

Though 14 is not the anticipated 20 switch states (see **Fig. 5.1**), this is thought to be due to the condensation of the Li@C$_{60}$ into a 2D array reducing the 12 sites in levels 3 and 4 to 6 in the hybrid state of level 3/4. Access to all 20 C6-faces would be expected if the manipulation were achieved on an isolated Li@C$_{60}$. Though this was not attempted during the data collection of this project, Li-migration within isolated molecules is not expected to be possible due to the extreme manipulation parameters required to activate it. Scattering across the surface or desorption of the Li@C$_{60}$ is anticipated before the desired migration would be achieved.

One concern for the Li-manipulation is whether the Li migrates between coordination sites within a fixed cage or if the fullerene itself rotates to adopt these new orientations. Firstly, rotating the molecule would inherently bring in more variation to end states. Each of the 14 reversible switch states described above exhibits discrete azimuthal orientations which result in the C6-faces of the cage occupying an identical position when comparing those of the final and native states. Over such a large data set this is statistically very improbable and some unaligned but recognisable switch states would be expected. A random rotation of the fullerene would eventually result in a fullerene swapping between

M-C6-Li@C_{60} and m-C6-Li@C_{60} but this has never been observed in 307 reported manipulation events. Secondly, the confident identification of the level 3/4 hybrid state shows that the switch cannot simply be a rotation of the Li@C_{60} since the Li-cage coordination in this state is fundamentally different from that of the native state. It is for these reasons we can safely state that the Li migrates around the inside of the C_{60} cage before stabilising into one of the 14 coordination sites.

By considering the requirement for such extreme parameters, a new manipulation mechanism is proposed. Vibrational excitation of Li@C_{60} by resonant tunnelling through the $p_{x,y}$-SAMOs activates a rapid internal migration of the Li around a fixed C_{60} cage. Spontaneous stabilisation of the Li results in the adoption of one of 15 final states: 14 reversible switched states (as detailed above) and a rare, irreversible 15th state which has been identified as Li-ejection. The rattling motion of the Li around the modified inner surface potential of the C_{60} is how the molecule became known, within our group, as the molecular maraca.

Finally, attempts have been made to explore the effect of resonant tunnelling on the decomposition of both C_{60} and Li@C_{60} by vibrational excitation. The intention was to replicate and expand upon the work of Schulze *et al.*[2,3] but various issues with the method have led to inconclusive data. Thus, no further observations have been made and we can only speculate on the effect that resonant tunnelling into SAMOs would have on the current required to trigger decomposition of either C_{60} or Li@C_{60}.

5.5 - <u>References</u>

(1)   Bakowies, D.; Thiel, W. MNDO Study of Large Carbon Clusters. *J. Am. Chem. Soc.* **1991**, *113* (10), 3704–3714. https://doi.org/10.1021/ja00010a012.

(2)   Schulze, G.; Franke, K. J.; Gagliardi, A.; Romano, G.; Lin, C. S.; Rosa, A. L.; Niehaus, T. A.; Frauenheim, T.; Di Carlo, A.; Pecchia, A.; Pascual, J. I. Resonant Electron Heating and Molecular Phonon Cooling in Single C60 Junctions. *Phys. Rev. Lett.* **2008**, *100* (13), 136801. https://doi.org/10.1103/PhysRevLett.100.136801.

(3)   Schulze, G.; Franke, K. J.; Pascual, J. I. Resonant Heating and Substrate-Mediated Cooling of a Single C60 Molecule in a Tunnel Junction. *New J. Phys.* **2008**, *10*, 065005. https://doi.org/10.1088/1367-2630/10/6/065005.

(4)   Jorn, R.; Zhao, J.; Petek, H.; Seideman, T. Current-Driven Dynamics in Molecular Junctions: Endohedral Fullerenes. *ACS Nano* **2011**, *5* (10), 7858–7865. https://doi.org/10.1021/nn202589p.

(5)   Yamada, Y.; Kuklin, A. V.; Sato, S.; Esaka, F.; Sumi, N.; Zhang, C.; Sasaki, M.; Kwon, E.;

Kasama, Y.; Avramov, P. V.; Sakai, S. Electronic Structure of Li+@C60: Photoelectron Spectroscopy of the Li+@C60[PF6−] Salt and STM of the Single Li+@C60 Molecules on Cu(111). *Carbon N. Y.* **2018**, *133* (111), 23–30. https://doi.org/10.1016/j.carbon.2018.02.106.

(6)   Bernshtein, V.; Oref, I. Surface Migrations of Endohedral Li+ on the Inner Wall of C60. *Phys. Rev. A* **2000**, *62* (February), 033201. https://doi.org/10.1103/PhysRevA.62.033201.

(7)   Aoyagi, S.; Tokumitu, A.; Sugimoto, K.; Okada, H.; Hoshino, N.; Akutagawa, T. Tunneling Motion and Antiferroelectric Ordering of Lithium Cations Trapped inside Carbon Cages. *J. Phys. Soc. Japan* **2016**, *85* (9), 094605. https://doi.org/10.7566/JPSJ.85.094605.

(8)   Kwon, E.; Komatsu, K.-I.; Kawachi, K.; Kasama, Y.; Endo, T. Dynamic Behavior of Lithium-Cation in a C60 Fullerene Cage Elucidated by Terahertz Spectroscopy. *Mol. Cryst. Liq. Cryst.* **2014**, *598* (1), 28–31. https://doi.org/10.1080/15421406.2014.933294.

(9)   Suzuki, H.; Ishida, M.; Yamashita, M.; Otani, C.; Kawachi, K.; Kasama, Y.; Kwon, E. Rotational Dynamics of Li+ Ions Encapsulated in C60 Cages at Low Temperatures. *Phys. Chem. Chem. Phys.* **2016**, *18* (46), 31384–31387. https://doi.org/10.1039/C6CP06949E.

(10)   Aoyagi, S.; Sado, Y.; Nishibori, E.; Sawa, H.; Okada, H.; Tobita, H.; Kasama, Y.; Kitaura, R.; Shinohara, H. Rock-Salt-Type Crystal of Thermally Contracted C60 with Encapsulated Lithium Cation. *Angew. Chemie - Int. Ed.* **2012**, *51* (14), 3377–3381. https://doi.org/10.1002/anie.201108551.

(11)   Huang, T.; Zhao, J.; Feng, M.; Popov, A. A.; Yang, S.; Dunsch, L.; Petek, H. A Molecular Switch Based on Current-Driven Rotation of an Encapsulated Cluster within a Fullerene Cage. *Nano Lett.* **2011**, *11* (12), 5327–5332. https://doi.org/10.1021/nl2028409.

(12)   Huang, T.; Zhao, J.; Feng, M.; Popov, A. A.; Yang, S.; Dunsch, L.; Petek, H. A Multi-State Single-Molecule Switch Actuated by Rotation of an Encapsulated Cluster within a Fullerene Cage. *Chem. Phys. Lett.* **2012**, *552*, 1–12. https://doi.org/10.1016/j.cplett.2012.09.064.

(13)   Liu, L.; Liu, S.; Chen, X.; Li, C.; Ling, J.; Liu, X.; Cai, Y.; Wang, L. Switching Molecular Orientation of Individual Fullerene at Room Temperature. *Sci. Rep.* **2013**, *3* (111), 3062. https://doi.org/10.1038/srep03062.

(14)   Neel, N.; Limot, L.; Kroger, J.; Berndt, R. Rotation of C60 in a Single-Molecule Contact. *Phys. Rev. B* **2008**, *77* (October 2007), 125431. https://doi.org/10.1103/PhysRevB.77.125431.

(15)   Delaney, P.; Greer, J. C. C60 as a Faraday Cage. *Appl. Phys. Lett.* **2004**, *84* (3), 431–433. https://doi.org/10.1063/1.1640783.

(16)   Daughton, D. R.; Gupta, J. A. Orientation Dependence of Charge Transfer for C60 on Cu(100). *Appl. Phys. Lett.* **2011**, *98* (13), 133303. https://doi.org/10.1063/1.3569719.

(17)   Schull, G.; Néel, N.; Becker, M.; Kröger, J.; Berndt, R. Spatially Resolved Conductance of Oriented C60. *New J. Phys.* **2008**, *10* (6), 065012. https://doi.org/10.1088/1367-2630/10/6/065012.

(18)   Stefanou, M.; Chandler, H. J.; Mignolet, B.; Williams, E.; Nanoh, S. A.; Thompson, J. O. F.; Remacle, F.; Schaub, R.; Campbell, E. E. B. Angle-Resolved Photoelectron Spectroscopy and Scanning Tunnelling Spectroscopy Studies of the Endohedral Fullerene Li@C60. *Nanoscale* **2019**, *11*, 2668–2678. https://doi.org/10.1039/c8nr07088a.

(19)   Ohno, K.; Maruyama, Y.; Esfarjani, K.; Kawazoe, Y.; Sato, N.; Hatakeyama, R.; Hirata, T.; Niwano, M. Ab Initio Molecular Dynamics Simulations for Collision between C60- and

Alkali-Metal Ions: A Possibility of Li@C60. *Phys. Rev. Lett.* **1996**, *76*, 3590–3593. https://doi.org/10.1103/PhysRevLett.76.3590.

(20)   Wan, Z.; Christian, J. F.; Basir, Y.; Anderson, S. L. Collision of Alkali Ions with C60/C70: Insertion, Thermionic Emission, and Fragmentation. *J. Chem. Phys.* **1993**, *99* (8), 5858–5870. https://doi.org/10.1063/1.465939.

(21)   Tellgmann, R.; Krawez, N.; Lin, S.-H.; Hertel, I. V.; Campbell, E. E. B. Endohedral Fullerene Production. *Nature* **1996**, *382* (6590), 407–408. https://doi.org/10.1038/382407a0.

(22)   Campbell, E. E. B.; Tellgmann, R.; Krawez, N.; Hertel, I. V. Production and LDMS Characterisation of Endohedral Alkali-Fullerene Films. *J. Phys. Chem. Solids* **1997**, *58* (11), 1763–1769.

(23)   Alemani, M.; Peters, M. V.; Hecht, S.; Rieder, K. H.; Moresco, F.; Grill, L. Electric Field-Induced Isomerization of Azobenzene by STM. *J. Am. Chem. Soc.* **2006**, *128* (45), 14446–14447. https://doi.org/10.1021/ja065449s.

(24)   Kornilovitch, P. E.; Bratkovsky, A. M.; Williams, R. S. Bistable Molecular Conductors with a Field-Switchable Dipole Group. *Phys. Rev. B - Condens. Matter Mater. Phys.* **2002**, *66* (24), 1–7. https://doi.org/10.1103/PhysRevB.66.245413.

(25)   Collier, C. P.; Mattersteig, G.; Wong, E. W.; Luo, Y.; Beverly, K.; Sampaio, J.; Raymo, F. M.; Stoddart, J. F.; Heath, J. R. A [2]Catenane-Based Solid State Electronically Reconfigurable Switch. *Science (80-.).* **2000**, *289* (5482), 1172–1175. https://doi.org/10.1126/science.289.5482.1172.

(26)   Yasutake, Y.; Shi, Z.; Okazaki, T.; Shinohara, H.; Majima, Y. Single Molecular Orientation Switching of an Endohedral Metallofullerene. *Nano Lett.* **2005**, *5* (6), 1057–1060. https://doi.org/10.1021/nl050490z.

(27)   Raggi, G.; Stace, A. J.; Bichoutskaia, E. Polarisation Charge Switching through the Motion of Metal Atoms Trapped in Fullerene Cages. *Phys. Chem. Chem. Phys.* **2014**, *16* (43), 23869–23873. https://doi.org/10.1039/c4cp02672a.

(28)   Leoni, T.; Guillermet, O.; Walch, H.; Langlais, V.; Scheuermann, A.; Bonvoisin, J.; Gauthier, S. Controlling the Charge State of a Single Redox Molecular Switch. *Phys. Rev. Lett.* **2011**, *106* (21), 216103. https://doi.org/10.1103/PhysRevLett.106.216103.

(29)   Foroutan-Nejad, C.; Andrushchenko, V.; Straka, M. Dipolar Molecules inside C70: An Electric Field-Driven Room-Temperature Single-Molecule Switch. *Phys. Chem. Chem. Phys.* **2016**, *18* (48), 32673–32677. https://doi.org/10.1039/C6CP06986J.

(30)   Simpson, G. J.; Hogan, S. W. L.; Caffio, M.; Adams, C. J.; Früchtl, H.; Van Mourik, T.; Schaub, R. New Class of Metal Bound Molecular Switches Involving H-Tautomerism. *Nano Lett.* **2014**, *14* (2), 634–639. https://doi.org/10.1021/nl4038517.

(31)   Choi, B. Y.; Kahng, S. J.; Kim, S.; Kim, H.; Kim, H. W.; Song, Y. J.; Ihm, J.; Kuk, Y. Conformational Molecular Switch of the Azobenzene Molecule: A Scanning Tunneling Microscopy Study. *Phys. Rev. Lett.* **2006**, *96* (15), 156106. https://doi.org/10.1103/PhysRevLett.96.156106.

(32)   Scheil, K.; Gopakumar, T. G.; Bahrenburg, J.; Temps, F.; Maurer, R. J.; Reuter, K.; Berndt, R. Switching of an Azobenzene-Tripod Molecule on Ag(111). *J. Phys. Chem. Lett.* **2016**, *7* (11), 2080–2084. https://doi.org/10.1021/acs.jpclett.6b01011.

(33)   Pavliček, N.; Fleury, B.; Neu, M.; Niedenführ, J.; Herranz-Lancho, C.; Ruben, M.; Repp, J. Atomic Force Microscopy Reveals Bistable Configurations of Dibenzo[a,h]Thianthrene and Their Interconversion Pathway. *Phys. Rev. Lett.* **2012**, *108* (8), 086101.

https://doi.org/10.1103/PhysRevLett.108.086101.

(34)   Zhang, M.; Harding, L. B.; Gray, S. K.; Rice, S. A. Quantum States of the Endohedral
         Fullerene Li@C60. *J. Phys. Chem. A* **2008**, *112*, 5478–5485.
         https://doi.org/10.1021/jp801083m.

(35)   Guo, H.; Zhao, C.; Zheng, Q.; Lan, Z.; Prezhdo, O. V.; Saidi, W. A.; Zhao, J. Superatom
         Molecular Orbital as an Interfacial Charge Separation State. *J. Phys. Chem. Lett.* **2018**, *9*
         (12), 3485–3490. https://doi.org/10.1021/acs.jpclett.8b01302.

(36)   Pavanello, M.; Jalbout, A. F.; Trzaskowski, B.; Adamowicz, L. Fullerene as an Electron
         Buffer: Charge Transfer in Li@C60. *Chem. Phys. Lett.* **2007**, *442*, 339–343.
         https://doi.org/10.1016/j.cplett.2007.05.096.

(37)   Popok, V. N.; Azarko, I. I.; Gromov, A. V.; Jönsson, M.; Lassesson, A.; Campbell, E. E. B.
         Conductance and EPR Study of the Endohedral Fullerene Li@C60. *Solid State Commun.*
         2005, *133* (8), 499–503. https://doi.org/10.1016/j.ssc.2004.12.014.

(38)   Campbell, E. E. B.; Fanti, M.; Hertel, I. V.; Mitzner, R.; Zerbetto, F. The Hyperpolarisability
         of an Endohedral Fullerene: Li@C60. *Chem. Phys. Lett.* **1998**, *288* (1), 131–137.
         https://doi.org/10.1016/S0009-2614(98)00255-3.

(39)   Gromov, A.; Krawez, N.; Lassesson, A.; Ostrovskii, D. I.; Campbell, E. E. B. Optical
         Properties of Endohedral Li@C60. *Curr. Appl. Phys.* **2002**, *2* (1), 51–55.
         https://doi.org/10.1016/S1567-1739(01)00101-8.

(40)   Gromov, A.; Ostrovskii, D.; Lassesson, A.; Jönsson, M.; Campbell, E. E. B. Fourier
         Transform Infrared and Raman Spectroscopic Study of Chromatographically Isolated
         Li@C60 and Li@C70. *J. Phys. Chem. B* **2003**, *107* (41), 11290–11301.
         https://doi.org/10.1021/jp030403w.

(41)   Li, Y. S.; Tománek, D. How Free Are Encapsulated Atoms in C60? *Chem. Phys. Lett.* **1994**,
         221 (5–6), 453–458. https://doi.org/10.1016/0009-2614(94)00297-5.

(42)   Hernández-Rojas, J.; Bretón, J.; Gomez Llorente, J. M. Rotational Spectra for Off-Center
         Endohedral Atoms at C60 Fullerene. *J. Chem. Phys.* **1996**, *104* (4), 1179–1186.
         https://doi.org/10.1063/1.470778.

(43)   Auwärter, W.; Seufert, K.; Bischoff, F.; Ecija, D.; Vijayaraghavan, S.; Joshi, S.;
         Klappenberger, F.; Samudrala, N.; Barth, J. V. A Surface-Anchored Molecular Four-Level
         Conductance Switch Based on Single Proton Transfer. *Nat. Nanotechnol.* **2012**, *7* (1), 41–
         46. https://doi.org/10.1038/nnano.2011.211.

6 - <u>Conclusions</u>

This project set out with the intention of being the first to unambiguously experimentally identify the electronic structure of Li@C_{60} and compare it with that of C_{60} in order to ascertain the electronic stabilisation effect of Li-encapsulation. This stabilisation has been determined by combining our efforts on the low temperature scanning tunnelling microscope (LT-STM) with those of our collaborators[1]. Both the gas phase photoelectron spectroscopy (PES) and time-dependent density functional theory (TDDFT) calculations from collaborators at the University of Edinburgh and University of Liège, respectively, aided greatly in deciphering the single molecule electronic spectra achieved with the LT-STM.

Upon being the first to report on an STM study of the Li@C_{60}/Au(111) system[1,2], the second goal for these experiments was to determine the potential for Li@C_{60} to act as a single molecule switch. Since it is well known that the Li favourably stabilises off-centre towards 1 of the 20 C6-faces on the carbon cage, it has been suggested for decades[3] that Li@C_{60} could be utilised as a single molecule switch. Though some migration of Li around the internal surface of the C_{60} has been observed experimentally in both the gas phase and bulk crystal, these result from either thermal excitation[4,5] or application of terahertz radiation[6,7]. Neither of these previously used techniques are capable of achieving observation or excitation of single molecules, unlike STM.

6.1 - <u>Summary of experimental observations</u>

Using methods detailed in **Chapter 2** to examine the molecular systems prepared with the conditions described in **Chapter 3**, the distribution of Li@C_{60} and C_{60} across Au(111) and Cu(110)-(2×1)O was analysed and discussed in **Chapter 4**. The first requirement for the surface exploration was to identify the endohedral fullerenes. Upon post-adsorption annealing the Au(111) surface to ~570 K, the deposited fullerenes formed large 2D arrays which adopted the $(2\sqrt{3}×2\sqrt{3})$R30° packing structure. Imaging at +2.5 V revealed that there was some bias dependence to the molecular appearance which revealed that 12.6% of the fullerenes lost any structural definition in the molecular appearance. Instead these fullerenes lit up like beacons, appearing circular and diffuse unlike the remaining 87.4% of fullerenes which retained structural information. This is similar to what Yamada *et al*. observed for Li@C_{60} on Cu(111)[8]. Examining the electronic structure of the 4 types of fullerene with scanning tunnelling spectroscopy (STS) revealed that these beacons were Li@C_{60} and all remaining fullerenes were simply different adsorption orientations of C_{60} (as shown in **Fig. 6.1**).
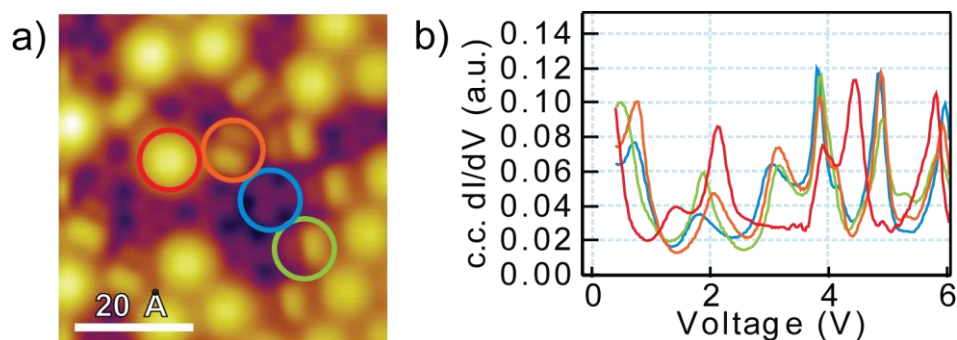
Figure 6.1: a) *STM image (+2.5 V, 0.1 nA) of a portion of a large* $(2\sqrt{3}\times2\sqrt{3})R30°$ *array of fullerenes on Au(111).* **b)** *c.c. dI/dV spectra of the 4 fullerenes in* **a)**. *The colours indicate the following adsorption configurations: C6-Li@C_{60} (red), 6:6-C_{60} (orange), C6-C_{60} (blue), and C-C_{60} (green).*

The STM image (+2.5 V, 0.1 nA) illustrates the 4 molecular appearances present in the $(2\sqrt{3}\times2\sqrt{3})R30°$ array and matches them, by way of coloured rings, to the corresponding c.c. *dI/dV* spectra. The red spectrum is distinctly different from the other 3 spectra and thus the Li@C_{60} was identified as the diffuse molecular appearance within the 2D arrays imaged at +2.5 V. The three remaining spectra and molecular appearances represent different adsorption orientations of C_{60}: 6:6-C_{60} (orange), C6-C_{60} (blue), and C-C_{60} (green). Once differentiation between the Li@C_{60} and C_{60} had been achieved, the resonance peaks of each were compared with the PES data from our collaborators[1] and with calculations from Feng *et al*.[9] in order to identify the electronic structure. This afforded direct comparison between specific peaks allowing recognition of the effect that Li-encapsulation had on the electronic structure of the C_{60}, as illustrated by the spectra in **Fig. 6.2**.

The *dI/dV* spectra in **Figs. 6.2 (a)** and **(b)** depict the resonance peak structures of C6-C_{60} and C6-Li@C_{60}, respectively. Direct comparison between the two affords identification of the stabilisation resulting from the Li-encapsulation. For example, the $p_{x,y}$-SAMO is stabilised by ~0.5 eV for Li@C_{60}, the *s*-SAMO by almost 2 eV and the p_z-SAMO by ~4 eV. The peak assignments made in **Fig. 6.2** (described in greater detail in **section 4.1.4**) are the result of comparing the STS data with the PES data provided by our collaborators[1]. These results are the seminal experimental confirmation of the theoretical calculations which predicted that the *s*- and p_z-SAMOs of C_{60} would be strongly stabilised upon encapsulation of Li[9].

In an attempt to provide additional evidence towards the peak assignment discussed above, constant current differential conductance scanning tunnelling microscopy (c.c. *dI/dV* STM) was also utilised. It was anticipated that this technique would reveal the spatial distribution of the SAMOs, thus affording
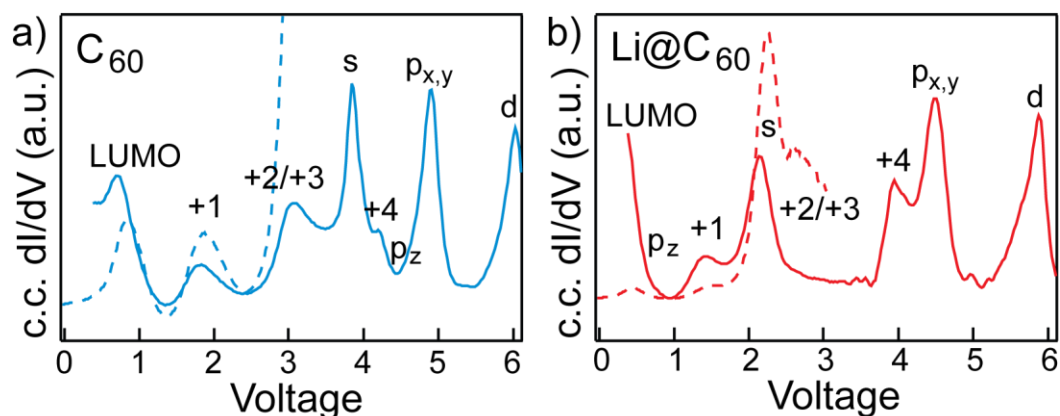
Figure 6.2: *C.c. dI/dV spectra (solid lines) and c.h. dI/dV spectra (dashed lines) illustrating the resonance peak structure of: **a)** C6-C_{60}, and **b)** C6-Li@C_{60} in a $\left(2\sqrt{3}\times2\sqrt{3}\right)R30°$ array on Au(111).*

unambiguous identification of the resonance peaks. However, such experiments were largely inconclusive for the 3 molecular systems which were prepared: large 2D arrays on Au(111), small 2D arrays and isolated fullerenes on Au(111), and isolated fullerenes on Cu(110)-(2×1)O.

With the peak structure for Li@C_{60} identified, attempts were then made to determine whether internal migration of the Li could be activated with single molecular precision (see **Chapter 5**). By employing extreme tunnelling parameters (+5.0 V, 1.85 ±0.15 µA), 307 Li@C_{60} constrained in large 2D arrays were selectively manipulated, resulting in the recognition of 14 reversible states and 1 irreversible state (caused by Li-ejection). Using a combination of microscopy and spectroscopy to differentiate between these discrete states resulted in the models shown in **Fig. 6.3** which depict the 14 proposed Li-cage coordination sites which can be adopted during the Li-migration.

8 of the 14 states correspond with the Li coordinating with C6-faces in levels 1, 2, 5 and 6 of the carbon cage. The remaining 6 states present the Li as having adopted hybrid positions referred to as level 3/4. These equatorial positions are suggested to be the result of intermolecular interactions between fullerenes in the 2D array altering the internal potential energy landscape of the carbon cage such that the 12 C6-faces in levels 3 and 4 are less favourable than a hybrid state between the two. The state with Li in level 1 is referred to as the native state since this is adopted by all Li@C_{60} after the preparation of the sample; this state is observed as the most favourable for the fullerene. The other 13 reversible states are referred to as switched states and, despite the different types of positions which can be adopted, a statistical analysis of these identified that there is no preference between these Li-cage coordinations. The Li-migration, therefore, is a random process and must utilise a mechanism which affords this.
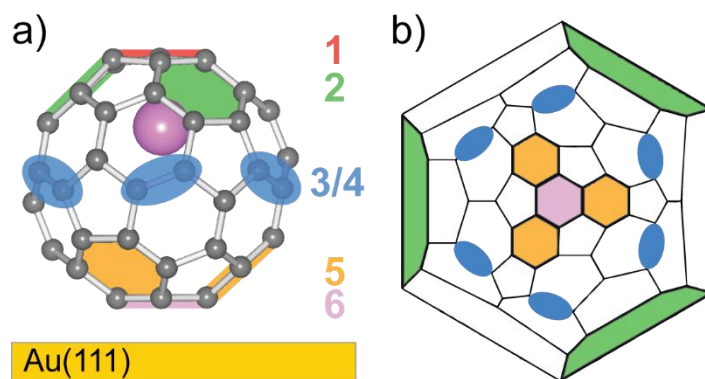
Figure 6.3: *The 14 proposed Li-cage coordination sites adopted during the manipulation of Li@C$_{60}$ are depicted here in **a)** a ball and stick model and **b)** a Schlegel diagram (level 1 and Li removed for clarity).*

Combining the work of Schulze *et al.*[10,11], Guo *et al.*[12] and Jorn *et al.*[13], a new mechanism was proposed which involved resonant tunnelling into the higher energy SAMOs (see **section 5.2.5**). Coupling with these, namely the $p_{x,y}$-SAMOs, was identified as the method by which the mechanism avoids both decomposition of the molecule and rapid conduction of the incidental electrons to the surface states. Further exploration of the conductivity of the SAMOs by observing the decomposition current for both C$_{60}$ and Li@C$_{60}$ (thus replicating and expanding upon the work of Schulze *et al.*[10,11]) was unsuccessful. However, considering the observations made by Guo *et al.* regarding facile conduction through SAMOs of C$_{60}$[12], enhanced conductivity of the SAMOs of Li@C$_{60}$ is also expected. It is suggested, therefore, that resonant tunnelling into the p_z- and s-SAMOs results in rapid conduction into the surface states due to the substantial overlap between the two. Whereas coupling with $p_{x,y}$-SAMOs reduces this conduction (due to minimal overlap) allowing the incidental electrons to penetrate the C$_{60}$ and excite the Li. The excitation then triggers the Li into rattling between the 14 coordination sites distributed around the interior of the carbon cage, hence the nickname molecular maraca.

The observations detailed above describe interesting behaviour for the Li@C$_{60}$ but there are additional questions which must be answered by further experimental, or theoretical, study of the molecular system. These are the focus of the following section.

6.2 - Further exploration for the C$_{60}$/Li@C$_{60}$ system on Au(111)

Building on the experiments already completed, and detailed in **Chapters 4** and **5**, a plethora of directions for further study can be easily considered. A selection of these are briefly mentioned below for the purpose of sparking discussion.

The first is to unequivocally identify the adsorption site for the fullerenes in the $\left(2\sqrt{3}\times2\sqrt{3}\right)$R30° array on Au(111). For a truly unambiguous identification, the exploration would require theoretical and experimental aspects in an attempt to avoid the assumptions which are observed in some other discussions of the molecular system. The theoretical study would be extensive since a map of the energetics involved in the adsorption configurations within the large 2D array of mixed fullerenes (C_{60} and Li@C_{60}) would be required. The calculations would predominantly be used to determine the most favourable surface sites for each adsorption orientation and to identify the barrier for rotation and translation between these sites. This would allow identification of the configuration of the most thermodynamically stable 2D array, in particular the adsorption site with the intention to settle the dispute over preference for hcp surface sites or nanopits for the C6-fullerene. This is where the STM-based exploration could prove most useful.

Upon preparation of the $\left(2\sqrt{3}\times2\sqrt{3}\right)$R30° arrays of mixed fullerenes on Au(111), manipulations of C_{60} could be used to prove or refute the concept of nanopits. By comparison of the "natural" fullerenes (those which adopt adsorption orientations as a result of the sample preparation) with those which are manufactured by manipulations, any apparent heights difference between the two should be clearly observable. For example, if a natural C6-C_{60} adsorbed to a nanopit is manipulated such that it adopts a 6:6-C_{60} orientation, it will appear shorter than a natural 6:6-C_{60} since it is adsorbed to a single atom vacancy. The potential for variation in the manipulated fullerenes is large, however, and this could cause the data collection to be a considerably time-consuming process.

Once the adsorption configuration of each fullerene is known unequivocally, the interfacial charge transfer can be accurately calculated. This, in turn, will allow more detailed calculations exploring the spatial distribution of the SAMOs for surface-bound C_{60} and Li@C_{60}, including those for the switched states. A greater understanding of the interaction between the SAMOs and the empty surface states would aid the discussion of both the conductivity of the SAMOs and the mechanism for Li-migration. Though these SAMO distributions will largely rely on DFT calculations, the degree of coupling of the SAMOs can be qualitatively determined by exploring the effect of resonant tunnelling into SAMOs on both the decomposition of the fullerenes and the parameters required to activate the Li-migration. Exploring the effect on decomposition was briefly attempted at the end of this project (as detailed in **section 5.3**) but it is hoped that further analysis would yield data which is more consistent with what is observed in the literature[10,11].

Besides identifying the spatial distribution of the SAMOs for each switched state and the effect of resonant tunnelling on the switch parameters, there are many other aspects of the Li-migration which could be explored with an STM. For example, attempting to activate Li-migration on an isolated

Li@C_{60}, and studying the effect of temperature on a surface-bound molecular system. The work of Aoyagi *et al*. noted the temperature dependence of the Li-migration in the bulk crystal phase[4,5], but attempts to study Li-migration as a function of temperature have yet to be explored with STM. The surface interaction may be sufficient to allow the Li-migration to be explored at higher temperatures, similarly utilising a different substrate may also have an effect on the Li-migration. For example, a stronger surface interaction or a different surface symmetry could alter the preference for certain cage-coordination sites or altering the number of available states entirely. Another aspect which would be interesting to explore is the potential for activating the Li-migration with photons. By using UV photons (~4 eV), for example, photonic coupling with the $p_{x,y}$-SAMOs (~4 V) may be observed resulting in activation of the Li-migration. Finally, as mentioned in **section 1.3**, one property which makes fullerenes such an attractive molecule for molecular electronics is the functionalisation which can be achieved without fundamentally altering the molecular properties. The addition of functional groups to the external surface of the endohedral fullerene could facilitate construction of large arrays by polymerisation. Moreover, such modifications to the carbon cage may also alter the internal surface potential experienced by the Li. In turn, this could afford a degree of control over the number or position of stable Li-cage coordination sites. The observation of 14 switched states for Li@C_{60} instead of 20 is evidence that this is possible. The interactions resulting in this behaviour are discussed in greater detail in **section 5.2.3.1**.

The possible experimental avenues for this molecule are widespread, those mentioned above merely consider the exploration with STM with the aid of some DFT but employing other techniques could evaluate yet more areas of interest. Considering the general outlook for exploration in the field of molecular electronics and application of the knowledge gained from this thesis, there are two key observations which are of particular interest. Firstly, the capacity for a single molecule to exhibit 14 discrete switch states could dramatically enhance the capacity for data storage compared to what is currently achieved with binary storage devices. More generally though, the observation that the SAMOs of fullerenes are capable of efficient electron transport and that the energy of these can be altered merely by encapsulation of different species, as was theorised by Zhao *et al*.[14]. Such facile electron transport could be utilised in a variety of material designs beyond molecular electronics, including such sectors as energy conversion as suggested by Guo *et al*.[12].

6.3 - <u>References</u>

(1)   Stefanou, M.; Chandler, H. J.; Mignolet, B.; Williams, E.; Nanoh, S. A.; Thompson, J. O. F.; Remacle, F.; Schaub, R.; Campbell, E. E. B. Angle-Resolved Photoelectron Spectroscopy and Scanning Tunnelling Spectroscopy Studies of the Endohedral Fullerene Li@C60. *Nanoscale* **2019**, *11*, 2668–2678. https://doi.org/10.1039/c8nr07088a.

(2)   Chandler, H. J.; Stefanou, M.; Campbell, E. E. B.; Schaub, R. Li@C60 as a Multi-State Molecular Switch. *Nat. Commun.* **2019**, *10* (1), 2283. https://doi.org/10.1038/s41467-019-10300-2.

(3)   Bakowies, D.; Thiel, W. MNDO Study of Large Carbon Clusters. *J. Am. Chem. Soc.* **1991**, *113* (10), 3704–3714. https://doi.org/10.1021/ja00010a012.

(4)   Aoyagi, S.; Tokumitu, A.; Sugimoto, K.; Okada, H.; Hoshino, N.; Akutagawa, T. Tunneling Motion and Antiferroelectric Ordering of Lithium Cations Trapped inside Carbon Cages. *J. Phys. Soc. Japan* **2016**, *85* (9), 094605. https://doi.org/10.7566/JPSJ.85.094605.

(5)   Aoyagi, S.; Sado, Y.; Nishibori, E.; Sawa, H.; Okada, H.; Tobita, H.; Kasama, Y.; Kitaura, R.; Shinohara, H. Rock-Salt-Type Crystal of Thermally Contracted C60 with Encapsulated Lithium Cation. *Angew. Chemie - Int. Ed.* **2012**, *51* (14), 3377–3381. https://doi.org/10.1002/anie.201108551.

(6)   Kwon, E.; Komatsu, K.-I.; Kawachi, K.; Kasama, Y.; Endo, T. Dynamic Behavior of Lithium-Cation in a C60 Fullerene Cage Elucidated by Terahertz Spectroscopy. *Mol. Cryst. Liq. Cryst.* **2014**, *598* (1), 28–31. https://doi.org/10.1080/15421406.2014.933294.

(7)   Suzuki, H.; Ishida, M.; Yamashita, M.; Otani, C.; Kawachi, K.; Kasama, Y.; Kwon, E. Rotational Dynamics of Li+ Ions Encapsulated in C60 Cages at Low Temperatures. *Phys. Chem. Chem. Phys.* **2016**, *18* (46), 31384–31387. https://doi.org/10.1039/C6CP06949E.

(8)   Yamada, Y.; Kuklin, A. V.; Sato, S.; Esaka, F.; Sumi, N.; Zhang, C.; Sasaki, M.; Kwon, E.; Kasama, Y.; Avramov, P. V.; Sakai, S. Electronic Structure of Li+@C60: Photoelectron Spectroscopy of the Li+@C60[PF6−] Salt and STM of the Single Li+@C60 Molecules on Cu(111). *Carbon N. Y.* **2018**, *133* (111), 23–30. https://doi.org/10.1016/j.carbon.2018.02.106.

(9)   Feng, M.; Zhao, J.; Petek, H. Atomlike, Hollow-Core–Bound Molecular Orbitals of C60. *Science (80-.).* **2008**, *320*, 359–362. https://doi.org/10.1126/science.1155866.

(10)   Schulze, G.; Franke, K. J.; Pascual, J. I. Resonant Heating and Substrate-Mediated Cooling of a Single C60 Molecule in a Tunnel Junction. *New J. Phys.* **2008**, *10*, 065005. https://doi.org/10.1088/1367-2630/10/6/065005.

(11)   Schulze, G.; Franke, K. J.; Gagliardi, A.; Romano, G.; Lin, C. S.; Rosa, A. L.; Niehaus, T. A.; Frauenheim, T.; Di Carlo, A.; Pecchia, A.; Pascual, J. I. Resonant Electron Heating and Molecular Phonon Cooling in Single C60 Junctions. *Phys. Rev. Lett.* **2008**, *100* (13), 136801. https://doi.org/10.1103/PhysRevLett.100.136801.

(12)   Guo, H.; Zhao, C.; Zheng, Q.; Lan, Z.; Prezhdo, O. V.; Saidi, W. A.; Zhao, J. Superatom Molecular Orbital as an Interfacial Charge Separation State. *J. Phys. Chem. Lett.* **2018**, *9* (12), 3485–3490. https://doi.org/10.1021/acs.jpclett.8b01302.

(13)   Jorn, R.; Zhao, J.; Petek, H.; Seideman, T. Current-Driven Dynamics in Molecular Junctions: Endohedral Fullerenes. *ACS Nano* **2011**, *5* (10), 7858–7865. https://doi.org/10.1021/nn202589p.

(14)   Zhao, J.; Feng, M.; Yang, J.; Petek, H. The Superatom States of Fullerenes and Their Hybridization into the Nearly Free Electron Bands of Fullerites. *ACS Nano* **2009**, *3* (4), 853–864. https://doi.org/10.1021/nn800834k.